Development of Superconducting Detectors for Millimeter-Wave Astronomy and Cosmology

by

Samantha Walker

B.A., Fordham University, 2016

M.S., University of Colorado Boulder, 2018

A thesis submitted to the

Faculty of the Graduate School of the

University of Colorado in partial fulfillment

of the requirements for the degree of

Doctor of Philosophy

Department of Astrophysical & Planetary Sciences

2023

Committee Members:

Nils Halverson, Chair

Johannes Hubmayr

Joel Ullom

David Brain

Meredith MacGregor

Walker, Samantha (Ph.D., Astrophysical & Planetary Sciences)

Development of Superconducting Detectors for Millimeter-Wave Astronomy and Cosmology

Thesis directed by Dr. Johannes Hubmayr

Superconducting detectors have revolutionized the field of millimeter-wave (mm-wave) and submillimeter-wave astrophysics and cosmology over the past twenty years. These detectors work at very low temperatures, typically well below 1 K, and exploit phenomena in superconductivity, such as the superconducting phase transition, to enable photon-noise-limited performance. Large arrays of superconducting detectors are being more frequently used as the detector of choice for current and future (sub)mm-wave instruments on ground-based telescopes. For example, by using arrays numbering nearly 10^5 detectors total, the upcoming ground-based experiment Simons Observatory (SO) will measure the very faint temperature and polarization anisotropies of the cosmic microwave background (CMB). Despite the prevalence of these detectors, challenges remain in operating large arrays of these detectors and optimizing their performance under dynamic loading conditions as seen when observing on-sky from ground-based observatories. My dissertation addresses the development and characterization of superconducting detectors, transition-edge sensor (TES) bolometers and microwave kinetic inductance detectors (MKIDs), at the National Institute of Standard and Technology (NIST) to study the mm-wave Universe. In this work, we discuss the optical characterization of TES bolometer pixels, consisting of four detectors, one for each passband and polarization, for the highest frequency passbands of SO. We describe our new MKID tuning method to optimize operation of MKID arrays, consisting of hundreds of resonators on the same feedline, for TolTEC, a mm-wave imaging polarimeter at the Large Millimeter Telescope. We also investigate the system noise of the TolTEC 1.1 mm array and comment on future steps towards improving its current readout configuration and noise.

Dedication

This thesis is dedicated to my parents for their unwavering love and support.

Acknowledgements

I would like to thank Johannes Hubmayr for his guidance and mentorship during graduate school and for his detailed comments and feedback throughout the thesis writing process. I am grateful to Jason Austermann, Jiansong Gao, Joel Ullom, Jordan Wheeler, Randy Doriese, Shannon Duff, Michael Vissers, Nils Halverson, David Brain, Benjamin Brown, and Meredith MacGregor. I would also like to thank the professors in the APS department, the researchers in the Quantum Sensors Division at NIST Boulder, and the scientific collaborations I have been involved with during graduate school (Simons Observatory, AliCPT, TolTEC) that have helped me grow so much as a scientist. From 2017–2020, I was supported by the National Science Foundation Graduate Research Fellowship under Grant No. DGE-1144083. From 2020–2023, I was supported by the NASA Future Investigators in NASA Earth and Space Science and Technology (FINESST) program under Grant No. 19-ASTRO20-0075.

Contents

Chapter

Tables

Table

Figures

Figure

Chapter 1

Introduction

This thesis concerns the development of two types of superconducting detectors and their application to astronomical observations. In this introductory chapter, we describe the scientific motivation for the development of these sensors. We then introduce the superconducting transition-edge sensor (TES) bolometer and the microwave kinetic inductance detector (MKID).

Low temperature, specifically superconducting, detectors have been of immense interest to the astronomy community over the past twenty years. Advances in the use of superconducting detector technologies have been motivated by challenges in ground-based millimeter-wave (mm-wave) and submillimeter-wave astronomy. Increasingly larger arrays of these detectors have enabled us to learn a tremendous amount about the history of the Universe and its contents. These detectors have also demonstrated powerful capabilities for observing electromagnetic radiation across wavelengths spanning many orders of magnitude, from millimeter to gamma-ray wavelengths. A few science case studies in (sub)millimeter-wave astronomy are described in the following section.

1.1 Science motivation

1.1.1 ΛCDM cosmology and the cosmic microwave background

Λ Cold Dark Matter (ΛCDM) is a predictive cosmological model. It is the simplest model allowed by current observational constraints and consists of only six parameters. This model provides a framework for understanding the composition, expansion, and evolution of the Universe. It describes a Universe consisting of ordinary matter or baryonic matter, radiation, non-baryonic matter such as neutrinos, cold or

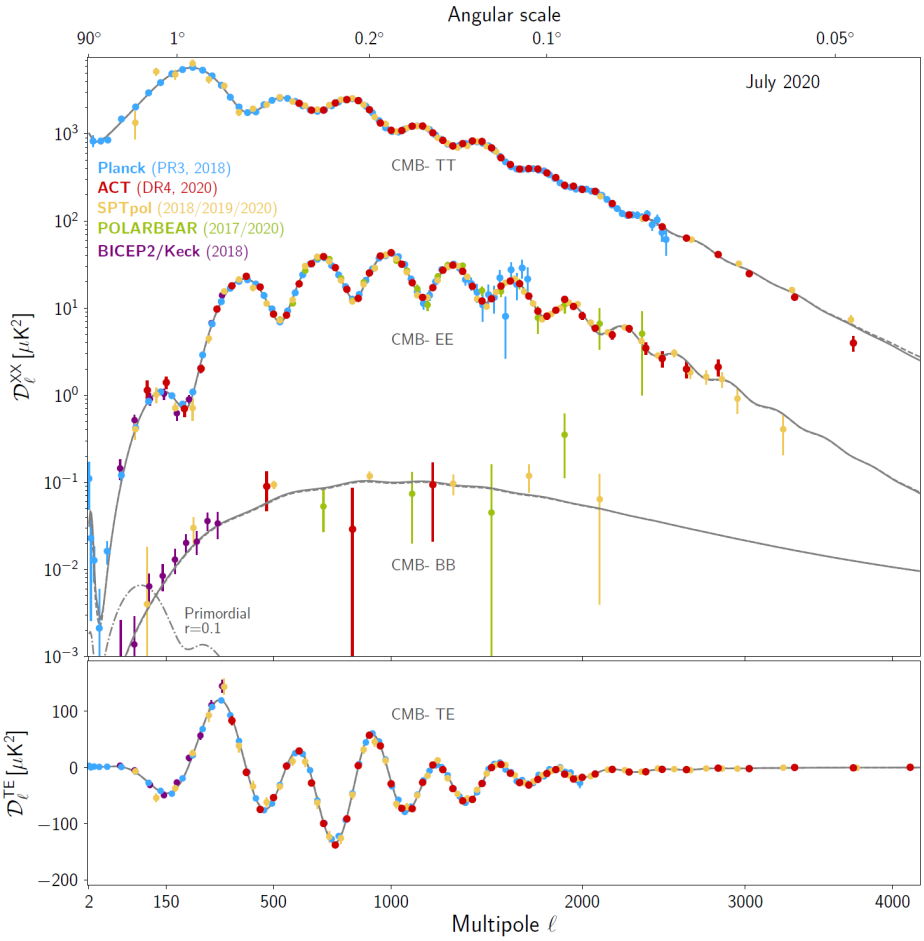

Figure 1.1: Recent measurements of CMB temperature anisotropy and polarization for the Planck, ACT, SPTpol, POLARBEAR, and BICEP2/Keck collaborations, from Choi et al. (2020) [39]. ΛCDM cosmological models (grey lines) fit well to measurements (colored points) of the CMB temperature anisotropy (TT), E-mode polarization (EE), B-mode polarization (BB), and cross-correlation power (TE) at a range of angular scales/multipoles ℓ. The dash dotted grey line corresponds to the primordial BB signal at $r = 0.1$. This signal of significant science interest is a few orders of magnitude below other CMB signals, making its detection very difficult.

non-relativistic dark matter (CDM), and a cosmological constant Λ associated with a dark energy or vacuum energy. Λ is responsible for the observed accelerated expansion of the Universe [136] in this model. The six parameters of ΛCDM [141] are the baryon density parameter $\Omega_{\rm b}$, the CDM density parameter Ω_c, the angular acoustic scale $\Theta_{\rm s}$ or the angular diameter distance to the sound horizon at last scattering [136], the scalar spectral index $n_{\rm s}$ associated with the spectrum of primordial scalar fluctuations, the amplitude of primordial scalar fluctuations $A_{\rm s}$, and the reionization optical depth τ. Also, of particular interest in cosmology, is the Hubble constant H_0 which describes how fast the Universe is expanding in units of $\mathrm{km\,s^{-1}\,Mpc^{-1}}$. Ω is defined as the ratio of the density parameter denote by the subscript relative to the critical density $\rho_{\rm crit} = 3H_0^2/(8\pi G)$. The critical density is the matter density of a spatially flat Universe, given in terms of the Hubble constant and the gravitational constant G. The density parameters may also be expressed as physical density values such as the physical baryon density $\Omega_{\rm b}h^2$ and physical CDM density $\Omega_{\rm c}h^2$, where h is the reduced Hubble constant such that $h = H_0/(100\,\mathrm{km\,s^{-1}\,Mpc^{-1}})$.

From these cosmological parameters, other model values which provide additional physical insight can be derived. These include H_0 and the age of the Universe t_0. This model is also defined by a set of assumptions, such as that general relativity (GR) is the correct theory to describe gravity on cosmological scales. ΛCDM has proven to be extremely successful in explaining a wide variety of cosmological observations, including the accelerating expansion of the Universe [147, 137], the statistical properties of large-scale structure [34], the observed abundances of different types of light elements such as hydrogen and helium [44], and the power spectrum and statistical properties of the cosmic microwave background (CMB) [135]. Despite these successes, with the increasing precision of cosmological and astrophysical data, some of these approaches are in tension with the ΛCDM model. For example, in the H_0 tension [53], there is a greater than 4σ difference between ΛCDM cosmology from CMB measurements [141] and methods that probe the more local Universe [146, 186].

There are many extensions considered for the ΛCDM model in the community (e.g. [136]), although most are not needed to match the current precision of measurements. While not required for ΛCDM to fit to cosmological data, something additional is needed to explain the otherwise huge coincidences of the "horizon" and "flatness" problems. Cosmic inflation is a leading theory, or extension (e.g., [72]), to

explain these open problems in cosmology. It describes a period of exponential expansion that occurred immediately after the Big Bang. In this thesis, the ΛCDM model serves as the framework for understanding measurements of the cosmic microwave background.

Millimeter-wave measurements of the cosmic microwave background have been a powerful tool for probing the earliest moments of the Universe (e.g., [92, 79, 140]). The CMB is the relic radiation created as the Universe cooled down and matter decoupled from photons. It is microwave radiation that is everywhere in the observable Universe. The existence of this background provided landmark evidence for the Big Bang theory as it can be used to explain the origin of this background. The CMB contains measurable, minute fluctuations that are hypothesized to have been seeded by primordial quantum fluctuations [95, 36] imprinted on the Universe during cosmic inflation. Early measurements of the CMB, including with the Cosmic Background Explorer (COBE) in 1992 [157], firmly established [2] the ΛCDM cosmological model beginning in the late 1990s [147]. Precision measurements of anisotropies in the CMB have also enabled us to learn a tremendous amount about the history of the Universe and its contents within the context of ΛCDM.

Furthermore, precision measurements of anisotropies in the polarization of the CMB also have the potential to reveal the existence of tensor perturbations from primordial gravitational waves [94] produced during cosmic inflation, where the amplitude of these gravitational waves would create CMB B-mode polarization (BB). The strength of these gravitational waves is parameterized by the tensor-to-scalar ratio, r, the ratio of tensor fluctuations to scalar fluctuations, and the energy density of the Universe. Figure 1.1 shows recent measurements [39, 142, 152, 41, 5] of the CMB temperature anisotropy (TT), E-mode polarization (EE), B-mode polarization (BB), and cross-correlation (TE) at a range of angular scales from [39], including a model of the primordial BB signal at $r = 0.1$. Each of these collaborations has used large arrays of TES bolometers for these measurements. As can be seen in this figure, the primordial B-mode polarization is much fainter than other CMB signals, making its detection extremely difficult.

CMB measurements are further complicated by astrophysical foregrounds, like synchrotron emission and galactic dust, which also emit at millimeter wavelengths. Higher frequency observations [35] will measure polarized Galactic dust emission that can aid in their removal. Figure 1.2 shows the root mean

square brightness temperature for polarization of different foregrounds compared to the CMB and how broad frequency coverage can disentangle their contribution to CMB measurements.

CMB experiments utilize large arrays, with thousands to tens of thousands of detectors across multiple arrays in current generation cameras. These arrays have broad spectral coverage to distinguish between these astrophysical foregrounds and the CMB since their spectral energy distributions (SEDs) are distinct. State of the art CMB experiments use TES bolometer pixels that are sensitive to both linear polarizations and have two or more passbands. One of the goals of upcoming CMB observatories, like SO, will be to reduce bounds on, perhaps even confirm, primordial gravitational waves by an order of magnitude over current experiments through measurements of CMB B-mode polarization at large angular scales. For example, one of the main science goals of SO [7] is to measure r to $\sigma(r) = 0.003$ for an $r = 0$ model, or $r \geq 0.01$ at 3σ. In Chapter 4, I discuss my work in [176] on the development and characterization of TES bolometer pixels with broad spectral coverage for the highest frequency passbands of SO and how they will enable us to better distinguish between astrophysical foregrounds and much fainter signals, like the CMB.

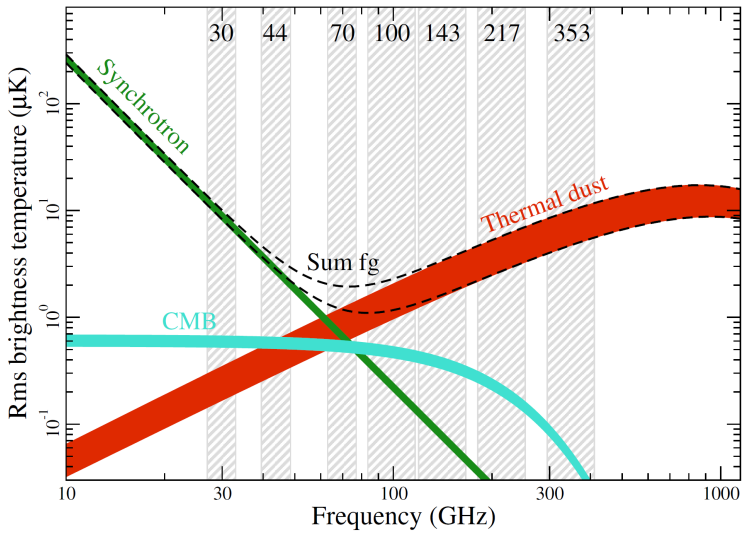

Figure 1.2: Root mean square brightness temperature for polarization as a function of frequency and astrophysical component, from Planck X (2016) [138]. The green and red curves denote significant foreground sources, synchrotron and thermal dust emission, respectively. The CMB polarization is denoted by the cyan curve. The dashed lines correspond to foreground when observing 73% (top) or 93% (bottom) of the sky. Horizontal bars denote instrument passbands, similar to Simons Observatory and CCAT-prime. Instruments with multiple passbands are needed to distinguish between the CMB and foreground sources.

1.1.2 Galaxy clusters and the Sunyaev–Zeldovich effect

Galaxy clusters are the most massive self-gravitating structures in the Universe and consist of many galaxies gravitationally bound together [103]. By studying their properties, galaxy clusters can serve as sensitive probes of cosmology [8, 154, 50]. They have offered particularly strong evidence for dark matter and dark energy [190]. They can also be used to trace the formation and evolution of large scale structure through cosmic time [158]. However, there remains much to learn about the complex dynamical processes in clusters [129] and to connect cosmological hydrodynamical simulations of these objects to observations.

Millimeter-wave observations of galaxy clusters are identified and studied with the Sunyaev-Zeldovich (SZ) effect [162, 163]. The SZ effect is a small spectral distortion to the CMB due to inverse Compton scattering of CMB photons by hot free electrons in the intracluster medium (ICM) of galaxy clusters and has enabled studies of some of the most massive galaxy clusters to date [78]. The SZ spectrum consists of two distinct effects that are independent of redshift known as the thermal SZ effect (tSZ) and kinetic SZ effect (kSZ). In the case of the tSZ effect, it is caused by the scattering of CMB photons by thermal electrons. This makes it a good probe of the thermal energy of electrons in the ICM and the total cluster mass of galaxy clusters. The amplitude of the tSZ effect at the center of a galaxy cluster is commonly described by the Compton y-parameter. The Compton y-parameter is a dimensionless measure of the line-of-sight integral of the electron pressure through the cluster [57] and is calculated as:

$$y = \frac{\sigma_{\rm T}}{m_{\rm e}c^2} \int n_{\rm e} k T_{\rm e} dl \tag{1.1}$$

where l is length, $\sigma_{\rm T}$ is the Thomson cross-section, c is the speed of light, k is the Boltzmann constant, $m_{\rm e}$ is electron mass, $n_{\rm e}$ is the electron density, and $T_{\rm e}$ is the electron temperature. Also, the Compton y-parameter is proportional to the cluster optical depth where $\tau_{\rm e} = \sigma_{\rm T} \int n_{\rm e}(r) dl$. Figure 1.4 shows the thermal SZ spectrum from [35] and how this spectrum changes with electron temperature. As can been seen in this figure, the tSZ spectrum has a characteristic spectral shape with a null at 217.5 GHz, a decrement in intensity at frequencies below this null, and an increment at higher frequencies.

There are also non-negligible relativistic corrections to the tSZ, called the relativistic SZ (rSZ). The rSZ is caused by hot thermal electrons, with energies of several keV (e.g., [91]), in the ICM of galaxy

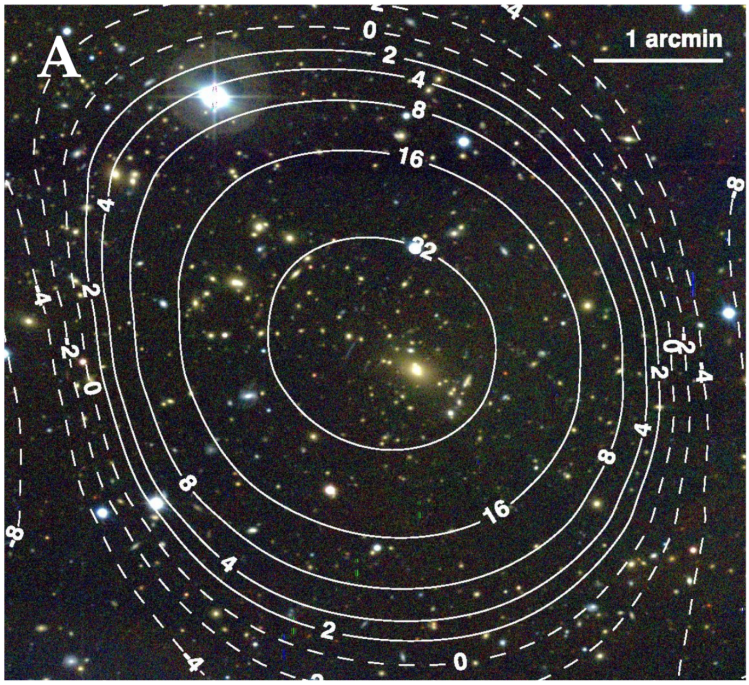

Figure 1.3: Example of a galaxy cluster from the 2500 deg^2 SPT-SZ cluster catalog, adapted from Bleem et al. (2015) [32]. This cluster (SPT-CL J2248–4431) is displayed as its optical/near-infrared RGB image (MPG/ESO WFI *IRV*-band image) with the thermal Sunyeav-Zeldovich detection contours over-plotted.

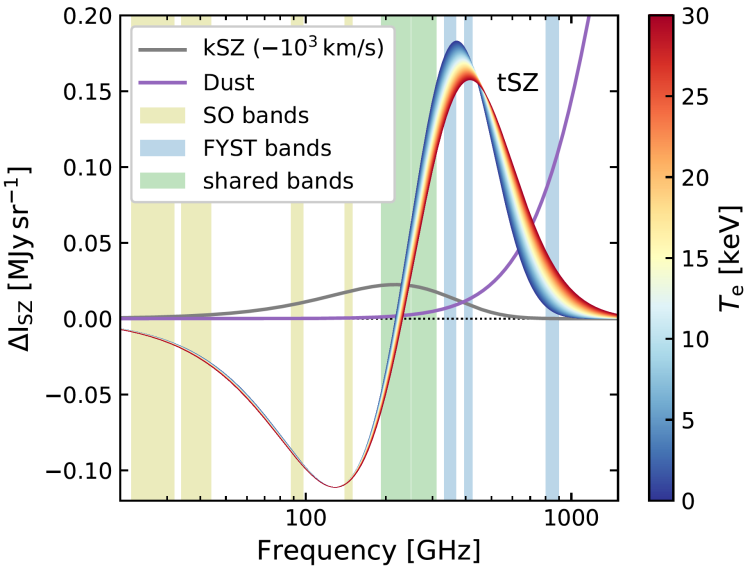

Figure 1.4: Spectrum of the thermal (tSZ) and kinetic Sunyeav-Zeldovich (kSZ) effects, from CCAT-prime Collaboration (2023) [35]. The horizontal bars denote the frequency coverage of SO and the CCAT-prime collaboration/Fred Young Submillimeter Telescope (FYST). Shown also is a model for the dust intensity. On the right, a color bar shows how this spectrum changes as a function of electron temperature (T_e) of galaxy clusters, the relativistic correction to the thermal SZ effect. A wealth of information about galaxy clusters can be gleaned from measurements of the SZ spectrum.

clusters. These electrons cause the tSZ spectrum to become a function of electron temperature, where higher temperatures shift the null towards higher frequencies, modulate the spectrum amplitude, and broaden the spectrum increment. Large surveys of galaxy clusters, including more than a thousand of some of the most massive clusters (cluster mass $M > 10^{14} M_{\odot}$), have been successfully measured using the tSZ effect by ground-based CMB observatories like the Atacama Cosmology Telescope (ACT) (e.g., [78]) and the South Pole Telescope (SPT) (e.g., [32, 31]).

Another SZ effect is the kinetic SZ effect. It is caused by the Doppler shift of scattered CMB photons by electrons with line-of-sight bulk flows in the rest frame of the CMB (e.g., [30]). This makes it a potential probe of the peculiar velocities of galaxy clusters. Compared to the tSZ effect, the rSZ correction to the tSZ and the kSZ effect are much smaller, which has made their detection very difficult to date [86, 3].

Upcoming (sub)mm observatories [7, 35] as well as mm-wave instruments like TolTEC [185] will measure galaxy clusters via the tSZ effect with unprecedented sensitivity and resolution. TolTEC is a mm-wave imaging polarimeter for the Large Millimeter Telescope (LMT), a 50 m single-dish steerable telescope in Sierra Negra, Mexico. Its camera consists of 7718 polarization sensitive MKIDs in three arrays with pass-bands centered at 1.1 mm, 1.4 mm, and 2.0 mm. By observing in these passbands simultaneously, TolTEC will measure the full tSZ spectrum, including the decrement at 150 GHz, the null at 217.5 GHz, and the increment at 270 GHz, and to greater sensitivity than comparable millimeter-wave MKID cameras to date [116]. Deep, high-resolution measurements of a large number of clusters will set better constraints on cluster mass by resolving cluster substructure. These observations will also enable a more complete picture of the thermodynamics of galaxy clusters independent of X-ray measurements, by resolving gas distributions and pressure fluctuations in the ICM. They could also provide new ways to constrain cosmological parameters.

In Chapter 6, we describe a new MKID tuning method and the application of this method to better optimize detector operation during TolTEC observations. In Chapter 7, we describe the characterization of the system noise of the TolTEC 1.1 mm array.

1.2 Superconducting detectors for millimeter/submillimeter-wave astronomy

An early example of bolometric detectors used in astronomy and particle detection, including (sub)mm cameras like SCUBA [81], BOLOCAM [66], and HAWC [75], was the neutron transmutation doped (NTD) germanium (Ge) thermistor [15]. These detectors have high impedance and are read out using low noise JFET amplifiers cooled down to $\sim 120\,\mathrm{K}$. Despite the maturity of these detectors, it is challenging to read out large arrays of these detectors, since JFET amplifiers are operated at much higher temperatures than the detectors so that heat dissipation to the bolometers is a concern [175]. More importantly, NTD Ge thermistors cannot be multiplexed, or where detector signals are read out with a small number of channels. This limitation greatly constrains the maximum number of detectors per array. It lead to the adoption of arrays of transition-edge sensor bolometers about twenty years ago and the use of arrays of microwave kinetic inductance detectors within the past decade.

Compared to early detector technologies like NTD Ge thermistors, another type of detectors used in (sub)millimeter-wave astronomy are superconducting detectors. By operating detectors at very low temperatures, well below 1 K, these detectors are extremely sensitive and achieve photon-noise-limited performance. The heat capacity C of a superconductor decreases exponentially with temperature [56] so that by operating in a regime well below a detector's superconducting transition temperature T_c, even a miniscule amount of heat or energy can be detected or resolved using a thermometer. In an example of this implementation called a thermistor bolometer, the detector uses a combination of an absorber, thermometer, and heat bath/sink. More specifically, the absorber is connected to a heat bath through a weak thermal link and a thermometer attached to the absorber is used to detect small changes in temperature. This temperature change can be due to a single photon in the case of X-ray and gamma-ray detection or a stream of photons at longer wavelengths, like the millimeter and/or submillimeter regime relevant to this work.

1.2.1 Sensitivity

To most efficiently map the CMB or other astrophysical sources, we aim to design and use detectors that are photon-noise-limited. In photon-noise-limited detectors, the noise from incident photons is the

dominant source of noise and is greater than the quadrature sum of all other noise sources. Noise is usually given in terms of noise equivalent power (NEP) or the uncertainty in detected power in a bandwidth of 1 Hz or one-half second integration. This means that lower NEP relates to more sensitive detectors. The photon NEP in units of W/$\sqrt{\text{Hz}}$ is given by [188]:

$$\begin{aligned} NEP^2_{\text{photon}} &= \int_0^\infty 2\frac{dP_{\text{abs}}}{d\nu} h\nu(1+\eta(\nu)m(\nu))d\nu \\ &\approx 2P_{\text{abs}} h\nu(1+\eta m) \end{aligned} \tag{1.2}$$

where ν is the band averaged center frequency, $dP_{\text{abs}}/d\nu$ is the power absorbed by the detector per frequency, h is the Planck constant, $\eta(\nu)$ is the optical efficiency, $m(\nu)$ is the photon occupation number, and $d\nu$ is the bandwidth. For CMB observations, $m(\nu)$ is a blackbody source so that $m(\nu) = \frac{1}{exp(h\nu/kT)-1}$. In the second part of Eqn 1.2, we assumed that our detectors are sensitive to light in a narrow bandwidth. In Eqn 1.2, the first term is referred to as Poisson/shot noise from uncorrelated photons and the second term is referred to as wave noise and is due to wave bunching. In addition to this photon noise, there are other sources of noise that originate from the detector itself and from the readout electronics used to operate these detectors. These noise sources need to be lower than and in some cases mitigated in the system to achieve photon-noise-limited performance. The following subsections will briefly introduce two types of superconducting detectors that are highly relevant to (sub)millimeter-wave astronomy and are the topic of this thesis, the TES bolometer and the MKID.

1.2.2 Transition-edge sensor bolometers

One type of thermistor bolometer which makes some of the most sensitive superconducting detectors and has been demonstrated at wavelengths spanning several orders of magnitudes across the electromagnetic spectrum is the transition-edge sensor (TES) bolometer. A TES bolometer is a very sensitive and stable thermal detector that measures incident radiation through heating of a temperature-dependent resistor [90], a superconducting film which is the TES itself. The TES is operated within its superconducting phase transition, which is extremely sharp and exists between its normal and superconducting states. The TES bolometer can be modeled as a temperature-dependent resistor of resistance R_{TES}, the combined heat

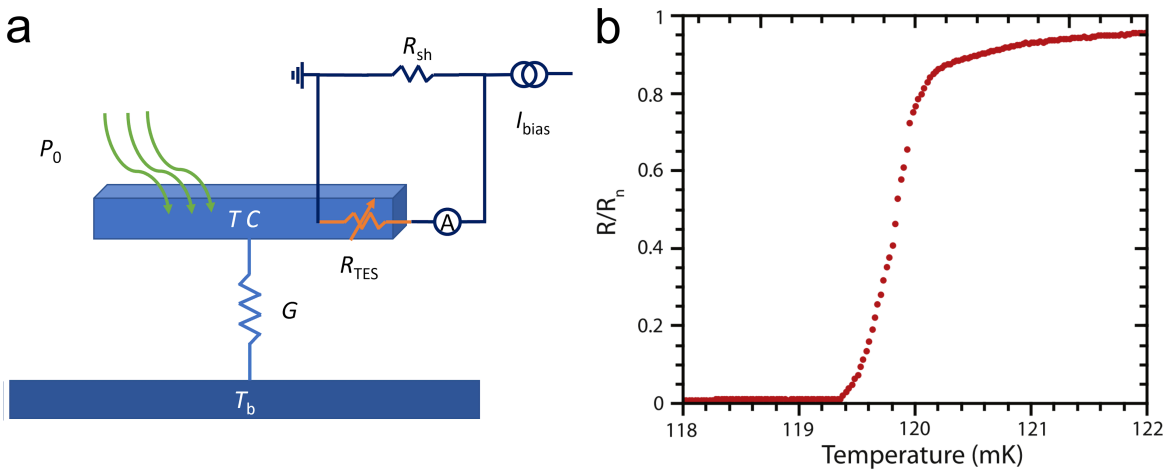

Figure 1.5: *a:* Diagram of a transition-edge sensor bolometer. Incident optical power P_0 heats a heat capacity C at temperature T with a very sensitive resistor R_{TES}, to measure the associated temperature change. The heat capacity and resistor are connected to a stable thermal reservoir at bath temperature T_{b} through a weak link with thermal conductance G. Also, shown is the TES input-circuit diagram. A bias current I_{bias} is applied to a shunt resistor R_{sh} in parallel with a sensitive ammeter for readout and a variable resistor R_{TES}, the TES. As power is incident on the heat capacity and heats it up, the resistance of the TES increases and this creates a detectable drop in current following $V = IR$. *b:* A measurement of the resistance of a TES as a function of temperature in response to a small excitation current, from Ullom and Bennett (2015) [170]. The resistance is plotted as a fraction of its normal resistance (R_{n}) and spans the superconducting-to-normal transition.

capacity of this resistor and an absorber C at temperature T and their connection to a stable thermal reservoir at bath temperature T_b through a weak link with thermal conductance G [89]. This is visualized in the conceptual drawing in Fig 1.5a. The value of G and C sets the natural time constant for this detector, the time required between independent measurements in the absence of electrothermal feedback, as $\tau \equiv C/G$. The TES can also be designed as a microcalorimeter to resolve the incident energy of individual photons [170].

TES bolometers are usually operated by voltage-biasing within their superconducting phase transition so that operation can be well-stabilized even after power absorption due to negative electrothermal feedback [90]. To operate the TES in this way, its input circuit includes a bias current $I_{\rm bias}$ that is applied to a small shunt resistor $R_{\rm sh}$ in parallel with sensitive ammeter for readout and a variable resistor, which is the TES itself. $R_{\rm sh}$ is small compared to a typical operating $R_{\rm TES}$ value, so the TES is operating toward the limit of a hard voltage bias, with $V \sim I_{\rm bias} R_{\rm sh}$. Figure 1.5b includes a circuit diagram of the TES input circuit discussed here. The sensitive ammeter represents an input coil inductively coupled to a single element superconducting quantum interference device (SQUID). The SQUID is a sensitive magnetic flux to voltage transducer that is used as a current sensor in this configuration.

The TES bolometer operates as a relative power meter. When optical power is dissipated on a TES bolometer, its temperature and resistance will increase as it is operated within its superconducting transition. This increase in resistance will create a corresponding drop in current since $V = IR$, following Ohm's Law. Through inductive coupling of an input coil to a SQUID, this temporary change in current will manifest as a change in input flux to the SQUID, whose output is further amplified and read out by room temperature electronics. Large arrays of detectors can be multiplexed, where detector signals are read out to a smaller number of channels, using SQUIDs. The specific details of the SQUIDs and their associated circuits depends on the type of readout employed.

This thesis describes the physics of a TES bolometer in more detail in Chapter 2. In Chapter 4, we discuss the design and characterization of TES bolometer pixels [176], consisting of four detectors, one for each passband and polarization, for the highest frequency passbands of the upcoming ground-based CMB observatory, SO [7]. In Chapter 5, we discuss dark, or non optically-coupled, measurements of TES bolome-

ter devices [177] for the upcoming CMB experiment, Ali CMB Polarization Telescope (AliCPT) [106]. This work is motivated by using large TES bolometer arrays with broad spectral coverage. For example, SO will utilize six frequency bands from 27 GHz to 280 GHz, to distinguish between astrophysical foregrounds, like synchrotron emission and galactic dust, and the CMB since their spectral energy distributions are distinct.

1.2.3 Microwave kinetic inductance detectors

Another category of superconducting detectors operates as quasiparticle detectors, that is they directly measure quasiparticles, or unpaired electrons, created in a superconducting film as a single photon or many photons break Cooper pairs. In superconductivity, a Cooper pair is a pair of electrons that move freely in a superconductor below the critical temperature T_c of the superconducting transition. They enable zero DC resistance in the material in this regime. An example of a type of quasiparticle detector is the microwave kinetic inductance detector (MKID).

MKIDs consist of superconducting films deposited on insulating substrates, such as silicon, with lithography to create thin-film, high quality factor (Q) micro-resonators [189]. In a superconductor, the formation of Cooper pairs below $T < T_c$ leads to zero DC resistance; however, there is still a small, but nonzero AC impedance due to the finite inertia of Cooper pairs [111]. There also exists in superconductors a small fraction of electrons thermally excited from their Cooper pairs at $T > 0$. The complex surface impedance of a superconductor is $Z_s = R_s + j\omega L_s$ where $\omega L_s >> R_s$ [189]. When operating a resonator, the AC circuit contributes a kinetic inductance L_k to the total surface inductance. MKIDs detect incident radiation when absorption of photons of energy $hf > 2\Delta \approx 3.52kT_c$ [169] breaks Cooper pairs in the superconducting film and create quasiparticles, where h is the Planck constant, f is frequency, Δ is the superconducting energy gap, and k is the Boltzmann constant.

Figure 1.5b shows the circuit of a single MKID. This MKID resonator is an LC circuit with capacitance C, variable kinetic inductance L_k, and magnetic inductance L_m that is capacitively coupled C_c to a feedline whose forward transmission S_{21} is measured. The L_k of a superconducting film changes with an increase in quasiparticle density.

In a MKID, when the quasiparticle density increases, it leads to a small change in the surface

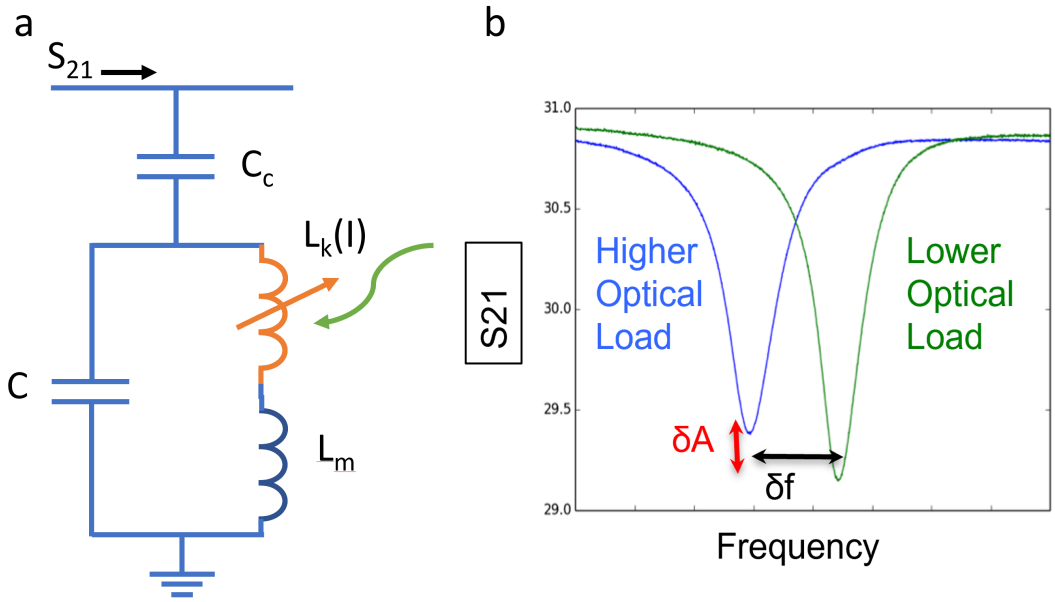

Figure 1.6: *a:* A MKID circuit diagram. A MKID resonator is an *LC* circuit with capacitance C, variable kinetic inductance $L_{\rm k}$, and magnetic inductance $L_{\rm m}$ that is capacitively coupled $C_{\rm c}$ to a feedline whose forward transmission S_{21} is measured. The $L_{\rm k}$ of a superconducting film changes with an increase in quasiparticle density. *b:* S_{21} measurement as function of frequency for a MKID resonator at two different optical loads/bath temperatures, from Galitzki et al. (2016) [61]. As the kinetic inductance and resistance of the MKID increase with greater quasiparticle production/higher loading, this leads to a measurable decrease in the resonant frequency δf and amplitude of the resonance δA. Courtesy of J. Austermann (NIST).

impedance of the film δZ_s, specifically a change in the kinetic inductance and resistance. The change in L_k leads to a measurable decrease in the resonant frequency while the change in resistance leads to a reduction in the quality factor of the MKID, respectively. Figure 1.6b shows two measurements at different loadings/bath temperatures for a MKID from the BLAST-TNG balloon experiment [61]. A reduction in kinetic inductance and resistance with increased loading can be clearly seen by a decrease in resonant frequency δf and a decrease in the amplitude of the resonance or quality factor δA.

While superconducting micro-resonators, of which MKIDs are one type, have been around since the 1960s [189], interest has grown dramatically (e.g., [68, 73]) in the almost two decades since their first demonstration as sensitive detectors by Caltech/JPL [49]. MKIDS are well suited to operating in large arrays since thousands of high Q resonators, or pixels, may be frequency-division multiplexed, or read out using a single pair of coaxial cables [189]. As such, these detectors can vastly simplify cryogenic readout and detector packaging of arrays compared to TES bolometers, the current workhorse of ground-based (sub)mm astronomy [83]. Since their inception, MKIDs have been developed for a variety of far-IR and (sub)mm instruments, including imaging cameras and spectrometers, that have either been deployed [68, 126, 62, 73, 14] or are currently in development, including the TolTEC camera [185] which is discussed in Chapter 6 and Chapter 7. MKIDs have also been demonstrated through UV, optical, and near-infrared observations [117, 123, 178].

This thesis describes the physics of MKIDs in more detail in Chapter 3. In Chapter 6, we discuss the development of a new method for optimal tuning of MKID arrays, consisting of hundreds of resonators on the same feedline for TolTEC [185], a mm-wave imaging polarimeter at the Large Millimeter Telescope. Then, in Chapter 7, we present a characterization of the system noise of the TolTEC 1.1 mm array due to sub-optimal readout-dominated noise performance during commissioning. Finally, we comment on future steps towards achieving photon-noise-limited performance of TolTEC detector arrays.

1.3 Examples of superconducting detectors

NIST has a heritage in developing arrays of feedhorn-coupled superconducting detectors for a number of experiments that operate from 1 mm to 4 mm [185, 131, 13, 156, 26]. In one approach to coupling light

from a feedhorn array, where there is one feedhorn for each detector, we utilize a circular waveguide with probes with superconducting transmission line to route signal to the detectors. This method can be used in tandem with superconducting integrated circuits (ICs) for dual-polarization as well as multichroic, or multi-passband, capabilities with on-chip filtering [83]. Figure 1.7a shows an example of TES bolometer studied in this thesis. We integrated four of these TES bolometers per detector pixel. We describe the development and characterization of this architecture in Chapter 4 for the highest frequency passbands of SO (220 GHz/280 GHz). This approach has matured over the past decades with TES bolometers and has been demonstrated with ground-based CMB experiments, including SPTPol [13] and AdvACT [77], as well as (sub)mm balloons, like SPIDER [58] and BLAST [62]. It is an active area of research to integrate MKIDs with an OMT in a similar manner [167, 21].

In a second approach, light is coupled from a feedhorn array directly to an impedance-matched direct absorber. This approach enables efficient coupling and dual-polarization sensitivity and has been used with MKID imaging cameras, including MUSIC [68], NIKA [126], and TolTEC [185]. Figure 1.7b shows an MKID pixel developed at NIST for TolTEC from [14]. Important components of this device, which has two MKIDs, one for each polarization, are highlighted in white. In Chapter 6, I discuss our work to develop a new tuning method for TolTEC MKID arrays. In Chapter 7, we describe our characterization of the system noise of TolTEC's 1.1 mm array.

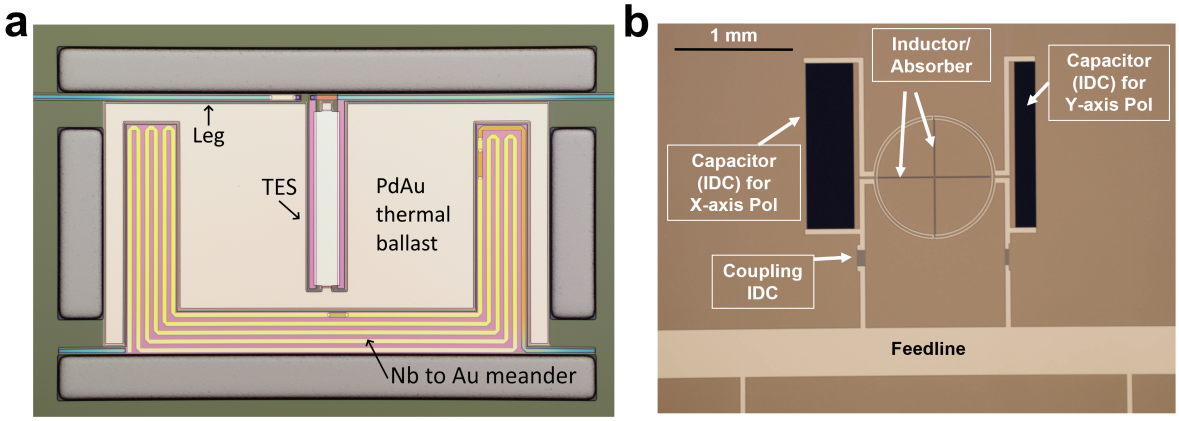

Figure 1.7: *a:* Micrograph of a TES bolometer for SO. Light couples from the feedhorn to a circular waveguide with probes (shown in Chapter 4). The circuit is terminated on the TES bolometer using a dissipative niobium (Nb) to gold (Au) transition. The TES is thermally isolated using a membrane and four legs. The TES heat capacity is increased with a palladium gold (PdAu) alloy thermal ballast that is electrically connected to the TES. *b:* Micrograph of a MKID pixel for TolTEC, from Austermann et al. (2018) [14]. Light couples from a feedhorn to an absorber which also serves as the inductor of two resonators, one for each polarization. Afterwards, radiation is coupled to each interdigitated capacitor (IDC) of a resonator and this circuit in turn capacitively coupled to a common feedline.

Chapter 2

Theory of transition-edge sensor bolometers

In this chapter, we discuss the underlying physics of transition-edge sensor (TES) bolometers. A TES bolometer is a very sensitive and stable thermal detector that measures the intensity of incident radiation through heating of a temperature-dependent resistor [90]. The main parts are a radiation absorber and a superconducting film. The TES is operated within its superconducting phase transition, which is extremely sharp and exists between its normal and superconducting states. When optical power is dissipated on a thermally isolated membrane connected to a TES, the TES temperature and resistance increase when it is operated within its superconducting transition. Through voltage-biasing within this transition, operation will be well-stabilized even after power absorption due to negative electrothermal feedback [90].

In this chapter, we begin with a discussion of the TES bolometer circuit, including what is measured to characterize these devices. Next, we briefly explain the characteristics of the superconducting transition of a TES and how it is used to make a very sensitive detector. We then talk about the TES response in the small-signal limit, which is broadly applicable to a variety of operating conditions. Afterwards, we discuss the TES electrical and thermal responses, including criteria for stability, saturation, and negative electrothermal feedback. We then go into detail about TES bolometer sensitivity, including different sources of noise, and finally what constitutes a photon-noise-limited detector.

2.1 The superconducting transition

A transition-edge sensor (TES) bolometer is a very sensitive thermal detector consisting of a photon absorber and a superconducting film that acts as a temperature-dependent resistor [90]. This film is operated

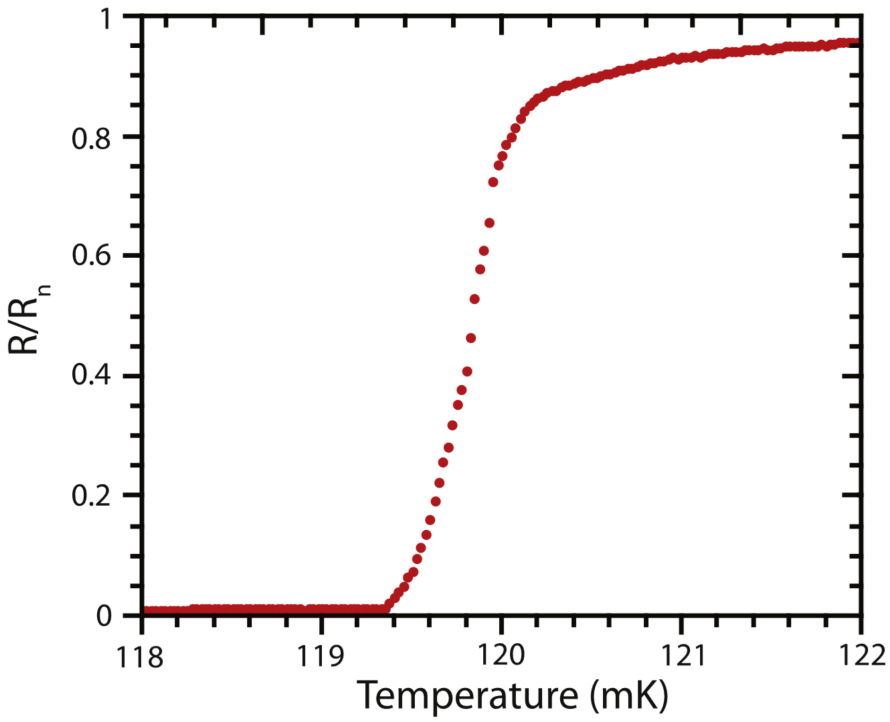

Figure 2.1: A measurement of the resistance of a TES as a function of temperature in response to a small excitation current, from Ullom and Bennett (2015) [170]. The resistance is plotted as a fraction of its normal resistance (R_n) and spans the superconducting-to-normal transition.

within its superconducting phase transition, an extremely sharp temperature region between the normal and superconducting states. Figure 2.1 shows an example measurement of the resistance of a TES as a function of temperature in response to a small excitation current [170]. The resistance is plotted as a fraction of its normal resistance $R_{\rm n}$, where the film has zero electrical resistance when superconducting and is at its normal-metal value when warmer than this transition temperature. The sharpness of this transition is quantified by the logarithmic sensitivity $\alpha_I = d\log R/d\log T$. This TES thermometer can be used as a bolometer to measure incident power, as discussed in this chapter, or as a microcalorimeter to resolve the incident energies of individual photons. This sensitivity enables thermal detectors with a small threshold to detect energy. We will now discuss some of the physics that influence the width and sharpness of this transition.

In the microscopic Bardeen, Cooper, and Schrieffer (BCS) theory [16, 169], superconductivity occurs when sets of free electrons bind together into Cooper pairs. In particular, a Cooper pair is formed when a free-flowing electron in a superconductor attracts positive ions in the lattice. These interactions with positive ions are mediated by phonons, or quantized vibrations of the lattice. This creates a cloud of positive charge that in turn attracts a second electron. The energy that binds Cooper pairs is referred to as the superconducting energy gap of the material, Δ. The formation of Cooper pairs in a superconductor prevents scattering and enables zero DC resistance below $T_{\rm c}$. The size of the Cooper-pair wave function depends on the temperature-dependent coherence length $\xi(T)$ such that $\xi(0) \approx 0.18 v_{\rm F}/(kT_{\rm c})$, where $\xi(0)$ is the zero-temperature coherence length, $v_{\rm F}$ is the Fermi velocity of the material, k is the Boltzmann constant, and $T_{\rm c}$ is the critical temperature of the superconductor. At temperatures above $T_{\rm c}$, Cooper pairs are broken spontaneously into their two constituent electrons or quasiparticles by thermal energies of order $kT_{\rm c}$ [90]. A hallmark of BCS theory is the relationship between the superconducting energy gap and the critical temperature such that $2\Delta \approx 3.52 kT_{\rm c}$ [169]. BCS theory is applicable to low-$T_{\rm c}$ materials, with $T_{\rm c} < 1$ K, such as the TES bolometers and MKIDs designed and characterized in this thesis.

Near the superconducting transition, a superconductor is well described by the macroscopic Ginzburg-Landau theory [65, 90]. The Ginzburg-Landau theory was derived from a Taylor expansion of the phenomenological order parameter, Ψ, which is proportional to the density of superconducting pairs [71]. As part of this theory, there is a dimensionless Ginzburg-Landau parameter, $\kappa \equiv \lambda_{\rm eff}(T)/\xi(T)$, where $\lambda_{\rm eff}(T)$ is

an effective penetration depth that quantifies how much an applied magnetic field is screened by an induced Cooper-pair supercurrent. The value of κ determines whether a superconducting film, the TES, is a Type I ($\kappa < 1/\sqrt{2}$) or Type II ($\kappa > 1/\sqrt{2}$) superconductor. The type of superconductor influences the physics of the superconducting transition and its noise, current-carrying capability, and sensitivity to applied magnetic field [90]. For transition-edge sensors, superconducting films are usually in the dirty limit, where $\xi(T) > 1$ μm and electron mean free path l are a few tens or hundreds of nanometers. For a film in the dirty limit at $T = T_c$, the Ginzburg-Landau parameter κ is [169]:

$$\kappa \approx 0.715\lambda_L(0)/l(d) \tag{2.1}$$

where $\lambda_L(0)$ is the zero temperature penetration depth or London penetration depth and l is the electron mean free path as a function of film thickness d.

The superconducting transition has a finite width even in the case of a uniform film with near-zero applied current and no external magnetic field. Phenomena related to flux motion lead to this finite transition and differ for Type I and Type II superconductors. These mechanisms are described in more detail by Irwin & Hilton (2005) [90]. The transition widths measured under bias in actual TESs are much larger in practice, on the order of a few milliKelvin with typical bias currents as seen in Figure 2.1. The broadening of the superconducting transition is compounded by non-ideal effects, including nonuniformity of film T_c, external magnetic fields, large bias currents, and variations in temperature within the film due to Joule heating and other sources of loading.

Careful detector design can help address some of these non-ideal effects. For example, TES self-heating can cause temperature variations across the device, leading to reduced sensitivity and even instability. In the case of uniform heat flow from the TES to a heat bath, Irwin et al. (1998) [89] found that the condition for stability against geometric separation into superconducting and normal phases for a rectangular film is [90]:

$$R_n < \pi^2 \frac{L_0 T_c n}{G\alpha_I} \tag{2.2}$$

where R_n is the normal resistance, L_0 is the Lorenz number, n is an exponent related to power flow to a heat bath, and G is the thermal conductance to the heat bath. From Eqn 2.2, we see that T_c and α_I are important

quantities. For a TES with R_n low enough to satisfy Eqn 2.2, self-heating can be minimized.

The critical temperature, T_c, must be chosen to achieve the necessary sensitivity and response time for a TES. These quantities strongly depend on temperature because the heat capacity, thermal conductance, noise, and other parameters also exhibit a temperature dependence. It is therefore important to choose a transition temperature appropriate for each application. This can be done by choosing an elemental superconductor with an appropriate T_c or tuning the T_c by using the proximity effect in a normal/superconductor bilayer (e.g. [174]) or using magnetic dopants (e.g. [52]). In Chapter 4 and Chapter 5, we describe measurements of TES bolometers made of a doped aluminium-manganese (Al-Mn) alloy [55] and in Chapter 6 and Chapter 7, we describe measurements of MKIDs with a superconducting film of varying titanium nitride (TiN) and titanium (Ti) layer thicknesses, specifically a TiN/Ti/TiN trilayer [14] made using the proximity effect.

2.2 TES small-signal limit

In the small-signal limit, we may solve for the TES response to different input signals and use those expressions to derive conditions for TES stability, negative electrothermal feedback, and TES saturation power among other things. Following the work of Irwin & Hilton (2005) [90], we describe the TES bolometer circuit, the TES electrical and thermal responses, including its response to an incident power load as in a bolometer or the power-to-current responsivity, criteria for TES stability, negative electrothermal feedback, and TES saturation.

2.2.1 The TES bolometer circuit

We discuss the electrothermal bias circuit of a TES via two coupled differential equations, one describing its thermal behavior and one its electrical behavior. We model a TES as a temperature- and current-dependent resistor, $R(T, I)$. The combined heat capacity of this resistor and its absorber is C at a temperature T. They are connected to a stable thermal reservoir at bath temperature T_b through a weak link with thermal conductance G [89]. This is visualized in the conceptual drawing in Fig 2.2. The values of G and C set the natural time constant for this detector, the time required between independent measurements in the absence

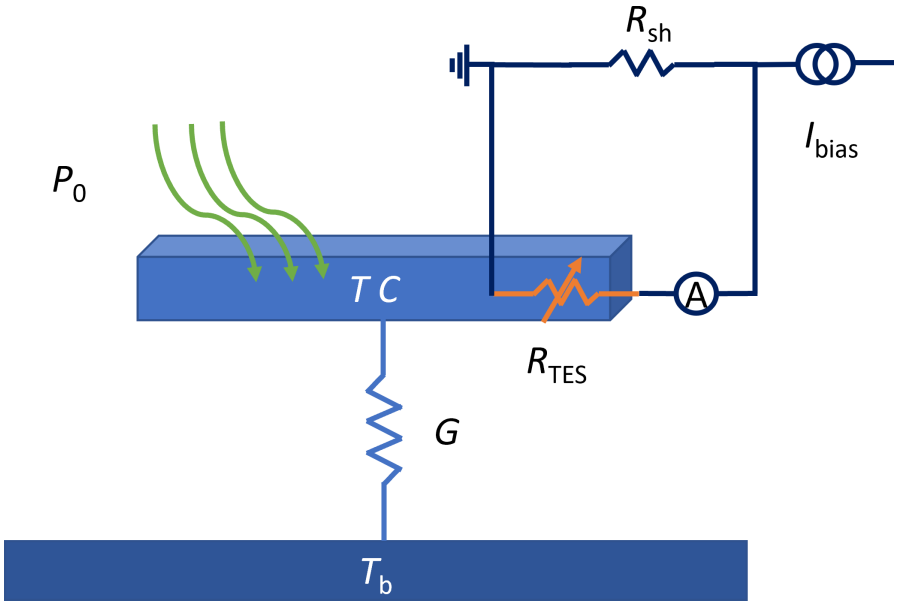

Figure 2.2: Diagram of a transition-edge sensor bolometer. Incident optical power P_0 heats a heat capacity C at temperature T with a very sensitive resistor R_{TES} to measure the associated temperature change. The heat capacity and resistor are connected to a stable thermal reservoir at bath temperature T_{b} through a weak link with thermal conductance G. Also shown is the TES input-circuit diagram. A bias current I_{bias} is applied to a shunt resistor R_{sh} in parallel with a sensitive ammeter for readout and a variable resistor R_{TES}, the TES. R_{sh} is small compared to a typical operating R_{TES} value, so the TES is operating toward the limit of a hard voltage bias, with $V \sim I_{\mathrm{bias}} R_{\mathrm{sh}}$. As power is incident on the heat capacity and heats it up, the resistance of the TES increases and this creates a detectable drop in current following $V = IR$.

of any electrothermal feedback, as $\tau \equiv C/G$.

The TES circuit includes a real source impedance ranging from zero when constant voltage-biased to infinite when constant current-biased. Historically, TESs were current-biased and read out via a voltage amplifier because sufficiently sensitive ammeters were not practical [90]. In the modern era, after 1995 [87], TESs are often voltage-biased using a small shunt resistor $R_{\rm sh}$ in parallel with the TES resistance $R_{\rm TES}$, such that $R_{\rm TES} \gg R_{\rm sh}$, and read out via a superconducting quantum interference device (SQUID) current amplifier. By voltage-biasing a TES within its superconducting transition, operation is well-stabilized even after power absorption due to negative electrothermal feedback. This low impedance configuration includes a reactance from parasitic inductance in the leads and inductance from a SQUID input coil and we often add other L intentionally to slow down the electrical response. The input coil is used to inductively couple the TES circuit to a SQUID. The SQUID acts a sensitive magnetic flux-to-voltage transducer that is used as an ammeter for the current through its input coil that creates flux.

The TES operates as a relative power meter. In a voltage-biased TES, the input circuit includes a bias current, $I_{\rm bias}$, that is applied to a small shunt resistor $R_{\rm sh}$, for a voltage $V = I_{\rm bias}R_{\rm sh}$, in parallel with any parasitic resistance $R_{\rm par}$ in the circuit (not shown). The sensitive ammeter represents an input coil with inductance L coupled to a SQUID. The SQUID is part of the voltage-biased readout and acts as a sensitive ammeter. Large arrays of detectors can be multiplexed, where detector signals are read out to a smaller number of channels, using SQUIDs. SQUID amplifiers are operated at low temperatures and read out with room temperature electronics. The specific details of the SQUIDs and their associated circuits depends on the type of readout employed. The input coil is in series with a variable resistor, which is the TES itself. Figure 2.2 includes a circuit diagram of the TES bias circuit.

2.2.2 TES electrical and thermal response

The response of the TES is described by a system of two coupled differential equations for the electrical and thermal circuits. The thermal differential equation, which describes how the temperature T of the

TES changes with time t is given by [90, 115]:

$$\begin{aligned} C\frac{dT}{dt} &= P_{\text{J}} + P_{\text{opt}} - P_{\text{bath}} = P_{\text{diss}} - P_{\text{bath}} \\ &= P_{\text{diss}} - \int_{T_{\text{b}}}^{T} G(T')dT' \end{aligned} \tag{2.3}$$

where C is the lumped heat capacity, including the TES and absorber, P_{bath} is the power flowing from the TES to the heat bath, P_{J} is the Joule electrical power dissipation, and P_{opt} is the signal/optical power. We have also defined the total power dissipated in the absorber and TES as $P_{\text{diss}} = P_{\text{J}} + P_{\text{opt}}$. The Joule power dissipation is related to the voltage bias V_{bias} and TES resistance as $P_{\text{J}} = V_{\text{bias}}^2/R_{\text{TES}}(T,I)$. In the second part of Eqn 2.3, we have related P_{bath} to the thermal link with thermal conductance G since $G \equiv dP_{\text{bath}}/dT$. Also, for power flow to the heat bath P_{bath}, we usually assume a power law dependence so that:

$$P_{\text{bath}} = K(T^n - T_{\text{b}}^n) \tag{2.4}$$

where K and n depend on the nature of the thermal weak link to the heat bath and T_{b} is the bath temperature. K is related to the thermal conductance as $K = G/(nT^{n-1})$. The electrical differential equation, which describes how the current I through the TES changes with time is given by:

$$L\frac{dI}{dt} = V - IR_{\text{L}} - IR_{\text{TES}}(T,I) \tag{2.5}$$

where $R_{\text{TES}}(T,I)$ is the electrical resistance of the TES which depends on both temperature and current.

From Eqn 2.3 and Eqn 2.5, we see that in the case of a voltage-biased TES within its superconducting transition, when optical power is dissipated on a TES bolometer or bath temperature is increased, the temperature of the absorber/TES and also TES resistance $R_{\text{TES}}(T,I)$ rise. Since the TES is operated at near constant voltage, this increase in resistance will create a corresponding drop in current through the thermometer since $V = IR$, following Ohm's Law. It also reduces the dissipated Joule electrical power P_{J}. These two changes stabilize the TES temperature within its superconducting transition. Through inductive coupling of an input coil to a SQUID, this temporary current drop will manifest as a change in input flux to the SQUID, whose output is further amplified and read out by room temperature electronics. The relationship between the electrical readout circuit and thermal properties of the system with time is called electrothermal feedback. To help quantify the dependence of the TES resistance, it is common to define a unitless

logarithmic temperature sensitivity α_I and current sensitivity β_I as:

$$\alpha_I \equiv \left.\frac{\partial \log R}{\partial \log T}\right|_{I_0} = \left.\frac{T}{R}\frac{\partial R}{\partial T}\right|_{I_0} \tag{2.6}$$

and

$$\beta_I \equiv \left.\frac{\partial \log R}{\partial \log I}\right|_{T_0} = \left.\frac{I}{R}\frac{\partial R}{\partial I}\right|_{T_0} \tag{2.7}$$

In the small-signal limit, nonlinear terms in Eqn 2.3 and Eqn 2.5 can be linearized around the steady-state values of resistance R_0, temperature T_0, and current I_0. In this limit, we can also use steady-state values of heat capacity C and thermal conductance G. If we expand Eqn 2.3 for a small oscillation in absorbed optical power at frequency ω, or $\delta P_{\rm opt} e^{j\omega t}$, we find that [115]:

$$j\omega C\delta T = \delta P_{\rm opt} + \frac{\partial P_{\rm J}}{\partial T}\delta T - G\delta T \tag{2.8}$$

where $\delta T = T - T_0$ in the small-signal limit. From Eqn 2.8, we rearrange terms to write $\delta P_{\rm opt}$ as:

$$\delta P_{\rm opt} = (j\omega C + G + \alpha_I P_{\rm J}/T)\delta T \tag{2.9}$$

where we have used Eqn 2.6 for α_I. We can expand the TES resistance around for small signals to first order too so that [90]:

$$\begin{aligned} R(T,I) &\approx R_0 + \left.\frac{\partial R}{\partial T}\right|_{I_0}\delta T + \left.\frac{\partial R}{\partial I}\right|_{T_0}\delta I \\ &\approx R_0 + \alpha_I\frac{R_0}{T_0}\delta T + \beta_I\frac{R_0}{I_0}\delta I \end{aligned} \tag{2.10}$$

where $\delta I = I - I_0$. Likewise, the Joule power can be expanded to first order such that:

$$P_{\rm J} = I^2 R \approx P_{\rm J,0} + 2I_0R_0\delta I + \alpha_I\frac{P_{\rm J,0}}{T_0}\delta T + \beta_I\frac{P_{\rm J,0}}{I_0}\delta I \tag{2.11}$$

where the steady-state Joule power is $P_{\rm J,0} = I_0^2 R_0$.

From Eqn 2.10, we observe that for a TES at constant temperature, the dynamic resistance of the TES can be simplified to:

$$R_{\rm dyn} \equiv \left.\frac{\partial V}{\partial I}\right|_{T_0} = R_0(1+\beta_I) \tag{2.12}$$

Another quantity of interest in operating a TES is the low-frequency loop gain under constant current which we define as:

$$\mathscr{L}_I \equiv \frac{P_{\mathrm{J},0}\alpha_I}{GT_0} \tag{2.13}$$

To solve the system of coupled equations, consisting of the TES thermal differential equation (Eqn 2.3) and current differential equation (Eqn 2.5), they can be linearized by substituting in the above expansions around steady-state values for P_{bath}, $R(T,I)$, and P_{J} and using $\mathscr{L}_I$ and the natural time constant $\tau \equiv C/G$. Afterwards, this system can be solved by using harmonic expansion or a matrix change of variables approach. The specific details of how perform this change of variables [109] can be found in Irwin & Hilton (2005) [90].

In bolometric applications, where the power levels of arrays of TES detectors are monitored, the power-to-current responsivity s_I [A/W] of a TES to changes in absorbed optical power under constant voltage bias is one of the most important parameters. It enables measured currents to be referred back to input power signals. We have denoted this quantity by a lowercase s to differentiate it from the noise power spectral density discussed later. The power-to-current responsivity s_I is [115]:

$$\begin{aligned} s_I &= \frac{dI}{dR}\frac{dR}{dT}\frac{dT}{dP_{\mathrm{opt}}} = -\frac{V_{\mathrm{bias}}}{R^2}\frac{dR}{dT}\frac{1}{j\omega C + G + \alpha_I P_{\mathrm{J}}/T} \\ &= -\frac{1}{V_{\mathrm{bias}}}\frac{\alpha_I P_{\mathrm{J}}/GT}{1+\alpha_I P_{\mathrm{J}}/GT + j\omega C/G}\left[\frac{A}{W}\right] \end{aligned} \tag{2.14}$$

where we have used Eqn 2.9 for dT/dP_{opt} and $V_{\mathrm{bias}} = IR$ in the first part. In the second part of Eqn 2.14, we have also used $P_{\mathrm{J}} = V_{\mathrm{bias}}^2/R(T,I)$.

We can also express the power-to-current responsivity S_I in terms of the loop gain $\mathscr{L}_I$ so that:

$$s_I = -\frac{1}{V_{\mathrm{bias}}}\frac{\mathscr{L}_I}{\mathscr{L}_I+1}\frac{1}{1+j\omega\tau_{\mathrm{eff}}}\left[\frac{A}{W}\right] \tag{2.15}$$

where we have used the effective time constant $\tau_{\mathrm{eff}} = \tau/(\mathscr{L}_I+1)$. This expression (Eqn 2.15) does not take into account non-ideal properties of the TES and readout electronics. We refer to Irwin & Hilton (2005) [90], an analysis of additional effects, including the nonlinear TES resistance $R_{\mathrm{TES}}(T,I)$, parasitic resistance in the circuit, and inductance in the readout.

2.2.3 TES stability

Generally, the stability of a TES depends on whether its response is damped or oscillating and whether it is being operated using a current or voltage bias. The desire for stable operation with strong feedback $\mathscr{L}_I \gg 1, \beta_I$ motivated the use of voltage-biased detectors. We follow the discussion in Irwin & Hilton (2005) [90] for the TES stability under different damping conditions.

In the case of an overdamped TES, the response will be stable for steady-state resistance R_0 and load resistor $R_L = R_{\rm sh} + R_{\rm par}$ when [90]:

$$R_0 > \frac{\mathscr{L}_I - 1}{\mathscr{L}_I + 1 + \beta_I} R_{\rm L} \tag{2.16}$$

For a current-biased TES, this constrains the value of the load resistor that can be used and prevent thermal runaway from positive feedback when $\mathscr{L}_I > 1$. By comparison, for a voltage-biased TES, this condition is always satisfied since $R_0 > R_{\rm L}$ so an overdamped or critically-damped TES is stable.

In the case of an underdamped TES, the stability criterion is now:

$$\mathscr{L}_I \leq 1, \textbf{ or } \mathscr{L}_I > 1 \text{ and } L < \frac{\tau}{\mathscr{L}_I - 1}(R_L + R_0(1+\beta_I)) \tag{2.17}$$

as a constraint on the inductance L. When a TES is critically damped, Eqn 2.16 and Eqn 2.17 are equivalent conditions.

2.2.3.1 Negative electrothermal feedback

A TES is considered to be operated with strong negative electrothermal feedback (ETF) when the voltage bias is such that $R_{\rm L} \ll R_0$ and there is high low-frequency constant current loop gain such that $\mathscr{L}_I \gg 1, \beta_I$. In this limit, the TES is stable against thermal runaway even at high loop gain $\mathscr{L}_I$/faster response time since the reduction in Joule power with increased temperature will act as a restoring force. At $T_{\rm b} \ll T_{\rm c}$, Joule power dissipation also causes a TES to self-bias in temperature within its transition. This characteristic reduces sensitivity to TES parameter differences, like $T_{\rm c}$, allowing for operation of large arrays of TES detectors.

From the thermal (Eqn 2.3) and electrical (Eqn 2.5) differential equations, we see that an increase in temperature of the TES leads to a corresponding increase in the TES resistance $R_{\rm TES}(T, I)$. For a TES biased

at a near constant voltage, this change in resistance leads a drop in current through the TES following $V = IR$ and a drop in dissipated Joule electrical power. This causes the temperature of the TES to stabilize.

Electrothermal feedback can be either positive or negative depending on a few factors. In a TES, the logarithmic temperature sensitivity α_I is positive so the resistance of a TES increases with temperature while biased in its superconducting transition, such as Figure 2.1. When operating a TES under current-bias conditions, or $R_{\rm L} \gg R_0$, temperature, resistance, Joule power $P_{\rm J} = I^2R$ increase. This corresponds to positive ETF. By comparison, when operating a TES under voltage-bias conditions, or $R_{\rm L} \ll R_0$, $P_{\rm J} = V^2/R$ decreases with increasing temperature. This corresponds to negative ETF.

A overdamped/critically-damped TES (Eqn 2.16) is stable when the TES is voltage-biased since $R_0 > R_{\rm L}$. By comparison, a damped current-biased TES where $R_{\rm L} \gg R_0$ will only stable against thermal runaway when $\mathscr{L}_I \leq 1$. These stability conditions greatly restrict the available operational parameters of current-biased TESs.

The complex impedance of a TES is useful probe of the linear circuit parameters of a TES. The circuit complex impedance and complex impedance of the TES $Z_{\rm TES}$ are given by [90]:

$$Z_\omega = V_\omega / I_\omega = R_{\rm L} + i\omega L + Z_{\rm TES} \tag{2.18}$$

and

$$Z_{\rm TES} = R_0(1+\beta_I) + \frac{R_0\mathscr{L}_I}{1-\mathscr{L}_I}\frac{2+\beta_I}{1+j\omega\tau_I} \tag{2.19}$$

where $\tau_I = \tau/(1-\mathscr{L}_I)$ is the steady-state current-biased thermal time constant. In Chapter 5, we discuss complex impedance measurements of dark, or non-optically coupled, Al-Mn TES bolometers. These measurements enabled us to characterize the dynamics of TES bolometers with different geometries and thermal conductance over a range of detector bias and loading conditions. From this, we were able to choose a bolometer design with optimal stability for AliCPT before fabrication of arrays.

2.2.3.2 TES saturation

In the limit of large signals, power loads on a TES bolometer are capable of saturating the TES by driving it outside of its narrow transition region. The saturation power of a TES bolometer is given by [90]:

$$P_{\rm sat} = P_{\rm bath}(T) - \left(\frac{V}{R_{\rm L}+R_{\rm n}}\right)^2 R_{\rm n} \tag{2.20}$$

where $P_{\rm bath}(T) = K(T^n - T_{\rm b}^n)$ is the power flowing to the heat bath at temperature T, $R_{\rm n}$ is the normal resistance of the superconductor, and R_0 is the steady-state resistance. We can simplify Eqn 2.20 since a voltage-biased TES will have $R_{\rm L} = 0$ and a narrow superconducting transition will have an approximately constant $P_{\rm bath}$. Equation 2.20 thus simplifies to:

$$P_{\rm sat} = \left(1 - \frac{R_0}{R_{\rm n}}\right) P_{\rm bath} \tag{2.21}$$

When the signal power exceeds this saturation power $P_{\rm sat}$, a TES bolometer loses all sensitivity. This condition for device saturation motivates the selection of a larger thermal conductance G for the weak link connecting the TES and heat capacity to the bath to avoid this occurring. However, careful selection of G is needed as larger values will degrade detector NEP even at low signal powers.

2.3 Sensitivity

In astronomical applications, in which the photon signal is faint, we strive to design detectors that are photon-noise-limited or background-limited, that is where the noise from incident photons is the dominant source of noise in the detector. When a measurement is dominated photon noise, specifically by the shot noise component of the photon noise (Eqn 2.23), the signal-to-noise ratio (SNR) will increase as $\sqrt{N}$, where N is the number of measurements. Detectors are said to be operating in the background-limited infrared photodetector limit (BLIP) when they are limited by the shot noise of in-band background photons from the receiver, optics, atmosphere, and astrophysical source being observed.

The sensitivity of a (sub)millimeter-wave detector is usually given in terms of noise equivalent power (NEP) and in units of W/$\sqrt{\rm Hz}$. The NEP is the uncertainty in detected power in a bandwidth of 1 Hz or one-half second integration. This means that lower NEP relates to more sensitive detectors. It is common

to express the NEP in terms of the power detected or absorbed $P_{\rm abs}$, called the the electrical NEP ($NEP_{\rm el}$), or in terms of power at the output of the source, called the optical NEP ($NEP_{\rm opt}$). The power absorbed by a detector is $P_{\rm abs} = \eta P_{\rm opt}$ where η is the optical efficiency. The electrical NEP is related to the optical NEP such that $NEP_{\rm el}^2 = \eta^2 NEP_{\rm opt}^2$. To date, lab measurements of dark, or non-optically coupled, TES bolometers have been measured with electrical $NEP_{\rm el} \sim 2 \times 10^{-19}$ W/$\sqrt{\rm Hz}$ have been demonstrated [145, 101, 165], which will be sufficient for a future space-based far-infrared spectrometer.

The photon NEP for wide passbands is given by [188]:

$$NEP_{\rm phot}^2 = \int_0^\infty 2\frac{dP_{\rm abs}}{d\nu} h\nu(1+\eta(\nu)m(\nu))d\nu \tag{2.22}$$

where ν is the band averaged center frequency, $dP_{\rm abs}/d\nu$ is the power absorbed by a detector per frequency, h is the Planck constant, $\eta(\nu)$ is the optical efficiency, and $m(\nu)$ is the photon occupation number. Also, the factor of 2 in this equation is from the Nyquist factor relating bandwidth to integration time, specifically $\delta f = 1/2\delta t$. For a single mode detector operating in a narrow bandwidth, Eqn 2.22 can be further reduced using $P_{\rm abs} = \eta m h \nu \Delta\nu$ such that [115]:

$$\begin{aligned} NEP_{\rm phot}^2 = NEP_{\rm shot}^2 + NEP_{\rm wave}^2 &= 2P_{\rm abs}h\nu(1+\eta m) \\ &= 2P_{\rm abs}h\nu + \frac{2P_{\rm abs}^2}{\Delta\nu} \end{aligned} \tag{2.23}$$

This electrical NEP can also be converted to an optical NEP so that:

$$\begin{aligned} \frac{NEP_{\rm phot}^2}{\eta^2} &= \frac{2P_{\rm opt}h\nu(1+\eta m)}{\eta} \\ &= \frac{2h\nu P_{\rm opt}}{\eta} + \frac{2P_{\rm opt}^2}{\Delta\nu} \end{aligned} \tag{2.24}$$

where we measure $P_{\rm opt}$ at the output of the source. In Eqn 2.23, the first term comes from Poisson/shot noise from uncorrelated photons and the second term is wave noise due to wave bunching. The shot noise term dominates for low occupation number m such that $h\nu/kT \gg 1$. While the wave bunching term dominates for high m such that $h\nu/kT \ll 1$.

In addition to photon noise, there are other sources of noise that originate from the detector itself and from the readout electronics used to operate these detectors. These noise sources need to be lower than and in some cases mitigated in the system to achieve photon-noise-limited performance. In TES bolometers,

the total NEP includes contributions from photon noise, thermal fluctuation noise (TFN) from phonons, Johnson-Nyquist noise in the TES, Johnson-Nyquist noise in the load resistor $R_{\rm L}$, SQUID noise related to the readout, and excess noise. In the following subsections, we will discuss the different sources of noise in TEss with the exception of the SQUID noise, which is usually subdominant to other sources of noise.

2.3.1 Thermodynamic noise

One of the fundamental noise sources in a TES is the thermal fluctuation noise (TFN) or phonon noise from thermodynamic fluctuations associated with a thermal impedance. Another noise source is Johnson or Nyquist noise from thermodynamic fluctuations associated with an electrical resistance. In Irwin & Hilton (2005) [90], the thermodynamic noise in a TES is analyzed by applying the Fluctuation-Dissipation Theorem (FDT) to the differential equations for temperature (Eqn 2.3) and current (Eqn 2.5). In this case, the power and voltage signals are considered stochastic forces that depend on correlations in the state variables from thermodynamic fluctuations. From the FDT, the power spectral density (PSD) at equilibrium and for small fluctuations is:

$$S_{u_i}(\omega) = 4kT\,\mathrm{Re}[Y_{ii}(\omega)] \tag{2.25}$$

where i is the vector index, u_i is the velocity state variable, and $Y_{ii}(\omega)$ is the corresponding diagonal element of the admittance matrix. Also, $Y_{ii}(\omega) \equiv Z_{ii}^{-1}(\omega)$. We consider work done on a voltage source internal to the TES, like a Johnson noise voltage $V_{\rm noise}$, that would cause power dissipation in the thermal circuit of the TES. The Joule power dissipation is then $P_J = IV_{TES}$, where $V_{\rm TES} = IR + V_{\rm noise}$. By applying Eqn 2.25 to an equilibrium internal impedance matrix, which includes internal voltage noise sources, the Nyquist noise voltage of the TES, the Nyquist noise voltage of the load resistor $R_{\rm L}$, and the TFN across the thermal conductance G can be calculated. The Nyquist noise voltage of the TES is then $S_{V_{\rm TES}} = 4kT_0R_0$. The Nyquist noise voltage of the load resistor is $S_{V_{\rm L}} = 4kT_0R_{\rm L}$. Also, to account for nonlinearity in the TES resistor, $S_{V_{\rm TES}}$ may be rewritten as:

$$S_{V_{\rm TES}} = 4kT_0R_0\xi(I_0) \tag{2.26}$$

where $\xi(I_0)$ is a function determined at the steady-state bias current I_0 for a resistor with a current-dependent nonlinearity or $\beta_I \neq 0$. In the linear approximation, $\xi(I_0) = 1$ while for a quadratic nonlinear resistor $\xi(I_0) = 1 + 2\beta_I$.

The TES thermal fluctuation noise can be written as:

$$S_{\mathrm{TFN}} = 4kT_0^2 G F_{\mathrm{link}}(T_0, T_{\mathrm{b}}) \tag{2.27}$$

where the unitless function F_{link} depends on the thermal conductance exponent and type of phonon reflections. Compared to the Nyquist noise voltage of the TES, this noise has a T_0^2 dependence.

We can convert the voltage noise power spectral densities for TFN (Eqn 2.27), Johnson noise in the TES (Eqn 2.26), and Johnson in the load resistor to current noise by multiplying by the squared magnitude of either the internal or external admittance of the TES circuit. The external admittance which affects the Johnson noise of load resistor is [90]:

$$Y_{\mathrm{ext}}(\omega) \equiv \frac{I(\omega)}{V_{\mathrm{ext}}(\omega)} = s_I(\omega) I_0 \frac{\mathscr{L}_I - 1}{\mathscr{L}_I}(1 + j\omega\tau_I) \tag{2.28}$$

The internal admittance which affects the Johnson noise of the TES is also:

$$Y_{\mathrm{int}}(\omega) \equiv \frac{I(\omega)}{V_{\mathrm{int}}(\omega)} = -s_I(\omega) I_0 \frac{1}{\mathscr{L}_I}(1 + j\omega\tau) \tag{2.29}$$

where τ is the natural, or no feedback, time constant, τ_I is the constant current time constant, and $s_I(\omega)$ is the power-to-current responsivity. The current noise for each noise source can then be converted to a power-referred noise by dividing by the squared magnitude of the power-to-current responsivity of the TES or $|s_I(\omega)|^2$. In this way, the PSD of the power-referred Nyquist noise in the TES is:

$$S_{P_{\mathrm{TES}}}(\omega) = \frac{S_{V_{\mathrm{TES}}} |Y_{\mathrm{int}}(\omega)|^2}{|s_I(\omega)|^2} = 4kT_0 I_0^2 R_0 \frac{\xi(I_0)}{\mathscr{L}_I^2}(1 + \omega^2\tau^2) \left[\frac{W^2}{\mathrm{Hz}}\right] \tag{2.30}$$

and the PSD of the power-referred Nyquist noise in the load resistor R_L is:

$$S_{P_{\mathrm{L}}}(\omega) = \frac{S_{V_{\mathrm{L}}} |Y_{\mathrm{ext}}(\omega)|^2}{|s_I(\omega)|^2} = 4kT_0 I_0^2 R_{\mathrm{L}} \frac{(\mathscr{L}_I - 1)^2}{\mathscr{L}_I^2}(1 + \omega^2\tau_I^2) \left[\frac{W^2}{\mathrm{Hz}}\right] \tag{2.31}$$

The PSD of the power-referred thermal fluctuation noise is also:

$$S_{P_{\mathrm{TFN}}}(\omega) = 4kT_0^2 G F_{\mathrm{link}}(T_0, T_{\mathrm{b}}) \left[\frac{W^2}{\mathrm{Hz}}\right] \tag{2.32}$$

where the additional unitless function F_{link} depends on the thermal conductance exponent and type of phonon reflections, T_0 is the steady-state temperature of the TES, and T_b is the bath temperature.

2.3.2 Excess noise

TESs have been measured to have excess noise from sources internal to the TES itself that is greater than that predicted by existing noise models based on fundamental sources of noise. These additional noise sources include internal thermal fluctuation noise (e.g. [113]) and excess electrical noise (e.g. [182]). Excess electrical noise in particular has been found to impact many different TES materials and geometries [90]. Recent noise modeling has shown that a possible mechanism of the excess electrical noise in TESs is based on high-frequency Johnson noise that is mixed down into the signal band by Josephson oscillations due to a nonlinear voltage–current relationship in TESs. Figure 2.3 shows the total current noise in a measured TES device, including a model of the quadrature sum of noise components discussed in the chapter, such as thermal fluctuation noise and Johnson noise from the TES and bias circuit. A number of mitigation strategies have been developed (e.g [170]) to reduce the contributions from these excess noise sources to be smaller than thermal fluctuation noise or photon noise

2.3.3 Ratio of thermal fluctuation noise to photon noise

A useful quantity to calculate is the ratio of the thermal fluctuation noise to the photon noise in a TES [115]. From this ratio, we can find the base temperature needed for a TES bolometer to be photon-noise-limited given incident photons with central frequency ν. When the bath temperature T_b is low compare to critical temperature T_c, we can approximate the thermal fluctuation noise in the TES due to phonons as:

$$\begin{aligned} S_{P_{\text{TFN}}} = NEP^2_{\text{phonon}} &= F_{\text{link}} 4kT_\text{c}^2 G_0 \\ &\approx F_{\text{link}} 4kT_\text{c}^2 n(1+\gamma)\frac{P_{\text{opt}}}{T_\text{c}} \left[\frac{W^2}{\text{Hz}}\right] \end{aligned} \tag{2.33}$$

In going from the first part of Eqn 2.33 to the second, we have assumed a ratio of saturation power to average or minimum absorbed optical power $P_\text{J} = \gamma P_{\text{opt}}$ and a thermal conductance of the form $G(T) = G_0(T/T_\text{c})^{n-1}$. Recall from before that the total amount of power dissipated in the absorber and TES is $P_{\text{diss}} = P_\text{J} + P_{\text{opt}}$.

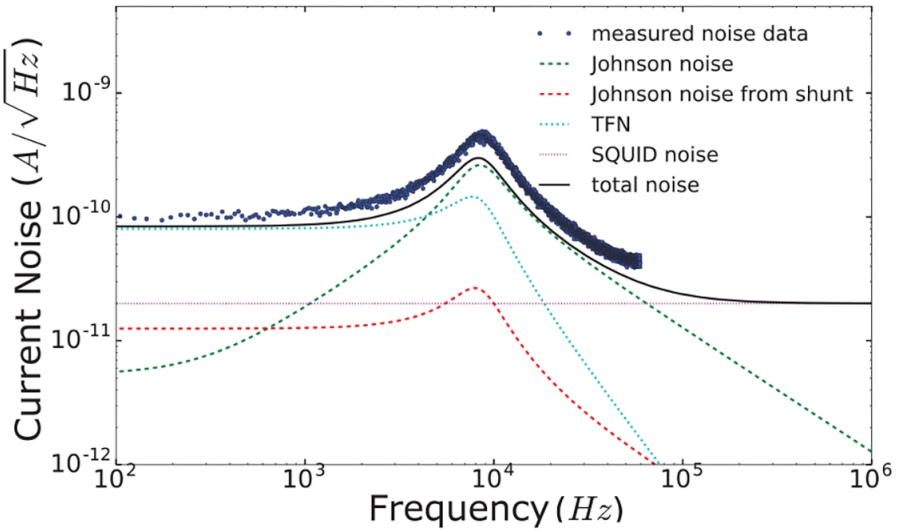

Figure 2.3: Total current noise in a TES, adapted from Wessels et al. (2019) [182]. Blue points are measured data whiles the lines are the predicted contributions of different noise sources, including the thermal fluctuation noise (cyan dash-dotted), SQUID noise (purple dashed), Johnson noise in the TES with the $(1+2\beta_I)$ enhancement (green dashed), Johnson noise from the shunt resistor (red dashed), and the quadrature sum of the noise components (black solid). The measured data has excess noise above this quadrature sum as represented by the gap from the total predicted noise.

Using Eqn 2.3 for a constant temperature with time, we can express $P_{\rm diss}$ as:

$$\begin{aligned} P_{\rm diss} = (1+\gamma)P_{\rm opt} &= \int_{T_{\rm b}}^{T_{\rm c}} G(T)dT \\ &= \frac{G_0}{n}\left[T_{\rm c}\left(1-\left(\frac{T_{\rm b}}{T_{\rm c}}\right)^n\right)\right] \end{aligned} \tag{2.34}$$

Using Eqn 3.63 for the photon noise in a single mode detector with a narrow passband and the thermal fluctuation noise from above (Eqn 2.33), we can calculate the ratio of the two as:

$$\frac{NEP^2_{\rm phot}}{NEP^2_{\rm phonon}} \approx \frac{h\nu}{kT_{\rm c}}\frac{1+\eta m}{2F_{\rm link}n(1+\gamma)} \tag{2.35}$$

Then, for the thermal fluctuation noise in a TES to be equal to the photon noise, the critical temperature $T_{\rm c}$ of a TES needs to be lower than:

$$T_{\rm c} \leq \frac{h\nu}{k}\frac{1+\eta m}{2F_{\rm link}n(1+\gamma)} \tag{2.36}$$

2.3.4 Total TES bolometer NEP

The total optical noise equivalent power $NEP_{\rm tot}$ for a detector is calculated from the sum of the contributions of different noise sources added in quadrature. For a photon-noise-limited TES bolometer, the dominant noise source is from incident photon fluctuations and this photon noise is greater than the sum of squares of other noise terms. In the absence of excess noise, the components that typically contribute most to least to the total NEP are photon noise, Johnson-Nyquist noise in the TES, thermal fluctuation noise, SQUID noise related to the readout, and Johnson-Nyquist noise in the load resistor. Most of these sources have been discussed throughout this section with the exception of SQUID noise. The total NEP can be calculated as [90]:

$$\begin{aligned} NEP^2_{\rm tot} = S_{P_{\rm tot}}(f) + S_{\rm phot}(f) &= S_{P_{\rm TFN}} + S_{V_{\rm TES}}I_0^2\frac{1}{\mathscr{L}_I^2}(1+\omega^2\tau^2) + \\ &\quad S_{V_{\rm L}}I_0^2\frac{(\mathscr{L}_I-1)^2}{\mathscr{L}_I^2}(1+\omega^2\tau_I^2) + \frac{S_{I_{\rm amp}}(\omega)}{|s_I(\omega)|^2} + S_{\rm phot}(f) \\ &= 4kT_0^2GF_{\rm link}(T_0,T_{\rm b}) + 4kT_0R_0\xi(I_0)I_0^2\frac{1}{\mathscr{L}_I^2}(1+\omega^2\tau^2) + \\ &\quad 4kT_0R_{\rm L}I_0^2\frac{(\mathscr{L}_I-1)^2}{\mathscr{L}_I^2}(1+\omega^2\tau_I^2) + 2P_{\rm abs}h\nu(1+\eta m)\left[\frac{W^2}{\rm Hz}\right] \end{aligned} \tag{2.37}$$

where τ is the natural, or no feedback, time constant, τ_I is the constant current time constant, $s_I(\omega)$ is the power-to-current responsivity, and $S_{I_{\rm amp}}$ is the current-referred SQUID/amplifier noise. In the second part of Eqn 2.37, the TFN power noise $S_{P_{\rm TFN}}$, TES voltage noise $S_{V_{\rm TES}}$, and load voltage noise $S_{V_{\rm L}}$ have been substituted. For the TES voltage noise, $\xi(I_0) = 1$ in the linear and $\xi(I_0) = 1 + 2\beta_I$ in the quadratic approximations, respectively. Equation 2.37 does not include any additional sources of excess noise (e.g. [182]). The NEP of a TES bolometer is the square root of the PSD of the total power-referred noise or $NEP(\omega) = \sqrt{S_P(\omega)}$ in units of W/$\sqrt{\rm Hz}$.

Chapter 3

Theory of microwave kinetic inductance detectors

In this chapter, we discuss the underlying physics of microwave kinetic inductance detectors (MKIDs). A MKID is a type of detector that consists of superconducting films deposited on insulating substrates with lithography to create thin-film, high quality factor (Q) micro-resonators [189]. Photons with energy $h\nu > 2\Delta \approx 3.52kT_c$ [169] absorbed by this superconducting film will break a Cooper pair in the superconducting film into its two constituent electrons or quasiparticles (QP), where h is the Planck constant, ν is frequency, Δ is the superconducting energy gap, and k is the Boltzmann constant. This breaking apart of Cooper pairs can be used to estimate the total power absorbed by a device. Specifically, in an MKID, the breaking of Cooper pairs is measured through the corresponding change in the kinetic inductance of the film.

In this chapter, we start with a discussion of the MKID resonator response, including what is measured to characterize these devices in practice. Next, we explain the complex conductivity of a superconductor using the Drude model as well as BCS theory and Mattis-Bardeen. We then talk about the surface impedance and kinetic inductance of a superconducting resonator and their relationship to the complex conductivity. We then go into detail about the MKID responsivity to changes in temperature and optical power. Finally, we go through the contribution of different sources of noise on the MKID sensitivity and what constitutes a photon-noise-limited detector.

3.1 Resonator response

The MKIDs described in this thesis are exclusively of the lumped-element type. We therefore focus on lumped element MKIDs. This resonator is an *LC* circuit that consists of a capacitance C and variable kinetic inductance $L_{\rm k}$ in series with a magnetic inductance $L_{\rm m}$ such that $L_{\rm tot} = L_{\rm k} + L_{\rm m}$. This circuit is usually either capacitively coupled C_c or weakly inductively coupled to a feedline. The kinetic inductance of a superconducting film changes with an increase in quasiparticle density. More details about the kinetic inductance especially as it pertains to MKIDs are discussed in Section 3.4. Figure 3.1a shows the lumped element resonant circuit of a single MKID, where different components are labeled. Also, shown is an arrow denoting the forward scattering parameter S_{21} or transmission measured for this circuit.

For a capacitively coupled resonator, the resonant frequency is given by:

$$\omega_{\rm r} = 2\pi f_{\rm r} = \frac{1}{\sqrt{L_{\rm tot}(C + C_{\rm c})}} \tag{3.1}$$

For an MKID, the resonant frequency will shift to lower frequencies with an increase to the kinetic inductance of the superconducting film. The kinetic inductance can be affected by changes in absorbed optical power, bath temperature, and microwave probe tone power. When the quasiparticle density increases, it leads to a small change in the surface impedance of the film $\delta Z_{\rm s}$, specifically a change in the kinetic inductance and resistance. The change in $L_{\rm k}$ leads to a measurable decrease in the resonant frequency while the change in resistance leads to reduction in the quality factor of the MKID, respectively. The kinetic inductance of a superconducting film, especially as it pertains to a MKID, is discussed in more detail in Section 3.4. If we take the derivative of the resonant frequency (Eqn 3.1) with respect to the kinetic inductance, we find that:

$$\frac{df_{\rm r}}{dL_{\rm k}} = -\frac{\alpha f_{\rm r}}{2L_{\rm k}} \tag{3.2}$$

where $\alpha = L_{\rm k}/L_{\rm tot}$ is the kinetic inductance fraction. We have also substituted in $C = 1/(L_{\rm tot}\omega_{\rm r}^2)$, ignoring $C_{\rm c}$ for the coupling capacitance to the feedline.

Generally, a resonator will lose energy due to dissipative losses and also from coupling to an external circuit, including a feedline or waveguide. The total quality factor of a superconducting resonator $Q_{\rm r}$, such

as an MKID, is given by:

$$\frac{1}{Q_\mathrm{r}} = \frac{1}{Q_\mathrm{i}} + \frac{1}{Q_\mathrm{c}} = \frac{f_\mathrm{r}}{\Delta f} \tag{3.3}$$

where the internal quality factor Q_i describes dissipative losses and the coupling quality factor Q_c describes the strength of coupling to an external circuit. In the second part of this equation, f_r is the resonant frequency and Δf is the resonator bandwidth, or full width at half maximum (FWHM). The internal quality factor of a resonator is given by [189, 115]:

$$Q_\mathrm{i} = \frac{\mathrm{Im}(Z_\mathrm{r})}{\mathrm{Re}(Z_\mathrm{r})} = \frac{Q_\mathrm{r}}{\min(|S_{21}|)} \tag{3.4}$$

where Z_r is the resonator impedance, specifically of the inductive part. The coupling factor of a resonator is given by [69, 189]:

$$Q_\mathrm{c} = \frac{2(C+C_\mathrm{c})}{\omega_\mathrm{r} C_\mathrm{c}^2 Z_0} = \frac{Q_\mathrm{r}}{1-\min(|S_{21}|)} \tag{3.5}$$

where Z_0 is the impedance of the feedline.

The resonator impedance Z_r depends on frequency as well as the resonator detuning, or the fractional detuning of a tone frequency f from the resonance frequency $x = (f - f_\mathrm{r})/f_\mathrm{r}$. To first order in x, $Z_\mathrm{r}(f)$ can be expressed as [115]:

$$Z_\mathrm{r}(f) \simeq Z_0 \left[\frac{Q_\mathrm{c}}{2Q_\mathrm{i}} + jQ_\mathrm{c}x\right] \frac{1}{1+j\varepsilon_\mathrm{a}} \tag{3.6}$$

where ε_a is an asymmetry parameter such that $\varepsilon_\mathrm{a} = C/(C_\mathrm{c}Q_\mathrm{i})$. In general, the transmission of a signal traveling along a transmission line with impedance Z_0 and a circuit with shunt impedance to ground Z_r is given by [115]:

$$S_{21}(f) = 1 - \frac{1}{1+2Z_\mathrm{r}(f)/Z_0} \tag{3.7}$$

We can then plug in Eqn 3.6 for $Z_\mathrm{r}(f)$ and rewrite Eqn 3.7 as:

$$S_{21}(f) = 1 - \frac{1+j\varepsilon_\mathrm{a}}{1+j\varepsilon_\mathrm{a}\frac{Q_\mathrm{r}}{Q_\mathrm{c}}} \frac{Q_\mathrm{r}}{Q_\mathrm{c}} \left[\frac{1}{1+2jQ_\mathrm{r}x/(1+j\varepsilon_\mathrm{a}\frac{Q_\mathrm{r}}{Q_\mathrm{c}})}\right] \tag{3.8}$$

When $\varepsilon_\mathrm{a} \ll 1$ this reduces further to:

$$S_{21}(f) \simeq 1 - \frac{Q_\mathrm{r}}{Q_\mathrm{c}} \frac{1}{1+2jQ_\mathrm{r}x} \tag{3.9}$$

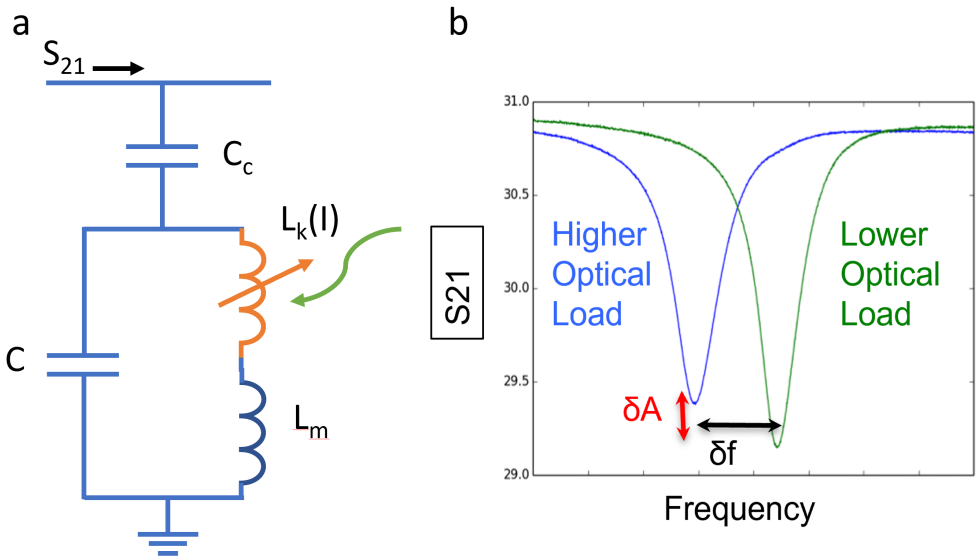

Figure 3.1: *a:* A MKID circuit diagram. A lumped-element MKID resonator is an *LC* circuit with capacitance C, variable kinetic inductance L_k, and magnetic inductance L_m that is capacitively coupled C_c to a feedline whose forward microwave transmission S_{21} is measured. The L_k of a superconducting film changes with an increase in quasiparticle density. *b:* S_{21} magnitude measurement vs frequency for a MKID resonator at two different optical loads/bath temperatures. As photons are absorbed in the superconducting film, extra quasiparticles are created, which increases kinetic inductance L_k and subsequently decreases the resonator frequency f_r and its amplitude A. This change in frequency and amplitude is a measure of the absorbed photon power. Courtesy of J. Austermann (NIST).

which is the standard model for a single MKID commonly used in the literature [189]. We can multiply Eqn 3.9 by a few other parameters for the feedline so that $S_{21}(f)$ for a single MKID now becomes:

$$S_{21}(f) = Ae^{-2\pi jf\tau}\left(1 - \frac{Q_\mathrm{r}}{Q_\mathrm{c}}\frac{e^{j\phi_0}}{1+2jQ_\mathrm{r}x}\right) \tag{3.10}$$

where A is a complex constant accounting for the gain, loss, and phase shift in the system, τ is a cable delay constant due to the length of cables, and ϕ_0 accounts for impedance mismatch. This model of $S_{21}(f)$ for a resonator corresponds to a Lorentzian shape in $|S_{21}|$ vs frequency space and traces out a circle in the complex S_{21} domain. Figure 3.1b shows two measurements at different loadings/bath temperatures for a MKID from the BLAST-TNG balloon experiment [61]. A reduction in kinetic inductance and resistance with increased loading can be clearly seen by a decrease in resonant frequency δf and a decrease in the amplitude of the resonance or quality factor δA.

For an MKID array, there are now many LC resonator circuits capacitively coupled to a common feedline. The array is read out simultaneously using a technique called frequency multiplexing in which a comb of complex carrier/probe tone signals, consisting of many different frequencies, is sent from port 1 to propagate down a transmission line shared with the MKIDs. Each tone in this comb is tailored to match the resonance frequency of a device. For each MKID, at its resonance frequency, the magnitude of the forward transmission reaches its minimum where $\min(|S_{21}|) = 1 - Q_\mathrm{r}/Q_\mathrm{c}$, while far away from resonance, the transmission approaches unity $|S_{21}| \to 1$. Each probe tone will interact with the MKID and monitor a change in phase while the rest of the comb will travel past. After propagating past all resonators in the array at port 2, the comb of probe tones enters a low noise amplifier (LNA). The noise associated with this amplifier is discussed in Section 3.7.2. Figure 3.2 shows the equivalent circuit of a small subset of a frequency-multiplexed array of shunt-coupled MKIDs. Three LC resonators are shown, each with resonance frequency $\omega_{\mathrm{r,n}} = 1/\sqrt{L_\mathrm{n}C_\mathrm{n}}$ where n is the resonator number. In current generation MKID experiments, the readout supports up to 1000 probe tones/resonators. More details on frequency multiplexing readout, particularly related to TolTEC, can be found in Chapter 7. We will now go into detail about the complex conductivity of a superconductor. The measured change in kinetic inductance is related to this.

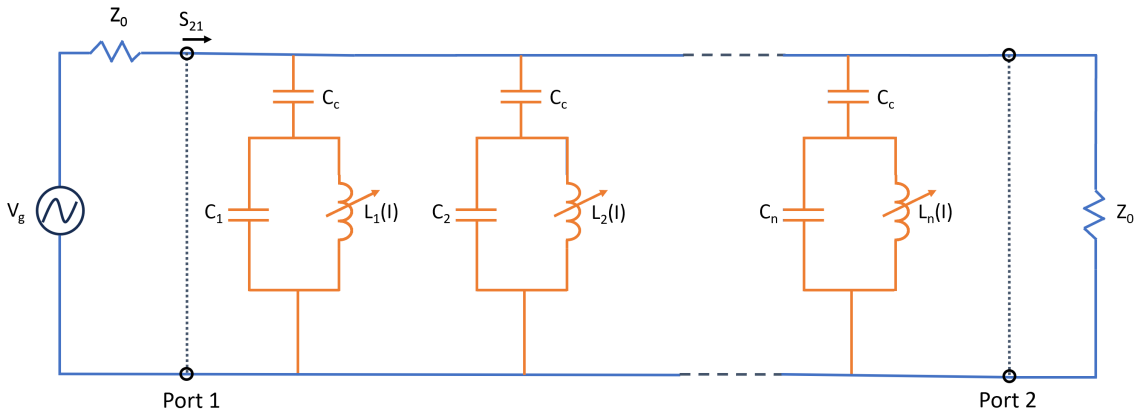

Figure 3.2: Circuit diagram of a subset of a MKID array read out using frequency multiplexing. The solid lines represent transmission line sections. Each *n*th MKID is represented as a LC circuit, with capacitance C_{n} and current-dependent total inductance $L_{\mathrm{n}}(I)$, capacitively coupled C_{c} to a shared feedline. The array is read out simultaneously by sending a comb of carrier/probe tones with generator voltage V_{g} into port 1. Each port is denoted by dotted lines. After propagating past all resonators in the array, the comb of probe tones, with changed amplitude and phase, enters a low noise amplifier with input impedance Z_0 at port 2.

3.2 Complex conductivity

In a superconductor, the formation of Cooper pairs below $T < T_c$ leads to zero DC resistance; however, there is still a small, but nonzero AC impedance due to the finite inertia of Cooper pairs [111]. There also exists in superconductors a small fraction of free electrons, or quasiparticles, thermally excited from their Cooper pairs at $T > 0$. A superconductor experiences a perturbation to the complex conductivity, $\sigma(\omega) = \sigma_1 - j\sigma_2$ when Cooper pairs are broken into quasiparticles. This manifests as perturbations to the dissipative σ_1 and reactive σ_2 components such that $\delta\sigma(\omega) = \delta\sigma_1 - j\delta\sigma_2$. In the following subsections, we will explain the complex conductivity of a superconductor using a simplified model, the Drude model, and follow-up with a more thorough discussion using BCS theory and Mattis-Bardeen with a treatment of quasiparticles.

3.2.1 Complex conductivity from the Drude model

Using the Drude model, we can relate the effect of the inertia of quasiparticles in a superconductor to the normal conductivity. This model makes the simplifying assumption that electrons behave like a gas, that is that they do not interact with each other and are randomly scattered. For a superconductor, quasiparticles are substituted for electrons in this case. From this, the complex AC conductivity can be expressed as [63]:

$$\sigma(\omega) = \frac{ne^2\tau}{m}\frac{1}{1+j\omega\tau} = \frac{\sigma_n}{1+j\omega\tau} \tag{3.11}$$

where ω is the frequency, σ_n is the normal-state conductivity such that $\sigma_n = ne^2\tau/m$, m, n, and e are the mass, density, and charge of an electron. Also, in Eqn 3.11 is the scattering time τ, or the characteristic time between collisions, of free electrons. This time is related to the mean free path l and Fermi velocity v_0 of electrons such that $\tau = l/v_0$. The $j\omega\tau$ term represents a phase lag due to the inertia of electrons. At room temperature, τ is usually less that 1 picosecond, so that $\omega\tau \ll 1$, even at microwave frequencies, and $\sigma \approx \sigma_n$.

An electromagnetic field also penetrates into a normal metal to a finite length, or the skin depth δ. The skin depth is related to σ_n such that $\delta \approx \sqrt{2/\omega\mu\sigma}$, where μ is the magnetic permeability of the metal such that $\mu \approx \mu_0$ usually.

Eqn 3.11 can also be written as real and imaginary components such that the complex conductivity is now:

$$\sigma(\omega) = \frac{\sigma_n}{1+\omega^2\tau^2} - j\frac{\omega\tau\sigma_n}{1+\omega^2\tau^2} = \sigma_1(\omega) - j\sigma_2(\omega) \tag{3.12}$$

At low temperatures $T \ll T_c$, the normal conductivity $\sigma_n \to \infty$ and $\omega\tau \to \infty$. However, in Eqn 3.11, the ratio $\sigma/\omega\tau$ also remains finite such that the AC conductivity is almost purely inductive or $\sigma_2 \gg \sigma_1$. In a conductor, a local version of Ohm's Law applies such that current density $\overrightarrow{J}$ and electric field $\overrightarrow{E}$ are related as:

$$\overrightarrow{J} = \sigma\overrightarrow{E} = \frac{\sigma_n}{1+j\omega\tau}\overrightarrow{E} \tag{3.13}$$

where Eqn 3.11 has been used for σ. Eqn 3.11 for the complex conductivity and classic skin depth are valid when $l \ll \delta$. At high enough frequencies and/or low enough temperatures, as in a superconductor, Ohm's law is not an adequate description of the electrodynamics. Non-local contributions to $\overrightarrow{J}$ and σ must also be considered [63].

3.2.2 Complex conductivity from BCS theory and Mattis-Bardeen

Using BCS theory, Mattis-Bardeen derived a more general, non-local form of the complex AC conductivity. The equations for the real and imaginary components of the complex conductivity relative to σ_n can be written as [169]:

$$\frac{\sigma_1(\omega)}{\sigma_n} = \frac{2}{\hbar\omega}\int_\Delta^\infty dE \frac{E^2+\Delta^2+\hbar\omega E}{\sqrt{E^2-\Delta^2}\sqrt{(E+\hbar\omega)^2-\Delta^2}}[f(E)-f(E+\hbar\omega)] \tag{3.14}$$

and

$$\frac{\sigma_2(\omega)}{\sigma_n} = \frac{1}{\hbar\omega}\int_\Delta^{\Delta+\hbar\omega} dE \frac{E^2+\Delta^2-\hbar\omega E}{\sqrt{E^2-\Delta^2}\sqrt{\Delta^2-(E-\hbar\omega)^2}}[1-2f(E)] \tag{3.15}$$

where $\hbar$ is the reduced Planck constant or $\hbar = h/2\pi$, ω is angular frequency, E is the energy, and $f(E)$ is the distribution function of unpaired normal electrons.

At zero temperature $T = 0\,\mathrm{K}$, the penetration depth of an electromagnetic field is given by the London penetration depth:

$$\lambda_{L0} = \sqrt{\frac{m}{\mu_0 n e^2}} = \sqrt{\frac{l}{\mu_0\sigma_n v_0}} \tag{3.16}$$

where σ_n is the normal-state conductivity. This is related to the coherence length of a superconductor, similar to the minimum size of a Cooper pair [63], $\xi_0 = \hbar v_0/\pi\Delta_0$, where Δ_0 is the gap energy at zero temperature.

3.2.2.1 Complex conductivity of a Fermi gas in thermal equilibrium

In MKIDs, quasiparticles (QPs) may be thermally generated due to a change in temperature of the device, where temperature fluctuations create phonons that interact with the crystal lattice of a superconductor. Excess QPs are also generated from breaking of Cooper pairs with the absorption of photons with energy $hf > 2\Delta$. As these are two separate mechanisms for QP generation, they can be modeled as two different populations. The total number density of quasiparticles in a superconductor can be written as [189, 115]:

$$\begin{aligned} n_{\mathrm{qp,tot}} &= n_{\mathrm{qp}}(T) + n_{\mathrm{qp}}(P) \\ &= 4N_0 \int_{\Delta}^{\infty} dE \frac{E}{\sqrt{E^2-\Delta^2}} f(E) \end{aligned} \tag{3.17}$$

where $n_{\mathrm{qp}}(T)$ are the number density of thermal quasiparticles and $n_{\mathrm{qp}}(P)$ is the number density of optically generated, excess quasiparticles. In the second part of Eqn 3.17, E is the energy, N_0 is the single spin density of states at the Fermi energy or $N(E=0)$, and $f(E)$ is the distribution function for unpaired normal electrons or QPs.

We can substitute $f(E)$ with a Fermi-Dirac distribution that has been modified to include an effective chemical potential for excess quasiparticles [134, 63] such that:

$$f(E;\mu^*,T) = \frac{1}{1+e^{\frac{E-\mu^*}{kT}}} \tag{3.18}$$

where μ^* is an effective chemical potential and T is the temperature. Equation 3.18 treats the QPs as a Fermi gas in thermal equilibrium.

If we insert Eqn 3.18 into Eqn 3.17, then $n_{\mathrm{qp,tot}}$ can be written as:

$$\begin{aligned} n_{\mathrm{qp,tot}} &= 4N_0 \int_{\Delta}^{\infty} dE \frac{E}{\sqrt{E^2-\Delta^2}} f(E;\mu^*,T) \\ &= 4N_0 \int_{\Delta}^{\infty} dE \frac{E}{\sqrt{E^2-\Delta^2}} \frac{1}{1+e^{\frac{E-\mu^*}{kT}}} \end{aligned} \tag{3.19}$$

At low temperatures $T \ll T_c$, such that $kT \ll \Delta$, and satisfying the condition $\hbar\omega \ll \Delta$, the quasiparticle

density can be approximated to [63]:

$$n_{\mathrm{qp,tot}} \simeq 2N_0\sqrt{2\pi kT\Delta}e^{-\frac{\Delta-\mu^*}{kT}} \tag{3.20}$$

Quasiparticles also have the effect of suppressing the energy gap Δ relative to its zero temperature value Δ_0 such that [189]:

$$\frac{\Delta_0-\Delta}{\Delta_0} \approx -\ln\left(\frac{\Delta}{\Delta_0}\right) = 2\int_\Delta^\infty dE \frac{1}{\sqrt{E^2-\Delta^2}} f(E;\mu^*,T) \tag{3.21}$$

It is also important to consider how long quasiparticles will exist in a superconducting volume before recombining into Cooper pairs. As part of this process, QPs will emit a phonon as they recombine and this phonon will escape from the volume. The QP lifetime τ_{qp} in MKIDs has been found empirically to vary with the number density of thermal quasiparticles $n_{\mathrm{qp}}(T)$ such that [189]:

$$\tau_{\mathrm{qp}} = \frac{\tau_{\mathrm{max}}}{1+n_{\mathrm{qp}}(T)/n^*} \tag{3.22}$$

where n^* is the crossover number density, observed to be $\sim 100-500$ $\mu\mathrm{m}^{-3}$ for many materials [179] and τ_{max} is the experimentally measured maximum QP lifetime. Typical values are $\tau_{\mathrm{max}} = 100-1000$ µs for materials with a superconducting critical temperature $T_{\mathrm{c}} \sim 1$ K, like those used in submillimeter and millimeter-wave MKIDs.

We can also use Eqn 3.18 for a Fermi-Dirac distribution of quasiparticles to rewrite Eqn 3.14 and Eqn 3.15 for the real and imaginary components of the complex conductivity compared to σ_{n} as:

$$\frac{\sigma_1(\omega)}{\sigma_{\mathrm{n}}} = \frac{2}{\hbar\omega}\int_\Delta^\infty dE \frac{E^2+\Delta^2+\hbar\omega E}{\sqrt{E^2-\Delta^2}\sqrt{(E+\hbar\omega)^2-\Delta^2}}[f(E;\mu^*,T)-f(E+\hbar\omega;\mu^*,T)] \tag{3.23}$$

and

$$\frac{\sigma_2(\omega)}{\sigma_{\mathrm{n}}} = \frac{1}{\hbar\omega}\int_\Delta^{\Delta+\hbar\omega} dE \frac{E^2+\Delta^2-\hbar\omega E}{\sqrt{E^2-\Delta^2}\sqrt{\Delta^2-(E-\hbar\omega)^2}}[1-2f(E;\mu^*,T)] \tag{3.24}$$

3.2.3 Changes in complex conductivity due to quasiparticles

The number of quasiparticles in a MKID is not fixed and varies with a change in temperature as well as with pair-breaking photons that are absorbed by the superconductor volume. Thermal quasiparticles are

generated by a change in temperature. At low temperatures $T \ll T_c$, such that $kT \ll \Delta$, and satisfying the condition $\hbar\omega \ll \Delta$, the number density of thermal quasiparticles $n_{qp}(T)$ is [70]:

$$n_{qp}(T) \simeq 2N_0\sqrt{2\pi kT\Delta_0}e^{-\frac{\Delta_0}{kT}} = \frac{N_{qp}(T)}{V} \tag{3.25}$$

where we have set $\mu^* = 0$. Also, $N_{qp} = n_{qp}V$ and V is the active volume of the MKID, in this case the inductor. The number of optically generated quasiparticles generated per absorbed photon can be calculated from the ratio of the photon energy to the superconducting energy gap as:

$$N_{qp,per}(\nu) = \frac{\eta_{det}h\nu}{\Delta} \tag{3.26}$$

where P_{opt} is the optical power and η_{det} is the detector quantum efficiency. The detector quantum efficiency is typically about $\sim$0.7-0.8. Using Eqn 3.26, the total number of optically generated quasiparticles is then:

$$N_{qp}(P) = \frac{N_{qp,per}(\nu)\tau_{qp}P_{opt}}{h\nu} \tag{3.27}$$

From Gao (2008) [63], for $T \ll T_c$ and $\hbar\omega \ll \Delta$, the real and imaginary components of the complex conductivity can be approximated as separate expressions due to thermal QPs (*therm*) and excess QPs (*opt*) such that:

$$\frac{\sigma_{1,therm}(T)}{\sigma_n} = \frac{4\Delta_0}{\hbar\omega}e^{-\frac{\Delta_0}{kT}}\sinh(\xi)K_0(\xi) \tag{3.28}$$

$$\frac{\sigma_{2,therm}(T)}{\sigma_n} = \frac{\pi\Delta_0}{\hbar\omega}\left[1 - \sqrt{\frac{2\pi kT}{\Delta_0}}e^{-\frac{\Delta_0}{kT}} - 2e^{-\frac{\Delta_0}{kT}}e^{-\xi}I_0(\xi)\right] \tag{3.29}$$

$$\frac{\sigma_{1,opt}(n_{qp},T)}{\sigma_n} = \frac{2\Delta_0}{\hbar\omega}\frac{n_{qp}}{N_0\sqrt{2\pi kT\Delta_0}}\sinh(\xi)K_0(\xi) \tag{3.30}$$

$$\frac{\sigma_{2,opt}(n_{qp},T)}{\sigma_n} = \frac{\pi\Delta_0}{\hbar\omega}\left[1 - \frac{n_{qp}}{2N_0\Delta_0}\left(1 + \sqrt{\frac{2\Delta_0}{\pi kT}}e^{-\xi}I_0(\xi)\right)\right] \tag{3.31}$$

where $\xi = \hbar\omega/2kT$, $\mu^* = 0$, and I_n, K_n are the nth order (zero order) modified Bessel function of the first and second kind. From these equations, the derivatives $d\sigma/dn_{qp}$, specifically $\frac{\partial\sigma(T)/\partial T}{\partial n_{qp}(T)/\partial T}$ or $\frac{\partial\sigma(n_{qp},T)}{\partial n_{qp}}$ can be evaluated for thermal QP and excess QP from pair breaking photons, respectively. The factor of $1/\omega$ in these equations is related to the finite inertia of Cooper pairs such that at $T \ll T_c$, the dissipative σ_1 is much smaller than the reactive σ_2 or $\sigma_1 \ll \sigma_2$.

3.3 Surface impedance

The surface impedance of a superconductor is a complex quantity such that:

$$Z_s = R_s + jX_s = R_s + j\omega L_s = R_s + j\omega\mu_0\lambda_{eff} \tag{3.32}$$

where R_s is the surface resistance, X_s is the surface reactance, L_s is the surface inductance, ω is the angular frequency, and μ_0 is the vacuum permeability. At low temperatures, $T \ll T_c$, such as where MKIDs are usually operated, $\omega L_s >> R_s$ [189] and Z_s is almost purely inductive. To relate the surface impedance to the complex conductivity, we will consider several limiting cases/approximations for a superconductor volume/film following the work of [63, 189]. For these cases, it is useful to define a purely reactive surface impedance at zero temperature $Z_s(\omega, T)$:

$$Z_s(\omega, 0) = j\omega\mu_0\lambda_{eff} \tag{3.33}$$

where λ_{eff} is the effective penetration depth, or the distance over which an electromagnetic field penetrates into a superconductor. The effective penetration depth changes depending on the limiting case and film thickness.

Case 1, Local limit and thick films: The local limit approximation is valid for a superconductor volume under two conditions, 1) the coherence length $\xi_0 \ll \lambda_{L0}$ or 2) the mean free path $l \ll \lambda_{L0}$, where λ_{L0} is given by Eqn 3.16. These two conditions can be further relaxed to 1) $\xi_0 \ll \lambda_{eff}$ or 2) $l \ll \lambda_{eff}$ [63]. These two conditions imply that the magnetic field varies slowly in space compared to the characteristic length scale of the Cooper pair system. Also, in the local limit, the effective penetration depth λ_{local} is equivalent to [189]:

$$\lambda_{local} = \sqrt{\frac{\hbar}{\pi\Delta\mu_0\sigma_n}} \tag{3.34}$$

where σ_n is the normal-state conductivity.

For thick films in the local limit, the surface impedance and AC conductivity are related such that [189]:

$$Z_s(\omega, T) = \sqrt{\frac{j\mu_0\omega}{\sigma(\omega, T)}} = \frac{Z_s(\omega, 0)}{\sqrt{1 + j\delta\sigma(\omega, T)/\sigma_2(\omega, 0)}} \tag{3.35}$$

where $Z_s(\omega,0)$ is given by Eqn 3.33 and the change in conductivity is $\delta\sigma(\omega,T) = \sigma(\omega,T) - \sigma(\omega,0) = \sigma_1(\omega,T) - j\delta\sigma_2(\omega,T)$.

Case 2, Extreme anomalous limit and thick films: The extremely anomalous limit approximation is valid for a superconductor volume under two conditions, 1) the coherence length $\xi_0 \gg \lambda_{L0}$ or 2) the mean free path $l \gg \lambda_{L0}$. These two conditions can be further relaxed to 1) $\xi_0 \gg \lambda_{\text{eff}}$ or 2) $l \gg \lambda_{\text{eff}}$ [63]. These two conditions imply that the characteristic length scale of the Cooper pair system is long compared to distance over which the penetrating magnetic field varies significantly. In the extremely anomalous regime, λ_{ea} is equivalent to [189]:

$$\lambda_{\text{ea}} = \lambda_{\text{local}} \left[\frac{\sqrt{3}l}{2\pi\lambda_{\text{local}}} \right]^{1/3} \tag{3.36}$$

For thick films in the extremely anomalous limit, the surface impedance and complex conductivity are related such that [189]:

$$Z_s(\omega,T) = j\mu_0\omega\lambda_{\text{ea}}[1 + j\delta\sigma(\omega,T)/\sigma_2(\omega,0)]^{-1/3} \tag{3.37}$$

Case 3, local limit and thin films: In the regime of thin films, the superconducting film thickness t is smaller than the electron mean free path l. This suggests that $l \approx t$ since it will be limited by surface scattering. The effective penetration depth for thin films is $\lambda_{\text{thin}} = \lambda_{\text{local}}^2/t$. If $t \ll \lambda_{\text{eff}}$, the electromagnetic field will completely penetrate that film and the current density will be nearly constant throughout the film. The relationship between the surface impedance and complex conductivity in this case is then [63]:

$$Z_s(\omega,T) = \frac{1}{(\sigma_1 - j\sigma_2)t} = \frac{1}{\sigma(\omega)t} \tag{3.38}$$

Also, since the mean free path is comparable to the film thickness $l \approx t$, σ has a $1/l \sim 1/t$ dependence and Z_s varies as $1/t^2$.

From these cases, we can summarize the change in Z_s, $\delta Z_s/Z_s$ to the change in complex conductance $\delta\sigma/\sigma$ for a MKID such that [63]:

$$\frac{\delta Z_s}{Z_s} = \gamma\frac{\delta\sigma}{\sigma} \tag{3.39}$$

where γ is case-dependent factor. In particular, γ corresponds to the power dependence in Eqn 3.35, Eqn 3.37,

and Eqn 3.38 such that:

$$\gamma = \begin{cases} -1/2 & \text{thick films, local limit} \\ -1/3 & \text{thick films, extreme anomalous limit} \\ -1 & \text{thin films, local limit} \end{cases} \tag{3.40}$$

From Eqn 3.39, we can see that the responsivity of MKIDs is related to dZ_s/dn_{qp} and to $d\sigma/dn_{qp}$ as discussed in Section 3.2.3. For the MKIDs discussed in this thesis, the thin film and local limit is most appropriate given that the film thickness satisfies $t \ll \lambda_{eff}$, particularly $t = 18$ nm and $\lambda_{eff} \sim 100 - 300$ nm for the film materials (TiN, Ti) [174].

3.4 Kinetic inductance

The inductance L is related to the magnetic field outside a conductor. Inductance is defined as the ratio of the applied voltage to the rate of change of current such that $L = V/(dI/dt)$. This inductance depends purely on the geometry of the conductor, specifically film length l, width w, and thickness t, and is referred to as the geometric or magnetic inductance L_m. The energy stored in the inductance is $E = \frac{1}{2}LI^2$.

For a superconducting film, the magnetic field extends into the material by a distance given by the penetration depth λ_{eff} described in Section 3.3. There is a supercurrent flowing in this layer that carries a substantial amount of the kinetic energy (velocity) of the Cooper pairs and quasiparticles with an associated inertia.

This kinetic inductance L_k also contributes to the total inductance such that:

$$L_{tot} = L_m + L_k \tag{3.41}$$

It is useful to define a kinetic inductance fraction α such that:

$$\alpha = \frac{L_k}{L_{tot}} \tag{3.42}$$

or the ratio of the kinetic inductance to the total inductance. In MKIDs, a larger α translates to a more responsive detector since this factor represents the fraction of the inductance that is able to change with the quasiparticle density and Cooper generation and recombination.

For a thin superconducting film with thickness t, the surface impedance Z_s is given by (Eqn 3.38) such that:

$$Z_s = \frac{1}{\sigma(\omega)t} \simeq \frac{1}{t}\frac{\sigma_1 + j\sigma_2}{\sigma_2^2} = \mathscr{R} + j\omega\mathscr{L}_k(\Omega/\square) \tag{3.43}$$

where $\mathscr{R} = \sigma_1/\sigma_2^2 t$ is the resistance per square and $\mathscr{L}_k = \frac{1}{\sigma_2 \omega t}$ is the kinetic inductance per square.

In the low frequency limit $\hbar\omega \ll kT$, the Mattis Bardeen equation for the imaginary complex conductivity can be expressed as [11]:

$$\sigma_2 = \frac{\sigma_n \pi\Delta}{\hbar\omega}\tanh\left(\frac{\Delta_0}{2kT}\right) \tag{3.44}$$

where Δ_0 is the zero temperature energy gap. We now substitute Eqn 3.44 into the expression for $\mathscr{L}_k$ so that the kinetic inductance per square becomes [70]:

$$\mathscr{L}_k = \frac{\hbar\mathscr{R}_s}{\pi\Delta} \tag{3.45}$$

where $\mathscr{R}_s = 1/\sigma_n t$ is the sheet resistance of the film in the normal state and $\tanh(x)$ approaches 1 at low temperatures $T \ll T_c$. Equation 3.45 suggests that superconducting materials with higher normal state sheet resistance $\mathscr{R}_s$ and/or smaller energy gaps Δ will have higher intrinsic kinetic inductance fractions α.

3.5 Temperature responsivity

Now that we have discussed the physics needed to how understand how QPs affect the kinetic inductance, surface impedance, and complex conductivity of an MKID, we will briefly discuss the change in MKID resonant frequency in response to a change in bath temperature following Mauskopf (2018) [115]. Recall that the resonant frequency f_r and total quality factor Q_r are affected by changes in the quasiparticle density of the superconducting volume. The shift in the resonant frequency due to changes in bath temperature may be expressed as:

$$\frac{df_r}{dT} = \frac{df_r}{d\sigma_2}\frac{d\sigma_2}{dn_{qp}}\frac{dn_{qp}}{dT} \tag{3.46}$$

For a thin superconducting film with thickness t, the kinetic inductance is $L_k = \frac{1}{\sigma_2\omega}$. From this we can solve for the change in L_k due to the change in the imaginary conductivity as:

$$\frac{dL_k}{d\sigma_2} = -\frac{1}{\omega\sigma_2^2} = -\frac{L_k}{\sigma_2} \tag{3.47}$$

We can then use Eqn 3.2 and Eqn 3.47 to solve for how the resonant frequency changes with σ_2 such that:

$$\frac{df_r}{d\sigma_2} = \frac{df_r}{dL_k}\frac{dL_k}{d\sigma_2} = \frac{\alpha f_r}{2\sigma_2} \tag{3.48}$$

The quasiparticle density at low temperatures $T \ll T_c$ is given by:

$$\frac{dn_{qp}}{dT} \simeq \frac{n_{qp}}{T}\left(\frac{1}{2} + \frac{\Delta}{kT}\right) \tag{3.49}$$

Finally, the Mattis Bardeen equation for σ_2 in the case of thermal quasiparticle generation (Eqn 3.29) can be used to find $d\sigma_2/dn_{qp}$.

Then Eqn 3.46 can be solved analytically so that the resonant frequency depends on bath temperature as:

$$\frac{df_r}{dT} = \frac{\alpha f_r e^{-\frac{\Delta}{kT}}}{T}\sqrt{\frac{2\pi kT}{\Delta_0}}\left(\frac{1}{2} + \frac{\Delta}{kT}\right)\left(1 + \sqrt{\frac{2\Delta_0}{\pi kT}}e^{-\xi}I_0(\xi)\right) \tag{3.50}$$

As can be seen, there is an explicit dependence on the zero temperature energy gap Δ_0 and kinetic inductance fraction α. It is possible to find these values by fitting to the temperature dependence of the resonant frequency.

3.6 Optical responsivity

In this section, we will discuss the change in an MKID's resonant frequency in response to a change in absorbed optical power following discussions in Mauskopf (2018) [115] and Gordon (2019) [70]. When optical power is absorbed by an MKID, with photons of energy $h\nu > 2\Delta$, this leads to a change in the quasiparticle density of the device. This causes a corresponding change in the real and imaginary components of the complex conductivity and thus the surface impedance of the superconducting films (see Section 3.2.2 and Section 3.3). With this change in the surface impedance, particularly the increase in the kinetic inductance (Section 3.4), the resonance frequency shifts δf_r and the total quality factor is also affected δQ_r. When using a fixed probe tone on or near resonance for each MKID, the transmitted tone will experience a change in amplitude and phase.

At a fixed bath temperature, the shift in resonant frequency in response to a change in absorbed optical

power is given by:

$$\frac{df_r}{dP_{abs}} = \frac{df_r}{d\sigma_2}\frac{d\sigma_2}{dn_{qp}}\frac{dn_{qp}}{dP_{abs}} \tag{3.51}$$

The Mattis Bardeen equations, specifically Eqn 3.15 and Eqn 3.17, can be used to approximate the change in σ_2 to change in quasiparticle density n_{qp} such that:

$$\frac{d\sigma_2}{dn_{qp}} \simeq -\frac{\sigma_2}{2N_0\Delta_0}\left(1+\sqrt{\frac{2\Delta_0}{\pi kT}}\right) \tag{3.52}$$

Using Eqn 3.48 for the change in resonance frequency with respect to σ_2, we find that the one of the products in Eqn 3.51 is:

$$\frac{df_r}{d\sigma_2}\frac{d\sigma_2}{dn_{qp}} \simeq -\frac{\alpha f_r}{4N_0\Delta_0}\left(1+\sqrt{\frac{2\Delta_0}{\pi kT}}\right) \tag{3.53}$$

This shows that the MKID geometry (α, f_r), temperature of the device (T), and superconducting material properties (N_0,Δ_0) play a role in the device optical responsivity.

However, the change in quasiparticle density due to absorbed optical power dn_{qp}/dP_{abs} is case dependent. The quasiparticle density in a MKID depends on the rate of quasiparticle generation, where we consider here phonons, absorbed optical power, microwave readout power, and the rate of recombination of quasiparticles into Cooper pairs. If we balance these rates then we find that:

$$\begin{aligned}\frac{dn_{qp}}{dt} &= \Gamma_{opt} + \Gamma_{read} + \Gamma_{therm} - \Gamma_{rec} \\ &= \frac{\eta P_{abs}}{\Delta V} + \frac{\varepsilon P_{read}}{\Delta V} + \gamma N_0^2 8\pi kT\Delta e^{-2\Delta/kT} - \frac{n_{qp}}{\tau_{qp}}\end{aligned} \tag{3.54}$$

where Γ_{opt}, Γ_{read}, and Γ_{therm} are the QP generation rate due to absorbed optical power, microwave readout power, or thermal phonons, respectively, and Γ_{rec} is the QP recombination rate back into Cooper pairs. In the second part of Eqn 3.54, η is the internal quasiparticle generation efficiency for absorbed optical power, V is the volume of the superconductor, ε is the internal quasiparticle generation efficiency for absorbed/dissipated readout power, and $\gamma = 1/(n_{qp}\tau_{qp})$ is a constant relating the number density of quasiparticles to the QP recombination time. This is a simplification of more comprehensive equations for the rate of change of quasiparticles (e.g. [37, 67]).

Case 1: Quasiparticle generation dominated by absorption of optical photons

In Case 1, the rate of quasiparticle generation due to absorbed optical power is much larger than the readout

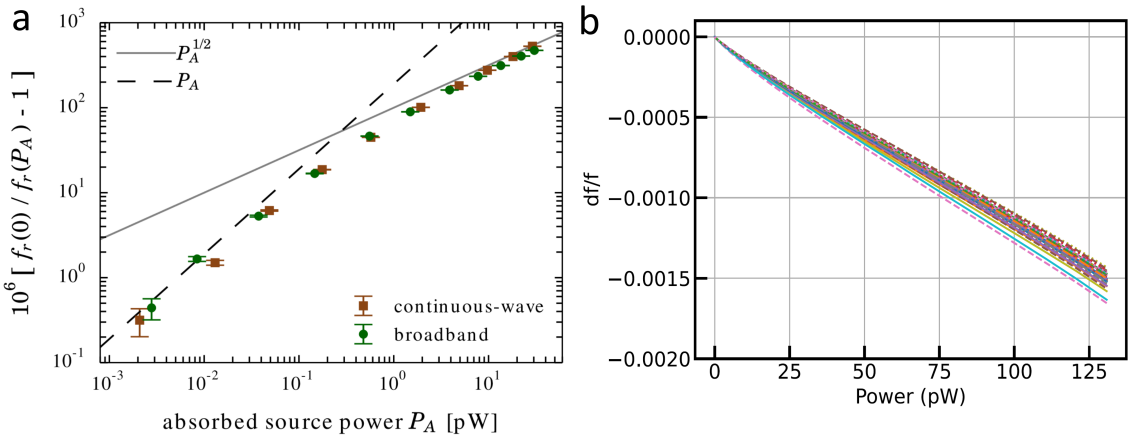

Figure 3.3: *a:* Measured fractional frequency response df_r/f_r vs absorbed optical power for an Al MKID measured using a source with continuous-wave (brown square) and broadband (green circle) modes, from Flanigan et al. (2016) [59]. The dashed black line (linear) and solid gray line show how this response changes at low and high absorbed powers. This response is consistent with Case 1 or a regime where quasiparticle generation is dominated by absorption of optical photons at higher powers. *b:* Measured normalized fractional frequency response df_r/f_r vs absorbed optical power for TiN/Ti/TiN trilayer MKIDs where power is varied using a cryogenic blackbody source, from Wheeler et al. (2022) [183]. This linear response over a wide range of powers is consistent with Case 2 or where the recombination time of quasiparticles is independent of absorbed optical power.

or thermal contributions so that Eqn 3.54 reduces to:

$$\frac{dn_{\rm qp}}{dt} = \frac{\eta P_{\rm abs}}{\Delta V} - \gamma n_{\rm qp}^2 \tag{3.55}$$

Also, for a fixed amount of absorbed power, the steady state solution to $\frac{dn_{\rm qp}}{dt} = 0$ using Eqn 3.55 is:

$$n_0 = \sqrt{\frac{\eta P_{\rm abs}}{\gamma \Delta V}} \tag{3.56}$$

Using Eqn 3.56 in the small signal limit [144], the change in the number density of quasiparticles due to the absorbed optical power $\frac{dn_{\rm qp}}{dP_{\rm abs}}$ can be shown to be [115]:

$$\begin{aligned} \frac{dn_{\rm qp}}{dP_{\rm abs}} &= \frac{1}{2}\sqrt{\frac{\eta}{\gamma P_{\rm abs}\Delta V}}\frac{1}{1+j\omega\tau_{\rm qp}/2} \\ &= \frac{n_0}{2P_{\rm abs}}\frac{1}{1+j\omega\tau_{\rm qp}/2} \end{aligned} \tag{3.57}$$

Behavior corresponding to Case 1 has been observed in aluminum (Al) MKIDs within the literature (e.g [51, 59]). Figure 3.3 shows the measured fractional frequency response $\delta f_{\rm r}/f_{\rm r}$ with a change in optical power, using a cryogenic blackbody source to vary loading on the MKIDs. For the Al MKIDs measured in Fig 3.3a from [59], there is a notable transition from linear response at low powers to a regime where quasiparticle generation is dominated by the absorption of optical photons at higher powers.

Case 2: Quasiparticle generation dominated by thermal phonons or with recombination time independent of absorbed optical power

In Case 2, the thermal quasiparticle generation rate is constant so that Eqn 3.54 reduces to:

$$\frac{dn_{\rm qp}}{dt} \simeq \frac{\eta P_{\rm abs}}{\Delta V} + \Gamma_{\rm therm} - \frac{n_{\rm qp}}{\tau_{\rm eff}} \tag{3.58}$$

where $\Gamma_{\rm therm}$ and $\tau_{\rm eff}$ are constant at a fixed phonon temperature.

Using Eqn 3.58 in conjunction with the small signal approximation [144], the change in the number density of quasiparticles due to the absorbed optical power $\frac{dn_{\rm qp}}{dP_{\rm abs}}$ can be shown to be:

$$\frac{dn_{\rm qp}}{dP_{\rm abs}} \simeq \frac{\eta\tau_{\rm eff}}{\Delta V}\frac{1}{1+j\omega\tau_{\rm eff}} \tag{3.59}$$

Behavior corresponding to Case 2 has been observed in TiN MKIDs and TiN/Ti/TiN trilayer MKIDs within the literature (e.g [84, 183]). For the TiN/Ti/TiN trilayer MKIDs measured in Fig 3.3b from [183], a linear response is observed over a wide range of absorbed optical powers.

Case 3: Intermediate case, with a population of thermal quasiparticles

In Case 3, there is an effective "dark" power loading P_0 that generates a constant population of quasiparticles. This has the effect of limiting the quasiparticle lifetime at low optical powers. Due to this population, Eqn 3.54 in the steady-state solution can now be written as:

$$\frac{\eta P_{\rm abs}}{\Delta V} + \gamma N_0^2 8\pi kT\Delta e^{-2\Delta/kT} - \gamma n_{\rm qp}^2 = 0 \tag{3.60}$$

In the general case, using Eqn 3.60, the number density of quasiparticles $n_{\rm qp}$ can be found to be [115]:

$$n_{\rm qp} = \sqrt{\frac{\Gamma_0 + \eta P_{\rm abs}/\Delta V}{\gamma}} \tag{3.61}$$

Taking the derivative of Eqn 3.61 with respect to $P_{\rm abs}$ gives:

$$\frac{dn_{\rm qp}}{dP_{\rm abs}} = \sqrt{\frac{\eta}{\Delta V\gamma}}\frac{1}{\sqrt{P_0 + P_{\rm abs}}} \tag{3.62}$$

This effective "dark" power loading P_0 could originate from thermal phonons, stray light, or quasiparticle trapping among others.

3.7 Sensitivity

In astronomical applications, in which the photon signal is faint, we strive to design detectors that are photon-noise-limited or background-limited, that is where the noise from incident photons is the dominant source of noise in the detector. More details about the photon noise are discussed in Chapter 2. For a single mode detector, the photon NEP in units of W/$\sqrt{\rm Hz}$ is:

$$NEP_{\rm phot}^2 = NEP_{\rm shot}^2 + NEP_{\rm wave}^2 = 2P_{\rm abs}h\nu(1+\eta m) \tag{3.63}$$

which is referenced to power absorbed by a detector $P_{\rm abs}$. Using $P_{\rm abs} = \eta m h\nu\Delta\nu$, we can also rewrite Eqn 3.63 as:

$$NEP_{\rm phot}^2 = 2P_{\rm abs}h\nu + \frac{2P_{\rm abs}^2}{\Delta\nu} \tag{3.64}$$

In Eqn 3.64, the first term comes from Poisson/shot noise from photons and the second term is a correction due to wave bunching. The shot noise term dominates for low occupation number m such that $h\nu/kT \gg 1$. While the wave bunching term dominates for high m such that $h\nu/kT \ll 1$.

In addition to photon noise, there are other sources of noise that originate from the detector itself and from the readout electronics used to operate these detectors. These noise sources need to be lower than and in some cases mitigated in the system to achieve photon-noise-limited performance. In MKIDs, the total NEP includes contributions from photon noise, quasiparticle generation-recombination (GR) noise, amplifier noise, readout noise, and excess noise from two level systems (TLS) that cause fluctuations in the resonator capacitance. In the following subsections, we will discuss the different sources of noise in MKIDs with the exception of readout noise. A more detailed discussion of readout noise, particularly as it pertains to TolTEC, will follow in Chapter 7.

3.7.1 Generation-recombination noise

The fundamental noise source in MKIDs is generation-recombination noise. GR noise is caused by the intrinsic uncertainty in the Cooper pair recombination and generation rates. The fluctuation in the Cooper pair number δN_{cp} can be written in terms of the recombination (Γ_{rec}) rate as:

$$\delta N_{\mathrm{cp}} = \sqrt{\Gamma_{\mathrm{rec}} \delta t} = \sqrt{\frac{N_{\mathrm{qp}} \delta t}{2\tau_{\mathrm{qp}}}} \tag{3.65}$$

where Γ_{rec} is the number of Cooper pairs recombining per second and $\delta t = 1/2\delta f$ is the measurement integration time with measurement bandwidth δf. The number of Cooper pairs broken per optical photon is:

$$N_{\mathrm{gen}} = \frac{\eta_{\mathrm{pb}} h\nu}{2\Delta} \tag{3.66}$$

while the number of quasiparticles generated per optical photon is just twice this or:

$$N_{\mathrm{qp}} = \frac{\eta_{\mathrm{pb}} h\nu}{\Delta} \tag{3.67}$$

where η_{pb} is the pair-breaking efficiency of converting absorbed power to quasiparticles.

Using Eqn 3.65 for δN_{cp} and Eqn 3.66 for N_{gen}, the uncertainty in the absorbed energy due to the recombination of quasiparticles into Cooper pairs δE_{rec} is:

$$\begin{aligned} \delta E_{\mathrm{rec}} &= \frac{\delta N_{\mathrm{cp}}}{N_{\mathrm{gen}}} h\nu = \frac{2\Delta \delta N_{\mathrm{cp}}}{\eta_{\mathrm{pb}}} = \frac{2\Delta}{\eta_{\mathrm{pb}}} \sqrt{\Gamma_{\mathrm{rec}} \delta t} \\ &= \frac{2\Delta}{\eta_{\mathrm{pb}}} \sqrt{\frac{N_{\mathrm{qp}} \delta t}{2\tau_{\mathrm{qp}}}} = \sqrt{\frac{2\Delta P_{\mathrm{abs}} \delta t}{\eta_{\mathrm{pb}}}} [J] \end{aligned} \tag{3.68}$$

where $P_{\rm abs} = h\nu/\tau_{\rm qp}$ has been used. Energy can be converted to power by dividing a time interval δt such that:

$$\delta P_{\rm rec} = \sqrt{\frac{2\Delta P_{\rm abs}}{\eta_{\rm pb}\delta t}}[W] \tag{3.69}$$

Furthermore, this can be converted to a noise equivalent power ($NEP_{\rm GR}$) by dividing Eqn 3.69 by the square root of the bandwidth $\sqrt{\delta f} = \sqrt{1/2\delta t}$ so that:

$$NEP_{\rm GR} = \sqrt{\frac{4\Delta P_{\rm abs}}{\eta_{\rm pb}}}\left[\frac{W}{\sqrt{\rm Hz}}\right] \tag{3.70}$$

where the additional factor of $\sqrt{2}$ comes from the fact that quasiparticles are generated and recombine in pairs [60]. This expression for $NEP_{\rm GR}$ applies in the limit that the quasiparticle recombination noise is significant. Recall that $P_{\rm abs}$ can also be referenced to the optical source power since $P_{\rm abs} = \eta P_{\rm opt}$ where η is the system efficiency. We can rewrite Eqn 3.70 as an optical NEP such that:

$$\frac{NEP_{\rm GR}}{\eta} = \sqrt{\frac{4\Delta P_{\rm opt}/\eta_{\rm pb}}{\eta}} \tag{3.71}$$

3.7.2 Amplifier noise

When operating an MKID array, the cryogenic low noise amplifier (LNA) at the output of the array adds thermal, or Johnson-Nyquist, noise with an associated noise temperature $T_{\rm amp}$. The LNA is used to amplify the probe tone comb. The voltage noise/power spectral density at the input of the amplifier is:

$$e_{\rm V,amp} = 4kT_{\rm amp}Z_{\rm amp}\left[\frac{V^2}{\rm Hz}\right] \tag{3.72}$$

where $Z_{\rm amp}$ is the input impedance of the amplifier. This amplifier noise (Eqn 3.72) can be converted to frequency units by dividing the voltage responsivity so that:

$$e^2_{\rm f_r,amp} = \frac{e^2_{\rm V,amp}}{|dV_{\rm out}/df_{\rm r}|^2}\left[\frac{\rm Hz^2}{\rm Hz}\right] \tag{3.73}$$

where $f_{\rm r}$ is the resonance frequency. The voltage responsivity is related to the input voltage ($V_{\rm in}$) and output voltage ($V_{\rm out}$) of the amplifier such that:

$$\begin{aligned}\frac{dV_{\rm out}}{df_{\rm r}} &= \frac{d}{df_{\rm r}}V_{\rm in}S_{21} \\ &\simeq -2jV_{\rm in}\frac{Q_{\rm r}^2 f}{Q_{\rm c}f_{\rm r}^2}\frac{1}{(1+2jQ_{\rm r}x)^2}\end{aligned} \tag{3.74}$$

where we have taken the derivative of Eqn 3.9 for S_{21} and $x = (f - f_r)/f_r$ where f is the readout frequency. On resonance, such that $x = 0$, Eqn 3.74 reaches its maximum value $dV_{out}/df_r \simeq -2jV_{in}Q_r^2/(Q_c f_r)$. Using Eqn 3.73 for the voltage responsivity, we can now rewrite the amplifier noise near resonance $x \ll 1$ as:

$$\begin{aligned} e^2_{f_r,amp} &= 4kT_{amp}Z_{amp}\left(\frac{Q_c^2 f_r^2}{4V_{in}^2 Q_r^4}\right) \\ &= kT_{amp}\left(\frac{Q_c^2 f_r^2}{Q_r^4 P_r}\right)\left[\frac{\text{Hz}^2}{\text{Hz}}\right] \end{aligned} \tag{3.75}$$

where we have used $P_r = V_{in}^2/Z_{amp}$ for the readout power.

The LNA contribution to the NEP (NEP_{amp}) can be written as:

$$NEP_{amp} = e_{f_r,amp}/\left(\frac{df_r}{dP_{abs}}\right)\left[\frac{W}{\sqrt{\text{Hz}}}\right] \tag{3.76}$$

where $\frac{df_r}{dP_{abs}}$ is the optical responsivity derived in Section 3.6 for different QP cases. The $1/\sqrt{P_r}$ dependence in NEP_{amp} shows that using higher readout powers will suppress this noise contribution.

3.7.3 Excess noise: TLS noise

In addition to the noise sources listed above, there is an additional source of excess noise in MKIDs caused by two-level systems (TLS) in the surfaces of amorphous dielectric materials near the resonator (eg. [63, 189]). Two-level systems are tunneling states, where one or a group of atoms can tunnel between two sites, in amorphous materials that can be activated at low temperatures and induce an additional resonance frequency shift/pure phase (frequency) noise and dielectric loss. Gao (2008) [63] studied the power, temperature, material, and geometry dependences of TLS-induced noise and developed a semi-empirical noise model to explain the power and geometry dependence of this noise. The TLS have electric and elastic dipole moments which can cause variations in the permittivity, related to the electric field, and permeability, related to the magnetic field, of amorphous materials.

TLS are usually modeled as fluctuations in the capacitance of the MKID [63, 189]. The TLS-induced resonator frequency shift with temperature when the electric field is weak can be depend on: [63, 189]:

$$\frac{\delta f_r}{f_r} = \frac{F_{TLS}\delta_0}{\pi}\left[Re\Psi\left(\frac{1}{2} + \frac{1}{2\pi j}\frac{\hbar\omega}{kT}\right) - \ln\left(\frac{\hbar\omega}{kT}\right)\right] \tag{3.77}$$

where Ψ is the complex digamma function and $F_{\rm TLS}$ is a filling factor for the fraction of the electric field energy in the dielectric material with the TLS. This filling factor also relates the resonator dissipation to the TLS loss tangent $\delta_{\rm TLS}$ such that:

$$Q_{\rm i,TLS}^{-1}(\omega,T) = F_{\rm TLS}\delta_{\rm TLS}(\omega,T) \propto F_{\rm TLS}\left(1+\frac{P_{\rm int}}{P_{\rm c}}\right)^{-1/2} \tag{3.78}$$

where $P_{\rm int}$ is the internal microwave power stored in the resonator and is proportional to the readout power $P_{\rm r}$ such that $P_{\rm int} = 2Q_{\rm r}^2 P_{\rm r}/(\pi Q_{\rm c})$.

There are a number of strategies that have been developed for mitigating capacitive TLS noise. They include modifying the capacitor geometry [132]. Operating MKIDs at higher bath temperatures can also be used to suppress TLS noise as seen by the temperature dependence in Eqn 3.77. The TLS can also be suppressed by operating resonators with greater microwave powers as seen by the $1/\sqrt{P_{\rm int}}$ dependence in Eqn 3.78. Another active area of research is the use of crystalline instead of amorphous dielectric materials for the MKID capacitor (e.g. [181]).

The TLS noise has been observed to scale as $1/\sqrt{P_{\rm int}}$ like Eqn 3.78 and to increase with inductor volume as $\Sigma^{1/2}$ [115]. Substrate material can also change the way that optical responsivity (Section 3.6) depends on inductor volume. For Case 1, including Al MKIDs, the optical responsivity $df_{\rm r}/dP_{\rm abs}$ does not depend on Σ (Eqn 3.57) so the TLS noise only increases as $\Sigma^{1/2}$ and the inductor volume can be made large. For Case 2, including TiN MKIDs and TiN/Ti/TiN trilayer MKIDs, the optical responsivity instead has a Σ^{-1} dependence (Eqn 3.59) so these detectors are usually designed with smaller volumes to mitigate TLS noise.

The fractional frequency noise power spectral density due to TLS $S_{\rm xx,TLS}(\nu)$ or $S_{\delta f_{\rm r}/f_{\rm r}}(\nu)$ depends on frequency ν, temperature T, and readout power $P_{\rm r}$ such that [189]:

$$S_{\rm xx,TLS}(\nu) \propto \nu^{-1/2} \propto T^{-\beta} \propto P_{\rm r}^{-1/2}\left[\frac{1}{\rm Hz}\right] \tag{3.79}$$

where β is an empirical constant such that $\beta = 1.5-2$. This noise corresponds to fluctuations in the MKID transmission in a direction that is purely tangential to the resonance circle in IQ space. A more detailed, semi-empirical model of $S_{\rm xx,TLS}(\nu)$ can be found in Gao (2008) [63]. The TLS noise equivalent power $NEP_{\rm TLS}(\nu)$ can be found by dividing $S_{\rm xx,TLS}(\nu)$ by the case-specific optical responsivity in Section 3.6.

3.7.4 Total MKID NEP

The total optical noise equivalent power $NEP_{\rm tot}$ for a detector is calculated from the sum of the contributions of different noise sources added in quadrature. In a photon-noise-limited detector, the noise components that contribute most to least are photon noise, amplifier noise, generation-recombination noise, and readout noise. Most of these sources have been discussed throughout this section with the exception of readout noise. The total NEP can be calculated as:

$$NEP_{\rm tot} = (NEP^2_{\rm phot} + NEP^2_{\rm amp} + NEP^2_{\rm TLS} + NEP^2_{\rm GR} + NEP^2_{\rm read})^{1/2} \tag{3.80}$$

where $NEP_{\rm read}$ is the readout noise equivalent power. A systematic study of the noise of detector arrays for the TolTEC camera, including a discussion of readout noise, will follow in Chapter 7.

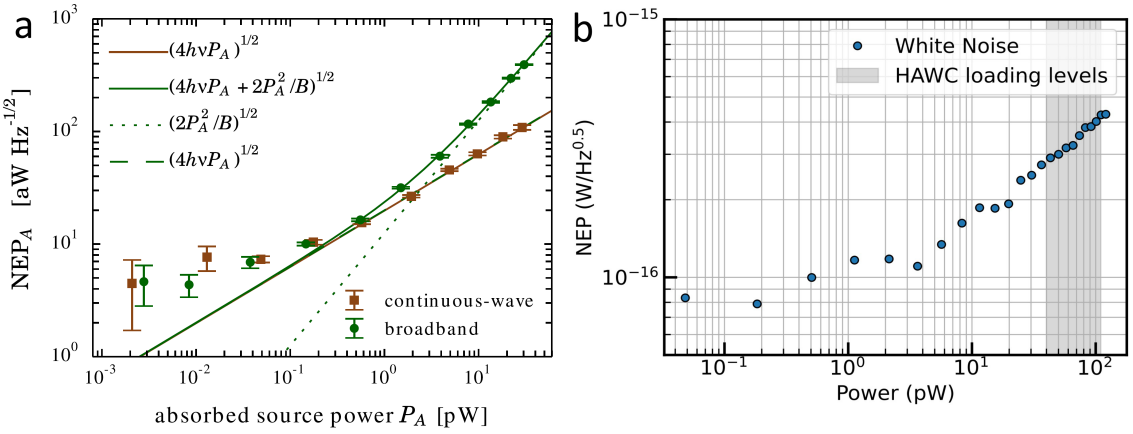

Figure 3.4: *a:* Measured noise-equivalent power (NEP) versus absorbed optical power for an Al MKID measured using a source with continuous-wave (brown square) and broadband (green circle) modes, from Flanigan et al. (2016) [59]. The lines, which are fits to this data given by the models on the upper left, are consistent with photon-noise-limited performance at higher powers (green dotted line). *b:* Measured NEP vs absorbed optical power for TiN/Ti/TiN trilayer MKIDs, from Wheeler et al. (2022) [183]. The white noise level at each point was extracted from measured PSDs and is consistent with photon-noise-limited performance in the gray vertical band which correspond to expected loading levels.

Chapter 4

Demonstration of 220/280 GHz multichroic feedhorn-coupled TES polarimeter

This work was published as [176] and is reprinted identically in this chapter.

4.1 Abstract

We describe the design and measurement of feedhorn-coupled, transition-edge sensor (TES) polarimeters with two passbands centered at 220 GHz and 280 GHz, intended for observations of the cosmic microwave background. Each pixel couples polarized light in two linear polarizations by use of a planar orthomode transducer and senses power via four TES bolometers, one for each band in each linear polarization. Previous designs of this detector architecture incorporated passbands from 27 GHz to 220 GHz; we now demonstrate this technology at frequencies up to 315 GHz. Observational passbands are defined with an on-chip diplexer, and Fourier-transform-spectrometer measurements are in excellent agreement with simulations. We find coupling from feedhorn to TES bolometer using a cryogenic, temperature-controlled thermal source. We determine the optical efficiency of our device is $\eta = 77\% \pm 6\%$ ($75\% \pm 5\%$) for 220 (280) GHz, relative to the designed passband shapes. Lastly, we compare two power-termination schemes commonly used in wide-bandwidth millimeter-wave polarimeters and find equal performance in terms of optical efficiency and passband shape.

Keywords: feedhorn, polarimeter, microwave, millimeter-wave, cosmic microwave background, CMB, transition-edge sensor, TES

4.2 Introduction

The cosmic microwave background (CMB) provides a powerful probe of the earliest moments of the universe. Precision measurements of CMB temperature and polarization aniso-tropies have played a crucial role in shaping our understanding of how the universe formed by providing rigorous constraints [141] on parameters of the standard cosmological model, ΛCDM. However, millimeter-wave observations are complicated by the presence of astrophysical foregrounds, such as synchrotron emission and galactic dust, which also radiate at these wavelengths. By designing detectors with broad spectral coverage, these foregrounds can be separated from the CMB because their spectral energy distributions are distinct. In addition, these detectors maximize the usage of telescope focal planes. For these reasons, several research groups are developing multichroic detectors [122] with different coupling architectures [164, 9, 45]. We are developing feedhorn-coupled transition-edge sensor (TES) polarimeters, which have been deployed in multiple experiments [80, 38, 102] over bands from 27 GHz to 220 GHz. In this work, we describe our first implementation of multichroic, dual-polarization-sensitive 220/280 GHz detectors for the Simons Observatory [4].

4.3 Design and simulated performance

We have designed and fabricated single-pixel, feedhorn-coupled, 220/280 GHz polarimeters. Devices were fabricated in the NIST Boulder Microfabrication Facility. The general feedhorn-coupled architecture is described by McMahon et al. [122]. Fabrication is described in more detail by Duff et al. [55]. Here we focus on aspects unique to this design. The device consists of four optically-coupled TES bolometers for passband measurements in two linear polarizations. Additionally, we include two dark TES bolometers for systematic checks. TESs consist of an AlMn alloy and were designed to have $T_c = 160\,\mathrm{mK}$ and $R_n = 8\,\mathrm{m\Omega}$. Detector pixels were also designed with two different bolometer-saturation powers (P_{Sats}). The first type has TESs with continuous membranes suitable for room-temperature Fourier-transform-spectrometer (FTS) measurements. The second type has TESs with released membranes suitable for ground-based photon loading in the Atacama Desert, Chile. Fig. 4.1 shows an optical micrograph of the detector pixel with components highlighted.

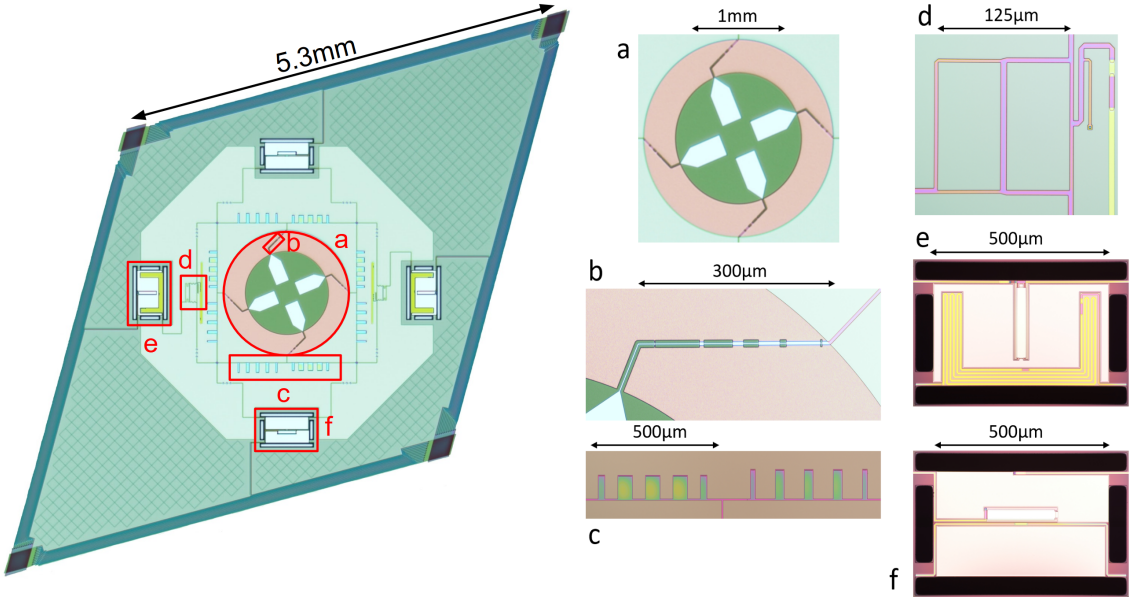

Figure 4.1: *Left:* Optical micrograph of 220/280 GHz multichroic detector with major components denoted by *red labels*. *Right:* Detailed micrographs of: **a** planar orthomode transducer (OMT), **b** co-planar waveguide-to-microstrip (CPW-to-MS) transition, **c** diplexer, **d** hybrid tee and **e** TES bolometer with Nb-to-Au MS transition for 'A-type' termination, and **f** TES bolometer with lumped termination resistor for 'B-type' termination. (Color figure online.)

As part of our first implementation, we also designed each polarization with a different power-termination: a hybrid tee coupled to a lossy Au distributed termination ('A-type') [40] or a PdAu lumped termination resistor ('B-type') [128]. The function of this termination is to dissipate only the lowest-order waveguide mode, TE_{11}, on the bolometer. At 2.3:1 bandwidth, the planar orthomode transducer (OMT) supports multiple waveguide modes; however, we only wish to couple the bolometer to the TE_{11} mode because it exhibits a well defined polarization state. Furthermore, coupling the bolometer to higher-order modes is undesirable as it degrades angular resolution [83]. In the A-type, filtered passbands are routed to a hybrid tee, which takes the input from two ports and produces sum and difference outputs. Higher-order modes are associated with the sum output and are terminated on the substrate, while power in the TE_{11} mode associated with the difference port is routed to the bolometer and dissipated in a lossy Nb-to-Au meander. In the B-type, a lumped termination resistor, thermally connected to the TES, is differentially fed signals from one pair of OMT probes. This termination scheme also results in a smaller bolometer than in the A-type, which could be beneficial for more tightly packed pixels.

The performance of the components listed in Fig. 4.1 was verified through electromagnetic (EM) simulations in Microwave Office (1D, www.awr.com), Sonnet (2.5D, www.-sonnetsoftware.com/), and HFSS (3D, www.ansys.com). We created a full 3D model in HFSS of the OMT (Fig. 4.1a), including a backshort and waveguide coupling. We calculated the scattering parameters of five waveports, one for the waveguide input and one for each of the four OMT probes. This model assumed no loss so that any power not found in these five waveports was assumed to be due to radiation that could leak out of the 25 μm gaps between the planar OMT above and below the waveguide. From this, we predict 95.4% (89.6%) co-polar coupling, 2.4% (2.8%) reflection, and 2.2% (7.6%) radiation, averaged over the 220 (280) GHz passband. The co-planar waveguide-to-microstrip (CPW-to-MS) transition (Fig. 4.1b) was optimized with a transmission-line model in Microwave Office and then verified in Sonnet. Mean reflection across the extended passband, 195 GHz to 315 GHz, was simulated to be -25 dB. The diplexer (Fig. 4.1c) was designed and verified in Sonnet. We estimate 94.7% (91.0%) transmission assuming SiN loss tangent ($\tan\delta$) = 0.0008, averaged over the 220 (280) GHz passband. For the A-type termination, separate hybrid tees (Fig. 4.1d) were designed in Sonnet for the 220 GHz and 280 GHz passbands, because they have intrinsically narrow bandwidths. From the

scattering parameters, the differential-odd mode, associated with the difference port, was calculated to have $> 99\%$ transmission for each type. The Nb-to-Au transition (Fig. 4.1e), like the CPW-to-MS transition, was optimized with a transmission-line model in Microwave Office and verified in Sonnet. Mean reflection across the extended passband was simulated to be -35 dB. For the B-type termination, the termination resistor (Fig. 4.1f) was simulated in Sonnet, assuming PdAu with sheet resistance $R = 3.2\,\Omega$/square and an ideal aspect ratio of length:width = 7:1. Mean reflection across the extended passband was simulated to be -25 dB.

4.4 Experimental setup

To test the devices, we packaged the dies in brass split-block modules coupled to prototype aluminum spline-profiled feedhorns [156], coupled to a time-division multiplexer (TDM) [54], and installed in a 100 mK adiabatic-demagnetization-refrigerator cryostat. We configured the cryostat in two ways for our two measurements. For measurement of detector passbands, we installed an optical-access window in the cryostat and used a Fourier-transform-spectrometer (FTS). The optical path from FTS to feedhorn consists of the following filters. At 300 K, we use a 8.89 cm diameter aperture stop and 5.08 cm thick polypropylene-based, expanded foam access window. At 50 K, we use a 2 cm thick single-layer anti-reflection (AR) coated PTFE filter. This AR coating has been optimized for transmission from 195 GHz to 420 GHz. At 4 K, we use a 14 cm^{-1} metal-mesh low pass filter [6] from Cardiff, a 1 cm thick Teflon filter, and a 1.5875 mm thick nylon stack with the same AR coating as the 50 K component. For measurement of detector optical efficiency, we used a cryogenic temperature-controlled thermal source heat-sunk to the 4 K stage. This thermal load consists of a 101.6 mm tesselating terahertz tile that has < -30 dB reflection at 300 GHz [149]. We therefore assume a perfect blackbody in our loading calculation discussed in the next section. Two uncalibrated thermometers on the backside of this thermal load are used to measure temperature changes. The source's exponential decay-time constant was measured to be ~ 2.5 minutes. We place 14 cm^{-1} and 11 cm^{-1} low pass filters from Cardiff at 4 K to further attenuate any out-of-band pickup.

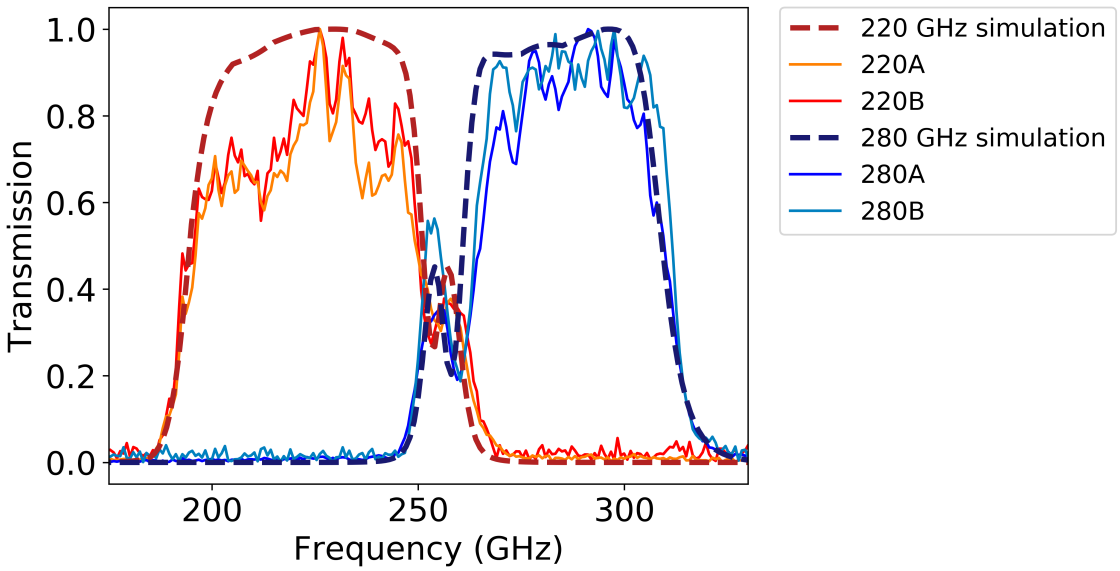

Figure 4.2: Passband measurements of the 220/280 GHz detector. A and B refer to orthogonal polarizations with different termination schemes described in more detail in Section 4.3. Data (*solid lines*) are in excellent agreement with simulations (*dashed lines*). Both data and simulations are peak normalized. (Color figure online.)

Type	Raw	With dark subtraction
220A	95%±1%	76%±2%
220B	97%±4%	79%±6%
280A	97%±4%	72%±4%
280B	103%±3%	78%±4%

Table 4.1: Optical efficiency for raw ΔP data ('Raw') and after subtracting the contribution to ΔP from dark TESs ('With dark subtraction'). Error bars are the one standard deviation statistical uncertainty from 42 independent measurements, two pixels, seven ΔT points, and three repeats, summed in quadrature.

4.5 Results

4.5.1 Passbands

Fig. 4.2 shows peak normalized FTS measurements of the 220/280 GHz detector along with separate 220 GHz and 280 GHz simulations that consist of the simulated peak normalized frequency response of the diplexer and OMT. There is excellent agreement with simulations and both A- and B-type terminations give well-matched passbands. This agreement also shows that the slight interaction between the two passbands at ∼250 GHz is understood; this was removed with a simple design change in subsequent wafer production. Furthermore, the anti-reflection coating used in our filter stack is non-ideal. Given our knowledge of the materials and distances in the optical path from FTS to feedhorn, we expect fringing at the level of 20% to 30%, which is also seen in the data.

4.5.2 Optical efficiency

Because CMB measurements are inherently of low signal-to-noise ratio, we seek to maximize the optical efficiency of our detectors. We define optical efficiency η as the ratio of the optical power dissipated in our TES bolometers (ΔP) to the calculated loading power we would expect $\Delta P_{\rm Load}$:

$$\eta = \Delta P / \Delta P_{\rm Load}. \tag{4.1}$$

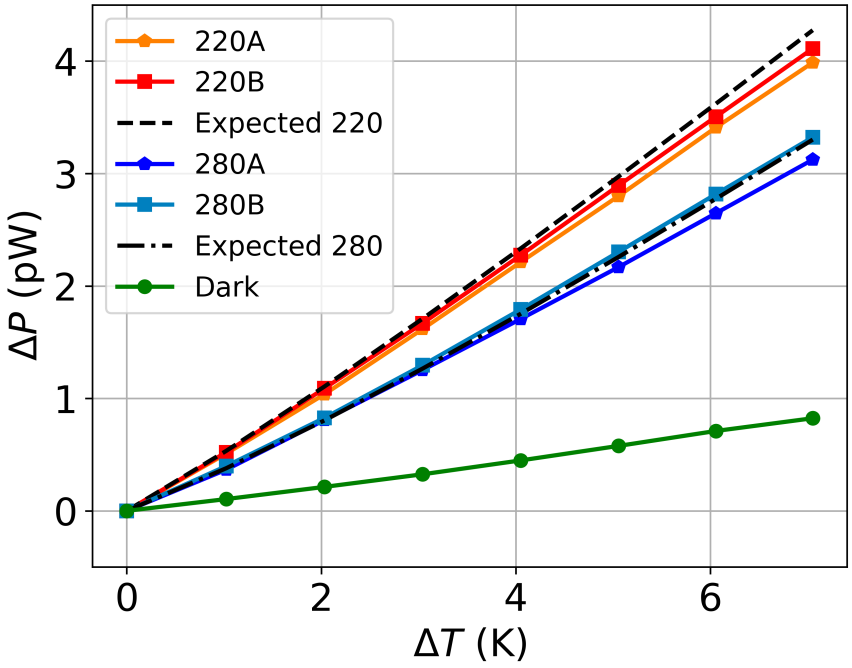

Figure 4.3: Power change in detectors as a function of temperature change of a cryogenic blackbody with reference to 5 K. *Solid lines* denote measurements and *dashed lines* correspond to theoretical loading ΔP_{Load}. (Color figure online.)

We vary the temperature of a beam-filling cryogenic blackbody load from 5 K to 12 K and measure the change in power in each TES through bolometer $I-V$ curves for P at 80% $R_{\rm n}$. Measurements are taken at each 1 K point after 21 minutes to allow the thermal load to fully equilibrate. We calculate $P_{\rm Load}$ for a single mode and ideal blackbody, including simulated passbands and corrections for free space filter loss, as

$$P_{\rm Load} = \int \frac{h\nu}{e^{\frac{h\nu}{k_{\rm B}T}} - 1} \prod_{i=1}^{4} F_i(\nu) d\nu, \tag{4.2}$$

where h is the Planck constant, ν is frequency, $k_{\rm B}$ is the Boltzmann constant, and T is the blackbody temperature in kelvin. $F_i(\nu)$ includes the peak normalized 220 GHz or 280 GHz simulated diplexer response, the peak normalized simulated OMT response, and the 300 K measured absolute transmission spectra of the $14\,{\rm cm}^{-1}$ and the $11\,{\rm cm}^{-1}$ low pass filters. Fig. 4.3 shows ΔP measurements of both optical and dark TES bolometer channels as a function of cryogenic blackbody temperature (referenced to 5 K) denoted by solid lines. Dashed lines correspond to calculations of expected loading power, $\Delta P_{\rm Load}$, using Eq. (4.2).

Optical efficiencies are calculated with Eq. (4.1) for each ΔT point. The average is reported in Table 4.1, both with ('With dark subtraction') and without ('Raw') dark bolometer power subtraction. Error bars in Table 4.1 are the one standard deviation statistical uncertainty from 42 independent measurements, two pixels, seven ΔT points, and three repeats, summed in quadrature. Assuming the ΔP of dark bolometers accurately monitors the parasitic power radiatively coupled to the optically coupled bolometers, we subtract dark ΔP from optical ΔP to estimate η. We calculate $\eta = 77\% \pm 6\%$ ($75\% \pm 5\%$) for the 220 (280) GHz passband. Factors that could account for this additional loss include: imprecise knowledge of load temperature, ideal versus measured passband shape, uncertainty in the gap size of the OMT, and the dark subtraction assumption itself. Given these factors, there is general agreement between measurements and expectations.

4.6 Conclusions

We have demonstrated a working prototype of a multichroic feedhorn-coupled 220/280 GHz detector pixel through electromagnetic simulations, FTS passband measurements, and cryogenic temperature-controlled blackbody measurements to calculate optical efficiency. Measured passbands are in excellent

agreement with simulations. We determine detector optical efficiency $\eta = 77\% \pm 6\%$ ($75\% \pm 5\%$) for the 220 (280) GHz passband. These results are consistent with expectations and demonstrate efficient optical coupling from feedhorn to TES bolometer. As part of our first implementation of these devices, we also investigated two power-termination schemes commonly used in wide-bandwidth millimeter-wave polarimeters: a hybrid tee coupled to a lossy Au distributed termination (A-type) or a PdAu lumped termination resistor (B-type). We find equal performance in terms of optical efficiency and passband shape.

After testing a second prototype of this detector pixel, this design will be implemented in arrays to be fielded in the Simons Observatory. In arrays to be deployed, an all-silicon assembly will reduce the OMT waveguide gap by more than a factor of 2. This will result in both an expected increase in co-polar coupling and a decrease in leakage radiation, improving the optical performance beyond what we demonstrate here.

Acknowledgements: This work was supported in part by the NASA APRA program, grant #NNX17AL23G. This material is based upon work supported by the National Science Foundation Graduate Research Fellowship under Grant No. DGE-1144083. Certain commercial software and materials are identified to specify the experimental study adequately. This does not imply endorsement by NIST nor that the software and materials are the best available for this purpose.

Chapter 5

Measurements of AlMn transition-edge sensor bolometers well described by a simple electrothermal model

This work was published as [177] and is reprinted identically in this chapter.

5.1 Abstract

Cosmic microwave background (CMB) polarization experiments utilize arrays of low temperature detectors, such as superconducting transition-edge sensor (TES) bolometers. Voltage-biased TES bolometers must be embedded in a readout circuit that allows for stable operation. To ensure stability and to test our physical and electrothermal model of these devices, measurements aimed at characterizing the dynamics of the sensor over the range of detector bias and loading conditions relevant to our application are carried out for multiple bolometer designs. In this work, we present bolometer electrothermal properties derived from current-voltage curves, effective electrothermal time constant measurements, and complex impedance measurements of AlMn TES bolometers intended for the Ali CMB Polarization Telescope (AliCPT). All bolometers consist of 385 nm thick 1400 ppma AlMn film with measured superconducting critical temperature $T_c = 480$ mK. The bolometers are well-described by a simple, one-pole electrothermal model with a natural time constant τ_0 that we adjust by varying the leg geometry and the amount of PdAu thermal ballast on the bolometer island. From these measurements, we determine that the volumetric heat capacity of sputtered PdAu (atomic percentages 67.6 % / 32.4 %) at 480 mK is 0.22 fJ/(K·μm^3). Finally, we present the TES parameters as a function of operational resistance and over a range of loading conditions.

Keywords: Microwave, millimeter-wave, cosmic microwave background, CMB, superconducting transition-

edge sensor, TES, bolometer, AliCPT

5.2 Introduction

Cosmic microwave background (CMB) polarization experiments utilize arrays of low temperature detectors, such as superconducting transition-edge sensor (TES) bolometers, to probe the earliest moments of the universe. Precision measurements of minute fluctuations in the CMB temperature and polarization have been transformative. They have shaped our understanding of the universe through improved constraints on parameters of the standard cosmological model, ΛCDM [34], from experiments like Planck [141]. Of particular interest among these parameters is the tensor-to-scalar ratio, r, which quantifies the tensor fluctuations caused by primordial gravitational waves encoded in CMB B-mode polarization in relation to the primordial scalar fluctuations hypothesized to have seeded temperature anisotropies in the CMB [95, 36]. The detection of CMB B-mode polarization continues to be a main science driver of CMB experimental cosmology [92, 79, 141], as this signal remains elusive. Current constraints place $r < 0.07$ at 2σ from BICEP2/Keck Array and Planck [28]. Upcoming experiments like the Ali CMB Polarization Telescope (AliCPT) [105], situated in the Tibetan Plateau, are poised to improve this constraint by one order of magnitude over current estimates with 3 years of observations and will open a new window for CMB observations in the Northern Hemisphere.

TES bolometers are a type of superconducting detector commonly used in CMB measurements. These detectors measure incident millimeter-wave radiation through heating of a temperature-dependent resistor, in this case, a superconducting film (the TES). Through voltage-biasing of the TES, which causes negative electrothermal feedback, operation can be well-stabilized within its superconducting transition [88]. Inductive coupling of TES bolometers to superconducting quantum interference devices (SQUIDs), which convert magnetic flux to voltage, allows arrays of these detectors to be read out, or multiplexed, to room temperature electronics. Future ground-based CMB experiments [1] require arrays on order $\mathcal{O}(10^5)$ TES detectors for increased gains in sensitivity [83]. To operate these arrays of voltage-biased TES bolometers, they must be embedded in a readout circuit that allows for stable operation. To ensure this stability and test our physical and electrothermal model of these devices before building full detector arrays, lab measure-

ments aimed at characterizing the dynamics of the sensor were carried out over the range of detector voltage bias and loading conditions relevant to our application.

In this work, we present bolometer electrothermal properties derived from current-voltage (I-V) curves, effective electrothermal time constant measurements, complex impedance measurements, and heat capacity measurements of aluminum manganese (AlMn) TES bolometers intended for AliCPT. Our measurements are well described by the simplest TES electrothermal model [107, 88], which describes a single pole. In Section 5.3, we describe our dark bolometer test chip, where bolometers are not optically coupled, and the experimental setup. Section 5.4 includes a brief review of the simple TES electrothermal model [107, 88], especially as it pertains to the measurements described in this work. In Section 5.5, we present bolometer electrothermal properties derived from I-V curves, effective electrothermal time constant measurements using a heater on the TES island, complex impedance measurements, and heat capacity calculations of AlMn TES bolometers. We conclude in Section 5.6 with the main results of this work.

5.3 Bolometer test chip and experimental setup

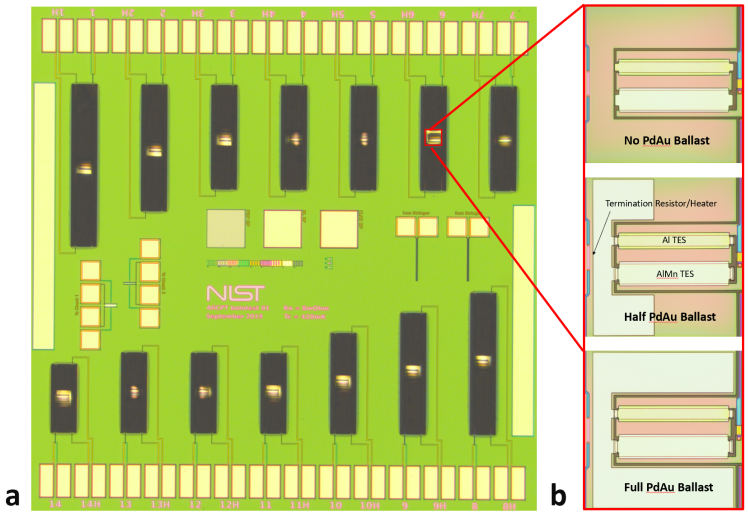

Figure 5.1: **a** Micrograph of a dark AlMn TES bolometer chip. Each chip has 14 different bolometer designs that vary in leg width, leg length, and PdAu thermal ballast for additional heat capacity. **b** Close-up micrographs of three different bolometer designs with varying fractions of PdAu thermal ballast on the TES island, no additional PdAu ballast or "No PdAu Ballast" (*Top*), "Half PdAu Ballast" (*Middle*), and "Full PdAu Ballast" (*Bottom*).

We designed and fabricated a dark bolometer test chip, where bolometers are not optically coupled, that contains 14 unique AlMn TES bolometer designs. These differences enable us to identify a bolometer design best suited for AliCPT. General details of the fabrication process can be found in Duff et al. (2016) [55]. Here we focus on features unique to this test chip. For all designs on this test die, the TES is located on a thermally isolated silicon nitride (SiN) membrane, or island, suspended by four narrow SiN legs [55], varying from 7 µm to 10 µm wide. Each TES consists of 385 nm thick 1400 ppma AlMn film, or 1400 parts per million atomic percent Mn in Al, with measured superconducting critical temperature $T_c = 480$ mK and normal resistance $R_n = 8$ mΩ. Designs vary in leg width, leg length, and sputtered palladium gold (PdAu) (atomic percentages 67.6 % / 32.4 %) thermal ballast for additional heat capacity [112, 64]. In addition, there is an aluminum (Al) TES bolometer more well suited for testing with room temperature sources [82] in series with the AlMn TES bolometer on the TES island. For this reason, the scope of this work concentrates on measurements of the AlMn TES bolometers. All designs utilize a lumped termination resistor [128] to deposit differentially fed signals as heat on the TES island. When our TES bolometers are coupled to the telescope and a planar orthomode transducer, this resistor is utilized to absorb the millimeter-wave radiation being measured. However, in this work, since the TES bolometers are dark, or not optically coupled, the resistor is used as an on-island heater to characterize the detector (see Section 5.5.2).

Figure 5.1 a shows a full view micrograph of the dark TES bolometer test chip. Figure 5.1 b includes close-up micrographs of the TES island for three designs with increasing fractions of PdAu thermal ballast from top to bottom, with no additional PdAu, with PdAu ballast of volume 984 µm^3 (“half” PdAu ballast), and with PdAu ballast of volume 1974 µm^3 (“full” PdAu ballast). In this work, we primarily present measurements of 10 of the 14 TES bolometer designs (designs 1–10), since they are most similar to the geometries used by the AliCPT optical prototype single pixels [151]. Table 5.1 describes the geometry differences between all fabricated designs in greater detail, though later sections will give results in aggregate when appropriate.

To test our dark TES bolometer chips, we utilize a test board, which houses up to 18 bolometer test die, and reads them out by use of a 3 x 32 (three column, 32 TES bolometer) time-division SQUID multiplexer (TDM) [143, 54]. Figure 5.2 a shows a close-up of this test board where important components

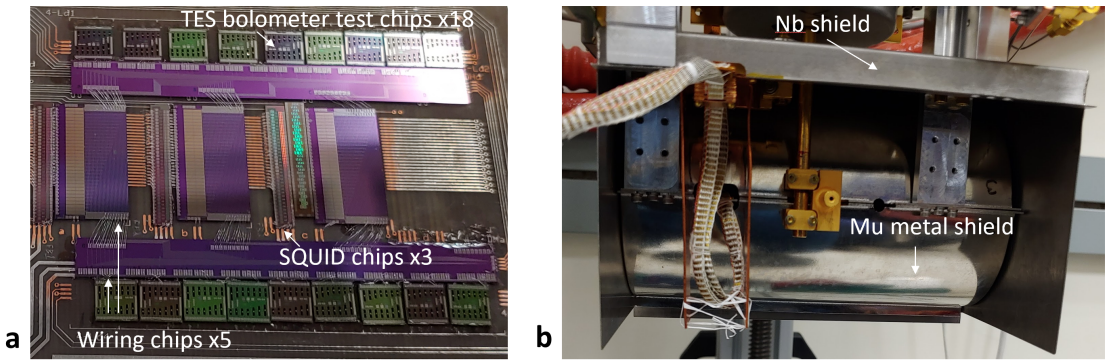

Figure 5.2: **a** Close-up of the dark bolometer chip test board, which can house up to eighteen chips. Important components like the bolometer test chips and the SQUID and wiring chips that enable time-division multiplexing readout are labeled in *white*. A cover goes over the whole test board, which is not shown. **b** Test board mounted in the cryostat to a 100 mK ADR stage. It is surrounded by a curved high-permeability magnetic shield and an outer Nb shield both mounted at 4 K [25] labeled in *white*.

Design	Area/length (μm)	Fraction of PdAu ballast
1	0.033	Full
2	0.044	Full
3	0.055	Full
4	0.055	Half
5	0.055	No
6	0.055	Full
7	0.055	No
8	0.055	Full
9	0.066	Full
10	0.065	Full
11	0.086	Full
12	0.086	Half
13	0.086	Full
14	0.107	Full

Table 5.1: Geometry details of all bolometer designs included on the dark TES bolometer test chip. Designs 11–14 were only used to characterize bolometer electrothermal properties in Section 5.5.1.

such as the bolometer test chips and the SQUID and wiring chips that enable time-division multiplexing readout are labeled. Similar designs were wired together in independent columns to allow for optimal stability deeper in their superconducting transitions. Figure 5.2 b shows this setup mounted to the 100 mK stage of an adiabatic-demagnetization-refrigerator (ADR) cryostat, where it is surrounded by an additional high-permeability magnetic shield and niobium (Nb) shield at the 4 K stage for magnetic shielding [25]. For the measurements described in this work, we used all 18 slots to connect redundant copies of each TES bolometer design, with and without the on-island heater connected in case there were systematic effects associated with the heater.

5.4 Simple TES model

In this section, we briefly review the simple electrothermal model [107, 88], which was used to describe TES bolometer impedance in this work, especially as it pertains to Section 5.5.3. Figure 5.3 shows a schematic of this model for a single thermal mass with a single time constant. The TES bolometer is represented as a temperature-dependent resistor of resistance $R(T)$, the TES itself, the combined heat capacity C of this resistor at temperature $T = T_{\mathrm{TES}}$, where T_{TES} is the temperature of the TES and is close to T_{c}, and

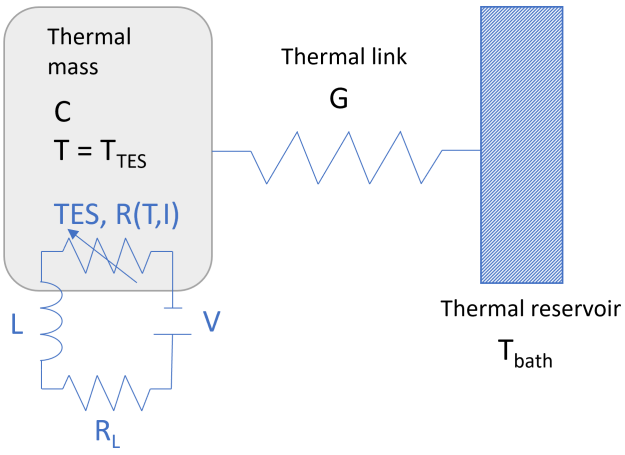

Figure 5.3: Schematic of the simple TES bolometer model. On the lower left, in light blue, is the Thevenin equivalent circuit of the TES. It consists of a Thevenin-equivalent voltage source V, a load resistor R_{L}, and an input coil L, for inductive coupling to the SQUID in series with a variable resistor $R(T)$, the TES itself. The rest of the figure shows how a thermal mass with heat capacity C at temperature $T = T_{\mathrm{TES}}$, which is close to T_{c}, is thermally isolated from a thermal reservoir at temperature T_{bath} through a weak thermal link with thermal conductance G.

its connection to a stable thermal reservoir at bath temperature, $T_{\rm bath} < T_{\rm c}$, through a weak link with thermal conductance G with no additional heat capacity [89]. The value of C and G sets the natural time constant of the detector without any feedback, $\tau_0 = C/G$. Also shown in Figure 5.3 is the Thevenin-equivalent bias circuit of the TES, consisting of a Thevenin-equivalent voltage source V, a load resistor $R_{\rm L}$, and an input coil L, for inductively coupling to the SQUID in series with a variable resistor $R(T)$, the TES itself. For our setup, $R_{\rm L}$ = 160 μΩ with negligible parasitic resistance. From this schematic, we see that complex impedance of the full TES circuit with respect to angular frequency ω is:

$$Z(\omega) = R_{\rm L} + i\omega L + Z_{\rm TES}(\omega)\,, \tag{5.1}$$

where $Z_{\rm TES} \equiv \frac{\delta V}{\delta I}$ is the complex impedance of the TES to small changes in voltage bias. When operating the TES, the power flowing through this weak thermal link in the steady state condition is called the saturation power, $P_{\rm sat}$, or the total input power needed to drive the TES into its normal state. When the TES is in its normal state, it will have a maximum resistance $R_{\rm N}$ and will no longer be sensitive to temperature changes, what we call saturated. Usually $P_{\rm sat}$ is the sum of input microwave signal P_0 and electrical bias power $P_{\rm e}$. However, since our test setup is designed to be dark, P_0 is effectively negligible when not using the on-island heater. We define saturation power as:

$$P_{\rm sat} = K(T^n - T_{\rm bath}^n)\,, \tag{5.2}$$

where K is related to the thermal conductance G, T is the temperature of the thermal mass or bolometer island, where $T = T_{\rm TES}$ which is close to $T_{\rm c}$, and n is related to the thermal link to the bath. We use Eq. 5.2 to fit for K, $T_{\rm c}$, and n in Section 5.5.1. Also, related to $P_{\rm sat}$ is the thermal conductance G of the weak link between the TES and the bath given by:

$$G \equiv \frac{dP_{\rm sat}}{dT}(T_{\rm c}) = nKT_{\rm c}^{n-1} \tag{5.3}$$

Therefore, once we fit for K, $T_{\rm c}$, and n, we can also calculate G.

To describe how the TES operates in the steady state, we can write the TES logarithmic temperature and current sensitivities as $\alpha = \frac{dlnR}{dlnT}\big|_{I_0}$ and $\beta = \frac{dlnR}{dlnI}\big|_{T_0}$, where R is the TES resistance, I_0 is the steady state

current, T_0 is the steady state temperature, and R_0 is the steady state resistance. When the TES bolometers are voltage-biased, the effects of negative electrothermal feedback can be quantified by the TES loop gain under constant-current, $\mathscr{L}(T = T_c) \equiv \frac{\alpha P_e}{G T_c}$ where $P_e = I_0^2 R_0$.

The complex impedance of the TES for the simple electrothermal model as a function of angular frequency ω [107, 88], as represented by Figure 5.3, is:

$$Z_{\mathrm{TES}} = R_0(1+\beta) + \frac{R_0\mathscr{L}}{1-\mathscr{L}} \frac{2+\beta}{1+i\omega\tau_I}, \tag{5.4}$$

where τ_I is the constant-current time constant of the TES with electrothermal feedback. τ_I is related to τ_0 without feedback by $\tau_I = \frac{\tau_0}{1-\mathscr{L}}$. In Section 5.5.3, we describe how we fit measurements of complex impedance to the model in Eq. 5.4 after calibrating out the other parts of the TES circuit in Eq. 5.1. This allows us to extract the TES parameters α, β, $\mathscr{L}$, τ_I, and C for different designs while varying loading conditions, T_{bath} and $\%\, R_{\mathrm{N}}$.

5.5 Measurements and analysis

5.5.1 Characterization of bolometer electrothermal properties

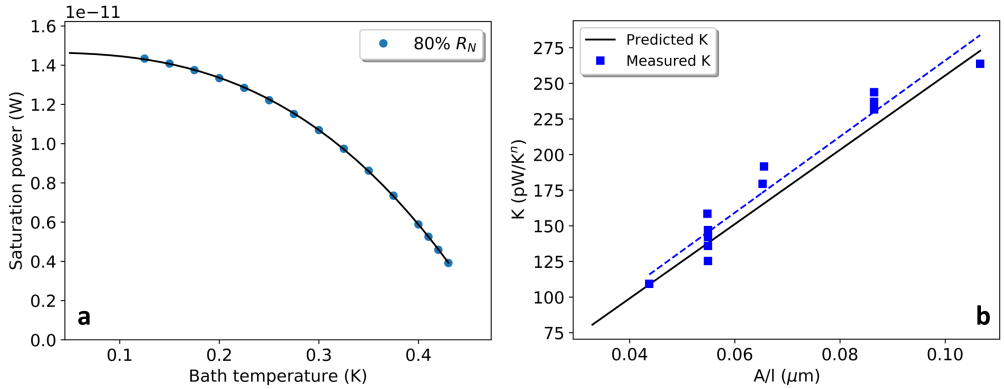

Figure 5.4: **a** P_{sat} vs. T_{bath} for one design from *I-V* curves at different T_{bath}, 125 mK to 430 mK. A representative dataset with full PdAu and P_{sat} evaluated at 80 % R_{N} is shown as *blue points* and fit to Eq. 5.2 as a *solid black line*. **b** Average K for each measured bolometer design vs. A/l (area/length) of the TES bolometer legs. The *solid black line* is a prediction of expected K based on previous measurements at NIST. The *blue points* and *blue dashed line* are what we measure and a fit to these data, respectively.

To characterize the electrothermal properties of all TES bolometer designs (designs 1–14), we took current-voltage (I-V) curves while changing T_{bath} over the range 125 mK–490 mK. By varying T_{bath}, we probe how P_{sat} changes as a function of T_{bath}, since we expect P_{sat} to decrease closer to the critical temperature following Eq. 5.2. Figure 5.4 a shows P_{sat} as a function of T_{bath} from 125 mK to 430 mK for a typical bolometer design with full PdAu and P_{sat} evaluated at 80 % R_{N}. The fit to this data is shown as a solid black line. By fitting to Eq. 5.2 with least squares minimization for P_{sat} evaluated at many different % R_{N}, typically about 90 % R_{N} to 30 % R_{N}, we extract an average K for each design and an average T_{c} and n based on all designs. Figure 5.4 b shows the average K for each measured bolometer design as a function of the area/length (A/l) of the TES bolometer legs. This will be used to predict TES properties dependent on island geometry in future fabrications. The solid black line is a prediction of expected K based on previous measurements at NIST. The blue points and blue dashed line are what we measure without the on-island heaters connected and a fit to this data, respectively. Both the prediction and fit are consistent within the uncertainty given by the fit. From measurements of all designs, the average T_{c} and n are 480 mK $\pm$ 1 mK and 2.82 ± 0.01, respectively, from non-heater channels. Error bars are statistical and the 1 σ standard error of the mean.

5.5.2 Effective electrothermal time constant measurements

We measure the effective electrothermal time constant τ_{eff} of our TES bolometers (designs 1–10) individually by sending a small sinusoidal signal, $< 5\,\% P_{\mathrm{sat}}$, on the on-island heater line using an external function generator. The heater is equivalent to a small oscillating optical load for our TES bolometers. Simultaneously, we use a lock-in amplifier technique with this generator's sync signal to determine the in-phase (I) and quadrature (Q) bolometer response. By varying the frequency of the sinusoidal signal from 1 Hz to 100 kHz, we map out the TES transfer function.

We fit the I and Q components of the raw data to a one-pole filter at the same time to extract τ_{eff} using least squares minimization. We measure each bolometer individually to see how τ_{eff} varies with TES resistance, typically 98 % R_{N} to 90 % R_{N}, and with bath temperature, $T_{\mathrm{bath}} = 200$ mK to 430 mK. Using I-V curves taken at each bath temperature, we determine the voltage bias for each % R_{N}. We are limited to

looking at behavior at or before the *I-V* turnaround due to radio-frequency (RF) interference coupled down the heater line. We see that all TES designs act as a low-pass filter as expected. In Figures 5.5 a and 5.5 b, we show the real and imaginary parts of the electrothermal response of a TES bolometer (Full PdAu in Figure 5.5 c), respectively, measured at $T_{\rm bath} = 430\,{\rm mK}$ and four different bias conditions, corresponding to 98 %, 95 %, 92 %, and 90 % $R_{\rm N}$. The black solid lines are fits of a one-pole filter, which can be seen to describe the data well for all % $R_{\rm N}$ shown. For all measured designs, $\tau_{\rm eff}$ decreases deeper in the superconducting transition as expected. Additional PdAu ballast slows $\tau_{\rm eff}$ in general and reduces the speed up of $\tau_{\rm eff}$ lower in the transition. Figure 5.5 c shows $\tau_{\rm eff}$ as a function of % $R_{\rm N}$ at $T_{\rm bath} = 430\,{\rm mK}$ for designs with identical leg geometry (splits 3, 4, and 5) and different fractions of PdAu ballast (full, half, no). For this specific leg geometry and by changing the amount of PdAu thermal ballast, and therefore heat capacity, of the TES island, $\tau_{\rm eff}$ spans $1.57\,{\rm ms} \pm 0.01\,{\rm ms}$ to $3.45\,{\rm ms} \pm 0.02\,{\rm ms}$ at 90 % $R_{\rm N}$ and $T_{\rm bath} = 430\,{\rm mK}$. Error bars are the one standard deviation statistical uncertainty from one-pole filter fits to the data, which are similar to the variations with repeat datasets.

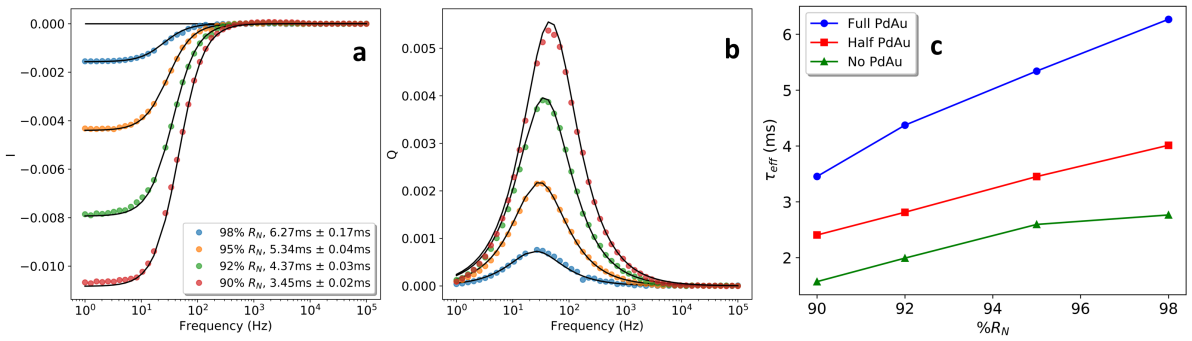

Figure 5.5: **a** The real and **b** imaginary parts of the electrothermal response of a TES bolometer (Full PdAu in *c*) using an on-island heater as measured at $T_{\rm bath} = 430\,{\rm mK}$ and four different bias conditions, corresponding to 98 %, 95 %, 92 %, and 90 % $R_{\rm N}$. Data is shown as *colored points* while the *solid black lines* are one-pole filter fits to the data, which describe the data well. **c** $\tau_{\rm eff}$ vs. % $R_{\rm N}$ for designs 3, 4, and 5 at $T_{\rm bath} = 430\,{\rm mK}$. These designs have identical leg geometries, but differing volumes of PdAu ballast, full, half, and none. By changing the amount of PdAu thermal ballast on the TES island, $\tau_{\rm eff}$ was varied as shown. Marker shape denotes fraction of PdAu thermal ballast, full (*dot*), half (*square*), and none (*triangle*). Due to radio-frequency interference with the heater line, we were unable to measure $\tau_{\rm eff}$ deep in the transition.

In addition, we measure heat capacity by voltage biasing each TES bolometer at the *I-V* turnaround where $\mathscr{L} \approx 1$, assuming negligible parasitic inductance in the circuit. At high % $R_{\rm N}$, we can simplify

$\tau_{\rm eff} \approx \frac{\tau_0}{1+\mathscr{L}}$. We use calculations of G (Eq. 5.3) from I-V curve measurements described in Section 5.5.1 to solve for C:

$$C \approx \tau_{\rm eff} G(1+\mathscr{L})\,. \tag{5.5}$$

This estimate of C is less involved to derive than that given by complex impedance measurements (see Section 5.5.3). However, this approximation assumes negligible circuit parasitics and that the voltage bias is high enough in the transition where $\beta \sim 0$ and the resistance of the TES bolometer $R(T) >> R_{\rm L}$.

5.5.3 Complex impedance measurements

We measure the complex impedance $Z(\omega)$ of each TES bolometer (designs 1–10) individually by sending a small sinusoidal signal on the detector bias line using an external function generator. This signal acts as an additive δV to a constant DC voltage bias, corresponding to a particular $\%\,R_{\rm N}$. Like $\tau_{\rm eff}$ measurements (Section 5.5.1), we use the same lock-in amplifier technique to determine the real ($\mathrm{Re}(Z_{\rm TES})$) and imaginary ($\mathrm{Im}(Z_{\rm TES})$) components of the complex impedance. To calibrate out the terms in $Z(\omega)$ (Eq. 5.1) not related to $Z_{\rm TES}$, we measure data in the superconducting state at each bath temperature measured and the normal state, at $T_{\rm bath} = 500\,\mathrm{mK}$ [108]. To characterize $Z_{\rm TES}$ over a range of loading conditions, we measure at $T_{\rm bath} = 200\,\mathrm{mK}$, 325 mK, 400 mK, and 430 mK, which varies $P_{\rm e}$, and at many different TES resistances, $95\,\%\,R_{\rm N}$ to $20\,\%\,R_{\rm N}$ as device stability allows. We fit this data to the simple TES model (Eq. 5.4) up to 20 kHz using orthogonal distance regression. For each fit, we use fixed values for n, $T_{\rm c}$, and G calculated from I-V curve measurements (Section 5.5.1). Also, for initial C inputs, we use the results of our $\tau_{\rm eff}$ measurements (Section 5.5.2). These measured parameters are assumed to have negligible uncertainties within the fit function. We use I-V curves taken at each bath temperature to inform our choice of voltage bias for a particular $\%\,R_{\rm N}$. For our fits, we also allow α and β to change with $\%\,R_{\rm N}$. In this way, we extract α, β, $\mathscr{L}$, and τ_I for each individual dataset and a global C for each TES bolometer design.

In Figure 5.6 a, we show the real and imaginary components of the complex impedance of a representative TES bolometer with full PdAu as a function of frequency at $T_{\rm bath} = 430\,\mathrm{mK}$. Figure 5.6 b shows this same data now in the complex plane. Only a few of the measured $\%\,R_{\rm N}$ are shown to demonstrate how well the simple electrothermal model fits the data at high (95 %), medium (80 %), and low (40 %) $\%\,R_{\rm N}$. By

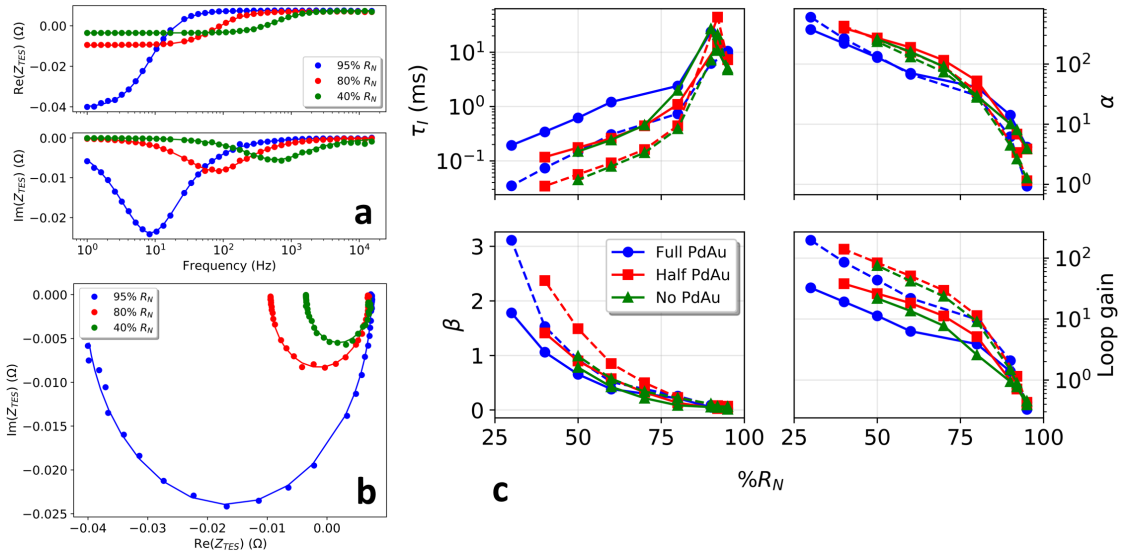

Figure 5.6: **a** Impedance data for a representative TES bolometer with full PdAu as the real (*Top*) and imaginary (*Bottom*) parts of complex impedance Z_{TES} vs. frequency at $T_{\mathrm{bath}} = 430\,\mathrm{mK}$. **b** Impedance data for the same design and data, now in the complex plane. *Colored points* denote measured data while *solid lines* of the same color are fits to Eq. 5.4 for high (95 %), medium (80 %), and low (40 %) $\%\,R_{\mathrm{N}}$. **c** τ_I, α, β, and loop gain vs. $\%\,R_{\mathrm{N}}$ for three designs with identical leg geometries, but differing volumes of PdAu ballast, full, half, and no. Parameters were extracted from simultaneous fits to Eq. 5.4 at low (200 mK) and high (430 mK) T_{bath}. Marker shape denotes fraction of PdAu thermal ballast, full (*dot*), half (*square*), and none (*triangle*). *Dashed* and *solid curves* represent data at $T_{\mathrm{bath}} = 200\,\mathrm{mK}$ or $T_{\mathrm{bath}} = 430\,\mathrm{mK}$, respectively.

fitting data for identical % R_N and multiple T_{bath} simultaneously for each design, typically at a low (200 mK) and high (430 mK) T_{bath}, we were able to reduce parameter covariance significantly. Figure 5.6 c shows τ_I, α, β, and loop gain $\mathscr{L}$ as a function of % R_N for designs with identical leg geometry (splits 3, 4, and 5) and different fractions of PdAu ballast (full, half, no). Parameters extracted from simultaneous fits to Eq. 5.4 at low (200 mK) and high (430 mK) T_{bath} are shown. At these T_{bath}, we varied loading conditions over the range, 3.5 pW to 21.3 pW at 50% R_N for all bolometer designs measured. We observed τ_I, β, and $\mathscr{L}$ to differ clearly and systematically with T_{bath} = 200 mK and 430 mK at identical % R_N as expected. We find α to be insensitive to T_{bath}, which is also expected. Loop gain and β trend higher and τ_I faster at lower T_{bath}. Like τ_{eff} measurements, τ_I speeds up significantly deeper in the transition for designs with no additional PdAu ballast. We are able to determine TES bolometer parameters over a large range of detector bias through the transition (30% R_N to 95% R_N). When voltage biased to 50% R_N and operated at $T_{bath} = 430$ mK, conditions which mimic the electrical power dissipated in the sensor anticipated in AliCPT when observing, τ_I varies from $\sim$ 0.12 ms–0.62 ms, $\alpha \sim$ 128–305, $\beta \sim$ 0.6–1.0, and $\mathscr{L} \sim$ 11–26 for all devices measured.

All studied bolometer designs are well described by the simple electrothermal model to $\sim$ 10 kHz. At higher frequencies, the behavior of our devices begins to deviate from this model. This demonstrates that the PdAu thermal ballast is well coupled to the TES compared to similar devices in the literature [64, 43]. Furthermore, both effective time constant and complex impedance measurements demonstrate that additional PdAu thermal ballast is not necessary for stable operation in this configuration. We describe our measurements of heat capacity, which vary with volume of PdAu thermal ballast, in greater detail in Section 5.5.4.

5.5.4 Heat capacity

We predict the expected heat capacity of the bolometer island by summing the contributions from electrons and phonons for all materials on the bolometer ($C_{predicted}$ in Table 5.2) for no, half, and full PdAu cases. We also measure the heat capacity for measured designs (designs 1–10) in two distinct ways. From τ_{eff} measurements (Section 5.5.1) at the *I-V* turnaround, τ_{eff} is sampled at four different bath temperatures, 200 mK, 325 mK, 400 mK, and 430 mK, to calculate an average τ_{eff} for each bolometer design. Heat capacity

Fraction of PdAu ballast	$C_{\text{predicted}}$ (pJ/K)	C_{heater} (pJ/K)	C_{complexZ} (pJ/K)
Full	0.62	0.76	0.69
Half	0.42	0.57	0.50
No	0.21	0.31	0.27

Table 5.2: Average heat capacities for fraction of PdAu thermal ballast looked at in this work, full, half, and none. Included is C predicted by summing the contributions from electrons and phonons for all materials on the bolometer ($C_{\text{predicted}}$) and from τ_{eff} (C_{heater}) and complex impedance (C_{complexZ}) measurements. There is good consistency between the two measurement methods.

(C_{heater}) is then approximated using Eq. 5.5. From complex impedance measurements (Section 5.5.3) at multiple T_{bath} and % R_{N}, we find heat capacity (C_{complexZ}) by fitting to the simple electrothermal TES model, Eq. 5.4. Measuring the complex impedance at multiple bath temperatures helps break degeneracies within the model parameters, particularly α and C. We average results for designs with similar volumes of PdAu ballast, regardless of leg geometry. Included in these averages are two designs with a reduced area ground plane layer since we expect the contribution to heat capacity from this layer to be very small.

Table 5.2 shows average heat capacities of designs with identical volumes of PdAu thermal ballast from τ_{eff} (C_{heater}) and Z_{TES} (C_{complexZ}) measurements as well our predictions ($C_{\text{predicted}}$). For our average of full PdAu designs, which includes 7 unique bolometers, $C_{\text{heater}} = 0.76 \pm 0.09$ pJ/K and $C_{\text{complexZ}} = 0.69 \pm 0.03$ pJ/K. Error bars are statistical and 1σ and include the standard error of the mean and output uncertainties on fit parameters. There is good consistency between the two methods within this measurement uncertainty. However, we also detect greater non-PdAu heat capacity than predicted, ~ 0.07 pJ/K based on C_{complexZ}. It is unclear what this excess heat capacity might be, though it is common to measure additional heat capacity in SiN films [99], like those used in our bolometers.

From C_{heater} and C_{complexZ}, the baseline heat capacity of our TES bolometers, without the addition of any PdAu ballast, is $0.29\,\text{pJ/K} \pm 0.02\,\text{pJ/K}$. We also calculate that the volumetric heat capacity of PdAu at 480 mK is $0.22\,\text{fJ/(K}\cdot\mu\text{m}^3) \pm 0.03\,\text{fJ/(K}\cdot\mu\text{m}^3)$. Error bars are the 1σ standard deviation statistical uncertainty, accounting for both types of measurements. We predict the volumetric heat capacity of sputtered PdAu (atomic percentages 67.6 % / 32.4 %) at 480 mK is $0.21\,\text{fJ/(K}\cdot\mu\text{m}^3)$, so measurements are consistent with expectations. This demonstrates how the use of PdAu thermal ballast for additional heat capacity in

our TES bolometers is well understood.

5.6 Conclusion

We present bolometer electrothermal properties derived from *I-V* curves, $\tau_{\rm eff}$ measurements, and complex impedance measurements primarily of 10 unique AlMn TES bolometer designs. As part of these designs, we explored increasing the TES heat capacity by up to a factor of ~ 3 with the addition of PdAu thermal ballast. This has the effect of slowing down the time constant, as seen in $\tau_{\rm eff}$ measurements and τ_I extracted from complex impedance measurements, and increasing the heat capacity of the bolometer. From this suite of measurements, our bolometers are well-described by a simple, one-pole electrothermal model to ~ 10 kHz, even with the addition of PdAu. We present TES parameters extracted from this model, α, β $\mathscr{L}$, and τ_I, as a function of operational resistance and over the range of loading conditions, ~ 3.5 pW to 21.3 pW at 50 % $R_{\rm N}$ for $T_{\rm bath} = 200$ mK and 430 mK. Without the addition of any PdAu, the baseline C of our TES bolometers is 0.29 pJ/K $\pm$ 0.02 pJ/K. We also calculate the volumetric heat capacity of sputtered PdAu (atomic percentages 67.6 % / 32.4 %) at 480 mK is 0.22 fJ/(K·μm^3) $\pm$ 0.03 fJ/(K·μm^3). The measurements presented in this work will enable us to optimize final designs of TES bolometers for AliCPT [150].

Acknowledgements: S. Walker gratefully acknowledges support from the National Science Foundation Graduate Research Fellowship under Grant No. DGE-1144083 and from the NASA FINESST program under Grant No. 19-ASTRO20-0075.

Chapter 6

Development of a new MKID tuning method

We developed a new method for optimal tuning of MKID arrays under dynamic atmospheric loading conditions and with hundreds of resonators per feed line. Careful selection of readout power/tone amplitude and probe tone frequency for each MKID can yield the best combination of linearity and sensitivity for these arrays. However, this tuning is further complicated by variations in background loading which can induce significant shifts in MKID resonance frequencies and reduce quality factors. When this happens, the MKIDs require a re-tuning, where the probe tone for each MKID is modified to return detectors to optimal operation. In this chapter, we describe the MKID nonlinear response due to the kinetic inductance ($L_{\rm k}$). Then, we introduce an improved resonator model that accounts for this nonlinear effect, including bifurcation in the resonator response at high enough readout powers. Using frequency sweeps of the forward transmission S_{21} of TiN/Ti/TiN trilayer MKIDs, we have demonstrated this model accurately fits the phase-frequency data of resonators under different loading conditions. This includes lab measurements where we vary the optical loading on these detectors with a cryogenic blackbody source and observations at the Large Millimeter Telescope (Chapter 7). Using this improved modeling, we have developed a new MKID tuning method that can be used to identify a microwave power and probe tone frequency for each MKID based on a desired/user-specified detector nonlinearity parameter a [166]. This method is broadly applicable to the operation of MKID arrays.

6.1 MKID nonlinear response and associated feedback

To better understand how this new MKID tuning method works, we first review the MKID nonlinear response and associated feedback due to the kinetic inductance, specifically bifurcation in the resonance curves of resonators driven at high readout powers. In general, MKIDs are usually operated in a regime where current in the resonator circuit I is non-negligible. Recall from Chapter 1 and Chapter 3, that the complex surface impedance of a superconductor is $Z_s = R_s + j\omega L_s$ where $\omega L_s >> R_s$ [189]. When operating a resonator like an MKID, the AC circuit contributes a kinetic inductance L_k to the total surface inductance. The kinetic inductance of a superconductor has an intrinsic nonlinearity that depends not only on temperature and power absorbed, but also on resonator current. The kinetic inductance of a superconducting strip at $T \ll T_c$ can be written in terms of I as [166]:

$$L_k(I) \simeq L_k(0)\left(1 + \frac{I^2}{I_*^2} + ...\right) \tag{6.1}$$

where the linear term as well as odd terms are excluded due to symmetry considerations and $L_k(0)$ is the kinetic inductance of the resonator in the low-power, linear limit. In Eqn 6.1, I_* is the characteristic current which sets the scale of this quadratic nonlinearity. It is expected to be of order the critical current [189].

This nonlinearity in the kinetic inductance causes a frequency shift in a resonator with a similar quadratic current dependence. The fractional detuning in the low-power and linear regime is $x_0 = (\omega - \omega_{r,0})/\omega_{r,0}$ where $\omega_{r,0}$ is the resonance frequency. The nonlinear frequency shift can be expressed as:

$$\begin{aligned} \delta x = \frac{\delta\omega_r}{\omega_{r,0}} &= -\frac{1}{2}\frac{\delta L}{L} = -\frac{\alpha}{2}\frac{I^2}{I_*^2} \\ &= -\frac{E}{E_*} \end{aligned} \tag{6.2}$$

where L is the total inductance, α is the kinetic inductance fraction such that $L_k = \alpha L$, and E is the energy stored in the resonator. By writing the last part of Eqn 6.2 in this way, we have defined a scaling energy $E_* \propto L_k I_*^2/\alpha^2$ that is of similar order to the condensation energy of the inductor when $\alpha \approx 1$. From Eqn 6.2, the shifted resonance frequency is then:

$$\omega_r(I) = \omega_{r,0} + \delta\omega_r = \omega_{r,0}\left(1 - \frac{\alpha}{2}\frac{I^2}{I_*^2}\right) \tag{6.3}$$

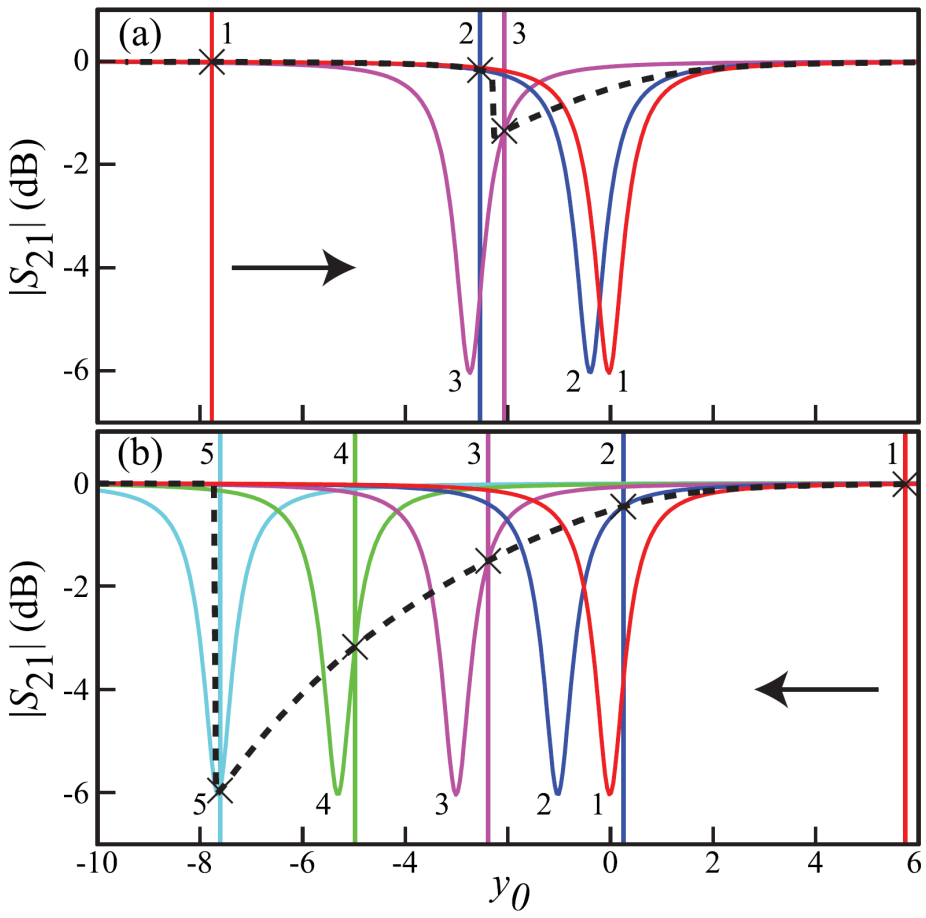

Figure 6.1: Conceptual diagram of MKID bifurcation regime due to the nonlinear kinetic inductance, from Swenson et al. (2013) [166]. $|S_{21}|$ versus fractional detuning in resonance linewidths $y_0 = Q_r x_0$ is shown. Different colored resonance curves are snapshots of the same resonator at various probe frequencies during a frequency sweep at high readout power such that $a > 0.77$. Probe frequencies are denoted by vertical lines of the same color and number as the corresponding resonator behavior. When *a:* sweeping upward or *b:* downward in probe frequency (arrows) during a frequency sweep, the observed MKID response is distinct and traces out a hysteretic transfer function (dashed lines).

The current in the resonator depends on the readout power P_r and E. The energy stored in the resonator can be expressed as [166]:

$$E = \frac{2Q_\mathrm{r}^2}{Q_c}\frac{1}{1+4Q_\mathrm{r}^2x^2}\frac{P_\mathrm{r}}{\omega_\mathrm{r}} = \frac{1}{2}LI^2 \tag{6.4}$$

where Q_r is the total quality factor and Q_c is the coupling quality factor of the resonator. From Eqn 6.4, we see that the fractional detuning can then be rewritten as:

$$x = x_0 + \frac{E}{E_*} \tag{6.5}$$

This expression can then be combined with Eqn 6.4 for the energy in the resonator so that the fractional detuning becomes:

$$x = x_0 + \frac{2Q_\mathrm{r}^2}{Q_\mathrm{c}}\frac{1}{1+4Q_\mathrm{r}^2x^2}\frac{P_\mathrm{r}}{\omega_\mathrm{r}E_*} \tag{6.6}$$

This expression for the fractional detuning includes feedback in the MKID due to the kinetic inductance nonlinearity. We now introduce two variables, $y = Q_\mathrm{r}x$ and $y_0 = Q_\mathrm{r}x_0$. They are the detuning measured in linewidths relative to the shifted resonance and low-power resonance, respectively. This can be seen from the definition of the total quality factor $Q_\mathrm{r} = \omega_\mathrm{r}/\Delta\omega$ so that $y = (\omega - \omega_\mathrm{r})/\Delta\omega$, where $\Delta\omega$ is the linewidth of the resonance. From Eqn 6.6, we can also define a nonlinearity parameter a to quantify the kinetic inductance nonlinearity effect as:

$$a = \frac{2Q_\mathrm{r}^3}{Q_\mathrm{c}}\frac{P_\mathrm{r}}{\omega_\mathrm{r}E_*} \tag{6.7}$$

Using y, y_0, and a, we can rewrite the fractional detuning as:

$$y = y_0 + \frac{a}{1+4y^2} \tag{6.8}$$

When solving Eqn 6.8 for different a, when $a > 4\sqrt{3}/9 \approx 0.77$, there are now multiple solutions for the fractional detuning y with y_0 or a non-monotonic relationship. As readout power is increased, or for moderate values of $a < 0.77$, the MKID resonance starts to become distorted and asymmetric. At high readout powers such that $a > 0.77$, the second order current term in the kinetic inductance (Eqn 6.1) causes the resonator response to exhibit nonlinear switching. Bifurcation is the nonlinear frequency switching regime of the resonance. This regime is hysteretic or depends on the direction of a frequency sweep, increasing

or decreasing in probe frequency, when tracing out the MKID resonance. Figure 6.1 shows a conceptual diagram of the MKID bifurcation regime from Swenson et al. (2013) [166] for the same resonator at different probe frequency snapshots. The top of the figure shows what happens during a frequency sweep when increasing (*a*) or decreasing (*b*) in probe frequency compared to the resonance. As can seen, there are two different accessible states depending on the direction the probe frequency is swept and they trace out a hysteretic transfer function (dashed lines). In Fig 6.1a, when sweeping upward in probe frequency starting from below the resonance, the resonator current I increases as the fractional detuning y_0 decreases. The change in the nonlinear kinetic inductance also causes the resonance frequency to shift downward. This acts as a positive feedback effect and causes y_0 to decrease further. As the probe tone enters the resonance, runaway positive feedback causes the resonance to enter the bifurcation regime, where the resonant frequency snaps to a lower frequency state. In Fig 6.1b, when sweeping downward in probe frequency starting from above the resonance, the resonant frequency also shifts downward as a negative feedback effect. When the probe tone is swept past the resonance minimum, the resonance enters the bifurcation regime, where the resonant frequency snaps back to a higher frequency state. Swenson et al. (2013) [166] found that sweeping downward in probe frequency gives full access to the high frequency side of the resonance at readout powers even after the onset of bifurcation.

MKIDs are usually biased at readout powers before this bifurcation regime to avoid switching between these two states. To optimize sensitivity, it is ideal to drive resonators with large readout power close to, but before bifurcation as this overcomes amplifier noise and suppresses two level systems (TLS) noise [63]. Also, the resonance depth is predicted to stay constant with readout power. This is indicative of a purely reactive nonlinearity which only affects the MKID frequency response.

6.2 Modeling nonlinear superconducting resonators

Now that we have discussed the MKID nonlinear response, which is dominated by the kinetic inductance nonlinearity at high readout powers, and the associated feedback from the kinetic inductance, we utilize an improved resonator model from Dai et al. (2023) [46] that can accurately fit the phase of a superconducting resonator driven in the nonlinear regime, even after the onset of bifurcation. This method

accounts for the varying resonator current I and the nonlinear kinetic inductance. After the resonator response bifurcates, standard fitting models (e.g. [63, 100]) that have been developed to model resonators in the linear, low-power regime no longer accurately trace the observed response. This approach also differs from the nonlinear modeling of Swenson et al. (2013) [166] in that it does not require solving an implicit cubic equation to implement. Using this improved resonator model, we have developed a new MKID fitting and tuning pipeline that can identify an optimal readout power for each MKID based on desired detector nonlinearity parameter a [166] using a wide sweep in readout power and at various optical loadings. This model can retrieve different resonator parameters, like quality factor and resonance frequency, at microwave readout powers where the response of the MKIDs is linear, as it starts to become nonlinear, and after the onset of bifurcation.

Recall from Chapter 3 that the complex forward transmission S_{21} at low power for a superconducting resonator capacitively coupled to a feed line is given by [63]:

$$z(f) = S_{21}(f) = Ae^{-2\pi jf\tau}\left(1 - \frac{Q_\mathrm{r}}{Q_\mathrm{c}}\frac{e^{j\phi_0}}{1+2jQ_\mathrm{r}\frac{f-f_{\mathrm{r},0}}{f_{\mathrm{r},0}}}\right) \tag{6.9}$$

where f is the probe frequency, A is a complex constant accounting for the gain, loss, and phase shift in the system, τ is a cable delay constant due to the length of cables, and ϕ_0 accounts for impedance mismatch. The phase θ of a superconducting resonator is:

$$\theta(f) = \theta_0 + 2\arctan(-2Q_\mathrm{r}x) \tag{6.10}$$

where θ_0 is the phase angle at the resonance frequency and the fractional detuning for each frequency point f is $x = (f - f_{\mathrm{r},0})/f_{\mathrm{r},0}$.

As discussed in the previous subsection, the MKID nonlinearity is related to the internal current in a resonator and the kinetic inductance nonlinearity. In this nonlinear modeling technique, Eqn 6.9 is modified so that instead of using a fixed resonance frequency $f_{\mathrm{r},0}$, there is now a current dependent resonance frequency $f_\mathrm{r}(I)$. The S_{21} is then modified and can be written as [46]:

$$z(f) = S_{21}(f) = Ae^{-2\pi jf\tau}\left(1 - \frac{Q_\mathrm{r}}{Q_\mathrm{c}}\frac{e^{j\phi_0}}{1+2jQ_\mathrm{r}\frac{f-f_\mathrm{r}(I)}{f_\mathrm{r}(I)}}\right) \tag{6.11}$$

where the MKID parameters, Q_r and Q_c, are assumed to be independent of current which is valid for very low dissipation. The resonance frequency $f_{r,0} = f_r(I = 0)$ can be found by fitting S_{21} sweep measured at low readout power to a linear MKID model.

We use a 3-port circuit network of a capacitively coupled resonator [46] to conceptualize the waves relevant to the complex forward transmission S_{21}, which we commonly measure, and the current I in a resonator which affects the kinetic inductance. The three ports include port 1 as the input of a transmission line, port 2 as the output of a transmission line, and port 3 as the input to a capacitively coupled resonator. In Figure 6.2a, there are two output waves relevant to S_{21}, the direct transmission A_2 which corresponds to transmission far from the resonance and a reflected wave B_2, which corresponds to the signal reflected from the resonator near resonance to the output port 2. In Fig 6.2b, we use a phasor diagram of S_{21} to show how these waves relate to the measured S_{21} of a resonator. From this diagram, A_2 corresponds to an arrow from the origin to an off-resonance point z_{off} and B_2 corresponds to an arrow from z_{off} to an arbitrary probe frequency point z. The sum of A_2 and B_2 then gives the forward transmission S_{21} from the origin to a probe frequency point z. Also, $|B_2|^2$ can be expressed as [46]:

$$|B_2|^2 = |z(f) - z_{off}|^2 \propto I^2 \tag{6.12}$$

Using Eqn 6.12 and $\omega = 2\pi f$, we can rewrite Eqn 6.3 for the shifted resonance frequency as:

$$f_r(I) = f_{r,0} - \beta |z(f) - z_{off}|^2 \tag{6.13}$$

where β is a proportionality factor related to the resonator nonlinearity and can be fitted for a given resonator. From Fig 6.2b and this new expression for $f_r(I)$ (Eqn 6.13), we see that the resonator phase can be modified such that [46]:

$$\begin{aligned} \theta(f) &= \theta_0 + 2\arctan\left(-2Q_r \frac{f - f_r(I)}{f_r(I)}\right) \\ &= \theta_0 + 2\arctan\left(-2Q_r \frac{f - f_{r,0} + \beta|z(f) - z_{off}|^2)}{f_{r,0}}\right) \end{aligned} \tag{6.14}$$

Using Eqn 6.14 to fit the phase of a nonlinear resonator, we can find $f_{r,0}$, Q_r, β, and θ_0. We have rewritten the fractional detuning $x = (f - f_r(I))/f_r(I) \approx (f - f_r(I))/f_{r,0}$. We have also substituted $z_{off} = re^{j(\theta_0+\pi)}$ since

the S_{21} data traces out a circle in complex/IQ space and resonance frequency point z_r and z_{off} are collinear [189].

6.3 MKID fitting and tuning pipeline

We developed a new MKID fitting and tuning pipeline that can identify an optimal readout power/tone amplitude and probe tone frequency corresponding to resonance for each MKID in an array based on a desired/user-defined nonlinearity parameter a [166]. This method uses the improved resonator modeling described in [46], specifically it utilizes frequency sweeps of resonator S_{21} measured for a range of readout powers and fits to the phase-frequency data using Eqn 6.11. This procedure has been verified on networks of TiN/Ti/TiN trilayer MKIDs, where ~ 600 resonators are read out per feedline. This code is called `kid_phase_fit` and can be found on GitHub.[1]

This procedure uses a wide sweep in readout power/drive attenuation and consists of five main steps. For a network of resonators, we:

(1) Remove the cable delay term in Eqn 6.11, that is multiply each S_{21} sweep by $e^{-2\pi j f \tau}$. The cable delay τ was measured previously in the lab for each network using a vector network analyzer.

(2) Perform a circle fit to the S_{21} data in the complex/IQ space to extract the circle center z_c and radius r for each sweep.

(3) Perform a fit to the phase frequency data using Eqn 6.10 for a linear, low-power dataset to find $f_{r,0}$, Q_r, and θ_0. These low-power resonator parameters are collectively called 'result0' and are used to help another phase fit later. This step is the main reason we use a wide sweep in readout power.

(4) Rotate and translate the S_{21} data to the origin using the transformation $z_{rot}(f) = (z_c - z(f))e^{-j\theta_{z_c}}$.

(5) Trim phase frequency data based on a user-specified number of resonator line widths. Afterwards, fit to this data using Eqn 6.14 to extract resonator parameters $f_{r,0}$, Q_r, θ_0, β. To aid with the fit, this

[1] https://github.com/swalker5/kid_phase_fit

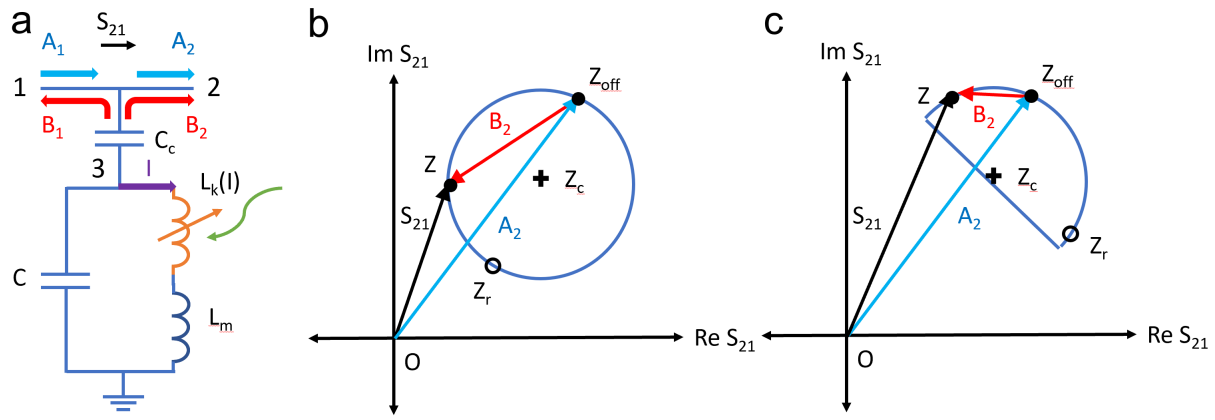

Figure 6.2: *a:* Three port circuit network for an MKID resonator that is capacitively coupled C_c to a feed line, where port 1 is the input of a transmission line, port 2 is the output of a transmission line, and port 3 is the input to a capacitively coupled resonator. The directions of the input wave (A_1) and directly transmitted wave (A_2) (light blue arrows) and reflected waves near resonance (B_1 and B_2) (red arrows) are shown. Also shown is the current that directly flows to the nonlinear kinetic inductance (labeled purple arrow). *b:* Corresponding phasor diagram of S_{21} in the linear regime. In the complex domain/IQ space, the MKID response traces out a circle at some offset from the origin O. The transmitted wave A_2 represents the transmission far from resonance to an off-resonance point z_{off} and the reflected wave B_2 is the signal reflected from the resonator to port 2. The total forward transmission to an arbitrary probe frequency z is then $S_{21} = A_2 + B_2$. Also shown here are the center of the circle z_c (black cross) and the resonance frequency point z_{r} (S_{21}). *c:* Phasor diagram of S_{21} in the nonlinear regime and after the onset of bifurcation.

model requires initial guesses for $f_{r,0}$, Q_r, θ_0, β, and r. This model also requires the frequency data f and $z_{rot}(f)$.

In Fig 6.3, we show a summary of pipeline steps that were taken to model a single TiN/Ti/TiN trilayer resonator swept in readout power. This particular resonator was measured in the lab under a 4 K cryogenic optical load. In Fig 6.3a, we plot $|S_{21}|^2$ versus frequency for a subset of readout powers where the resonator response is linear, starting to become nonlinear, and after the onset of bifurcation. Next, we look at the S_{21} data in complex S_{21}/IQ space and polar coordinates. Figure 6.3b includes the original data (cyan), data after removing the cable delay (blue) and performing a circle fit (red dashed), and data after rotation and translation to the origin (magenta). In Fig 6.3c, we plot phase frequency data after applying the steps in *b*, specifically after rotating and translating the S_{21} data. Data are fit using Eqn 6.14 (black dashed). We also plot the residuals versus frequency, θ_{data}–θ_{fit}, corresponding to the fits shown in *c* to investigate goodness of fit. In Fig 6.5, we show a close-up of the same phase frequency data in Fig 6.3c for a single TiN/Ti/TiN trilayer MKID measured at a range of readout powers. We fit this data to two different models for θ, specifically Eqn 6.10 (gray dashed) and Eqn 6.14 (black dashed). Through this comparison, we find that using a correction for the shifted resonance frequency $f_r(I)$ greatly improves model accuracy, especially for data near and after the onset of bifurcated response.

As a follow-up to Fig 6.3, we show that we can retrieve different resonator parameters, like quality factor and resonance frequency, at a variety of microwave readout powers below, near, and after the onset of bifurcated response. In Fig 6.4, we show some MKID parameters found from this fitting pipeline, particularly the shifted resonance frequency $f_r(I)$ (*a*), Q_i (*b*), Q_c (*c*), and nonlinearity parameter *a* (*d*) as a function of readout power.

After fitting all identified resonators in a network for a readout power sweep, the tuning procedure will solve for the mean E_* of this dataset. The equation for E_* as derived from Eqn 6.7 for nonlinearity parameter *a* is:

$$E_* = \frac{2Q_r^3}{Q_c}\frac{P_r}{\omega_r a} \tag{6.15}$$

where we calculate $\omega_r = \omega_{r,0} + \delta\omega_r$ using $\omega = 2\pi f$. P_r is the readout power converted from dB to W for

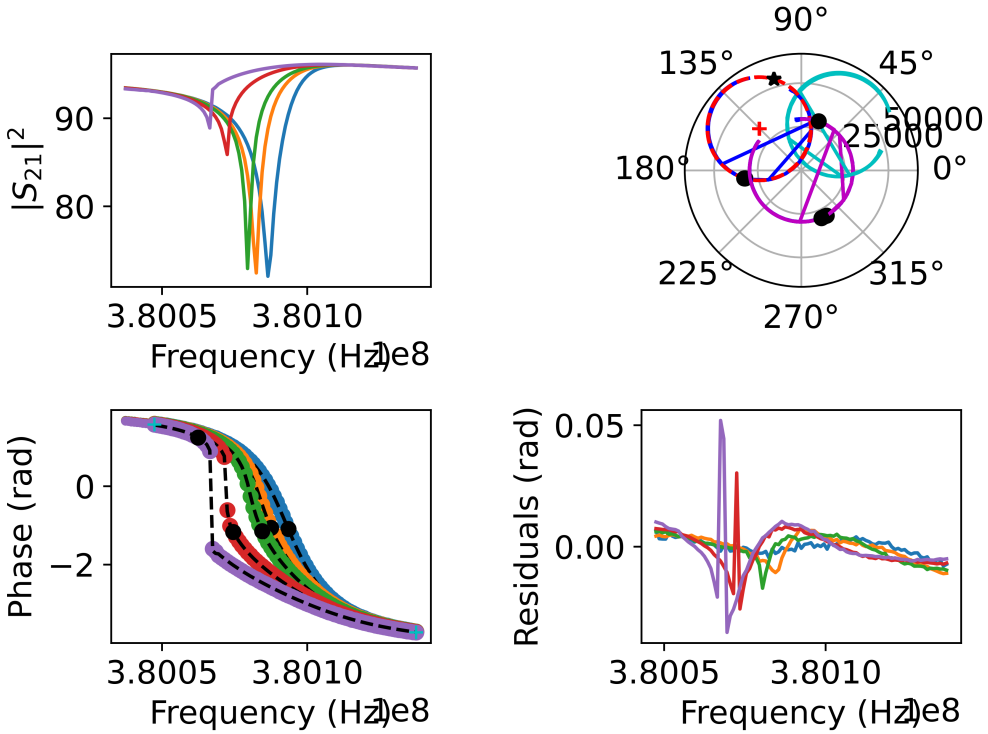

Figure 6.3: Summary of pipeline steps to model a single TiN/Ti/TiN trilayer MKID swept in readout power. *a:* $|S_{21}|^2$ versus frequency for a subset of readout powers where the resonator response is linear, starting to become nonlinear, and after the onset of bifurcation. *b:* Data for the resonator in complex S_{21}/IQ space and polar coordinates. The original data (cyan), data after removing the cable delay (blue), circle fit (red dashed), and data after rotation and translation (magenta) are shown, corresponding to different steps in the fitting procedure. *c:* Phase frequency data for this same resonator after the steps in *b*. Data (colored points) are fit using Eqn 6.14 (black dashed lines). Also shown is the resonance frequency $f_r(I)$ (black dots). *d:* Residuals versus frequency, $\theta_{\text{data}} - \theta_{\text{fit}}$, corresponding to the fits shown in *c*.

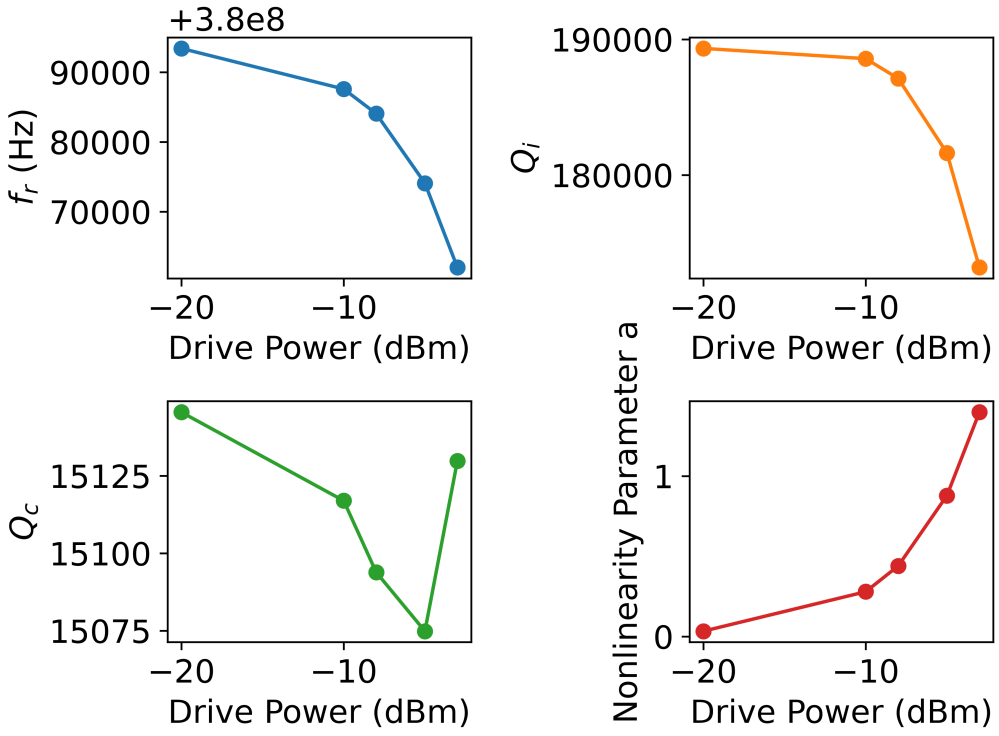

Figure 6.4: Fit parameters for a single TiN/Ti/TiN trilayer MKID, resonant frequency $f_r(I)$, *a:* resonant frequency, *b:* internal quality factor Q_i, *c:* coupling quality factor Q_c, *d:* and nonlinear parameter a as a function of drive power. Parameters are from the phase frequency fits shown in Fig 6.3c.

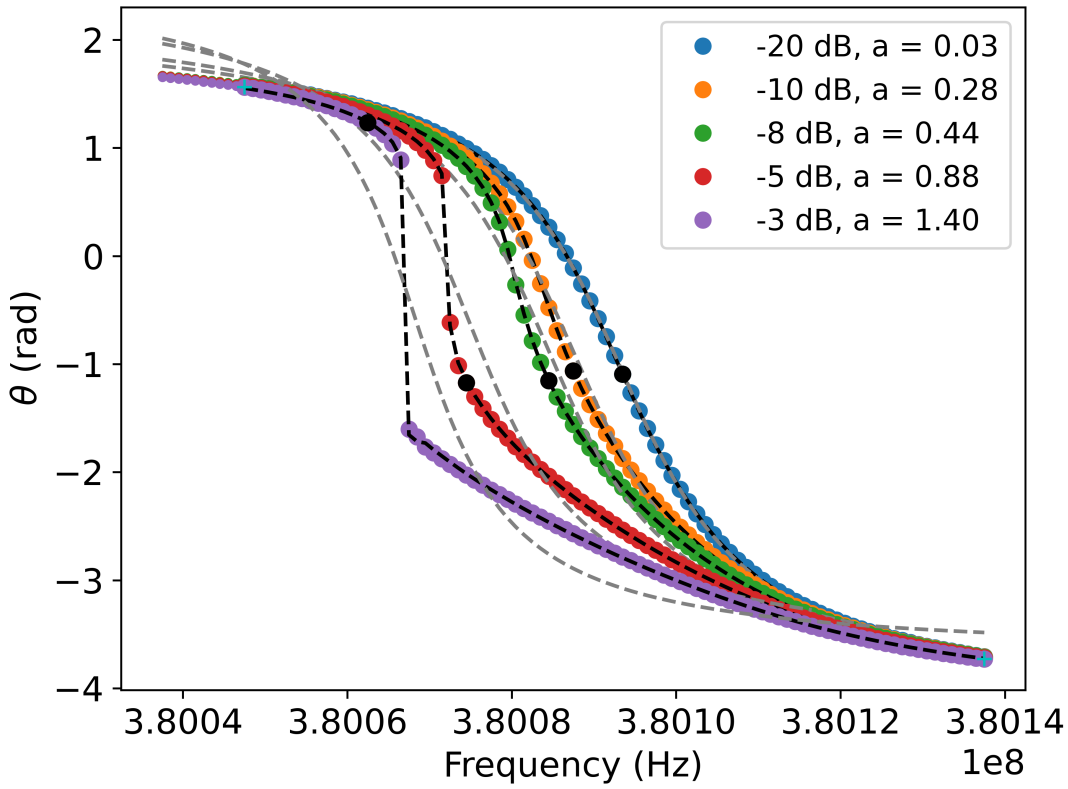

Figure 6.5: Phase frequency data for a single TiN/Ti/TiN trilayer MKID measured in the lab under a 4 K cryogenic optical load. Colors denote different readout powers where the resonator is linear, starting to become nonlinear, and after the onset of bifurcation. The measured data (solid points) is modeled well by Eqn 6.14 (black dashed lines). The legend also shows the corresponding nonlinearity parameter a from each fit. Also shown are fits using Eqn 6.10 (gray dashed lines).

each sweep. When calculating the mean E_*, we also exclude the lowest drive power and any flagged fits. This mean E_* is then used to calculate P_r for a chosen nonlinearity parameter a for a network of MKIDs. The equation for P_r is also derived from Eqn 6.7 for a and is:

$$P_\mathrm{r} = \frac{Q_c \omega_\mathrm{r} a}{2Q_\mathrm{r}^3} E_* \tag{6.16}$$

where the MKID parameters for the lowest drive power dataset are used for Q_r, Q_c, and ω_r. P_r is converted from units of W to dB.

We plan to demonstrate the capabilities of our new MKID tuning method, `kid_phase_fit`, using measurements of MKID arrays at the Large Millimeter Telescope as part of TolTEC commissioning.

TolTEC is a millimeter-wave imaging polarimeter which utilizes MKIDs. As part of this work, in Chapter 7, we describe our efforts to characterize the system noise of TolTEC's 1.1 mm array. This work was aimed at better understanding and improving its noise.

Chapter 7

Characterization of the system noise of the TolTEC 1.1 mm array

The TolTEC camera [185] is a mm-wave MKID imaging polarimeter that was commissioned for the Large Millimeter Telescope (LMT) in late 2022–2023. The LMT is a 50 m single-dish steerable telescope in Sierra Negra, Mexico. The TolTEC receiver consists of 7718 polarization sensitive MKIDs distributed across three arrays with passbands centered at 1.1 mm, 1.4 mm, and 2.0 mm. TolTEC achieves diffraction-limited beams with full width at half maximum (FWHM) values of 5 arcsec, 6.3 arcsec, and 10 arcsec, respectively. This dense arrangement of MKIDs enables TolTEC to achieve sub-10 arcsec beams that fill the LMT's 4 degree field of view. This will facilitate the creation of high-resolution, large-scale maps of nearby and extragalactic systems. We discussed a few relevant science cases in Chapter 1.

We originally planned for this chapter to include a demonstration of our new MKID tuning method on TolTEC data taken during real-time observations. This work is necessary to assess how effective our fitting and tuning pipeline will be in optimizing detector linearity and sensitivity. However, it became apparent that TolTEC is currently operating with readout-dominated noise performance. Therefore, we instead initiated a characterization of the system noise of the TolTEC 1.1 mm MKID array. This analysis was done by taking frequency sweeps and timestream measurements at the LMT with the cryostat window covered to simulate a low loading environment for the detectors. The goal of this work was to identify possible sources of excess noise and future steps to achieve photon-noise-limited performance.

In this chapter, we begin with an introduction of how timestream measurements of MKIDs can be used to calculate their noise. Then, we briefly discuss our expectations of the system noise, applying our discussion of noise sources in MKIDs in Chapter 3. Next, we describe our system noise analysis of the

TolTEC 1.1 mm array in depth. We investigated six networks of detectors, where there are ~ 600 resonators per network. In particular, we discuss measurements of noise power spectral densities, the network RF chain, median white noise, LNA power, and the impact to TolTEC's sensitivity. We follow with conclusions and future steps for improving this noise.

7.1 Conversion of raw timestreams to physical units

Timestream measurements of a MKID are taken by recording the complex forward transmission S_{21} at a fixed probe frequency near the resonant frequency. In TolTEC, the S_{21} is recorded by the ROACH readout in arbitrary analog-to-digital units (ADUs) during a frequency sweep. To compare data with expectations, we must project from ADUs to physical units of frequency shift or amplitude change. To do so requires a measurement of the resonant circle. In this section, we overview the projection of a raw timestream into frequency or dissipation timestreams using a measured resonant circle. In later sections, we make inferences about TolTEC's sensitivity based on power spectral densities (PSDs) computed from these converted timestreams.

It is necessary to calibrate timestream data using a corresponding frequency sweep before converting to noise in frequency units. The steps of this calibration for a single resonator, with a typical response among an array of detectors, is shown in Figure 7.1. In Figure 7.1 (*top left*), the measured raw data for the frequency sweep and timestream are shown as colored points, blue for the frequency sweep and orange for timestream data at a fixed probe tone. The first step in this calibration involves removing the cable delay, which is an additional multiplicative term from the cables when measuring MKIDs. This term can be removed by simply multiplying the timestream and frequency sweep by a factor of $e^{2\pi j\tau f}$, where τ is the cable delay or round trip time a microwave signal propagates through the RF readout cabling and f is the frequency. τ is typically expressed in units of nanoseconds and f in units of hertz (Hz). The data after removing the cable delay is shown in Figure 7.1 (*top right*) with the same colored points as Figure 7.1 (*top left*). Next, the corrected frequency sweep is fit to a circle to find its center point $(x_c + jy_c)$ and radius r. This center point is used to translate the timestream and frequency sweep to the origin by subtracting the fit center point. The timestream and frequency sweep are also rotated so that the timestream data is at a

position corresponding to a phase angle $\theta = 0$ rad. This is done by calculating the phase of the timestream data using $\theta = \arctan(Q/I)$, finding the median phase θ_{med}, and multiplying the timestream and frequency sweep by $e^{-j\theta_{\text{med}}}$. This rotation by θ_{med} prevents phase wrapping when plotting θ for the frequency sweep and timestream data. Figure 7.1 (*bottom left*) shows the circle fit to the frequency sweep as a solid blue curve and the translated and rotated frequency sweep and timestream data, where the timestream is now collinear with the origin at $\theta = 0$ rad.

After these calibration steps, to convert I/Q timestream data to fractional frequency df/f units of Hz^{-1}, we calculate the phase of the timestream and frequency sweep using $\theta = \arctan(Q/I)$. Afterwards, the frequency sweep phase $\theta_{\text{cal}}(f)$ and corresponding frequency information are used to find an interpolation function for frequency $f = \text{f}(\theta_{\text{cal}}(f))$. The interpolation function is used to calculate a corresponding frequency for each measured phase timestream $\theta(t)$ point. The mean of this new set of frequencies f_{mean} is calculated and used to convert $\theta(t)$ to a fractional frequency timestream $\frac{df}{f}(t)$. Figure 7.1 (*bottom right*) shows the phase vs frequency for the calibrated frequency sweep and timestream data where colored points correspond to data points. Also shown is the interpolation function as a dashed green curve. For the resonator shown, the interpolation is successful in tracing the relationship between phase and frequency.

This process where we remove the cable delay, perform a circle fit of the resonance circle, and translate and rotate the frequency sweep and timestream data is summarized by the following expression for the calibrated frequency sweep $S_{21,\text{cal}}$ as:

$$S_{21,\text{cal}} = (S_{21}e^{2\pi j\tau f} - x_{\text{c}} - jy_{\text{c}})e^{-j\theta_{\text{med}}} \tag{7.1}$$

We then calculate the phase of Eqn 7.1 and the corresponding timestream data. The conversion of the phase timestream $\theta(t)$ to a fractional frequency timestream $\frac{df}{f}(t)$ is then:

$$\frac{df}{f}(t) = \frac{\text{f}(\theta(t))}{f_{\text{mean}}} - 1 \tag{7.2}$$

where $\text{f}(\theta)$ is the calculated interpolation function for frequency from $\theta_{\text{cal}}(f)$.

By translating the frequency sweep and timestream data, slow changes in S_{21} can be described by adiabatic response coefficients $A(\omega)$ and $B(\omega)$ which correspond to the directions tangent and normal to the

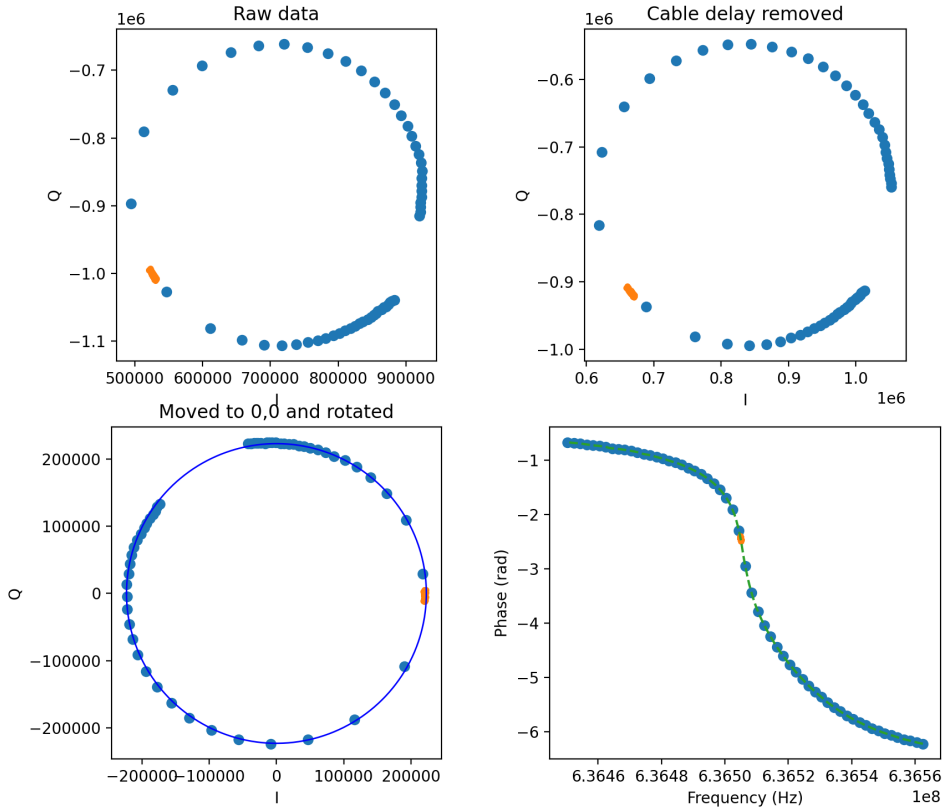

Figure 7.1: Frequency sweep and timestream data calibration steps for a single representative resonator. These steps are performed in order from top left to bottom right. *Top left:* Raw data of a single resonator in complex IQ space. The blue points are data measured from a frequency sweep while the orange points are timestream data measured at a single probe tone frequency near the resonant frequency. *Top right:* Frequency sweep and timestream data where the cable delay term has been removed. *Bottom left:* Frequency sweep and timestream data that has been translated to the origin and rotated so that the timestream data is collinear with the origin. The solid blue line corresponds to the circle fit of the resonance circle used to perform this translation. *Bottom right:* Phase vs frequency for the calibrated frequency sweep and timestream data. An interpolation using the S_{21} sweep phase and frequency was used to find corresponding frequencies for the timestream data. The interpolation function is shown as the dashed green line.

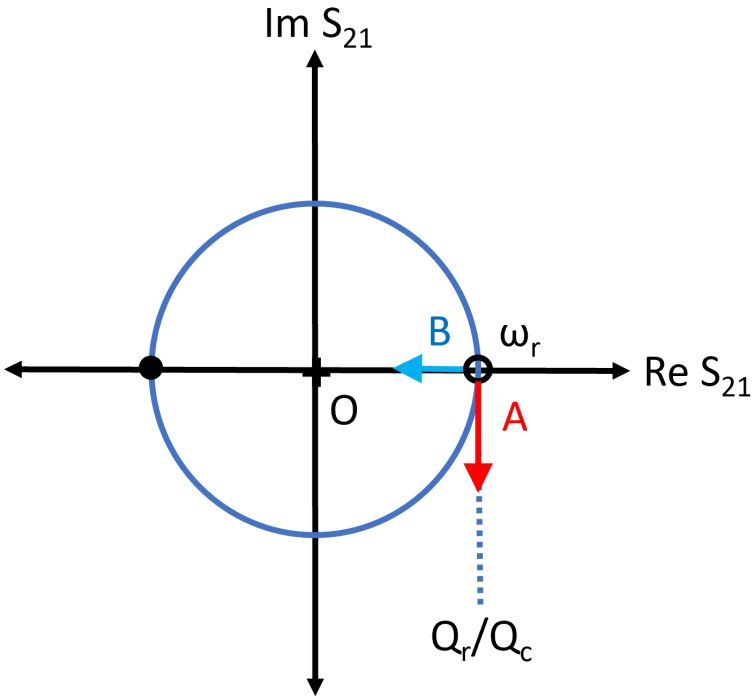

Figure 7.2: Conceptual diagram of the calibrated resonator complex transmission $S_{21,\mathrm{cal}}$ in real/imaginary or IQ space. The orientation of the resonance circle is identical to Figure 7.1 (*bottom left*) with a radius $r = Q_\mathrm{r}/Q_\mathrm{c}$, resonant frequency ω_r, and center at the origin O (cross). The arrows labeled A and B at the unfilled dot correspond to the directions tangent and normal to the resonance circle, respectively. With the data calibrated in this way, A corresponds to the frequency direction noise and B to the amplitude/dissipation direction noise.

resonance circle in complex IQ space, respectively. From Zmuidzinas (2012) [189], we may write the small change or perturbation in S_{21} with time as:

$$\delta S_{21}(t) = A(\omega)\delta x(t) + B(\omega)\delta Q_{\mathrm{i}}^{-1}(t) \tag{7.3}$$

where $\delta x(t)$ is a small change in resonator detuning with time and $\delta Q_{\mathrm{i}}^{-1}(t)$ is a small change in internal quality factor with time. The resonator detuning is a fractional shift of a probe frequency ω from the resonance frequency ω_{r} such that $x = (\omega - \omega_{\mathrm{r}})/\omega_{\mathrm{r}}$. Figure 7.2 shows a schematic of the complex forward transmission $S_{21,\mathrm{cal}}$ in the IQ plane with arrows corresponding to the directions tangent ($A(\omega)$) and normal ($B(\omega)$) to this circle. The orientation of the circle is identical to Figure 7.1 (*bottom left*).

7.2 Noise expectations

After converting phase timestreams for each resonator to fractional frequency timestreams, we can find the components that correspond to the directions tangent $A(\omega)$ and normal $B(\omega)$ to the resonance circle. The tangential component of the timestream data is the frequency direction and can be used to find the frequency noise. The frequency noise is fluctuations in the phase of the probe tone or changes in the resonator's resonance frequency. From Figure 7.2, we see that the direction tangent to the circle, or the red arrow labeled A, is the frequency direction. The normal component of the timestream data is the amplitude direction and can be used to find the amplitude noise. The amplitude noise is fluctuations in the amplitude of the probe tone or changes in the resonator's total quality factor Q. The total quality factor changes since resistive loss, or dissipation, from system components affect the internal quality factor Q_{i}. From Figure 7.2, we see that the direction normal to the circle, or the blue arrow labeled B, is the amplitude direction. This approximation of the equivalence between fluctuations in amplitude with dissipation and fluctuations in phase with frequency assumes that timestream data is measured using a probe signal at or near the resonance frequency, such as this work.

We perform fast Fourier transforms (FFTs) of the tangent and normal components of the fractional frequency timestreams $\frac{df}{f}(t)$ to calculate PSDs of the frequency direction noise and amplitude/dissipation direction noise, respectively. For voltage noise PSDs, the units are in raw analog-to-digital units (ADU^2/Hz)

unless an additional calibration to volts V is performed. For fractional frequency PSDs, as are calculated in this work, the units are 1/Hz. The frequency direction noise (S_{xx}) and amplitude direction noise (S_{yy}) can also be used to calculate the NEP for the array as $NEP = \sqrt{S_{\mathrm{xx}}}/R$, where R is the optical responsivity described in Chapter 3.

The main sources of noise for TolTEC are thought to be photons, generation and recombination of quasiparticles and Cooper pairs in MKIDs, the cryogenic low noise amplifier (LNA) at the output of the array, and sources of noise in the readout, including the digital-to-analog converter (DAC) used for frequency comb generation and the analog-to-digital converter (ADC). In Chapter 3, we discussed the sensitivity of a MKID and common noise sources in terms of the noise equivalent power (NEP) in units of W/$\sqrt{\mathrm{Hz}}$. The NEP is the uncertainty in detected power in a bandwidth of 1 Hz or one-half second integration. Our goal is to make an instrument with photon-noise-limited or background-limited sensitivity. In photon-noise-limited detectors, the photon noise term is equal to or higher than the quadrature sum of all other noise terms. Assuming that these different noise sources are uncorrelated, we can write the fractional frequency noise PSDs in the frequency (S_{xx}) and amplitude directions (S_{yy}) as the sum of squares such that:

$$S_{\mathrm{xx}} = e_{\mathrm{phot}}^2 + e_{\mathrm{GR}}^2 + e_{\mathrm{amp}}^2 + e_{\mathrm{read}}^2 \tag{7.4}$$

and

$$S_{\mathrm{yy}} \approx e_{\mathrm{amp}}^2 + e_{\mathrm{read}}^2 \tag{7.5}$$

where e_{phot} is the photon noise, e_{GR} is the generation-recombination noise, and e_{amp} is the amplifier noise. S_{xx} and S_{yy} are in units of 1/Hz. The photon noise and generation-recombination noise are the detector noise terms. These sources of noise are described in more detail in Chapter 3 (Eqn 3.63, Eqn 3.70, and Eqn 3.73, respectively). The readout noise includes DAC quantization noise and ADC noise among other readout noise sources.

Our expressions for the frequency quadrature noise PSD (Eqn 7.4) and amplitude quadrature noise PSD (Eqn 7.5) distinguish between noise intrinsic to the detector, or detector noise, and external noise added to the probe tone, such as from the low noise amplifier. The amplitude direction component includes noise sources that change the probe signal amplitude and resonator's total quality factor which manifests as

fluctuations in the direction normal to the resonance curve. These sources are dissipative and change the internal quality factor Q_i of the resonator. In MKIDs, the frequency optical responsivity (Section 3.6) is a factor of $\beta/2$ [22, 120] larger than the dissipation optical responsivity, where β is the ratio of frequency response to dissipation response. β has been measured to vary from $\sim$4–50 (e.g. [153, 155, 120, 119]) and scales with resonant frequency and temperature as $\beta \propto kT/\omega$ [189]. Photon and GR noise sources are therefore significantly reduced in the amplitude quadrature, divided by β^2, where $\beta^2 \gg 1$, when calculating NEP^2. This enables us to approximate the amplitude quadrature as being independent of photon noise and detector noise. The amplitude direction noise has also been observed to be independent of whether the probe frequency is tuned on or off resonance and to have a value that is consistent with the noise floor of the readout electronics, which is usually limited by the noise temperature of the LNA [63]. The amplitude quadrature PSD S_{yy} is therefore a good measure of dissipative noise sources external to the detectors, including noise from the readout electronics.

The frequency direction component includes noise sources that change the probe signal phase and resonator's resonance frequency and manifest as fluctuations in the direction tangent to the resonance curve. Detector noise and external noise modulate phase and frequency and include photon noise and generation-recombination noise and components in the RF readout chain like the low noise amplifier, respectively. Photon noise and GR noise contributions are significantly larger in the frequency quadrature due to the ratio β. Therefore, the frequency quadrature PSD S_{xx} is a good proxy for the total system noise, when measured using timestream data taken at or near the resonance frequency. From Eqn 7.4 and Eqn 7.5, we see that S_{xx} should be greater than S_{yy} when devices are operating in the photon-noise-limited regime. The difference of the two $S_{xx} - S_{yy}$ can be used to provide an estimate of the photon noise and detector noise contributions.

We predict a optical NEP of photon-noise limited detectors for the 1.1 mm array of 9.0×10^{-17} W/$\sqrt{\text{Hz}}$ assuming an expected loading of 10.7 pW [14]. This loading is calculated using an atmospheric model for the LMT site at median opacity during an observing season and includes estimates of emitted and scattered light from all optical elements in the system. In this NEP, we consider both fundamental sources of noise from photons (NEP_{phot}) and quasiparticle generation and recombination (NEP_{GR}) and a detector optical

efficiency $\eta \approx 0.8$ such that:

$$NEP^2 = \frac{NEP^2_{\text{phot}} + NEP^2_{\text{GR}}}{\eta} \tag{7.6}$$

For the amplifier noise, assuming a noise temperature of 5 K, we predict that $S_{\text{xx,amp}} = 1.6 \times 10^{-19}$ 1/Hz. This amplifier noise was calculated taking into account the measured median total quality factor Q_{r} (~ 13000) and coupling quality factor Q_{c} (~ 71000) in the linear, low power regime at 28 dB drive attenuation and after filtering for flagged resonators using the fitting and tuning pipeline described in Chapter 6. Since the designed and measured resonator Q_{r} and Q_{c} differ from the design values, this amplifier noise is about a factor of ~ 7 higher, which is still one order of magnitude below the expected photon-limited NEP.

7.3 Network RF chain

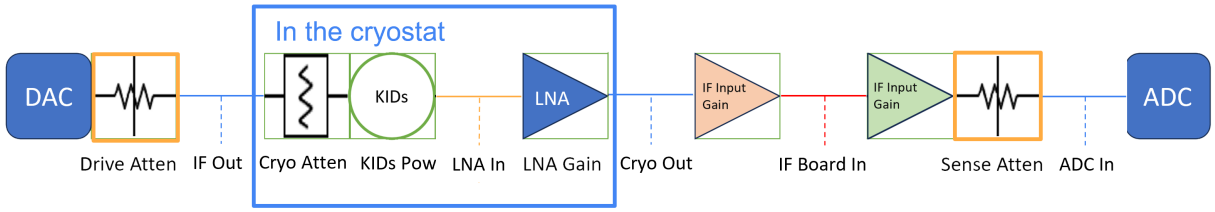

Figure 7.3: Circuit attenuation model of the total power flow through a TolTEC network from the DAC to the ADC. Sections surrounded by boxes represent components in the network while dotted lines denote reference planes of interest where the power is calculated. The large blue box denotes cryogenic components in the readout. Orange boxes denote the drive attenuation (Drive Atten) and sense attenuation (Sense Atten) which were varied for this analysis. The LNA input (LNA In) is shown as a orange dotted line since we calculate the input power to the LNA in Section 7.4.3. The red dotted line denotes predicted compression at the IF board input amplifier (IF Board In) based on this model. Model and figure courtesy of Grant Wilson (UMass).

For the 1.1 mm array, there are seven networks of detectors, each reading out approximately 600 resonators. However, only six networks were wired up for these measurements due to issues with network 5. Frequency sweeps were taken for each resonator after specifying a probe tone frequency near the resonant frequency of each identified MKID. Figure 7.3 shows a circuit attenuation model of the total power flow through the TolTEC network. Sections surrounded by boxes represent components in the network while dotted lines denote reference planes of interest where the power is calculated. From this diagram, one can convert readout-based settings to a physical power level at the MKID array and other components. The

DAC is used generate a comb of probe tones to read out all detectors in a network. As part of this, the voltage of each tone/tone amplitude for each MKID is set using a previously generated lookup table [70]. The transfer function of the tone amplitudes is informed by anti-aliasing filters near the edge frequencies of the network and a local oscillator (LO) near the middle frequencies. After the DAC, there is a variable attenuator called the drive attenuation (Drive Atten) which is one of the ways that we vary the power in the line, where the power is calculated at the output of each IF slice (IF Out), before entering the cryostat with the detector arrays. In this diagram, the cryogenic attenuator (Cryo Atten), KIDs array or power at the KIDs (KIDs Pow), and LNA gain represent the cryogenic components of the readout. The LNA input (LNA In) is one location where we calculate the power sent into the cryostat and is denoted by a orange dotted line. The output side from the cryostat to the analog-to-digital converter (ADC) is also shown, where the power coming out of the cryostat (Cryo Out), at the IF board input for each network (IF board In), and at the input to the ADC (ADC In) are calculated. Another way that we varied the microwave power in our system to the ADC was through a variable attenuator called the sense attenuation (Sense Atten). From this circuit attenuation diagram, we find that there is predicted compression at the input amplifier of the IF board (IF board In) as denoted by a red dotted line.

7.4 Measurements of noise power spectral density

7.4.1 Noise power spectral densities

Following the procedure described in Section 7.1, we measure power spectral densities for the RF lines of the TolTEC 1.1 mm array. Figure 7.4 shows the results of a typical MKID in one network and the median white noise of the network in both the frequency and amplitude/dissipation quadratures. We plot noise power spectral densities in both raw voltage units (ADU^2/Hz) (left) and converted to fractional frequency units (1/Hz) (right). The fractional frequency noise PSD is commonly referred to as S_{xx} or $S_{\delta f/f}$. The median noise PSDs are calculated using all resonators in the network (~ 600) to find the median value at each frequency. In Figure 7.4, noise PSDs were calculated at a drive attenuation of 14 dB and a sense attenuation of 14 dB, which corresponded to maximal timestream response or a more elongated shape in IQ

space. The blue solid and orange dashed curves correspond to PSDs for a single, representative detector in the frequency and amplitude directions while the thick black and gray curves correspond to the median PSDs.

The noise PSDs in the frequency and amplitude quadratures correspond to the directions tangent and normal to the resonance circle in complex IQ space, respectively (Figure 7.2). The shape of the noise PSD in the frequency direction is sensitive to optical signal and is expected to have a higher white noise level than the amplitude quadrature. The frequency noise PSD is also expected to have a $1/f$ knee at a few Hz. This is seen in other high critical temperature T_c TiN/Ti/TiN trilayer MKIDs with a white noise floor starting around 10 Hz [84] and an eventual roll-off in signal due to the MKID acting as a low pass filter at frequencies larger than one resonator bandwidth $\nu > \nu_r/(2Q_r)$. The photon noise also rolls off with the quasiparticle lifetime. While we see the $1/f$ knee, we do not see a roll-off in the white noise floor since our measured noise spectra are limited to ~ 60 Hz due to the timestream sampling frequency limitation of the room temperature electronics (122.1 Hz). The noise PSD in the amplitude direction by comparison is expected to be relatively flat. The amplitude direction noise is a good proxy for external noise terms like the LNA noise and readout noise that are dissipative and affect resonator internal quality factor Q_i.

Comparing the white noise levels of the frequency direction and amplitude direction PSDs, the frequency quadrature will be greater than the amplitude quadrature, or $S_{xx} > S_{yy}$, when LNA noise and readout noise contributions are subdominant to fundamental noise sources, that is photon noise and generation-recombination noise. This is one of the indications of a device operating in the photon-noise-limited regime. For our devices, we find that the separation between the median components of the frequency and dissipation quadratures (black and gray), which represent the separation on average for the network, is a median factor of 1.7 over the white noise range 10 Hz–61 Hz. Since the white noise level in the amplitude direction is similar to the frequency direction, we conclude that readout noise contributes substantially to the sensitivity of TolTEC.

We also looked at noise PSDs of dark, or non-optically coupled, detectors in the frequency and amplitude directions, of which there are generally less than five per network. Figure 7.5 shows the results of a dark, or non-optically coupled, detector in both the frequency and amplitude quadratures. We also include

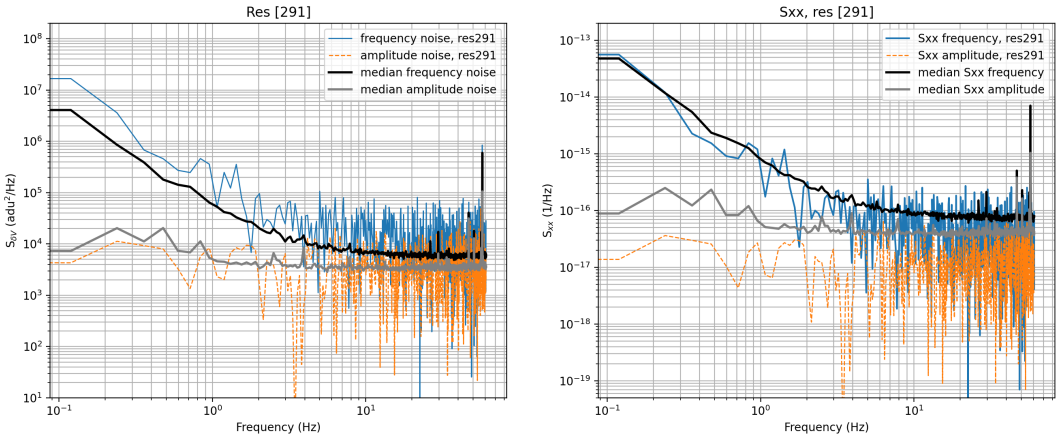

Figure 7.4: Noise power spectral densities for an optical detector. *Left:* Voltage PSDs in raw ADC units for a select optical detector in the frequency (solid blue) and amplitude directions (dashed orange). The white noise level starts around 10 Hz. The median frequency noise component (solid black) and amplitude noise component (solid grey) for the network, about 600 resonators total, are also shown. They represent the separation on average for the network. The small separation, a factor of 1.7, between the median components shows a significantly higher amplifier/readout noise than expected. *Right:* Fractional frequency noise PSDs (S_{xx}) in the frequency and amplitude directions for the same optical resonator as *left*. The median frequency noise and amplitude noise components are also shown. The same colors are used for all curves as *left*.

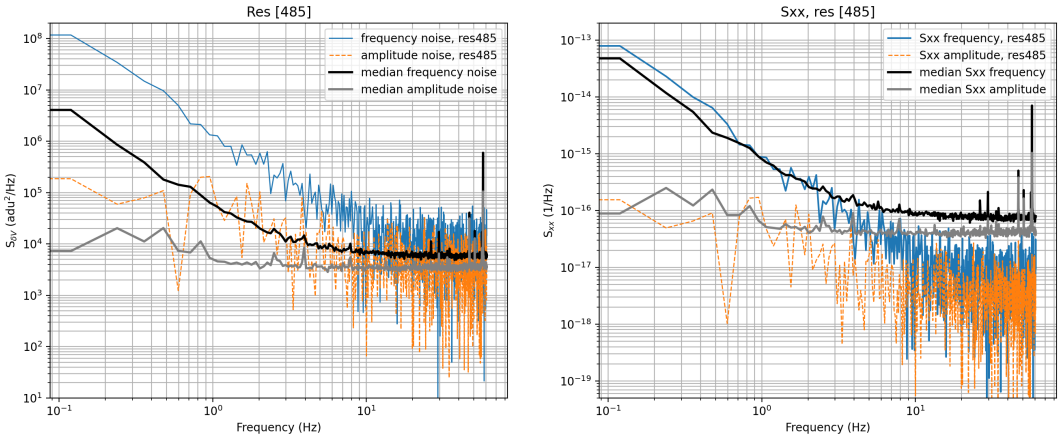

Figure 7.5: Noise power spectral densities for a dark, or non-optically coupled, detector. *Left:* Voltage PSDs in raw ADC units for a dark detector in the frequency (solid blue) and amplitude directions (dashed orange). The white noise level starts around 10 Hz. For this resonator, the two quadratures have a median separation factor of 1.5 over the white noise range 10 Hz–61 Hz. The median frequency noise component (solid black) and amplitude noise component (solid grey) for the network, about 600 resonators total, are also shown. The median curves are identical to 7.4 (*right*). *Right:* Fractional frequency noise PSDs (S_{xx}) in the frequency and amplitude directions for the same dark resonator and colors as the *left*. The median frequency and amplitude components are also shown. The median curves are identical to 7.4 (*left*). The same colors are used for all curves as *left*. The dark white noise level (blue and orange) is about one order of magnitude lower than the median due to having a higher total quality factor and not being coupled to optical power.

the same median PSDs of the frequency and amplitude quadratures as Figure 7.4. We observe that the frequency and amplitude direction white noise levels are comparable in raw ADC units (*left*) and fractional frequency units (*right*). For this resonator, the two quadratures have a median separation factor of 1.5 over the white noise range 10 Hz–61 Hz. This is consistent with the noise trend of optical resonators represented by the median PSDs. The comparable white noise level of both quadratures further supports the idea that readout noise is a significant part of TolTEC's system noise. We also find that compared to the median PSDs, the dark detector S_{xx} white noise is about one order of magnitude lower. This is due to a combination of the dark detectors having a higher total quality factor, a factor of $\sim$2 greater than optical detectors, and they are not coupled to optical power.

Linearity is a challenge in highly multiplexed microwave systems as non-linearity leads to sensitivity loss and an increase in cross-talk. To understand the linearity of the microwave readout system of TolTEC, we measured the noise in a 3D grid, changing the number of tones, the drive attenuation after the DAC, and the sense attenuation before the ADC. Timestream data of the complex forward transmission S_{21} was recorded at a single tone frequency for about 15 s and sampled at 122.1 Hz. Corresponding frequency sweeps of the resonance circle were sampled at 488.3 Hz. Data was measured for a large grid of sense attenuation values, from 30 dB to 0 dB in -2 dB steps, allowing different settings for the ADC and its effect on network noise to be explored. At each sense attenuation step, a large sweep in drive attenuation/readout power was performed, from 30 dB to 0 dB in -2 dB steps, to vary the microwave readout power on the network without changing the tone amplitudes. An identical grid in sense attenuation and drive attenuation was collected for datasets using different numbers of tone to vary the readout power on each MKID. We collected datasets using tones for all $\sim$ 600 resonators, about $\sim$ 300 resonators, and 10 resonators. We refer to these as 'full', half', and 'ten' tone datasets, respectively. In addition, we looked more closely at single/non-collided resonators identical to one or more of these datasets, which we refer to as a 'match', and dark, or not optically-coupled, detectors where the individual feedhorn was physically covered. By varying the number of tones per dataset, this allowed us to explore the effect of the DAC on the total noise. It also enabled us to investigate if one or more components in the readout chain may be going nonlinear and how well we are handling the microwave power on the RF chain in the current configuration. For the rest of this chapter, we

discuss only the full and half tone datasets since we found the ten tone datasets had timestream data where the tone frequencies were chosen far from resonance.

For the full and half tone datasets, we investigated the effect of ADC noise on the total system noise for each network through sweeps in sense attenuation. We found that the value of sense attenuation did not have much of an effect on the noise, except at the highest sense attenuation values 30 dB to 28 dB or at the lowest sense attenuation values explored $\sim$ 8 dB to 0 dB. This suggests that the ADC is subdominant to other sources of readout noise.

7.4.2 Median white noise

We calculated the median white noise, from 10 Hz to 61 Hz, at each drive attenuation step (30 dB to 0 dB in -2 dB steps) for each network of the 1.1 mm array. Figure 7.6 shows the median white noise S_{xx} as a function of drive attenuation for select networks 0, 1, 3, and 4. The solid curves and points in both plots correspond to S_{xx} in the frequency direction. The dashed curves and points correspond to S_{xx} in the amplitude direction. From Figure 7.6, we find that at low microwave tone powers, the noise is the same in the amplitude and frequency directions and scales linearly for networks 0, 1, 3, and 4. This relationship could possibly be explained as operating the networks in a readout-dominated regime since amplifier noise (Chapter 3) and other sources of readout noise decrease with greater P_r. We conclude that noise terms other than detector noise dominate in this array. We refer to "readout" here as all system components external to the detectors. We also observe that a minimum S_{xx} and S_{yy} occurs at a drive attenuation of 14 dB–16 dB, depending on the network, for these measurements. At this minimum, we observe a maximum separation factor of 2 between the frequency and amplitude directions. In particular, for network 4, $S_{xx} = 8 \times 10^{-17}$ 1/Hz versus $S_{yy} = 4 \times 10^{-17}$ 1/Hz at 14 dB drive attenuation. In our model, in which the amplitude direction is noise sources external to the detectors (Eqn 7.5) and the frequency direction is all noise sources (Eqn 7.4), including detector noise, we conclude that the detector noise contributes one part of S_{xx} and the readout contributes another equal part to the total system noise. The turnaround in both noise directions and increase of S_{xx} and S_{yy} at lower drive attenuation values than 14 dB–16 dB is unexpected. We believe this increased S_{xx} at higher microwave powers is the result of compression of one or more components within

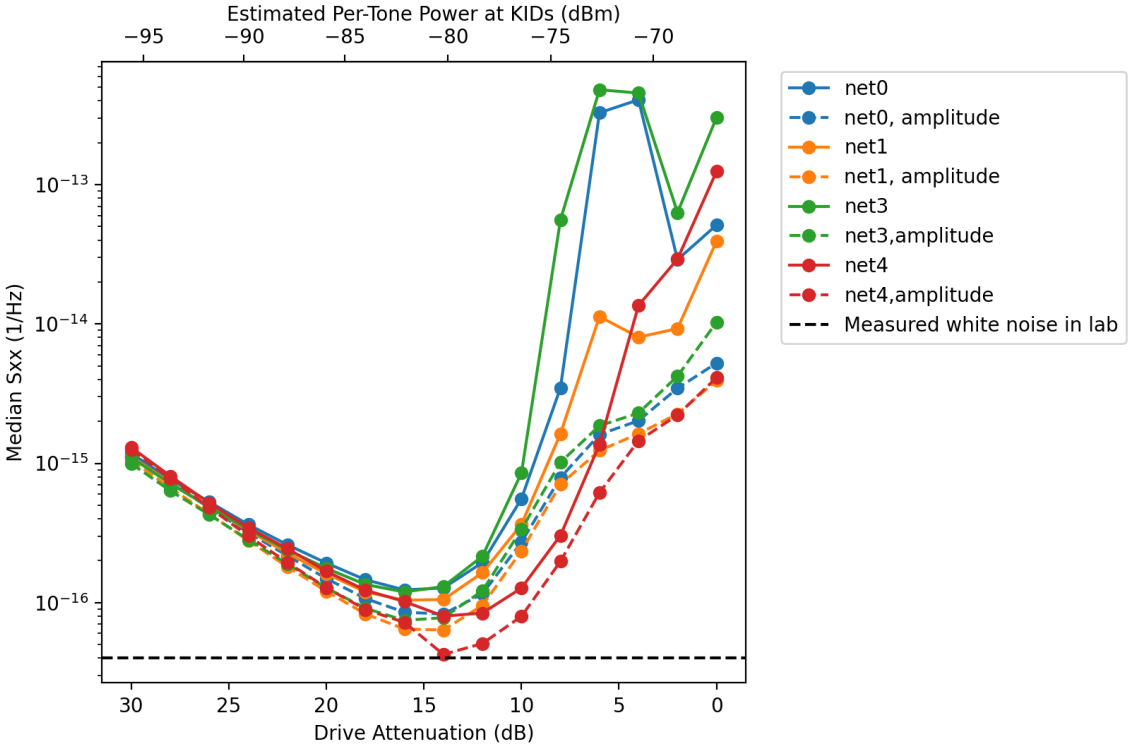

Figure 7.6: Median fractional frequency noise S_{xx} as a function of drive attenuation for several 1.1 mm array networks. The second x-axis at the top shows the conversion from drive attenuation in units of dB and 2 dB steps to an estimated mean per-tone power at the KIDs in units of dBm. The dots correspond to the median fractional frequency noise in the frequency (solid lines) and amplitude directions (dashed lines) calculated in the white noise regime, from 10 Hz–61 Hz. The black dashed line (4×10^{-17} 1/Hz) shows the measured white noise level at NIST. At low microwave tone powers, the noise is the same in the amplitude and frequency directions and scales linearly. This relationship shows noise terms other than the detector noise dominate. A minimum S_{xx} and S_{yy} occurs at 14 dB–16 dB drive attenuation, depending on the network, and the increased noise at lower drive attenuation values is unexpected. We suspect this behavior to be due to compression of one or more components within the RF readout chain.

the RF readout chain. We take a closer look at the LNA power in Section 7.4.3. The cause of this excess noise is under investigation.

In Figure 7.6, we also include a second x-axis at the top that shows the conversion from drive attenuation in units of dB to an estimated mean per-tone power at the KIDs in units of dBm. This estimated mean per-tone power was calculated using timestream data measured at each drive attenuation value in 2 dB steps and the circuit attenuation model for the network RF chain described in Section 7.3 and Section7.4.3. First, we find the mean per-tone power and one standard deviation (2.2 dBm) for each network, where there are $\sim$600 resonators and 16 steps in drive attenuation. Next, we determine a general per-tone power by calculating the average of the mean per-tone powers, including the four networks shown, and its one standard deviation (1.1 dBm). In this way, our procedure takes into account the variation in per-tone power within a network as well as the variation in a general per-tone power applicable to all networks. From a quadrature sum of these standard deviations, we find that the per-tone power at each drive attenuation step has a one standard deviation statistical uncertainty of 2.5 dBm. This estimated per-tone power can also be converted to the total power at the KIDs by multiplying by the total number of MKIDs per network, where there are $\sim$600 resonators each. To further improve the accuracy of our circuit attenuation model in calculating the overall power level at reference planes of interest, like the KID arrays, we plan to measure the transfer functions of readout components at the instrument instead of using estimates based on lookup tables.

We look at histograms of the measured white noise for each resonator, chosen at 20 Hz ($S_{xx,20}$), in the frequency and amplitude directions. We select a drive attenuation value of 16 dB near the minimum measured S_{xx} and S_{yy}. These histograms enable us to get an idea of the the distribution of noise in each network before the suspected onset of compression of one or more components within the readout chain. Previously, in Figure 7.6, we looked at the median white noise S_{xx} and S_{yy}. Figure 7.7a and Figure 7.7b show histograms of $\log(S_{xx,20})$ for the full tone dataset in the amplitude direction (left) and frequency direction (right). The histograms show how the distribution of the white noise for the resonators follows a mostly Gaussian distribution, particularly at higher drive attenuation values/lower microwave powers. This distribution shifts to a lower white noise with increasing readout power until a crucial drive attenuation less than 14 dB–16 dB, depending on the network, where the noise starts to increase. These histograms of the

amplitude direction (left) and frequency direction noise (right) peak at a comparable value $\log(S_{xx}) \sim -16$ in units of $\log(1/\mathrm{Hz})$. This is consistent with Figure 7.6 where the amplitude quadrature and frequency quadrature noise have similar values at high drive attenuation values/low readout powers. We also find that noise histograms of S_{yy} have a wider spread and vary by a factor of 100 compared to similar histograms of S_{xx}. This variation is not currently understood and suggests that a closer look at the end-to-end TolTEC readout RF chain is needed.

7.4.3 LNA power

As part of our noise analysis, we worked with another graduate student in the TolTEC collaboration to calculate the input power to the LNA as a function of drive attenuation and sense attenuation. This enabled us to investigate whether we might be driving the LNA nonlinear with microwave readout power. The complex forward transmission for each tone at the input to the LNA $S_{21,\mathrm{LNA}}$ in units of dBm is calculated taking into account different components in the readout chain as:

$$S_{21,\mathrm{LNA}} = S_{21,\mathrm{meas}} + C_{\mathrm{ADC}} + |A_{\mathrm{sense}}| - C_{\mathrm{sense}} - A_{\mathrm{corr}} \tag{7.7}$$

where $S_{21,\mathrm{meas}}$ is the measured complex forward transmission in units of dB, $C_{\mathrm{ADC}} = -162.4\,\mathrm{dBm/ADU}$ is a constant conversion factor that relates raw ADU units to dBm, and A_{sense} is the attenuation on the sense line which we varied for our measurements as part of our data grid. C_{sense} is a measured adjustment factor in dBm to account for the IF board/network gain on the sense side and is useful for calculating the power coming out of the cryostat. The factor A_{corr} is a gain factor along the sense line to the detector array and is 60 dB for the TolTEC readout chain.

We used Eqn 7.7 to calculate $S_{21,\mathrm{LNA}}$ in dBm for each tone in a network, where there are ~ 600 resonators total. We used timestream data for $S_{21,\mathrm{meas}}$ and calculate per-tone power to the LNA for datasets where the values of drive attenuation and sense attenuation were varied. Next, the $S_{21,\mathrm{LNA}}$ per tone is converted from dBm to mW and summed over to calculate the total input power into the LNA. Figure 7.9 shows a plot of the total power into the LNA in units of dBm for one network of the 1.1 mm array as a function of drive attenuation and sense attenuation. The colored curves correspond to different values of

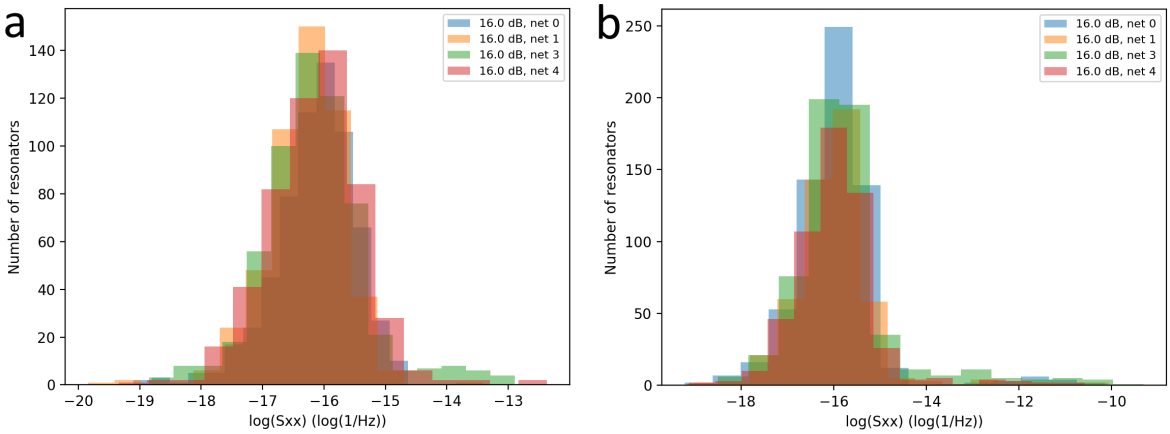

Figure 7.7: Histograms of the log of the fractional frequency noise ($\log(S_{xx})$) in the *a:* amplitude direction and *b:* frequency direction using the full tone dataset, about 600 resonators per network, for a large subset of the 1.1 mm array. Values of white noise S_{xx} are selected for each tone at 20 Hz. Different colors correspond to a network at 16 dB drive attenuation, near the minimum of Figure 7.6.

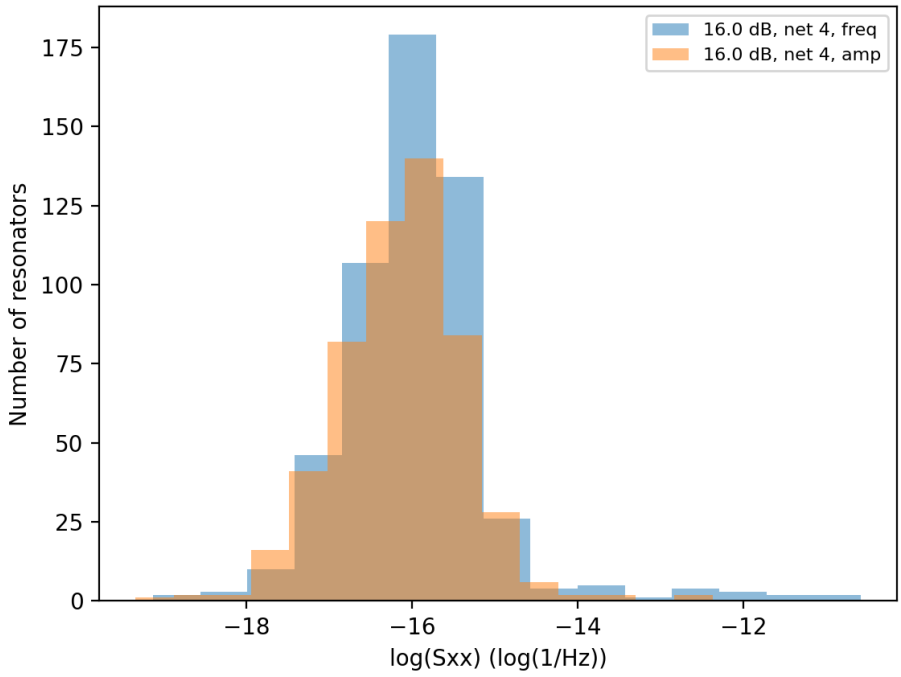

Figure 7.8: Histograms of the log of the fractional frequency noise ($\log(S_{xx})$) in the frequency and amplitude directions for one network of the 1.1 mm array. Histograms are identical to Figure 7.7 for one network. For this network, the median of the frequency and amplitude histograms are nearly incident.

sense attenuation and total calculated power (solid lines with dots). We find that the LNA is compressed and becomes nonlinear for drive attenuation less than 15 dB. At lower values of sense attenuation, we suspect compression of the ADC following the sense attenuator (Figure 7.3). This effect becomes more prominent for sense attenuation values of 8 dB or less. This suggests that one or more components in the RF readout chain are exceeding their dynamic range and at a power level coincident with the minimum in median fractional frequency white noise S_{xx} shown in Figure 7.6. This could impact the sensitivity of the 1.1 mm array. The total quality factor of resonators is also lower than designed, about $Q_r \sim 11,000$ for detectors when observing, and this complicates the issue.

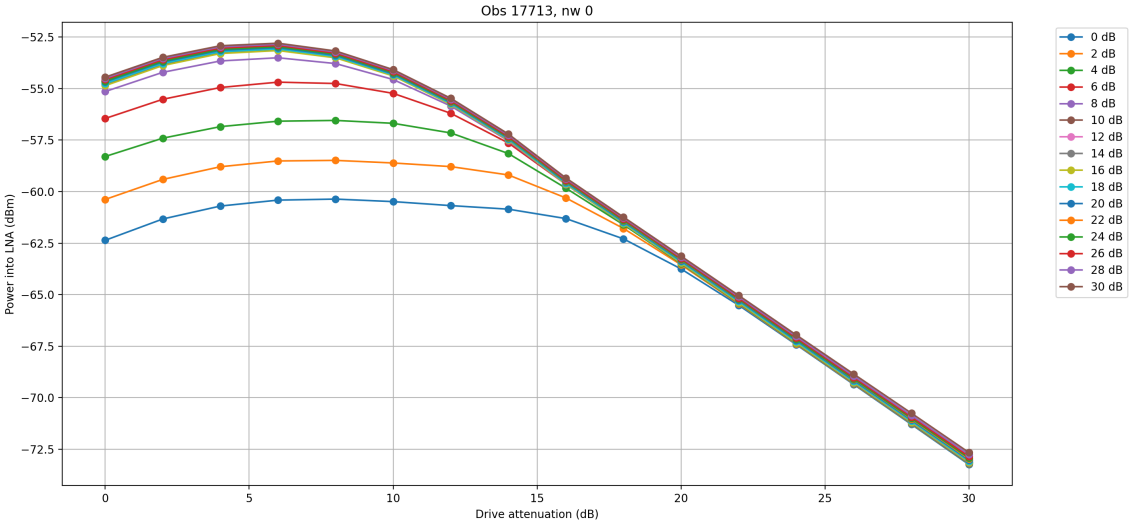

Figure 7.9: Power into the LNA for one network of the 1.1 mm array as a function of network drive attenuation and sense attenuation. Different colored curves correspond to the total tone power calculated for a grid of sense attenuation values. The LNA exhibits nonlinear behavior for drive attenuation values less than 15 dB. At lower values of sense attenuation, we suspect compression of the ADC following the sense attenuator. Courtesy of N. DeNigris (UMass).

7.4.4 Impact to TolTEC's sensitivity

From measurements of noise power spectral density, median white noise, and LNA power, we found that the readout noise, or all system components external to the detectors, contributes substantially to the sensitivity of TolTEC. In Section 7.2, we predicted that the amplifier noise would be $S_{xx,amp} = 1.6 \times 10^{-19}$ 1/Hz at 28 dB drive attenuation or -71.1 dBm input power to the LNA. This is an upper limit to the amplifier noise,

since we suppress the amplifier noise at higher powers due to a $1/P_{\mathrm{r}}$ dependence in $S_{\mathrm{xx,amp}}$ (Eqn 3.73). However, the amplitude quadrature also includes other readout noise sources that can be higher than this estimate. We measure a minimum median white noise of $S_{\mathrm{xx}} = 8.0 \times 10^{-17}$ 1/Hz and $S_{\mathrm{yy}} = 4.2 \times 10^{-17}$ 1/Hz at 14 dB drive attenuation for network 4 (Figure 7.6). We find that the amplitude quadrature is a factor of ~ 10 higher and the frequency quadrature is a factor of ~ 2 higher than previous lab measurements. This suggests that in the best case scenario the detector noise, that is photon noise and generation-recombination noise, contributes one part of S_{xx} and the readout contributes another equal part to the total system noise (Eqn 7.4).

We investigated sources of excess noise, with particular attention to room temperature amplifiers and the LNA. From an analysis of the median white noise across multiple networks of the 1.1 mm array (Section 7.4.2 and Figure 7.6), we found evidence that suggests the compression of one or more components within the network RF readout chain are compressing and exhibiting nonlinear behavior. Using a circuit attenuation model of the network RF chain also suggests that the IF board input amplifier (IF Board In) receives more power than its 1 dB compression point ($P1dB$) (Section 7.3). This is partially the result of a lower total quality factor Q_{r} than designed, either due to higher loading or higher base temperature than expected from previous lab measurements. Lower resonator quality factors can also impact amplifier performance and help contribute to the observed excess readout noise. In Section 7.4.3, we looked more closely at input power to the network LNAs in our datasets to investigate potential compression of the LNA. We found that the LNA is compressed for drive attenuation less than 15 dB, or readout power after tone generation with the DAC (Figure 7.9). At lower values of sense attenuation, we suspect compression of the ADC following the sense attenuator. From histograms of the measured white noise, such as Figure 7.7a and Figure 7.7b, we found that S_{yy} has a wider spread per network and varies by a factor of 100 compared to similar histograms of S_{xx}. This variation is not currently understood. In addition to what is evidenced in Figure 7.6), the fact that the amplitude direction noise varies by 100 suggests that we need to take a closer look at the details of the end-to-end TolTEC readout RF chain in order to improve TolTEC's sensitivity.

7.5 Conclusions

From our results, we have identified that a sub-optimal readout configuration currently exists in the TolTEC 1.1 mm array. The frequency quadrature noise, a proxy of the total system noise, is a factor of ~ 2 higher at 14 dB drive attenuation for network 4 (Figure 7.6) than expected from noise measurements taken at NIST before commissioning. This suggests that in the best case scenario the detector noise, that is photon noise and generation-recombination noise in MKIDs, contributes one part of S_{xx} and the readout, or all system components external to the detectors, contributes another equal part to the total system noise (Eqn 7.4). In this current configuration, the system noise can be minimized up to a point by reducing the network drive attenuation/increasing the microwave readout power on the system until right before one or more components in the RF chain compress and show nonlinear behavior (Figure 7.6). After this point, which is near 14 dB–16 dB drive attenuation depending on the network, although this will also vary depending on the optical loading, we find that the noise unexpectedly increases. We believe this increased S_{xx} at higher microwave powers is the result of compression of one or more components within the RF readout chain. This is consistent with our circuit attenuation model of the RF readout chain in which a room temperature amplifier was found to be compressed. From white noise histograms of S_{yy} and S_{xx} (Figure 7.7a and Figure 7.7b), we find that noise histograms of S_{yy} have a wider spread and vary by a factor of 100 compared to similar histograms of S_{xx}. This variation is not currently understood. Our measurements suggest that we need to take a closer look at the details of the end-to-end TolTEC readout RF chain. In the following section, we discuss a number of future steps we will take to better understand and address this excess noise. This will greatly improve TolTEC's sensitivity beyond what we have shown in this initial commissioning work.

After improving the system noise, we plan to optimize the sensitivity and dynamic range of each network of detectors, where there are about 600 resonators, by controlling three knobs in our MKID fitting and tuning pipeline (Chapter 6). These three settings are the network drive attenuation and tone amplitude, which set the microwave readout power on each resonator, and the probe tone frequency, which corresponds to near the resonant frequency of each MKID. Our new tuning method has been demonstrated on TiN/Ti/TiN trilayer resonators at a large range of readout powers when the resonator is linear, before the

onset of bifurcation, and afterwards for both lab and on-sky measurements. This method has also recently been implemented in the real-time observation software used by TolTEC. This will enable the quick and careful selection of probe tone frequencies, tone amplitudes, and a drive attenuation for each network that will operate detectors before bifurcation and push down noise in the amplitude quadrature.

7.6 Future steps

Through recent summer maintenance of TolTEC at the LMT, we were able to reconnect network 5, which was not measured for this analysis. Crucially, when re-evaluating microwave power at each part in the RF network chain, we discovered that the expected power at the 20 dB room temperature amplifier to the IF board/slice was approximately 5 dB higher than its $P1dB$ (see Figure 7.3). This issue had not been expected or discovered until installation since we utilized microwave powers approximately 10 dB lower while operating in the laboratory with lower optical loading. To address this compressed amplifier, we installed 12 dB attenuators on the input to this amplifier on each network to provide additional overhead on the readout power. We expect this will lead to significant improvement when operating this amplifier in its linear regime compared to before. In the near future, we plan to take steps to:

(1) Re-measure the system noise of the TolTEC 1.1 mm array in a similar manner to this work given these recent changes to the RF chain.

- Confirm that the amplitude noise is a smaller contribution to the overall noise budget.
- Check that the median white noise is no longer consistent with one or more amplifiers being compressed.

(2) Investigate how effective our new MKID tuning method is at optimizing the sensitivity and dynamic range of networks during real-time observations.

- As part of this, compare the selection of probe tone frequency, tone amplitude, and network drive attenuation to the current operation scheme.

Chapter 8

Conclusion

In this thesis, we developed and characterized two complementary superconducting detectors, TES bolometers and MKIDs, at the National Institute of Standard and Technology to study the (sub)mm-wave Universe. We developed TES bolometers for CMB applications with direct impact to the Simons Observatory (Chapter 4) and AliCPT (Chapter 5). We also developed an advanced MKID readout tuning technique for MKID arrays (Chapter 6) and characterized the system noise of the TolTEC 1.1 mm array (Chapter 7). In this concluding chapter, we comment on the outlook of these sensors for mm/submm-wave observations.

The search for inflationary B-modes continues to drive detector development, namely of TES bolometers. During the 2020s, upcoming CMB experiments, such as Advanced Simons Observatory, will use larger arrays of TES bolometers for improved sensitivity. Advanced Simons Observatory is a recently funded upgrade to SO and will complete its three 0.5 m small aperture telescopes (SATs) and populate all 13 optics tubes of its 6 m large aperture telescope (LAT), compared to 7 initially. This will lead to an additional $\sim 30,000$ TES bolometers or $\sim 100,000$ detectors in total across all four telescopes. These telescopes will map the sky from the Atacama Desert and are designed to measure CMB anisotropies from few-degree scales (SATs) to arcminute scales (LAT) [7]. These numbers of detectors will double the mapping speed and significantly increase the sensitivity of the LAT during its planned five year observing period through the early 2030s.

In the late 2020s/early 2030s, next generation CMB experiments, including LiteBIRD [76] and CMB Stage 4 (CMB-S4) [2] are planned to continue the search for the inflationary B-mode signal. These experiments will require significantly larger numbers of TES bolometer arrays or observe from space for

more gains in sensitivity. LiteBIRD is a planned space mission that will map the CMB polarization at the Sun-Earth Lagrangian point L2 for three years. It will consist of three telescopes and 4,339 detectors that observe in 15 frequency bands between 34 GHz and 448 GHz with a typical angular resolution of 0.5 degrees at 100 GHz. Compared to ground-based experiments, this space environment will enable a survey of the entire sky that is 30 times more sensitive than previous full-sky experiments [110]. Its main science goal is to search for inflationary B-modes and constrain the tensor-to-scalar ratio r to $r = 0.01$ with greater than 5σ significance, or $\sigma(r) = 0.001$ in a fiducial $r = 0$ model. CMB-S4 is designed to be the largest dedicated ground-based CMB experiment to date. It will utilize on order $\sim 500,000$ photon-noise-limited detectors across 12 telescopes divided between sites at the Atacama Desert and South Pole to map the CMB across multiple angular scales and greater than 50% sky fraction for 7 to 10 years. This scale of detectors is a factor of 10 greater than current experiments for improved sensitivity. One of the main science drivers of CMB-S4 is to search for the primordial B-mode signal to a target sensitivity of $\sigma(r) = 0.001$ [2] or an upper limit of $r = 0.01$, assuming a $r = 0$ model.

There are a few efforts to incorporate aspects of TES bolometer pixel design in MKID arrays for upcoming CMB experiments. There is recent work by the US and UK to develop planar orthomode transducer-coupled (OMT-coupled) multichroic MKID arrays (e.g. [93, 167, 21]) optimized at 90/150 GHz frequency bands for upcoming CMB experiments, including Simons Observatory. Current experiments with feedhorn-coupled MKID arrays, such as TolTEC [14], commonly utilize a direct absorber to couple incident radiation to two polarization-sensitive MKIDs per pixel, including Figure 1.7b. This architecture is simple and enables MKIDs with high optical efficiency ($\eta \sim 80\%$) to incident radiation. Coupling an OMT to a detector pixel is the architecture of choice for many CMB experiments with TES bolometer pixels developed by NIST (e.g. [187, 13, 48, 47, 82]) and collaborators (e.g. [121, 40]) over the past decade, including Figure 1.7a. This approach separates the detector and coupling architecture so that they can be individually optimized. OMT-coupled MKIDs will thus enable sensitive dual-polarization pixels, with $\eta > 80\%$, and have multiple passbands defined all on-chip.

In another approach to MKIDs designed for CMB polarimetry, there is recent work by Caltech and JPL to develop thermal kinetic inductance detectors (TKIDs) [160, 133] for CMB experiments, including

a pathfinder 150 GHz camera with 512 devices [180] for the Keck Array [27] and a larger 220/270 GHz receiver for the BICEP Array [85, 125] at the South Pole. A TKID is a sensitive superconducting detector which incorporates a superconducting resonator as a bolometer [179]. Similar to a TES bolometer, a TKID consists of a thermally isolated island with an absorber of heat capacity C at temperature T that converts absorbed radiative or optical power to heat. The island and absorber are connected to a stable thermal reservoir at bath temperature T_b through a weak link with thermal conductance G. The superconducting circuit of a TKID is a parallel LC resonator consisting of lumped element components that is capacitively coupled to a microstrip transmission line and to ground. The inductor is located on the island and acts as a sensitive thermometer by measuring changes in the kinetic inductance while the capacitor is located off the membrane. Similar to other MKIDs, TKIDs can be naturally frequency-division multiplexed to enable large format arrays with thousands of detectors. However, in a TKID, the absorber is in thermal contact with but now electrically separate from the inductor [179]. This approach electrically decouples the TKID absorber and resonator circuit compared to an absorber/inductor MKID design, such as Figure 1.7b. This characteristic of TKIDs offers more design flexibility by allowing the resonator circuit and absorber to be individually optimized. It also enables the TKID to replace a TES in a bolometer so that mature radiation-coupling technologies (e.g. [104, 187, 40, 12, 29, 77]) used successfully in TES bolometer pixels can be utilized.

There are several efforts to develop MKID arrays that are slightly higher frequency than nominal CMB frequency bands and will be fielded in the 2020s. SPT-3G+ is a new camera consisting of 34,100 feedhorn-coupled KIDs that will measure the CMB at passbands centered at 220 GHz, 285 GHz, and 345 GHz at the 10 m South Pole Telescope [10]. Each of its detector arrays will observe in a single frequency band and contain 4,875 detectors, with 7 arrays in total. A focal plane of these detectors will be demonstrated in 2023-2024 as part of a pathfinder spectrometer called SPT-SLIM [98]. MKIDs are well suited to operating in large arrays since thousands of high Q resonators can be naturally frequency-division multiplexed, or read out using a single pair of coaxial cables, to greatly simplify cryogenic readout and detector packaging of arrays compared to TES bolometers. This characteristic also facilitates much higher detector counts per MKID array, enabling faster mapping speeds per focal plane area. The 345 GHz

high frequency band of SPT-3G+ will help better characterize the impact of dust foregrounds on searches for inflationary B-modes. The upcoming (sub)mm CCAT Observatory with the Fred Young Submillimeter Telescope (FYST) is an experiment designed to address broad astrophysical questions, ranging from Big Bang cosmology through reionization to the formation of stars [35]. FYST is a 6 m aperture telescope on Cerro Chajnantor in Chile (5600 m altitude) with first observations planned in 2024. Its first-generation receiver cryostat, Prime-Cam, will consist of seven independent modules, two imaging spectrometer modules for line intensity mapping (210–420 GHz), and five broadband polarization-sensitive modules (220 GHz, 280 GHz, 350 GHz, 410 GHz, and 850 GHz), with more than 100,000 MKIDs when completed. By combining observations from AdvACT, SO, and FYST, these experiments will measure the entire spectrum of the SZ effect (Figure 1.4 from [35]). Prime-Cam's spectrometer will be used to map the line intensity of atomic fine-structure lines, particularly the bright 158 µm ionized-carbon transition [CII], to measure the 3-D Universe from redshift $z = 1$ to $z > 5$. In a complementary effort to SPT-3G+, CCAT higher frequency bands at 350 GHz and 410 GHz will measure polarized Galactic dust emission and far-infrared emission from dusty galaxies that act as foregrounds to CMB and SZ measurements. The submm 850 GHz (350 µm) passband will also enable surveys of dusty star-forming galaxies to better understand the cosmic star formation history [114] at high redshifts.

In the 2020s, there will be a few experiments to develop and field far-infrared (FIR) MKID arrays using stratospheric balloons. FIR wavelengths are inaccessible from the ground due to atmospheric extinction. One such funded next generation experiment is the Terahertz Intensity Mapper (TIM). TIM is an integral-field spectrometer to observe from 240–420 µm with a resolving power of 250. It will utilize 3600 dual-polarization KID pixels coupled to a low-emissivity carbon-fiber 2 m telescope installed on a stratospheric balloon with a flight planned from Antarctica at an altitude of 37 km. For more efficient spectroscopy, its KIDs will be split across two long-slit grating modules, a short wavelength module covering 240–317 µm and a long wavelength module covering 317–420 µm. One science goal of this instrument is to map the line intensity of atomic fine-structure lines, particularly the 158 µm [CII] emission line, to produce deep maps of the 3-D structure of the Universe from $0.52 < z < 1.67$. These measurements will enable new studies of the cosmic star formation history and evolution of galaxies. Another goal of this instrument is

to demonstrate technical milestones necessary for space-based FIR spectroscopy. TIM will validate a low-emissivity, high-throughput telescope and spectrometer optics and arrays of photon-noise-limited detectors that are scalable to greater than 10,000 pixel counts. These capabilities will enable future space-based FIR instrumentation.

In the far-infrared community, a space-based instrument with a 4 K cooled mirror drives the development of detectors with extreme per-pixel sensitivities, a few orders of magnitude lower than current ground-based (sub)mm experiments. This is a major contemporary development in the field of superconducting photon sensors. Potential future space-based FIR missions include a probe-class experiment in the 2030s recommended by the Decadal Survey on Astronomy and Astrophysics 2020 and the Origins Space Telescope on a longer timescale if selected. There are four probe-class missions currently under study [171], with two of the four planning to use kinetic inductance detectors in a polarimetric imager and/or spectrometer. For example, the Origins Space Telescope is planned to observe IR wavelengths from 25 μm to 588 μm and requires a per-pixel noise equivalent power (NEP) of 3.0×10^{-19} W/$\sqrt{\text{Hz}}$ for imaging and 3.0×10^{-20} W/$\sqrt{\text{Hz}}$ for spectroscopy with multiple arrays of $\sim 10^4$ detectors each. These sensitivity requirements, especially for FIR spectroscopy, are major design drivers. Efficient radiation coupling over shorter wavelengths compared to (sub)mm ground-based instruments, susceptibility to cosmic rays, and optimization of detector readout systems [159], including multiplexers, cold amplifiers, and warm readout electronics, are also design drivers in these applications. TES bolometers and MKIDs can be developed with lower NEPs by exploiting their detector physics as described in Chapter 2 and Chapter 3 of this thesis. We will briefly comment on a few active areas of detector development for TES bolometers and MKIDs that work to address these design challenges.

To improve the sensitivity of TES bolometers, there have been a few efforts to reduce the fundamental thermal fluctuation noise (Eqn 2.3.1) by decreasing the bolometer thermal conductance G. These efforts include developing TES bolometers with long diffusive legs (e.g. [145, 101, 165]), short ballistic leg bolometers (e.g. [20]), phononic filter bolometers with nanomachined legs designed to suppress phonon modes (e.g. [148, 184]), and hot electron bolometers (e.g. [96, 97]). To date, lab measurements of dark, or non-optically coupled, TES bolometers have an electrical $NEP_{\text{el}} = 2 \times 10^{-19}$ W/$\sqrt{\text{Hz}}$ and reasonable re-

sponse times (< 1 ms) [145, 101, 165], which will be sufficient for a future space-based far-infrared imager. By comparison, a factor of 100 reduction in G will be needed to make devices 10 times more sensitive and meet the spectrometer requirement of space observatories. Another consideration is that this reduction in thermal conductance will also make devices about 100 times slower [130] since the natural time constant $\tau \equiv C/G$.

For MKIDs, the system noise can be reduced in a few ways to achieve this space-based detector sensitivity requirement. Increasing MKID optical responsivity by reducing the active inductor/absorber volume of the detector will lead to a reduced NEP (Section 3.6). Excess noise in MKIDs such as TLS noise (Section 3.7.3) can be suppressed by optimizing capacitor geometry, by careful choice of substrate material [18], and by removing the exposed substrate surface from regions with high electric fields [19]. Noise in the amplitude/dissipation quadrature can also be reduced by optimizing coupling to the readout line [23] and readout power [74]. Ultrastable MKIDs whose sensitivity is limited by photon noise at signal frequencies as low as 50 mHz have been demonstrated with hybrid detectors utilizing a TiN interdigitated capacitor and Al inductor/absorber [173]. By employing a number of these considerations, Baselmans et al. (2022) [24] recently demonstrated hybrid Al/NbTiN antenna-coupled MKIDs with a mean experimental NEP $\sim 3.1 \times 10^{-20}$ W/$\sqrt{\text{Hz}}$ at readout frequency $f = 200$ Hz. Although, this design will require better $1/f$ performance at lower readout frequencies and the development of new architectures to build large arrays of several 10^4 pixels [159].

In this thesis, we developed and characterized TES bolometers for the upcoming CMB experiments, Simon Observatory and AliCPT. We also characterized MKID arrays of the TolTEC camera commissioned at the Large Millimeter Telescope in late 2022–2023. We developed a new tuning method to optimize operation of MKID arrays under dynamic loading conditions as seen when observing from ground-based observatories and investigated the system noise of the TolTEC 1.1 mm array. This research will enable TES bolometer arrays and MKID arrays across a broad range of mm/submm wavelengths and at the scale of detector and readout integration and optimization necessary for the far-infrared and (sub)mm astronomy communities in the coming decades.

Bibliography

[1] Kevork N. Abazajian, Peter Adshead, Zeeshan Ahmed, Steven W. Allen, David Alonso, Kam S. Arnold, Carlo Baccigalupi, James G. Bartlett, Nicholas Battaglia, Bradford A. Benson, Colin A. Bischoff, Julian Borrill, Victor Buza, Erminia Calabrese, Robert Caldwell, John E. Carlstrom, Clarence L. Chang, Thomas M. Crawford, Francis-Yan Cyr-Racine, Francesco De Bernardis, Tijmen de Haan, Sperello di Serego Alighieri, Joanna Dunkley, Cora Dvorkin, Josquin Errard, Giulio Fabbian, Stephen Feeney, Simone Ferraro, Jeffrey P. Filippini, Raphael Flauger, George M. Fuller, Vera Gluscevic, Daniel Green, Daniel Grin, Evan Grohs, Jason W. Henning, J. Colin Hill, Renee Hlozek, Gilbert Holder, William Holzapfel, Wayne Hu, Kevin M. Huffenberger, Reijo Keskitalo, Lloyd Knox, Arthur Kosowsky, John Kovac, Ely D. Kovetz, Chao-Lin Kuo, Akito Kusaka, Maude Le Jeune, Adrian T. Lee, Marc Lilley, Marilena Loverde, Mathew S. Madhavacheril, Adam Mantz, David J. E. Marsh, Jeffrey McMahon, Pieter Daniel Meerburg, Joel Meyers, Amber D. Miller, Julian B. Munoz, Ho Nam Nguyen, Michael D. Niemack, Marco Peloso, Julien Peloton, Levon Pogosian, Clement Pryke, Marco Raveri, Christian L. Reichardt, Graca Rocha, Aditya Rotti, Emmanuel Schaan, Marcel M. Schmittfull, Douglas Scott, Neelima Sehgal, Sarah Shandera, Blake D. Sherwin, Tristan L. Smith, Lorenzo Sorbo, Glenn D. Starkman, Kyle T. Story, Alexander van Engelen, Joaquin D. Vieira, Scott Watson, Nathan Whitehorn, and W. L. Kimmy Wu. Cmb-s4 science book, first edition, 2016.

[2] Kevork N. Abazajian, Peter Adshead, Zeeshan Ahmed, Steven W. Allen, David Alonso, Kam S. Arnold, Carlo Baccigalupi, James G. Bartlett, Nicholas Battaglia, Bradford A. Benson, Colin A. Bischoff, Julian Borrill, Victor Buza, Erminia Calabrese, Robert Caldwell, John E. Carlstrom, Clarence L. Chang, Thomas M. Crawford, Francis-Yan Cyr-Racine, Francesco De Bernardis, Tijmen de Haan, Sperello di Serego Alighieri, Joanna Dunkley, Cora Dvorkin, Josquin Errard, Giulio Fabbian, Stephen Feeney, Simone Ferraro, Jeffrey P. Filippini, Raphael Flauger, George M. Fuller, Vera Gluscevic, Daniel Green, Daniel Grin, Evan Grohs, Jason W. Henning, J. Colin Hill, Renee Hlozek, Gilbert Holder, William Holzapfel, Wayne Hu, Kevin M. Huffenberger, Reijo Keskitalo, Lloyd Knox, Arthur Kosowsky, John Kovac, Ely D. Kovetz, Chao-Lin Kuo, Akito Kusaka, Maude Le Jeune, Adrian T. Lee, Marc Lilley, Marilena Loverde, Mathew S. Madhavacheril, Adam Mantz, David J. E. Marsh, Jeffrey McMahon, Pieter Daniel Meerburg, Joel Meyers, Amber D. Miller, Julian B. Munoz, Ho Nam Nguyen, Michael D. Niemack, Marco Peloso, Julien Peloton, Levon Pogosian, Clement Pryke, Marco Raveri, Christian L. Reichardt, Graca Rocha, Aditya Rotti, Emmanuel Schaan, Marcel M. Schmittfull, Douglas Scott, Neelima Sehgal, Sarah Shandera, Blake D. Sherwin, Tristan L. Smith, Lorenzo Sorbo, Glenn D. Starkman, Kyle T. Story, Alexander van Engelen, Joaquin D. Vieira, Scott Watson, Nathan Whitehorn, and W. L. Kimmy Wu. CMB-S4 Science Book, First Edition. arXiv e-prints, page arXiv:1610.02743, October 2016.

[3] R. Adam, I. Bartalucci, G. W. Pratt, P. Ade, P. André, M. Arnaud, A. Beelen, A. Benoît, A. Bideaud, N. Billot, H. Bourdin, O. Bourrion, M. Calvo, A. Catalano, G. Coiffard, B. Comis, A. D'Addabbo,

M. De Petris, J. Démoclès, F. X. Désert, S. Doyle, E. Egami, C. Ferrari, J. Goupy, C. Kramer, G. Lagache, S. Leclercq, J. F. Macías-Pérez, S. Maurogordato, P. Mauskopf, F. Mayet, A. Monfardini, T. Mroczkowski, F. Pajot, E. Pascale, L. Perotto, G. Pisano, E. Pointecouteau, N. Ponthieu, V. Revéret, A. Ritacco, L. Rodriguez, C. Romero, F. Ruppin, K. Schuster, A. Sievers, S. Triqueneaux, C. Tucker, M. Zemcov, and R. Zylka. Mapping the kinetic Sunyaev-Zel'dovich effect toward MACS J0717.5+3745 with NIKA. , 598:A115, February 2017.

[4] P. Ade, James Aguirre, Zeeshan Ahmed, Simone Aiola, Aamir Ali, David Alonso, Marcelo A. Alvarez, Kam Arnold, Peter Ashton, Jason Austermann, Humna Awan, Carlo Baccigalupi, Taylor Baildon, Darcy Barron, Nick Battaglia, Richard Battye, Eric Baxter, Andrew Bazarko, James A. Beall, Rachel Bean, Dominic Beck, Shawn Beckman, Benjamin Beringue, Federico Bianchini, Steven Boada, David Boettger, J. Richard Bond, Julian Borrill, Michael L. Brown, Sarah Marie Bruno, Sean Bryan, Erminia Calabrese, Victoria Calafut, Paolo Calisse, Julien Carron, Anthony Challinor, Grace Chesmore, Yuji Chinone, Jens Chluba, Hsiao-Mei Sherry Cho, Steve Choi, Gabriele Coppi, Nicholas F. Cothard, Kevin Coughlin, Devin Crichton, Kevin D. Crowley, Kevin T. Crowley, Ari Cukierman, John M. D'Ewart, Rolando Dünner, Tijmen de Haan, Mark Devlin, Simon Dicker, Joy Didier, Matt Dobbs, Bradley Dober, Cody J. Duell, Shannon Duff, Adri Duivenvoorden, Jo Dunkley, John Dusatko, Josquin Errard, Giulio Fabbian, Stephen Feeney, Simone Ferraro, Pedro Fluxà, Katherine Freese, Josef C. Frisch, Andrei Frolov, George Fuller, Brittany Fuzia, Nicholas Galitzki, Patricio A. Gallardo, Jose Tomas Galvez Ghersi, Jiansong Gao, Eric Gawiser, Martina Gerbino, Vera Gluscevic, Neil Goeckner-Wald, Joseph Golec, Sam Gordon, Megan Gralla, Daniel Green, Arpi Grigorian, John Groh, Chris Groppi, Yilun Guan, Jon E. Gudmundsson, Dongwon Han, Peter Hargrave, Masaya Hasegawa, Matthew Hasselfield, Makoto Hattori, Victor Haynes, Masashi Hazumi, Yizhou He, Erin Healy, Shawn W. Henderson, Carlos Hervias-Caimapo, Charles A. Hill, J. Colin Hill, Gene Hilton, Matt Hilton, Adam D. Hincks, Gary Hinshaw, Renée Hložek, Shirley Ho, Shuay-Pwu Patty Ho, Logan Howe, Zhiqi Huang, Johannes Hubmayr, Kevin Huffenberger, John P. Hughes, Anna Ijjas, Margaret Ikape, Kent Irwin, Andrew H. Jaffe, Bhuvnesh Jain, Oliver Jeong, Daisuke Kaneko, Ethan D. Karpel, Nobuhiko Katayama, Brian Keating, Sarah S. Kernasovskiy, Reijo Keskitalo, Theodore Kisner, Kenji Kiuchi, Jeff Klein, Kenda Knowles, Brian Koopman, Arthur Kosowsky, Nicoletta Krachmalnicoff, Stephen E. Kuenstner, Chao-Lin Kuo, Akito Kusaka, Jacob Lashner, Adrian Lee, Eunseong Lee, David Leon, Jason S. Y. Leung, Antony Lewis, Yaqiong Li, Zack Li, Michele Limon, Eric Linder, Carlos Lopez-Caraballo, Thibaut Louis, Lindsay Lowry, Marius Lungu, Mathew Madhavacheril, Daisy Mak, Felipe Maldonado, Hamdi Mani, Ben Mates, Frederick Matsuda, Loïc Maurin, Phil Mauskopf, Andrew May, Nialh McCallum, Chris McKenney, Jeff McMahon, P. Daniel Meerburg, Joel Meyers, Amber Miller, Mark Mirmelstein, Kavilan Moodley, Moritz Munchmeyer, Charles Munson, Sigurd Naess, Federico Nati, Martin Navaroli, Laura Newburgh, Ho Nam Nguyen, Michael Niemack, Haruki Nishino, John Orlowski-Scherer, Lyman Page, Bruce Partridge, Julien Peloton, Francesca Perrotta, Lucio Piccirillo, Giampaolo Pisano, Davide Poletti, Roberto Puddu, Giuseppe Puglisi, Chris Raum, Christian L. Reichardt, Mathieu Remazeilles, Yoel Rephaeli, Dominik Riechers, Felipe Rojas, Anirban Roy, Sharon Sadeh, Yuki Sakurai, Maria Salatino, Mayuri Sathyanarayana Rao, Emmanuel Schaan, Marcel Schmittfull, Neelima Sehgal, Joseph Seibert, Uros Seljak, Blake Sherwin, Meir Shimon, Carlos Sierra, Jonathan Sievers, Precious Sikhosana, Maximiliano Silva-Feaver, Sara M. Simon, Adrian Sinclair, Praween Siritanasak, Kendrick Smith, Stephen R. Smith, David Spergel, Suzanne T. Staggs, George Stein, Jason R. Stevens, Radek Stompor, Aritoki Suzuki, Osamu Tajima, Satoru Takakura, Grant Teply, Daniel B. Thomas, Ben Thorne, Robert Thornton, Hy Trac, Calvin Tsai, Carole Tucker, Joel Ullom, Sunny Vagnozzi, Alexander van Engelen, Jeff Van Lanen, Daniel D. Van Winkle, Eve M. Vavagiakis,

Clara Vergès, Michael Vissers, Kasey Wagoner, Samantha Walker, Jon Ward, Ben Westbrook, Nathan Whitehorn, Jason Williams, Joel Williams, Edward J. Wollack, Zhilei Xu, Byeonghee Yu, Cyndia Yu, Fernando Zago, Hezi Zhang, Ningfeng Zhu, and The Simons Observatory collaboration. The Simons Observatory: science goals and forecasts. , 2019(2):056, Feb 2019.

[5] P. A. R. Ade, Z. Ahmed, R. W. Aikin, K. D. Alexander, D. Barkats, S. J. Benton, C. A. Bischoff, J. J. Bock, R. Bowens-Rubin, J. A. Brevik, I. Buder, E. Bullock, V. Buza, J. Connors, J. Cornelison, B. P. Crill, M. Crumrine, M. Dierickx, L. Duband, C. Dvorkin, J. P. Filippini, S. Fliescher, J. Grayson, G. Hall, M. Halpern, S. Harrison, S. R. Hildebrandt, G. C. Hilton, H. Hui, K. D. Irwin, J. Kang, K. S. Karkare, E. Karpel, J. P. Kaufman, B. G. Keating, S. Kefeli, S. A. Kernasovskiy, J. M. Kovac, C. L. Kuo, N. A. Larsen, K. Lau, E. M. Leitch, M. Lueker, K. G. Megerian, L. Moncelsi, T. Namikawa, C. B. Netterfield, H. T. Nguyen, R. O'Brient, R. W. Ogburn, S. Palladino, C. Pryke, B. Racine, S. Richter, A. Schillaci, R. Schwarz, C. D. Sheehy, A. Soliman, T. St. Germaine, Z. K. Staniszewski, B. Steinbach, R. V. Sudiwala, G. P. Teply, K. L. Thompson, J. E. Tolan, C. Tucker, A. D. Turner, C. Umiltà, A. G. Vieregg, A. Wandui, A. C. Weber, D. V. Wiebe, J. Willmert, C. L. Wong, W. L. K. Wu, H. Yang, K. W. Yoon, and C. Zhang. Constraints on primordial gravitational waves using *planck*, wmap, and new bicep2/*keck* observations through the 2015 season. Phys. Rev. Lett., 121:221301, Nov 2018.

[6] P. A. R. Ade, G. Pisano, C. Tucker, and S. Weaver. A review of metal mesh filters. In , volume 6275, page 62750U, Jun 2006.

[7] Peter Ade, James Aguirre, Zeeshan Ahmed, Simone Aiola, Aamir Ali, David Alonso, Marcelo A. Alvarez, Kam Arnold, Peter Ashton, Jason Austermann, Humna Awan, Carlo Baccigalupi, Taylor Baildon, Darcy Barron, Nick Battaglia, Richard Battye, Eric Baxter, Andrew Bazarko, James A. Beall, Rachel Bean, Dominic Beck, Shawn Beckman, Benjamin Beringue, Federico Bianchini, Steven Boada, David Boettger, J. Richard Bond, Julian Borrill, Michael L. Brown, Sarah Marie Bruno, Sean Bryan, Erminia Calabrese, Victoria Calafut, Paolo Calisse, Julien Carron, Anthony Challinor, Grace Chesmore, Yuji Chinone, Jens Chluba, Hsiao-Mei Sherry Cho, Steve Choi, Gabriele Coppi, Nicholas F. Cothard, Kevin Coughlin, Devin Crichton, Kevin D. Crowley, Kevin T. Crowley, Ari Cukierman, John M. D'Ewart, Rolando Dünner, Tijmen de Haan, Mark Devlin, Simon Dicker, Joy Didier, Matt Dobbs, Bradley Dober, Cody J. Duell, Shannon Duff, Adri Duivenvoorden, Jo Dunkley, John Dusatko, Josquin Errard, Giulio Fabbian, Stephen Feeney, Simone Ferraro, Pedro Fluxà, Katherine Freese, Josef C. Frisch, Andrei Frolov, George Fuller, Brittany Fuzia, Nicholas Galitzki, Patricio A. Gallardo, Jose Tomas Galvez Ghersi, Jiansong Gao, Eric Gawiser, Martina Gerbino, Vera Gluscevic, Neil Goeckner-Wald, Joseph Golec, Sam Gordon, Megan Gralla, Daniel Green, Arpi Grigorian, John Groh, Chris Groppi, Yilun Guan, Jon E. Gudmundsson, Dongwon Han, Peter Hargrave, Masaya Hasegawa, Matthew Hasselfield, Makoto Hattori, Victor Haynes, Masashi Hazumi, Yizhou He, Erin Healy, Shawn W. Henderson, Carlos Hervias-Caimapo, Charles A. Hill, J. Colin Hill, Gene Hilton, Matt Hilton, Adam D. Hincks, Gary Hinshaw, Renée Hložek, Shirley Ho, Shuay-Pwu Patty Ho, Logan Howe, Zhiqi Huang, Johannes Hubmayr, Kevin Huffenberger, John P. Hughes, Anna Ijjas, Margaret Ikape, Kent Irwin, Andrew H. Jaffe, Bhuvnesh Jain, Oliver Jeong, Daisuke Kaneko, Ethan D. Karpel, Nobuhiko Katayama, Brian Keating, Sarah S. Kernasovskiy, Reijo Keskitalo, Theodore Kisner, Kenji Kiuchi, Jeff Klein, Kenda Knowles, Brian Koopman, Arthur Kosowsky, Nicoletta Krachmalnicoff, Stephen E. Kuenstner, Chao-Lin Kuo, Akito Kusaka, Jacob Lashner, Adrian Lee, Eunseong Lee, David Leon, Jason S. Y. Leung, Antony Lewis, Yaqiong Li, Zack Li, Michele Limon, Eric Linder, Carlos Lopez-Caraballo, Thibaut Louis, Lindsay Lowry, Marius Lungu, Mathew Madhavacheril, Daisy Mak, Felipe Maldonado, Hamdi Mani, Ben Mates, Freder-

ick Matsuda, Loïc Maurin, Phil Mauskopf, Andrew May, Nialh McCallum, Chris McKenney, Jeff McMahon, P. Daniel Meerburg, Joel Meyers, Amber Miller, Mark Mirmelstein, Kavilan Moodley, Moritz Munchmeyer, Charles Munson, Sigurd Naess, Federico Nati, Martin Navaroli, Laura Newburgh, Ho Nam Nguyen, Michael Niemack, Haruki Nishino, John Orlowski-Scherer, Lyman Page, Bruce Partridge, Julien Peloton, Francesca Perrotta, Lucio Piccirillo, Giampaolo Pisano, Davide Poletti, Roberto Puddu, Giuseppe Puglisi, Chris Raum, Christian L. Reichardt, Mathieu Remazeilles, Yoel Rephaeli, Dominik Riechers, Felipe Rojas, Anirban Roy, Sharon Sadeh, Yuki Sakurai, Maria Salatino, Mayuri Sathyanarayana Rao, Emmanuel Schaan, Marcel Schmittfull, Neelima Sehgal, Joseph Seibert, Uros Seljak, Blake Sherwin, Meir Shimon, Carlos Sierra, Jonathan Sievers, Precious Sikhosana, Maximiliano Silva-Feaver, Sara M. Simon, Adrian Sinclair, Praween Siritanasak, Kendrick Smith, Stephen R. Smith, David Spergel, Suzanne T. Staggs, George Stein, Jason R. Stevens, Radek Stompor, Aritoki Suzuki, Osamu Tajima, Satoru Takakura, Grant Teply, Daniel B. Thomas, Ben Thorne, Robert Thornton, Hy Trac, Calvin Tsai, Carole Tucker, Joel Ullom, Sunny Vagnozzi, Alexander van Engelen, Jeff Van Lanen, Daniel D. Van Winkle, Eve M. Vavagiakis, Clara Vergès, Michael Vissers, Kasey Wagoner, Samantha Walker, Jon Ward, Ben Westbrook, Nathan Whitehorn, Jason Williams, Joel Williams, Edward J. Wollack, Zhilei Xu, Byeonghee Yu, Cyndia Yu, Fernando Zago, Hezi Zhang, Ningfeng Zhu, and Simons Observatory Collaboration. The Simons Observatory: science goals and forecasts. , 2019(2):056, February 2019.

[8] Steven W. Allen, August E. Evrard, and Adam B. Mantz. Cosmological Parameters from Observations of Galaxy Clusters. , 49(1):409–470, September 2011.

[9] A. J. Anderson, P. A. R. Ade, Z. Ahmed, J. E. Austermann, J. S. Avva, P. S. Barry, R. Basu Thakur, A. N. Bender, B. A. Benson, L. E. Bleem, K. Byrum, J. E. Carlstrom, F. W. Carter, T. Cecil, C. L. Chang, H. M. Cho, J. F. Cliche, T. M. Crawford, A. Cukierman, E. V. Denison, T. de Haan, J. Ding, M. A. Dobbs, D. Dutcher, W. Everett, A. Foster, R. N. Gannon, A. Gilbert, J. C. Groh, N. W. Halverson, A. H. Harke-Hosemann, N. L. Harrington, J. W. Henning, G. C. Hilton, G. P. Holder, W. L. Holzapfel, N. Huang, K. D. Irwin, O. B. Jeong, M. Jonas, T. Khaire, L. Knox, A. M. Kofman, M. Korman, D. Kubik, S. Kuhlmann, N. Kuklev, C. L. Kuo, A. T. Lee, E. M. Leitch, A. E. Lowitz, S. S. Meyer, D. Michalik, J. Montgomery, A. Nadolski, T. Natoli, H. Nguyen, G. I. Noble, V. Novosad, S. Padin, Z. Pan, J. Pearson, C. M. Posada, A. Rahlin, C. L. Reichardt, J. E. Ruhl, L. J. Saunders, J. T. Sayre, I. Shirley, E. Shirokoff, G. Smecher, J. A. Sobrin, A. A. Stark, K. T. Story, A. Suzuki, Q. Y. Tang, K. L. Thompson, C. Tucker, L. R. Vale, K. Vanderlinde, J. D. Vieira, G. Wang, N. Whitehorn, V. Yefremenko, K. W. Yoon, and M. R. Young. SPT-3G: A Multichroic Receiver for the South Pole Telescope. Journal of Low Temperature Physics, 193(5-6):1057–1065, Dec 2018.

[10] A. J. Anderson, P. Barry, A. N. Bender, B. A. Benson, L. E. Bleem, J. E. Carlstrom, T. W. Cecil, C. L. Chang, T. M. Crawford, K. R. Dibert, M. A. Dobbs, K. Fichman, N. W. Halverson, W. L. Holzapfel, A. Hryciuk, K. S. Karkare, J. Li, M. Lisovenko, D. Marrone, J. McMahon, J. Montgomery, T. Natoli, Z. Pan, S. Raghunathan, C. L. Reichardt, M. Rouble, E. Shirokoff, G. Smecher, A. A. Stark, J. D. Vieira, and M. R. Young. SPT-3G+: mapping the high-frequency cosmic microwave background using kinetic inductance detectors. In Jonas Zmuidzinas and Jian-Rong Gao, editors, Millimeter, Submillimeter, and Far-Infrared Detectors and Instrumentation for Astronomy XI, volume 12190 of Society of Photo-Optical Instrumentation Engineers (SPIE) Conference Series, page 1219003, August 2022.

[11] Anthony J. Annunziata, Daniel F. Santavicca, Luigi Frunzio, Gianluigi Catelani, Michael J. Rooks, Aviad Frydman, and Daniel E. Prober. Tunable superconducting nanoinductors. Nanotechnology, 21(44):445202, November 2010.

[12] K. Arnold, P. A. R. Ade, A. E. Anthony, D. Barron, D. Boettger, J. Borrill, S. Chapman, Y. Chinone, M. A. Dobbs, J. Errard, G. Fabbian, D. Flanigan, G. Fuller, A. Ghribi, W. Grainger, N. Halverson, M. Hasegawa, K. Hattori, M. Hazumi, W. L. Holzapfel, J. Howard, P. Hyland, A. Jaffe, B. Keating, Z. Kermish, T. Kisner, M. Le Jeune, A. T. Lee, E. Linder, M. Lungu, F. Matsuda, T. Matsumura, N. J. Miller, X. Meng, H. Morii, S. Moyerman, M. J. Myers, H. Nishino, H. Paar, E. Quealy, C. Reichardt, P. L. Richards, C. Ross, A. Shimizu, C. Shimmin, M. Shimon, M. Sholl, P. Siritanasak, H. Spieler, N. Stebor, B. Steinbach, R. Stompor, A. Suzuki, T. Tomaru, C. Tucker, and O. Zahn. The bolometric focal plane array of the POLARBEAR CMB experiment. In Wayne S. Holland and Jonas Zmuidzinas, editors, Millimeter, Submillimeter, and Far-Infrared Detectors and Instrumentation for Astronomy VI, volume 8452 of Society of Photo-Optical Instrumentation Engineers (SPIE) Conference Series, page 84521D, September 2012.

[13] J. E. Austermann, K. A. Aird, J. A. Beall, D. Becker, A. Bender, B. A. Benson, L. E. Bleem, J. Britton, J. E. Carlstrom, C. L. Chang, H. C. Chiang, H. M. Cho, T. M. Crawford, A. T. Crites, A. Datesman, T. de Haan, M. A. Dobbs, E. M. George, N. W. Halverson, N. Harrington, J. W. Henning, G. C. Hilton, G. P. Holder, W. L. Holzapfel, S. Hoover, N. Huang, J. Hubmayr, K. D. Irwin, R. Keisler, J. Kennedy, L. Knox, A. T. Lee, E. Leitch, D. Li, M. Lueker, D. P. Marrone, J. J. McMahon, J. Mehl, S. S. Meyer, T. E. Montroy, T. Natoli, J. P. Nibarger, M. D. Niemack, V. Novosad, S. Padin, C. Pryke, C. L. Reichardt, J. E. Ruhl, B. R. Saliwanchik, J. T. Sayre, K. K. Schaffer, E. Shirokoff, A. A. Stark, K. Story, K. Vanderlinde, J. D. Vieira, G. Wang, R. Williamson, V. Yefremenko, K. W. Yoon, and O. Zahn. SPTpol: an instrument for CMB polarization measurements with the South Pole Telescope. In Wayne S. Holland and Jonas Zmuidzinas, editors, Millimeter, Submillimeter, and Far-Infrared Detectors and Instrumentation for Astronomy VI, volume 8452 of Society of Photo-Optical Instrumentation Engineers (SPIE) Conference Series, page 84521E, September 2012.

[14] J. E. Austermann, J. A. Beall, S. A. Bryan, B. Dober, J. Gao, G. Hilton, J. Hubmayr, P. Mauskopf, C. M. McKenney, S. M. Simon, J. N. Ullom, M. R. Vissers, and G. W. Wilson. Millimeter-Wave Polarimeters Using Kinetic Inductance Detectors for TolTEC and Beyond. Journal of Low Temperature Physics, 193(3-4):120–127, November 2018.

[15] Simon Bandler, Eric Silver, Herbert Schnopper, Stephen Murray, Marco Barbera, Norm Madden, Don Landis, Jeff Beeman, Eugene Haller, and Greg Tucker. Ntd-ge-based microcalorimeter performance. Nuclear Instruments and Methods in Physics Research Section A: Accelerators, Spectrometers, Detectors and Associated Equipment, 444(1):273–277, 2000.

[16] J. Bardeen, L. N. Cooper, and J. R. Schrieffer. Theory of superconductivity. Phys. Rev., 108:1175–1204, Dec 1957.

[17] R. Barends, J. J. A. Baselmans, S. J. C. Yates, J. R. Gao, J. N. Hovenier, and T. M. Klapwijk. Quasiparticle Relaxation in Optically Excited High-Q Superconducting Resonators. , 100(25):257002, June 2008.

[18] R. Barends, H. L. Hortensius, T. Zijlstra, J. J. A. Baselmans, S. J. C. Yates, J. R. Gao, and T. M. Klapwijk. Noise in nbtin, al, and ta superconducting resonators on silicon and sapphire substrates. IEEE Transactions on Applied Superconductivity, 19(3):936–939, 2009.

[19] R. Barends, N. Vercruyssen, A. Endo, P. J. de Visser, T. Zijlstra, T. M. Klapwijk, and J. J. A. Baselmans. Reduced frequency noise in superconducting resonators. Applied Physics Letters, 97(3):033507, July 2010.

[20] E. M. Barrentine, K. Rostem, R. P. Brekosky, A. D. Brown, F. A. Colazo, N. P. Costen, J. P. Hays-Wehle, W. T. Hsieh, V. Kluengpho, A. S. Kutyrev, S. F. Maher, V. Mikula, T. M. Miller, J. B. Oxborrow, E. H. Sharp, T. Watanabe, E. J. Wollack, and S. H. Moseley. Characterization of Si Membrane TES Bolometer Arrays for the HIRMES Instrument. Journal of Low Temperature Physics, 193(3-4):241–248, November 2018.

[21] P. Barry, A. Anderson, B. Benson, J. Carlstrom, T. Cecil, Chihway Chang, M. Dobbs, M. Hollister, K. Karkare, G. Keating, D. Marrone, J. McMahon, Jeannine Montgomery, Zeye Pan, G. Robson, M. Rouble, E. Shirokoff, and G. Smecher. Design of the spt-slim focal plane: A spectroscopic imaging array for the south pole telescope. Journal of Low Temperature Physics, 209:1–10, 09 2022.

[22] Peter S. Barry. On the Development of SuperSpec; A Fully Integrated On-Chip Spectrometer for Far-Infrared Astronomy. PhD thesis, Cardiff University, 2014.

[23] J. J. A. Baselmans, J. Bueno, S. J. C. Yates, O. Yurduseven, N. Llombart, K. Karatsu, A. M. Baryshev, L. Ferrari, A. Endo, D. J. Thoen, P. J. de Visser, R. M. J. Janssen, V. Murugesan, E. F. C. Driessen, G. Coiffard, J. Martin-Pintado, P. Hargrave, and M. Griffin. A kilo-pixel imaging system for future space based far-infrared observatories using microwave kinetic inductance detectors. , 601:A89, May 2017.

[24] J. J. A. Baselmans, F. Facchin, A. Pascual Laguna, J. Bueno, D. J. Thoen, V. Murugesan, N. Llombart, and P. J. de Visser. Ultra-sensitive THz microwave kinetic inductance detectors for future space telescopes. , 665:A17, September 2022.

[25] D. A. Bennett, R. D. Horansky, D. R. Schmidt, A. S. Hoover, R. Winkler, B. K. Alpert, J. A. Beall, W. B. Doriese, J. W. Fowler, C. P. Fitzgerald, G. C. Hilton, K. D. Irwin, V. Kotsubo, J. A. B. Mates, G. C. O'Neil, M. W. Rabin, C. D. Reintsema, F. J. Schima, D. S. Swetz, L. R. Vale, and J. N. Ullom. A high resolution gamma-ray spectrometer based on superconducting microcalorimeters. Review of Scientific Instruments, 83(9):093113, 2012.

[26] A. S. Bergman, P. A. R. Ade, S. Akers, M. Amiri, J. A. Austermann, J. A. Beall, D. T. Becker, S. J. Benton, J. J. Bock, J. R. Bond, S. A. Bryan, H. C. Chiang, C. R. Contaldi, R. S. Domagalski, O. Doré, S. M. Duff, A. J. Duivenvoorden, H. K. Eriksen, M. Farhang, J. P. Filippini, L. M. Fissel, A. A. Fraisse, K. Freese, M. Galloway, A. E. Gambrel, N. N. Gandilo, K. Ganga, A. Grigorian, R. Gualtieri, J. E. Gudmundsson, M. Halpern, J. Hartley, M. Hasselfield, G. Hilton, W. Holmes, V. V. Hristov, Z. Huang, J. Hubmayr, K. D. Irwin, W. C. Jones, A. Khan, C. L. Kuo, Z. D. Kermish, S. Li, P. V. Mason, K. Megerian, L. Moncelsi, T. A. Morford, J. M. Nagy, C. B. Netterfield, M. Nolta, B. Osherson, I. L. Padilla, B. Racine, A. S. Rahlin, S. Redmond, C. Reintsema, L. J. Romualdez, J. E. Ruhl, M. C. Runyan, T. M. Ruud, J. A. Shariff, E. C. Shaw, C. Shiu, J. D. Soler, X. Song, A. Trangsrud, C. Tucker, R. S. Tucker, A. D. Turner, J. Ullom, J. F. van der List, J. Van Lanen, M. R. Vissers, A. C. Weber, I. K. Wehus, S. Wen, D. V. Wiebe, and E. Y. Young. 280 GHz Focal Plane Unit Design and Characterization for the Spider-2 Suborbital Polarimeter. Journal of Low Temperature Physics, 193(5-6):1075–1084, December 2018.

[27] BICEP2 and Keck Array Collaborations, P. A. R. Ade, R. W. Aikin, D. Barkats, S. J. Benton, C. A. Bischoff, J. J. Bock, K. J. Bradford, J. A. Brevik, I. Buder, E. Bullock, C. D. Dowell, L. Duband, J. P. Filippini, S. Fliescher, S. R. Golwala, M. Halpern, M. Hasselfield, S. R. Hildebrandt, G. C. Hilton, H. Hui, K. D. Irwin, J. H. Kang, K. S. Karkare, J. P. Kaufman, B. G. Keating, S. Kefeli, S. A. Kernasovskiy, J. M. Kovac, C. L. Kuo, E. M. Leitch, M. Lueker, K. G. Megerian, C. B. Netterfield, H. T. Nguyen, R. O'Brient, IV Ogburn, R. W., A. Orlando, C. Pryke, S. Richter, R. Schwarz,

C. D. Sheehy, Z. K. Staniszewski, R. V. Sudiwala, G. P. Teply, K. Thompson, J. E. Tolan, A. D. Turner, A. G. Vieregg, A. C. Weber, C. L. Wong, and K. W. Yoon. BICEP2/Keck Array. IV. Optical Characterization and Performance of the BICEP2 and Keck Array Experiments. , 806(2):206, June 2015.

[28] BICEP2 Collaboration, Keck Array Collaboration, P. A. R. Ade, Z. Ahmed, R. W. Aikin, K. D. Alexander, D. Barkats, S. J. Benton, C. A. Bischoff, J. J. Bock, R. Bowens-Rubin, J. A. Brevik, I. Buder, E. Bullock, V. Buza, J. Connors, B. P. Crill, L. Duband, C. Dvorkin, J. P. Filippini, S. Fliescher, J. Grayson, M. Halpern, S. Harrison, G. C. Hilton, H. Hui, K. D. Irwin, K. S. Karkare, E. Karpel, J. P. Kaufman, B. G. Keating, S. Kefeli, S. A. Kernasovskiy, J. M. Kovac, C. L. Kuo, E. M. Leitch, M. Lueker, K. G. Megerian, C. B. Netterfield, H. T. Nguyen, R. O'Brient, R. W. Ogburn, A. Orlando, C. Pryke, S. Richter, R. Schwarz, C. D. Sheehy, Z. K. Staniszewski, B. Steinbach, R. V. Sudiwala, G. P. Teply, K. L. Thompson, J. E. Tolan, C. Tucker, A. D. Turner, A. G. Vieregg, A. C. Weber, D. V. Wiebe, J. Willmert, C. L. Wong, W. L. K. Wu, and K. W. Yoon. Improved Constraints on Cosmology and Foregrounds from BICEP2 and Keck Array Cosmic Microwave Background Data with Inclusion of 95 GHz Band. , 116(3):031302, January 2016.

[29] BICEP2 Collaboration, Keck Array Collaboration, SPIDER Collaboration, P. A. R. Ade, R. W. Aikin, M. Amiri, D. Barkats, S. J. Benton, C. A. Bischoff, J. J. Bock, J. A. Bonetti, J. A. Brevik, I. Buder, E. Bullock, G. Chattopadhyay, G. Davis, P. K. Day, C. D. Dowell, L. Duband, J. P. Filippini, S. Fliescher, S. R. Golwala, M. Halpern, M. Hasselfield, S. R. Hildebrandt, G. C. Hilton, V. Hristov, H. Hui, K. D. Irwin, W. C. Jones, K. S. Karkare, J. P. Kaufman, B. G. Keating, S. Kefeli, S. A. Kernasovskiy, J. M. Kovac, C. L. Kuo, H. G. LeDuc, E. M. Leitch, N. Llombart, M. Lueker, P. Mason, K. Megerian, L. Moncelsi, C. B. Netterfield, H. T. Nguyen, R. O'Brient, IV Ogburn, R. W., A. Orlando, C. Pryke, A. S. Rahlin, C. D. Reintsema, S. Richter, M. C. Runyan, R. Schwarz, C. D. Sheehy, Z. K. Staniszewski, R. V. Sudiwala, G. P. Teply, J. E. Tolan, A. Trangsrud, R. S. Tucker, A. D. Turner, A. G. Vieregg, A. Weber, D. V. Wiebe, P. Wilson, C. L. Wong, K. W. Yoon, and J. Zmuidzinas. Antenna-coupled TES Bolometers Used in BICEP2, Keck Array, and Spider. , 812(2):176, October 2015.

[30] Mark Birkinshaw. The sunyaev–zel'dovich effect. Physics Reports, 310(2):97–195, 1999.

[31] L. E. Bleem, S. Bocquet, B. Stalder, M. D. Gladders, P. A. R. Ade, S. W. Allen, A. J. Anderson, J. Annis, M. L. N. Ashby, J. E. Austermann, S. Avila, J. S. Avva, M. Bayliss, J. A. Beall, K. Bechtol, A. N. Bender, B. A. Benson, E. Bertin, F. Bianchini, C. Blake, M. Brodwin, D. Brooks, E. Buckley-Geer, D. L. Burke, J. E. Carlstrom, A. Carnero Rosell, M. Carrasco Kind, J. Carretero, C. L. Chang, H. C. Chiang, R. Citron, C. Corbett Moran, M. Costanzi, T. M. Crawford, A. T. Crites, L. N. da Costa, T. de Haan, J. De Vicente, S. Desai, H. T. Diehl, J. P. Dietrich, M. A. Dobbs, T. F. Eifler, W. Everett, B. Flaugher, B. Floyd, J. Frieman, J. Gallicchio, J. García-Bellido, E. M. George, D. W. Gerdes, A. Gilbert, D. Gruen, R. A. Gruendl, J. Gschwend, N. Gupta, G. Gutierrez, N. W. Halverson, N. Harrington, J. W. Henning, C. Heymans, G. P. Holder, D. L. Hollowood, W. L. Holzapfel, K. Honscheid, J. D. Hrubes, N. Huang, J. Hubmayr, K. D. Irwin, D. J. James, T. Jeltema, S. Joudaki, G. Khullar, M. Klein, L. Knox, N. Kuropatkin, A. T. Lee, D. Li, C. Lidman, A. Lowitz, N. MacCrann, G. Mahler, M. A. G. Maia, J. L. Marshall, M. McDonald, J. J. McMahon, P. Melchior, F. Menanteau, S. S. Meyer, R. Miquel, L. M. Mocanu, J. J. Mohr, J. Montgomery, A. Nadolski, T. Natoli, J. P. Nibarger, G. Noble, V. Novosad, S. Padin, A. Palmese, D. Parkinson, S. Patil, F. Paz-Chinchón, A. A. Plazas, C. Pryke, N. S. Ramachandra, C. L. Reichardt, J. D. Remolina González, A. K. Romer, A. Roodman, J. E. Ruhl, E. S. Rykoff, B. R. Saliwanchik, E. Sanchez, A. Saro, J. T. Sayre, K. K. Schaffer,

T. Schrabback, S. Serrano, K. Sharon, C. Sievers, G. Smecher, M. Smith, M. Soares-Santos, A. A. Stark, K. T. Story, E. Suchyta, G. Tarle, C. Tucker, K. Vanderlinde, T. Veach, J. D. Vieira, G. Wang, J. Weller, N. Whitehorn, W. L. K. Wu, V. Yefremenko, and Y. Zhang. The SPTpol Extended Cluster Survey. , 247(1):25, March 2020.

[32] L. E. Bleem, B. Stalder, T. de Haan, K. A. Aird, S. W. Allen, D. E. Applegate, M. L. N. Ashby, M. Bautz, M. Bayliss, B. A. Benson, S. Bocquet, M. Brodwin, J. E. Carlstrom, C. L. Chang, I. Chiu, H. M. Cho, A. Clocchiatti, T. M. Crawford, A. T. Crites, S. Desai, J. P. Dietrich, M. A. Dobbs, R. J. Foley, W. R. Forman, E. M. George, M. D. Gladders, A. H. Gonzalez, N. W. Halverson, C. Hennig, H. Hoekstra, G. P. Holder, W. L. Holzapfel, J. D. Hrubes, C. Jones, R. Keisler, L. Knox, A. T. Lee, E. M. Leitch, J. Liu, M. Lueker, D. Luong-Van, A. Mantz, D. P. Marrone, M. McDonald, J. J. McMahon, S. S. Meyer, L. Mocanu, J. J. Mohr, S. S. Murray, S. Padin, C. Pryke, C. L. Reichardt, A. Rest, J. Ruel, J. E. Ruhl, B. R. Saliwanchik, A. Saro, J. T. Sayre, K. K. Schaffer, T. Schrabback, E. Shirokoff, J. Song, H. G. Spieler, S. A. Stanford, Z. Staniszewski, A. A. Stark, K. T. Story, C. W. Stubbs, K. Vanderlinde, J. D. Vieira, A. Vikhlinin, R. Williamson, O. Zahn, and A. Zenteno. Galaxy Clusters Discovered via the Sunyaev-Zel'dovich Effect in the 2500-Square-Degree SPT-SZ Survey. , 216(2):27, February 2015.

[33] Sean A. Bryan, Jason E. Austermann, Philip Mauskopf, Giles Novak, Sara M. Simon, Grant W. Wilson, Jeff McMahon, Daniel Ferrusca, Alfredo Montana, and David Sanchez-Arguelles. Optical design of the TolTEC millimeter-wave camera. In Jonas Zmuidzinas and Jian-Rong Gao, editors, Millimeter, Submillimeter, and Far-Infrared Detectors and Instrumentation for Astronomy IX. SPIE, jul 2018.

[34] Philip Bull, Yashar Akrami, Julian Adamek, Tessa Baker, Emilio Bellini, Jose Beltrán Jiménez, Eloisa Bentivegna, Stefano Camera, Sébastien Clesse, Jonathan H. Davis, Enea Di Dio, Jonas Enander, Alan Heavens, Lavinia Heisenberg, Bin Hu, Claudio Llinares, Roy Maartens, Edvard Mörtsell, Seshadri Nadathur, Johannes Noller, Roman Pasechnik, Marcel S. Pawlowski, Thiago S. Pereira, Miguel Quartin, Angelo Ricciardone, Signe Riemer-Sørensen, Massimiliano Rinaldi, Jeremy Sakstein, Ippocratis D. Saltas, Vincenzo Salzano, Ignacy Sawicki, Adam R. Solomon, Douglas Spolyar, Glenn D. Starkman, Danièle Steer, Ismael Tereno, Licia Verde, Francisco Villaescusa-Navarro, Mikael von Strauss, and Hans A. Winther. Beyond Λ CDM: Problems, solutions, and the road ahead. Physics of the Dark Universe, 12:56–99, June 2016.

[35] CCAT-Prime Collaboration, Manuel Aravena, Jason E. Austermann, Kaustuv Basu, Nicholas Battaglia, Benjamin Beringue, Frank Bertoldi, Frank Bigiel, J. Richard Bond, Patrick C. Breysse, Colton Broughton, Ricardo Bustos, Scott C. Chapman, Maude Charmetant, Steve K. Choi, Dongwoo T. Chung, Susan E. Clark, Nicholas F. Cothard, Abigail T. Crites, Ankur Dev, Kaela Douglas, Cody J. Duell, Rolando Dünner, Haruki Ebina, Jens Erler, Michel Fich, Laura M. Fissel, Simon Foreman, R. G. Freundt, Patricio A. Gallardo, Jiansong Gao, Pablo García, Riccardo Giovanelli, Joseph E. Golec, Christopher E. Groppi, Martha P. Haynes, Douglas Henke, Brandon Hensley, Terry Herter, Ronan Higgins, Renée Hložek, Anthony Huber, Zachary Huber, Johannes Hubmayr, Rebecca Jackson, Douglas Johnstone, Christos Karoumpis, Laura C. Keating, Eiichiro Komatsu, Yaqiong Li, Benjamin Magnelli, Brenda C. Matthews, Philip D. Mauskopf, Jeffrey J. McMahon, P. Daniel Meerburg, Joel Meyers, Vyoma Muralidhara, Norman W. Murray, Michael D. Niemack, Thomas Nikola, Yoko Okada, Roberto Puddu, Dominik A. Riechers, Erik Rosolowsky, Kayla Rossi, Kaja Rotermund, Anirban Roy, Sarah I. Sadavoy, Reinhold Schaaf, Peter Schilke, Douglas Scott, Robert Simon, Adrian K. Sinclair, Gregory R. Sivakoff, Gordon J. Stacey, Amelia M. Stutz, Juergen Stutzki,

Mehrnoosh Tahani, Karun Thanjavur, Ralf A. Timmermann, Joel N. Ullom, Alexander van Engelen, Eve M. Vavagiakis, Michael R. Vissers, Jordan D. Wheeler, Simon D. M. White, Yijie Zhu, and Bugao Zou. CCAT-prime Collaboration: Science Goals and Forecasts with Prime-Cam on the Fred Young Submillimeter Telescope. , 264(1):7, January 2023.

[36] Anthony Challinor. Cmb anisotropy science: a review. Proceedings of the International Astronomical Union, 8(S288):42–52, 2012.

[37] Jhy-Jiun Chang and D. J. Scalapino. Nonequilibrium superconductivity. Journal of Low Temperature Physics, 31(1-2):1–32, April 1978.

[38] S. K. Choi, J. Austermann, J. A. Beall, K. T. Crowley, R. Datta, S. M. Duff, P. A. Gallardo, S. P. Ho, J. Hubmayr, B. J. Koopman, Y. Li, F. Nati, M. D. Niemack, L. A. Page, M. Salatino, S. M. Simon, S. T. Staggs, J. Stevens, J. Ullom, and E. J. Wollack. Characterization of the Mid-Frequency Arrays for Advanced ACTPol. Journal of Low Temperature Physics, 193(3-4):267–275, Nov 2018.

[39] Steve K. Choi, Matthew Hasselfield, Shuay-Pwu Patty Ho, Brian Koopman, Marius Lungu, Maximilian H. Abitbol, Graeme E. Addison, Peter A. R. Ade, Simone Aiola, David Alonso, Mandana Amiri, Stefania Amodeo, Elio Angile, Jason E. Austermann, Taylor Baildon, Nick Battaglia, James A. Beall, Rachel Bean, Daniel T. Becker, J. Richard Bond, Sarah Marie Bruno, Erminia Calabrese, Victoria Calafut, Luis E. Campusano, Felipe Carrero, Grace E. Chesmore, Hsiao-mei Cho, Susan E. Clark, Nicholas F. Cothard, Devin Crichton, Kevin T. Crowley, Omar Darwish, Rahul Datta, Edward V. Denison, Mark J. Devlin, Cody J. Duell, Shannon M. Duff, Adriaan J. Duivenvoorden, Jo Dunkley, Rolando Dünner, Thomas Essinger-Hileman, Max Fankhanel, Simone Ferraro, Anna E. Fox, Brittany Fuzia, Patricio A. Gallardo, Vera Gluscevic, Joseph E. Golec, Emily Grace, Megan Gralla, Yilun Guan, Kirsten Hall, Mark Halpern, Dongwon Han, Peter Hargrave, Shawn Henderson, Brandon Hensley, J. Colin Hill, Gene C. Hilton, Matt Hilton, Adam D. Hincks, Renée Hložek, Johannes Hubmayr, Kevin M. Huffenberger, John P. Hughes, Leopoldo Infante, Kent Irwin, Rebecca Jackson, Jeff Klein, Kenda Knowles, Arthur Kosowsky, Vincent Lakey, Dale Li, Yaqiong Li, Zack Li, Martine Lokken, Thibaut Louis, Amanda MacInnis, Mathew Madhavacheril, Felipe Maldonado, Maya Mallaby-Kay, Danica Marsden, Loïc Maurin, Jeff McMahon, Felipe Menanteau, Kavilan Moodley, Tim Morton, Sigurd Naess, Toshiya Namikawa, Federico Nati, Laura Newburgh, John P. Nibarger, Andrina Nicola, Michael D. Niemack, Michael R. Nolta, John Orlowski-Sherer, Lyman A. Page, Christine G. Pappas, Bruce Partridge, Phumlani Phakathi, Heather Prince, Roberto Puddu, Frank J. Qu, Jesus Rivera, Naomi Robertson, Felipe Rojas, Maria Salatino, Emmanuel Schaan, Alessandro Schillaci, Benjamin L. Schmitt, Neelima Sehgal, Blake D. Sherwin, Carlos Sierra, Jon Sievers, Cristobal Sifon, Precious Sikhosana, Sara Simon, David N. Spergel, Suzanne T. Staggs, Jason Stevens, Emilie Storer, Dhaneshwar D. Sunder, Eric R. Switzer, Ben Thorne, Robert Thornton, Hy Trac, Jesse Treu, Carole Tucker, Leila R. Vale, Alexander Van Engelen, Jeff Van Lanen, Eve M. Vavagiakis, Kasey Wagoner, Yuhan Wang, Jonathan T. Ward, Edward J. Wollack, Zhilei Xu, Fernando Zago, and Ningfeng Zhu. The Atacama Cosmology Telescope: a measurement of the Cosmic Microwave Background power spectra at 98 and 150 GHz. , 2020(12):045, December 2020.

[40] D. T. Chuss, C. L. Bennett, N. Costen, E. Crowe, K. Denis, J. R. Eimer, N. Lourie, T. A. Marriage, S. H. Moseley, K. Rostem, T. R. Stevenson, D. Towner, K. U-Yen, G. Voellmer, E. J. Wollack, and L. Zeng. Electromagnetic Design of Feedhorn-Coupled Transition-Edge Sensors for Cosmic Microwave Background Polarimetry. Journal of Low Temperature Physics, 167(5-6):923–928, June 2012.

[41] The POLARBEAR Collaboration, P. A. R. Ade, M. Aguilar, Y. Akiba, K. Arnold, C. Baccigalupi, D. Barron, D. Beck, F. Bianchini, D. Boettger, J. Borrill, S. Chapman, Y. Chinone, K. Crowley, A. Cukierman, R. Dünner, M. Dobbs, A. Ducout, T. Elleflot, J. Errard, G. Fabbian, S. M. Feeney, C. Feng, T. Fujino, N. Galitzki, A. Gilbert, N. Goeckner-Wald, J. C. Groh, G. Hall, N. Halverson, T. Hamada, M. Hasegawa, M. Hazumi, C. A. Hill, L. Howe, Y. Inoue, G. Jaehnig, A. H. Jaffe, O. Jeong, D. Kaneko, N. Katayama, B. Keating, R. Keskitalo, T. Kisner, N. Krachmalnicoff, A. Kusaka, M. Le Jeune, A. T. Lee, E. M. Leitch, D. Leon, E. Linder, L. Lowry, F. Matsuda, T. Matsumura, Y. Minami, J. Montgomery, M. Navaroli, H. Nishino, H. Paar, J. Peloton, A. T. P. Pham, D. Poletti, G. Puglisi, C. L. Reichardt, P. L. Richards, C. Ross, Y. Segawa, B. D. Sherwin, M. Silva-Feaver, P. Siritanasak, N. Stebor, R. Stompor, A. Suzuki, O. Tajima, S. Takakura, S. Takatori, D. Tanabe, G. P. Teply, T. Tomaru, C. Tucker, N. Whitehorn, and A. Zahn. A measurement of the cosmic microwave background b-mode polarization power spectrum at subdegree scales from two years of polarbear data. The Astrophysical Journal, 848(2):121, oct 2017.

[42] Kevin T. Crowley, Jason E. Austermann, Steve K. Choi, Shannon M. Duff, Patricio A. Gallardo, Shuay-Pwu Patty Ho, Johannes Hubmayr, Brian J. Koopman, Federico Nati, Michael D. Niemack, Maria Salatino, Sara M. Simon, Suzanne T. Staggs, Jason R. Stevens, Joel N. Ullom, Eve M. Vavagiakis, and Edward J. Wollack. Advanced actpol tes device parameters and noise performance in fielded arrays. Journal of Low Temperature Physics, 193(3):328–336, November 2018.

[43] Kevin T. Crowley, Jason E. Austermann, Shannon M. Duff, Patricio A. Gallardo, Gene C. Hilton, Johannes Hubmayr, Sara M. Simon, Suzanne T. Staggs, Joel N. Ullom, and Edward J. Wollack. Electrothermal characterization of AlMn transition-edge sensor bolometers for advanced ACTPol. In Jonas Zmuidzinas and Jian-Rong Gao, editors, Millimeter, Submillimeter, and Far-Infrared Detectors and Instrumentation for Astronomy IX, volume 10708, pages 187 – 203. International Society for Optics and Photonics, SPIE, 2018.

[44] Richard H. Cyburt, Brian D. Fields, Keith A. Olive, and Tsung-Han Yeh. Big bang nucleosynthesis: Present status. Rev. Mod. Phys., 88:015004, Feb 2016.

[45] S. Dahal, M. Amiri, J. W. Appel, C. L. Bennett, L. Corbett, R. Datta, K. Denis, T. Essinger-Hileman, M. Halpern, K. Helson, G. Hilton, J. Hubmayr, B. Keller, T. Marriage, C. Nunez, M. Petroff, C. Reintsema, K. Rostem, K. U-Yen, and E. Wollack. The CLASS 150/220 GHz polarimeter array: Design, assembly, and characterization. Journal of Low Temperature Physics, 199(1-2):289–297, jan 2020.

[46] X. Dai, X. Liu, Q. He, Y. Chen, Z. Mai, Z. Shi, W. Guo, Y. Wang, L. F. Wei, M. R. Vissers, and J. Gao. New method for fitting complex resonance curve to study nonlinear superconducting resonators. Superconductor Science Technology, 36(1):015003, January 2023.

[47] R. Datta, J. Austermann, J. A. Beall, D. Becker, K. P. Coughlin, S. M. Duff, P. A. Gallardo, E. Grace, M. Hasselfield, S. W. Henderson, G. C. Hilton, S. P. Ho, J. Hubmayr, B. J. Koopman, J. V. Lanen, D. Li, J. McMahon, C. D. Munson, F. Nati, M. D. Niemack, L. Page, C. G. Pappas, M. Salatino, B. L. Schmitt, A. Schillaci, S. M. Simon, S. T. Staggs, J. R. Stevens, E. M. Vavagiakis, J. T. Ward, and E. J. Wollack. Design and Deployment of a Multichroic Polarimeter Array on the Atacama Cosmology Telescope. Journal of Low Temperature Physics, 184(3-4):568–575, August 2016.

[48] R. Datta, J. Hubmayr, C. Munson, J. Austermann, J. Beall, D. Becker, H. M. Cho, N. Halverson, G. Hilton, K. Irwin, D. Li, J. McMahon, L. Newburgh, J. Nibarger, M. Niemack, B. Schmitt, H. Smith,

S. Staggs, J. Van Lanen, and E. Wollack. Horn Coupled Multichroic Polarimeters for the Atacama Cosmology Telescope Polarization Experiment. Journal of Low Temperature Physics, 176(5-6):670–676, September 2014.

[49] Peter Day, Henry Leduc, Benjamin Mazin, Anastasios Vayonakis, and Jonas Zmuidzinas. A broadband superconducting detector suitable for use in large arrays. Nature, 425:817–21, 10 2003.

[50] T. de Haan, B. A. Benson, L. E. Bleem, S. W. Allen, D. E. Applegate, M. L. N. Ashby, M. Bautz, M. Bayliss, S. Bocquet, M. Brodwin, J. E. Carlstrom, C. L. Chang, I. Chiu, H. M. Cho, A. Clocchiatti, T. M. Crawford, A. T. Crites, S. Desai, J. P. Dietrich, M. A. Dobbs, A. N. Doucouliagos, R. J. Foley, W. R. Forman, G. P. Garmire, E. M. George, M. D. Gladders, A. H. Gonzalez, N. Gupta, N. W. Halverson, J. Hlavacek-Larrondo, H. Hoekstra, G. P. Holder, W. L. Holzapfel, Z. Hou, J. D. Hrubes, N. Huang, C. Jones, R. Keisler, L. Knox, A. T. Lee, E. M. Leitch, A. von der Linden, D. Luong-Van, A. Mantz, D. P. Marrone, M. McDonald, J. J. McMahon, S. S. Meyer, L. M. Mocanu, J. J. Mohr, S. S. Murray, S. Padin, C. Pryke, D. Rapetti, C. L. Reichardt, A. Rest, J. Ruel, J. E. Ruhl, B. R. Saliwanchik, A. Saro, J. T. Sayre, K. K. Schaffer, T. Schrabback, E. Shirokoff, J. Song, H. G. Spieler, B. Stalder, S. A. Stanford, Z. Staniszewski, A. A. Stark, K. T. Story, C. W. Stubbs, K. Vanderlinde, J. D. Vieira, A. Vikhlinin, R. Williamson, and A. Zenteno. Cosmological Constraints from Galaxy Clusters in the 2500 Square-degree SPT-SZ Survey. , 832(1):95, November 2016.

[51] P. J. de Visser, D. J. Goldie, P. Diener, S. Withington, J. J. A. Baselmans, and T. M. Klapwijk. Evidence of a Nonequilibrium Distribution of Quasiparticles in the Microwave Response of a Superconducting Aluminum Resonator. , 112(4):047004, January 2014.

[52] S. W. Deiker, W. Doriese, G. C. Hilton, K. D. Irwin, W. H. Rippard, J. N. Ullom, L. R. Vale, S. T. Ruggiero, A. Williams, and B. A. Young. Superconducting transition edge sensor using dilute AlMn alloys. Applied Physics Letters, 85(11):2137–2139, 09 2004.

[53] Eleonora Di Valentino, Olga Mena, Supriya Pan, Luca Visinelli, Weiqiang Yang, Alessandro Melchiorri, David F. Mota, Adam G. Riess, and Joseph Silk. In the realm of the Hubble tension-a review of solutions. Classical and Quantum Gravity, 38(15):153001, July 2021.

[54] W. B. Doriese, K. M. Morgan, D. A. Bennett, E. V. Denison, C. P. Fitzgerald, J. W. Fowler, J. D. Gard, J. P. Hays-Wehle, G. C. Hilton, K. D. Irwin, Y. I. Joe, J. A. B. Mates, G. C. O'Neil, C. D. Reintsema, N. O. Robbins, D. R. Schmidt, D. S. Swetz, H. Tatsuno, L. R. Vale, and J. N. Ullom. Developments in Time-Division Multiplexing of X-ray Transition-Edge Sensors. Journal of Low Temperature Physics, 184(1-2):389–395, Jul 2016.

[55] S. M. Duff, J. Austermann, J. A. Beall, D. Becker, R. Datta, P. A. Gallardo, S. W. Henderson, G. C. Hilton, S. P. Ho, J. Hubmayr, B. J. Koopman, D. Li, J. McMahon, F. Nati, M. D. Niemack, C. G. Pappas, M. Salatino, B. L. Schmitt, S. M. Simon, S. T. Staggs, J. R. Stevens, J. Van Lanen, E. M. Vavagiakis, J. T. Ward, and E. J. Wollack. Advanced ACTPol Multichroic Polarimeter Array Fabrication Process for 150 mm Wafers. Journal of Low Temperature Physics, 184(3-4):634–641, Aug 2016.

[56] P Duthil. Material Properties at Low Temperature. pages 77–95, 2014. Comments: 18 pages, contribution to the CAS-CERN Accelerator School: Superconductivity for Accelerators, Erice, Italy, 24 April - 4 May 2013, edited by R. Bailey.

[57] Jens Erler, Kaustuv Basu, Jens Chluba, and Frank Bertoldi. Planck's view on the spectrum of the Sunyaev–Zeldovich effect. Monthly Notices of the Royal Astronomical Society, 476(3):3360–3381, 02 2018.

[58] J. P. Filippini, P. A. R. Ade, M. Amiri, S. J. Benton, R. Bihary, J. J. Bock, J. R. Bond, J. A. Bonetti, S. A. Bryan, B. Burger, H. C. Chiang, C. R. Contaldi, B. P. Crill, O. Doré, M. Farhang, L. M. Fissel, N. N. Gandilo, S. R. Golwala, J. E. Gudmundsson, M. Halpern, M. Hasselfield, G. Hilton, W. Holmes, V. V. Hristov, K. D. Irwin, W. C. Jones, C. L. Kuo, C. J. MacTavish, P. V. Mason, T. E. Montroy, T. A. Morford, C. B. Netterfield, D. T. O'Dea, A. S. Rahlin, C. D. Reintsema, J. E. Ruhl, M. C. Runyan, M. A. Schenker, J. A. Shariff, J. D. Soler, A. Trangsrud, C. Tucker, R. S. Tucker, and A. D. Turner. SPIDER: a balloon-borne CMB polarimeter for large angular scales. In Wayne S. Holland and Jonas Zmuidzinas, editors, Millimeter, Submillimeter, and Far-Infrared Detectors and Instrumentation for Astronomy V, volume 7741 of Society of Photo-Optical Instrumentation Engineers (SPIE) Conference Series, page 77411N, July 2010.

[59] D. Flanigan, H. McCarrick, G. Jones, B. R. Johnson, M. H. Abitbol, P. Ade, D. Araujo, K. Bradford, R. Cantor, G. Che, P. Day, S. Doyle, C. B. Kjellstrand, H. Leduc, M. Limon, V. Luu, P. Mauskopf, A. Miller, T. Mroczkowski, C. Tucker, and J. Zmuidzinas. Photon noise from chaotic and coherent millimeter-wave sources measured with horn-coupled, aluminum lumped-element kinetic inductance detectors. Applied Physics Letters, 108(8):083504, February 2016.

[60] Daniel Flanigan. Kinetic inductance detectors for measuring the polarization of the cosmic microwave background. PhD thesis, Columbia University, 2018.

[61] Nicholas Galitzki, Peter Ade, Francesco E. Angilè, Peter Ashton, Jason Austermann, Tashalee Billings, George Che, Hsiao-Mei Cho, Kristina Davis, Mark Devlin, Simon Dicker, Bradley J. Dober, Laura M. Fissel, Yasuo Fukui, Jiansong Gao, Samuel Gordon, Christopher E. Groppi, Seth Hillbrand, Gene C. Hilton, Johannes Hubmayr, Kent D. Irwin, Jeffrey Klein, Dale Li, Zhi-Yun Li, Nathan P. Lourie, Ian Lowe, Hamdi Mani, Peter G. Martin, Philip Mauskopf, Christopher McKenney, Federico Nati, Giles Novak, Enzo Pascale, Giampaolo Pisano, Fabio P. Santos, Douglas Scott, Adrian Sinclair, Juan D. Soler, Carole Tucker, Matthew Underhill, Michael Vissers, and Paul Williams. Instrumental performance and results from testing of the BLAST-TNG receiver, submillimeter optics, and MKID detector arrays. In Wayne S. Holland and Jonas Zmuidzinas, editors, Millimeter, Submillimeter, and Far-Infrared Detectors and Instrumentation for Astronomy VIII, volume 9914, page 99140J. International Society for Optics and Photonics, SPIE, 2016.

[62] Nicholas Galitzki, Peter A. R. Ade, Francesco E. Angilè, Peter Ashton, James A. Beall, Dan Becker, Kristi J. Bradford, George Che, Hsiao-Mei Cho, Mark J. Devlin, Bradley J. Dober, Laura M. Fissel, Yasuo Fukui, Jiansong Gao, Christopher E. Groppi, Seth Hillbrand, Gene C. Hilton, Johannes Hubmayr, Kent D. Irwin, Jeffrey Klein, Jeff Van Lanen, Dale Li, Zhi-Yun Li, Nathan P. Lourie, Hamdi Mani, Peter G. Martin, Philip Mauskopf, Fumitaka Nakamura, Giles Novak, David P. Pappas, Enzo Pascale, Giampaolo Pisano, Fabio P. Santos, Giorgio Savini, Douglas Scott, Sara Stanchfield, Carole Tucker, Joel N. Ullom, Matthew Underhill, Michael R. Vissers, and Derek Ward-Thompson. The next generation blast experiment. Journal of Astronomical Instrumentation, 03(02):1440001, 2014.

[63] Jiansong Gao. The Physics of Superconducting Microwave Resonators. PhD thesis, California Institute of Technology, 2008.

[64] E. M. George, J. E. Austermann, J. A. Beall, D. Becker, B. A. Benson, L. E. Bleem, J. E. Carlstrom, C. L. Chang, H.-M. Cho, A. T. Crites, M. A. Dobbs, W. Everett, N. W. Halverson, J. W. Henning,

G. C. Hilton, W. L. Holzapfel, J. Hubmayr, K. D. Irwin, D. Li, M. Lueker, J. J. McMahon, J. Mehl, J. Montgomery, T. Natoli, J. P. Nibarger, M. D. Niemack, V. Novosad, J. E. Ruhl, J. T. Sayre, E. Shirokoff, K. T. Story, G. Wang, V. Yefremenko, K. W. Yoon, and E. Young. A study of al-mn transition edge sensor engineering for stability. Journal of Low Temperature Physics, 176(3):383–391, August 2014.

[65] V. L. Ginzburg and L. D. Landau. On the Theory of superconductivity. Zh. Eksp. Teor. Fiz., 20:1064–1082, 1950.

[66] Jason Glenn, James J. Bock, Goutam Chattopadhyay, Samantha F. Edgington, Andrew E. Lange, Jonas Zmuidzinas, Phil D. Mauskopf, Brooks Rownd, Lunming Yuen, and Peter A. Ade. Bolocam: a millimeter-wave bolometric camera. In Thomas G. Phillips, editor, Advanced Technology MMW, Radio, and Terahertz Telescopes, volume 3357 of Society of Photo-Optical Instrumentation Engineers (SPIE) Conference Series, pages 326–334, July 1998.

[67] D J Goldie and S Withington. Non-equilibrium superconductivity in quantum-sensing superconducting resonators. Superconductor Science and Technology, 26(1):015004, nov 2012.

[68] Sunil R. Golwala, Clint Bockstiegel, Spencer Brugger, Nicole G. Czakon, Peter K. Day, Thomas P. Downes, Ran Duan, Jiansong Gao, Amandeep K. Gill, Jason Glenn, Matthew I. Hollister, Henry G. LeDuc, Philip R. Maloney, Benjamin A. Mazin, Sean G. McHugh, David Miller, Omid Noroozian, Hien T. Nguyen, Jack Sayers, James A. Schlaerth, Seth Siegel, Anastasios K. Vayonakis, Philip R Wilson, and Jonas Zmuidzinas. Status of MUSIC, the MUltiwavelength Sub/millimeter Inductance Camera. In Wayne S. Holland, editor, Millimeter, Submillimeter, and Far-Infrared Detectors and Instrumentation for Astronomy VI, volume 8452, page 845205. International Society for Optics and Photonics, SPIE, 2012.

[69] M. Göppl, A. Fragner, M. Baur, R. Bianchetti, S. Filipp, J. M. Fink, P. J. Leek, G. Puebla, L. Steffen, and A. Wallraff. Coplanar waveguide resonators for circuit quantum electrodynamics. Journal of Applied Physics, 104(11):113904–113904–8, December 2008.

[70] Samuel Gordon. Highly multiplexed superconducting detectors and readout electronics for balloon-borne and ground-based far-infrared imaging and polarimetry. PhD thesis, Arizona State University, 2019.

[71] L P Gor'kov. Microscopic derivation of the ginzburg–landau equations in the theory of superconductivity. Sov. Phys. - JETP (Engl. Transl.); (United States).

[72] Alan H. Guth. Inflationary universe: A possible solution to the horizon and flatness problems. Phys. Rev. D, 23:347–356, Jan 1981.

[73] S. Hailey-Dunsheath, E. Shirokoff, P. S. Barry, C. M. Bradford, G. Chattopadhyay, P. Day, S. Doyle, M. Hollister, A. Kovacs, H. G. LeDuc, P. Mauskopf, C. M. McKenney, R. Monroe, R. O'Brient, S. Padin, T. Reck, L. Swenson, C. E. Tucker, and J. Zmuidzinas. Status of SuperSpec: a broadband, on-chip millimeter-wave spectrometer. In Wayne S. Holland and Jonas Zmuidzinas, editors, Millimeter, Submillimeter, and Far-Infrared Detectors and Instrumentation for Astronomy VII, volume 9153, page 91530M. International Society for Optics and Photonics, SPIE, 2014.

[74] Steven Hailey-Dunsheath, Reinier M. J. Janssen, Jason Glenn, Charles M. Bradford, Joanna Perido, Joseph Redford, and Jonas Zmuidzinas. Kinetic inductance detectors for the Origins Space Telescope. Journal of Astronomical Telescopes, Instruments, and Systems, 7:011015, January 2021.

[75] Doyal A. Harper, Christine A. Allen, Michael J. Amato, Troy Ames, Arlin Bartels, Sean C. Casey, Rebecca J. Derro, Rhodri Evans, Ian Gatley, Stephen J. Heimsath, Alfonso Hermida, Murzy D. Jhabvala, Joel H. Kastner, Robert F. Loewenstein, S. H. Moseley, Robert J. Pernic, T. Rennick, Harvey E. Rhody, Dale Sandford, Richard A. Shafer, Peter J. Shirron, G. Voellmer, Shu-i. Wang, and Jesse Wirth. HAWC: a far-infrared camera for SOFIA. In Ramsey K. Melugin and Hans-Peter Röser, editors, Airborne Telescope Systems, volume 4014 of Society of Photo-Optical Instrumentation Engineers (SPIE) Conference Series, pages 43–53, June 2000.

[76] M. Hazumi, P. A. R. Ade, A. Adler, E. Allys, K. Arnold, D. Auguste, J. Aumont, R. Aurlien, J. Austermann, C. Baccigalupi, A. J. Banday, R. Banjeri, R. B. Barreiro, S. Basak, J. Beall, D. Beck, S. Beckman, J. Bermejo, P. de Bernardis, M. Bersanelli, J. Bonis, J. Borrill, F. Boulanger, S. Bounissou, M. Brilenkov, M. Brown, M. Bucher, E. Calabrese, P. Campeti, A. Carones, F. J. Casas, A. Challinor, V. Chan, K. Cheung, Y. Chinone, J. F. Cliche, L. Colombo, F. Columbro, J. Cubas, A. Cukierman, D. Curtis, G. D'Alessandro, N. Dachlythra, M. De Petris, C. Dickinson, P. Diego-Palazuelos, M. Dobbs, T. Dotani, L. Duband, S. Duff, J. M. Duval, K. Ebisawa, T. Elleflot, H. K. Eriksen, J. Errard, T. Essinger-Hileman, F. Finelli, R. Flauger, C. Franceschet, U. Fuskeland, M. Galloway, K. Ganga, J. R. Gao, R. Genova-Santos, M. Gerbino, M. Gervasi, T. Ghigna, E. Gjerløw, M. L. Gradziel, J. Grain, F. Grupp, A. Gruppuso, J. E. Gudmundsson, T. de Haan, N. W. Halverson, P. Hargrave, T. Hasebe, M. Hasegawa, M. Hattori, S. Henrot-Versillé, D. Herman, D. Herranz, C. A. Hill, G. Hilton, Y. Hirota, E. Hivon, R. A. Hlozek, Y. Hoshino, E. de la Hoz, J. Hubmayr, K. Ichiki, T. Iida, H. Imada, K. Ishimura, H. Ishino, G. Jaehnig, T. Kaga, S. Kashima, N. Katayama, A. Kato, T. Kawasaki, R. Keskitalo, T. Kisner, Y. Kobayashi, N. Kogiso, A. Kogut, K. Kohri, E. Komatsu, K. Komatsu, K. Konishi, N. Krachmalnicoff, I. Kreykenbohm, C. L. Kuo, A. Kushino, L. Lamagna, J. V. Lanen, M. Lattanzi, A. T. Lee, C. Leloup, F. Levrier, E. Linder, T. Louis, G. Luzzi, T. Maciaszek, B. Maffei, D. Maino, M. Maki, S. Mandelli, E. Martinez-Gonzalez, S. Masi, T. Matsumura, A. Mennella, M. Migliaccio, Y. Minami, K. Mitsuda, J. Montgomery, L. Montier, G. Morgante, B. Mot, Y. Murata, J. A. Murphy, M. Nagai, Y. Nagano, T. Nagasaki, R. Nagata, S. Nakamura, T. Namikawa, P. Natoli, S. Nerval, T. Nishibori, H. Nishino, F. Noviello, C. O'Sullivan, H. Ogawa, H. Ogawa, S. Oguri, H. Ohsaki, I. S. Ohta, N. Okada, N. Okada, L. Pagano, A. Paiella, D. Paoletti, G. Patanchon, J. Peloton, F. Piacentini, G. Pisano, G. Polenta, D. Poletti, T. Prouvé, G. Puglisi, D. Rambaud, C. Raum, S. Realini, M. Reinecke, M. Remazeilles, A. Ritacco, G. Roudil, J. A. Rubino-Martin, M. Russell, H. Sakurai, Y. Sakurai, M. Sandri, M. Sasaki, G. Savini, D. Scott, J. Seibert, Y. Sekimoto, B. Sherwin, K. Shinozaki, M. Shiraishi, P. Shirron, G. Signorelli, G. Smecher, S. Stever, R. Stompor, H. Sugai, S. Sugiyama, A. Suzuki, J. Suzuki, T. L. Svalheim, E. Switzer, R. Takaku, H. Takakura, S. Takakura, Y. Takase, Y. Takeda, A. Tartari, E. Taylor, Y. Terao, H. Thommesen, K. L. Thompson, B. Thorne, T. Toda, M. Tomasi, M. Tominaga, N. Trappe, M. Tristram, M. Tsuji, M. Tsujimoto, C. Tucker, J. Ullom, G. Vermeulen, P. Vielva, F. Villa, M. Vissers, N. Vittorio, I. Wehus, J. Weller, B. Westbrook, J. Wilms, B. Winter, E. J. Wollack, N. Y. Yamasaki, T. Yoshida, J. Yumoto, M. Zannoni, and A. Zonca. LiteBIRD satellite: JAXA's new strategic L-class mission for all-sky surveys of cosmic microwave background polarization. In Makenzie Lystrup and Marshall D. Perrin, editors, Space Telescopes and Instrumentation 2020: Optical, Infrared, and Millimeter Wave, volume 11443 of Society of Photo-Optical Instrumentation Engineers (SPIE) Conference Series, page 114432F, December 2020.

[77] S. W. Henderson, R. Allison, J. Austermann, T. Baildon, N. Battaglia, J. A. Beall, D. Becker, F. De Bernardis, J. R. Bond, E. Calabrese, S. K. Choi, K. P. Coughlin, K. T. Crowley, R. Datta, M. J. Devlin, S. M. Duff, J. Dunkley, R. Dünner, A. van Engelen, P. A. Gallardo, E. Grace, M. Hasselfield, F. Hills, G. C. Hilton, A. D. Hincks, R. Hložek, S. P. Ho, J. Hubmayr, K. Huffenberger, J. P. Hughes, K. D.

Irwin, B. J. Koopman, A. B. Kosowsky, D. Li, J. McMahon, C. Munson, F. Nati, L. Newburgh, M. D. Niemack, P. Niraula, L. A. Page, C. G. Pappas, M. Salatino, A. Schillaci, B. L. Schmitt, N. Sehgal, B. D. Sherwin, J. L. Sievers, S. M. Simon, D. N. Spergel, S. T. Staggs, J. R. Stevens, R. Thornton, J. Van Lanen, E. M. Vavagiakis, J. T. Ward, and E. J. Wollack. Advanced ACTPol Cryogenic Detector Arrays and Readout. Journal of Low Temperature Physics, 184(3-4):772–779, August 2016.

[78] M. Hilton, C. Sifón, S. Naess, M. Madhavacheril, M. Oguri, E. Rozo, E. Rykoff, T. M. C. Abbott, S. Adhikari, M. Aguena, S. Aiola, S. Allam, S. Amodeo, A. Amon, J. Annis, B. Ansarinejad, C. Aros-Bunster, J. E. Austermann, S. Avila, D. Bacon, N. Battaglia, J. A. Beall, D. T. Becker, G. M. Bernstein, E. Bertin, T. Bhandarkar, S. Bhargava, J. R. Bond, D. Brooks, D. L. Burke, E. Calabrese, M. Carrasco Kind, J. Carretero, S. K. Choi, A. Choi, C. Conselice, L. N. da Costa, M. Costanzi, D. Crichton, K. T. Crowley, R. Dünner, E. V. Denison, M. J. Devlin, S. R. Dicker, H. T. Diehl, J. P. Dietrich, P. Doel, S. M. Duff, A. J. Duivenvoorden, J. Dunkley, S. Everett, S. Ferraro, I. Ferrero, A. Ferté, B. Flaugher, J. Frieman, P. A. Gallardo, J. García-Bellido, E. Gaztanaga, D. W. Gerdes, P. Giles, J. E. Golec, M. B. Gralla, S. Grandis, D. Gruen, R. A. Gruendl, J. Gschwend, G. Gutierrez, D. Han, W. G. Hartley, M. Hasselfield, J. C. Hill, G. C. Hilton, A. D. Hincks, S. R. Hinton, S. P. P. Ho, K. Honscheid, B. Hoyle, J. Hubmayr, K. M. Huffenberger, J. P. Hughes, A. T. Jaelani, B. Jain, D. J. James, T. Jeltema, S. Kent, K. Knowles, B. J. Koopman, K. Kuehn, O. Lahav, M. Lima, Y. T. Lin, M. Lokken, S. I. Loubser, N. MacCrann, M. A. G. Maia, T. A. Marriage, J. Martin, J. McMahon, P. Melchior, F. Menanteau, R. Miquel, H. Miyatake, K. Moodley, R. Morgan, T. Mroczkowski, F. Nati, L. B. Newburgh, M. D. Niemack, A. J. Nishizawa, R. L. C. Ogando, J. Orlowski-Scherer, L. A. Page, A. Palmese, B. Partridge, F. Paz-Chinchón, P. Phakathi, A. A. Plazas, N. C. Robertson, A. K. Romer, A. Carnero Rosell, M. Salatino, E. Sanchez, E. Schaan, A. Schillaci, N. Sehgal, S. Serrano, T. Shin, S. M. Simon, M. Smith, M. Soares-Santos, D. N. Spergel, S. T. Staggs, E. R. Storer, E. Suchyta, M. E. C. Swanson, G. Tarle, D. Thomas, C. To, H. Trac, J. N. Ullom, L. R. Vale, J. Van Lanen, E. M. Vavagiakis, J. De Vicente, R. D. Wilkinson, E. J. Wollack, Z. Xu, and Y. Zhang. The Atacama Cosmology Telescope: A Catalog of ¿4000 Sunyaev-Zel'dovich Galaxy Clusters. , 253(1):3, March 2021.

[79] G. Hinshaw, D. Larson, E. Komatsu, D. N. Spergel, C. L. Bennett, J. Dunkley, M. R. Nolta, M. Halpern, R. S. Hill, N. Odegard, L. Page, K. M. Smith, J. L. Weiland, B. Gold, N. Jarosik, A. Kogut, M. Limon, S. S. Meyer, G. S. Tucker, E. Wollack, and E. L. Wright. Nine-year Wilkinson Microwave Anisotropy Probe (WMAP) Observations: Cosmological Parameter Results. , 208(2):19, October 2013.

[80] S. P. Ho, J. Austermann, J. A. Beall, S. K. Choi, N. F. Cothard, K. T. Crowley, R. Datta, M. J. Devlin, S. M. Duff, P. A. Gallardo, M. Hasselfield, S. W. Henderson, G. Hilton, J. Hubmayr, B. J. Koopman, Y. Li, J. McMahon, M. D. Niemack, M. Salatino, S. M. Simon, S. T. Staggs, J. T. Ward, J. N. Ullom, E. M. Vavagiakis, and E. J. Wollack. Highly uniform 150 mm diameter multichroic polarimeter array deployed for CMB detection. In , volume 9914 of Society of Photo-Optical Instrumentation Engineers (SPIE) Conference Series, page 991418, Jul 2017.

[81] W. S. Holland, E. I. Robson, W. K. Gear, C. R. Cunningham, J. F. Lightfoot, T. Jenness, R. J. Ivison, J. A. Stevens, P. A. R. Ade, M. J. Griffin, W. D. Duncan, J. A. Murphy, and D. A. Naylor. SCUBA: a common-user submillimetre camera operating on the James Clerk Maxwell Telescope. Monthly Notices of the Royal Astronomical Society, 303(4):659–672, 03 1999.

[82] J. Hubmayr, J. E. Austermann, J. A. Beall, D. T. Becker, S. J. Benton, A. S. Bergman, J. R. Bond, S. Bryan, S. M. Duff, A. J. Duivenvoorden, H. K. Eriksen, J. P. Filippini, A. Fraisse, M. Gal-

loway, A. E. Gambrel, K. Ganga, A. L. Grigorian, R. Gualtieri, J. E. Gudmundsson, J. W. Hartley, M. Halpern, G. C. Hilton, W. C. Jones, J. J. McMahon, L. Moncelsi, J. M. Nagy, C. B. Netterfield, B. Osherson, I. Padilla, A. S. Rahlin, B. Racine, J. Ruhl, T. M. Rudd, J. A. Shariff, J. D. Soler, X. Song, J. N. Ullom, J. Van Lanen, M. R. Vissers, I. K. Wehus, S. Wen, D. V. Wiebe, and E. Young. Design of 280 GHz feedhorn-coupled TES arrays for the balloon-borne polarimeter SPIDER. In Millimeter, Submillimeter, and Far-Infrared Detectors and Instrumentation for Astronomy VIII, volume 9914 of , page 99140V, July 2016.

[83] J. Hubmayr, J. E. Austermann, J. A. Beall, D. T. Becker, B. Dober, S. M. Duff, J. Gao, G. C. Hilton, C. M. McKenney, J. N. Ullom, J. Van Lanen, and M. R. Vissers. Low-Temperature Detectors for CMB Imaging Arrays. Journal of Low Temperature Physics, 193(3-4):633–647, November 2018.

[84] J. Hubmayr, J. Beall, D. Becker, H. M. Cho, M. Devlin, B. Dober, C. Groppi, G. C. Hilton, K. D. Irwin, D. Li, P. Mauskopf, D. P. Pappas, J. Van Lanen, M. R. Vissers, Y. Wang, L. F. Wei, and J. Gao. Photon-noise limited sensitivity in titanium nitride kinetic inductance detectors. Applied Physics Letters, 106(7):073505, February 2015.

[85] Howard Hui, P. A. R. Ade, Z. Ahmed, R. W. Aikin, K. D. Alexander, D. Barkats, S. J. Benton, C. A. Bischoff, J. J. Bock, R. Bowens-Rubin, J. A. Brevik, I. Buder, E. Bullock, V. Buza, J. Connors, J. Cornelison, B. P. Crill, M. Crumrine, M. Dierickx, L. Duband, C. Dvorkin, J. P. Filippini, S. Fliescher, J. Grayson, G. Hall, M. Halpern, S. Harrison, S. R. Hildebrandt, G. C. Hilton, K. D. Irwin, J. Kang, K. S. Karkare, E. Karpel, J. P. Kaufman, B. G. Keating, S. Kefeli, S. A. Kernasovskiy, J. M. Kovac, C. L. Kuo, K. Lau, N. A. Larsen, E. M. Leitch, M. Lueker, K. G. Megerian, L. Moncelsi, T. Namikawa, C. B. Netterfield, H. T. Nguyen, R. O'Brient, R. W. Ogburn, S. Palladino, C. Pryke, B. Racine, S. Richter, R. Schwarz, A. Schillaci, C. D. Sheehy, A. Soliman, T. St. Germaine, Z. K. Staniszewski, B. Steinbach, R. V. Sudiwala, G. P. Teply, K. L. Thompson, J. E. Tolan, C. Tucker, A. D. Turner, C. Umiltà, A. G. Vieregg, A. Wandui, A. C. Weber, D. V. Wiebe, J. Willmert, C. L. Wong, W. L. K. Wu, E. Yang, K. W. Yoon, and C. Zhang. BICEP Array: a multi-frequency degree-scale CMB polarimeter. In Jonas Zmuidzinas and Jian-Rong Gao, editors, Millimeter, Submillimeter, and Far-Infrared Detectors and Instrumentation for Astronomy IX, volume 10708 of Society of Photo-Optical Instrumentation Engineers (SPIE) Conference Series, page 1070807, July 2018.

[86] G. Hurier. High significance detection of the tSZ effect relativistic corrections. , 596:A61, December 2016.

[87] K. D. Irwin. An application of electrothermal feedback for high resolution cryogenic particle detection. Applied Physics Letters, 66(15):1998–2000, 1995.

[88] K. D. Irwin and G. C. Hilton. Cryogenic Particle Detection, chapter Transition Edge Sensors, pages 63–150. Springer Verlag, Berlin, 2005.

[89] K. D. Irwin, G. C. Hilton, D. A. Wollman, and John M. Martinis. Thermal-response time of superconducting transition-edge microcalorimeters. Journal of Applied Physics, 83(8):3978–3985, 1998.

[90] K.D. Irwin and G.C. Hilton. Transition-Edge Sensors, pages 63–150. Springer Berlin Heidelberg, Berlin, Heidelberg, 2005.

[91] Naoki Itoh, Yasuharu Kohyama, and Satoshi Nozawa. Relativistic Corrections to the Sunyaev-Zeldovich Effect for Clusters of Galaxies. , 502(1):7–15, July 1998.

[92] A. H. Jaffe, P. A. R. Ade, A. Balbi, J. J Bock, J. R. Bond, J. Borrill, A. Boscaleri, K. Coble, B. P. Crill, P. de Bernardis, P. Farese, P. G. Ferreira, K. Ganga, M. Giacometti, S. Hanany, E. Hivon, V. V. Hristov, A. Iacoangeli, A. E. Lange, A. T. Lee, L. Martinis, S. Masi, P. D. Mauskopf, A. Melchiorri, T. Montroy, C. B. Netterfield, S. Oh, E. Pascale, F. Piacentini, D. Pogosyan, S. Prunet, B. Rabii, S. Rao, P. L. Richards, G. Romeo, J. E. Ruhl, F. Scaramuzzi, D. Sforna, G. F. Smoot, R. Stompor, C. D. Winant, and J. H. P. Wu. Cosmology from maxima-1, boomerang, and cobe dmr cosmic microwave background observations. Phys. Rev. Lett., 86:3475–3479, Apr 2001.

[93] B. R. Johnson, D. Flanigan, M. H. Abitbol, P. A. R. Ade, S. Bryan, H. M. Cho, R. Datta, P. Day, S. Doyle, K. Irwin, G. Jones, D. Li, P. Mauskopf, H. McCarrick, J. McMahon, A. Miller, G. Pisano, Y. Song, H. Surdi, and C. Tucker. Development of Multi-chroic MKIDs for Next-Generation CMB Polarization Studies. Journal of Low Temperature Physics, 193(3-4):103–112, November 2018.

[94] Marc Kamionkowski, Arthur Kosowsky, and Albert Stebbins. A probe of primordial gravity waves and vorticity. Physical Review Letters, 78(11):2058–2061, mar 1997.

[95] Marc Kamionkowski and Ely D. Kovetz. The quest for b modes from inflationary gravitational waves. Annual Review of Astronomy and Astrophysics, 54(1):227–269, 2016.

[96] Boris S. Karasik, Sergey V. Pereverzev, David Olaya, Michael E. Gershenson, Robin Cantor, Jonathan H. Kawamura, Peter K. Day, Bruce Bumble, Henry G. LeDuc, Steve P. Monacos, Dennis G. Harding, Daniel Santavicca, Faustin Carter, and Daniel E. Prober. Development of the nano-HEB array for low-background far-IR applications. In Wayne S. Holland and Jonas Zmuidzinas, editors, Millimeter, Submillimeter, and Far-Infrared Detectors and Instrumentation for Astronomy V, volume 7741, page 774119. International Society for Optics and Photonics, SPIE, 2010.

[97] Boris S. Karasik, Andrei V. Sergeev, and Daniel E. Prober. Nanobolometers for thz photon detection. IEEE Transactions on Terahertz Science and Technology, 1(1):97–111, 2011.

[98] K. S. Karkare, A. J. Anderson, P. S. Barry, B. A. Benson, J. E. Carlstrom, T. Cecil, C. L. Chang, M. A. Dobbs, M. Hollister, G. K. Keating, D. P. Marrone, J. McMahon, J. Montgomery, Z. Pan, G. Robson, M. Rouble, E. Shirokoff, and G. Smecher. SPT-SLIM: A Line Intensity Mapping Pathfinder for the South Pole Telescope. Journal of Low Temperature Physics, 209(5-6):758–765, December 2022.

[99] M. Kenyon, P. K. Day, C. M. Bradford, J. J. Bock, and H. G. Leduc. Heat capacity of absorbers for transition-edge sensors suitable for space-borne far-ir/submm spectroscopy. IEEE Transactions on Applied Superconductivity, 19(3):524–527, 2009.

[100] M. S. Khalil, M. J. A. Stoutimore, F. C. Wellstood, and K. D. Osborn. An analysis method for asymmetric resonator transmission applied to superconducting devices. Journal of Applied Physics, 111(5):054510–054510–6, March 2012.

[101] P. Khosropanah, T. Suzuki, M. L. Ridder, R. A. Hijmering, H. Akamatsu, L. Gottardi, J. van der Kuur, J. R. Gao, and B. D. Jackson. Ultra-low noise TES bolometer arrays for SAFARI instrument on SPICA. In Wayne S. Holland and Jonas Zmuidzinas, editors, Millimeter, Submillimeter, and Far-Infrared Detectors and Instrumentation for Astronomy VIII, volume 9914, page 99140B. International Society for Optics and Photonics, SPIE, 2016.

[102] B. J. Koopman, N. F. Cothard, S. K. Choi, K. T. Crowley, S. M. Duff, S. W. Henderson, S. P. Ho, J. Hubmayr, P. A. Gallardo, F. Nati, M. D. Niemack, S. M. Simon, S. T. Staggs, J. R. Stevens, E. M.

Vavagiakis, and E. J. Wollack. Advanced ACTPol Low-Frequency Array: Readout and Characterization of Prototype 27 and 39 GHz Transition Edge Sensors. Journal of Low Temperature Physics, 193(5-6):1103–1111, Dec 2018.

[103] Andrey V. Kravtsov and Stefano Borgani. Formation of Galaxy Clusters. , 50:353–409, September 2012.

[104] C. L. Kuo, J. J. Bock, J. A. Bonetti, J. Brevik, G. Chattopadhyay, P. K. Day, S. Golwala, M. Kenyon, A. E. Lange, H. G. LeDuc, H. Nguyen, R. W. Ogburn, A. Orlando, A. Transgrud, A. Turner, G. Wang, and J. Zmuidzinas. Antenna-coupled TES bolometer arrays for CMB polarimetry. In William D. Duncan, Wayne S. Holland, Stafford Withington, and Jonas Zmuidzinas, editors, Millimeter and Submillimeter Detectors and Instrumentation for Astronomy IV, volume 7020 of Society of Photo-Optical Instrumentation Engineers (SPIE) Conference Series, page 70201I, July 2008.

[105] Hong Li, Si-Yu Li, Yang Liu, Yong-Ping Li, Yifu Cai, Mingzhe Li, Gong-Bo Zhao, Cong-Zhan Liu, Zheng-Wei Li, He Xu, Di Wu, Yong-Jie Zhang, Zu-Hui Fan, Yong-Qiang Yao, Chao-Lin Kuo, Fang-Jun Lu, and Xinmin Zhang. Probing Primordial Gravitational Waves: Ali CMB Polarization Telescope. arXiv e-prints, page arXiv:1710.03047, October 2017.

[106] Hong Li, Si-Yu Li, Yang Liu, Yong-Ping Li, Yifu Cai, Mingzhe Li, Gong-Bo Zhao, Cong-Zhan Liu, Zheng-Wei Li, He Xu, Di Wu, Yong-Jie Zhang, Zu-Hui Fan, Yong-Qiang Yao, Chao-Lin Kuo, Fang-Jun Lu, and Xinmin Zhang. Probing primordial gravitational waves: Ali cmb polarization telescope. National Science Review, 6(1):145–154, January 2019.

[107] M. Lindeman, S. Bandler, R. Brekosky, J. Chervenak, E. Figueroa-Feliciano, F. Finkbeiner, M. Li, and C. Kilbourne. Impedance measurements and modeling of a transition-edge-sensor calorimeter. Review of Scientific Instruments, 75:1283–1289, 2004.

[108] Mark. A. Lindeman, Kathleen A. Barger, Donald E. Brandl, S. Gwynne Crowder, Lindsay Rocks, and Dan McCammon. Complex impedance measurements of calorimeters and bolometers: Correction for stray impedances. Review of Scientific Instruments, 78(4):043105, 2007.

[109] Mark Anton Lindeman. Microcalorimetry and the Transition-Edge Sensor. PhD thesis, University of California at Davis, 2000.

[110] LiteBIRD Collaboration, E. Allys, K. Arnold, J. Aumont, R. Aurlien, S. Azzoni, C. Baccigalupi, A. J. Banday, R. Banerji, R. B. Barreiro, N. Bartolo, L. Bautista, D. Beck, S. Beckman, M. Bersanelli, F. Boulanger, M. Brilenkov, M. Bucher, E. Calabrese, P. Campeti, A. Carones, F. J. Casas, A. Catalano, V. Chan, K. Cheung, Y. Chinone, S. E. Clark, F. Columbro, G. D'Alessandro, P. de Bernardis, T. de Haan, E. de la Hoz, M. De Petris, S. Della Torre, P. Diego-Palazuelos, M. Dobbs, T. Dotani, J. M. Duval, T. Elleflot, H. K. Eriksen, J. Errard, T. Essinger-Hileman, F. Finelli, R. Flauger, C. Franceschet, U. Fuskeland, M. Galloway, K. Ganga, M. Gerbino, M. Gervasi, R. T. Génova-Santos, T. Ghigna, S. Giardiello, E. Gjerløw, J. Grain, F. Grupp, A. Gruppuso, J. E. Gudmundsson, N. W. Halverson, P. Hargrave, T. Hasebe, M. Hasegawa, M. Hazumi, S. Henrot-Versillé, B. Hensley, L. T. Hergt, D. Herman, E. Hivon, R. A. Hlozek, A. L. Hornsby, Y. Hoshino, J. Hubmayr, K. Ichiki, T. Iida, H. Imada, H. Ishino, G. Jaehnig, N. Katayama, A. Kato, R. Keskitalo, T. Kisner, Y. Kobayashi, A. Kogut, K. Kohri, E. Komatsu, K. Komatsu, K. Konishi, N. Krachmalnicoff, C. L. Kuo, L. Lamagna, M. Lattanzi, A. T. Lee, C. Leloup, F. Levrier, E. Linder, G. Luzzi, J. Macias-Perez,

T. Maciaszek, B. Maffei, D. Maino, S. Mandelli, E. Martínez-González, S. Masi, M. Massa, S. Matarrese, F. T. Matsuda, T. Matsumura, L. Mele, M. Migliaccio, Y. Minami, A. Moggi, J. Montgomery, L. Montier, G. Morgante, B. Mot, Y. Nagano, T. Nagasaki, R. Nagata, R. Nakano, T. Namikawa, F. Nati, P. Natoli, S. Nerval, F. Noviello, K. Odagiri, S. Oguri, H. Ohsaki, L. Pagano, A. Paiella, D. Paoletti, A. Passerini, G. Patanchon, F. Piacentini, M. Piat, G. Pisano, G. Polenta, D. Poletti, T. Prouvé, G. Puglisi, D. Rambaud, C. Raum, S. Realini, M. Reinecke, M. Remazeilles, A. Ritacco, G. Roudil, J. A. Rubino-Martin, M. Russell, H. Sakurai, Y. Sakurai, M. Sasaki, D. Scott, Y. Sekimoto, K. Shinozaki, M. Shiraishi, P. Shirron, G. Signorelli, F. Spinella, S. Stever, R. Stompor, S. Sugiyama, R. M. Sullivan, A. Suzuki, T. L. Svalheim, E. Switzer, R. Takaku, H. Takakura, Y. Takase, A. Tartari, Y. Terao, J. Thermeau, H. Thommesen, K. L. Thompson, M. Tomasi, M. Tominaga, M. Tristram, M. Tsuji, M. Tsujimoto, L. Vacher, P. Vielva, N. Vittorio, W. Wang, K. Watanuki, I. K. Wehus, J. Weller, B. Westbrook, J. Wilms, B. Winter, E. J. Wollack, J. Yumoto, M. Zannoni, and Collaboration LiteB I R D. Probing cosmic inflation with the LiteBIRD cosmic microwave background polarization survey. Progress of Theoretical and Experimental Physics, 2023(4):042F01, April 2023.

[111] HEINZ LONDON. Production of heat in supraconductors by alternating currents. Nature, 133(3361):497–498, Mar 1934.

[112] M. Lueker, B. A. Benson, C. L. Chang, H. Cho, M. Dobbs, W. L. Holzapfel, T. Lanting, A. T. Lee, J. Mehl, T. Plagge, E. Shirokoff, H. G. Spieler, and J. D. Vieira. Thermal design and characterization of transition-edge sensor (tes) bolometers for frequency-domain multiplexing. IEEE Transactions on Applied Superconductivity, 19(3):496–500, 2009.

[113] I. J. Maasilta. Complex impedance, responsivity and noise of transition-edge sensors: Analytical solutions for two- and three-block thermal models. AIP Advances, 2(4):042110, December 2012.

[114] Piero Madau and Mark Dickinson. Cosmic Star-Formation History. , 52:415–486, August 2014.

[115] P. D. Mauskopf. Transition edge sensors and kinetic inductance detectors in astronomical instruments. Publications of the Astronomical Society of the Pacific, 130(990):1–28, 2018.

[116] F. Mayet, R. Adam, P. Ade, P. André, A. Andrianasolo, M. Arnaud, H. Aussel, I. Bartalucci, A. Beelen, A. Benoît, A. Bideaud, O. Bourrion, M. Calvo, A. Catalano, B. Comis, M. De Petris, F. X. Désert, S. Doyle, E. F. C. Driessen, A. Gomez, J. Goupy, F. Kéruzoré, C. Kramer, B. Ladjelate, G. Lagache, S. Leclercq, J. F. Lestrade, J. F. Macías-Pérez, P. Mauskopf, A. Monfardini, L. Perotto, G. Pisano, E. Pointecouteau, N. Ponthieu, G. W. Pratt, V. Revéret, A. Ritacco, C. Romero, H. Roussel, F. Ruppin, K. Schuster, S. Shu, A. Sievers, C. Tucker, and R. Zylka. Cluster cosmology with the NIKA2 SZ Large Program. In mm Universe @ NIKA2 - Observing the mm Universe with the NIKA2 Camera, volume 228 of European Physical Journal Web of Conferences, page 00017, June 2020.

[117] B. A. Mazin, S. R. Meeker, M. J. Strader, P. Szypryt, D. Marsden, J. C. van Eyken, G. E. Duggan, A. B. Walter, G. Ulbricht, M. Johnson, B. Bumble, K. O'Brien, and C. Stoughton. ARCONS: A 2024 Pixel Optical through Near-IR Cryogenic Imaging Spectrophotometer. , 125(933):1348, November 2013.

[118] Benjamin A. Mazin. Microwave Kinetic Inductance Detectors. PhD thesis, California Institute of Technology, 2005.

[119] Benjamin A. Mazin. In-flight Performance of the BLAST-TNG Balloon-borne Far-infrared Telescope and Development of a Reconfigurable Readout on the RFSoC Platform for Frequency Multiplexed Superconducting Detector Arrays. PhD thesis, Arizona State University, 2021.

[120] Heather McCarrick. Design and performance of kinetic inductance detectors for cosmic microwave background polarimetry. PhD thesis, Columbia University, 2018.

[121] J. McMahon, J. W. Appel, J. E. Austermann, J. A. Beall, D. Becker, B. A. Benson, L. E. Bleem, J. Britton, C. L. Chang, J. E. Carlstrom, H. M. Cho, A. T. Crites, T. Essinger-Hileman, W. Everett, N. W. Halverson, J. W. Henning, G. C. Hilton, K. D. Irwin, J. Mehl, S. S. Meyer, S. Mossley, M. D. Niemack, L. P. Parker, S. M. Simon, S. T. Staggs, C. Visnjic, E. Wollack, K. U. -Yen, K. W. Yoon, and Y. Zhao. Planar Orthomode Transducers for Feedhorn-coupled TES Polarimeters. In Betty Young, Blas Cabrera, and Aaron Miller, editors, The Thirteenth International Workshop on Low Temperature Detectors - LTD13, volume 1185 of American Institute of Physics Conference Series, pages 490–493, December 2009.

[122] J. McMahon, J. Beall, D. Becker, H. M. Cho, R. Datta, A. Fox, N. Halverson, J. Hubmayr, K. Irwin, J. Nibarger, M. Niemack, and H. Smith. Multi-chroic Feed-Horn Coupled TES Polarimeters. Journal of Low Temperature Physics, 167(5-6):879–884, Jun 2012.

[123] Seth R. Meeker, Benjamin A. Mazin, Alex B. Walter, Paschal Strader, Neelay Fruitwala, Clint Bockstiegel, Paul Szypryt, Gerhard Ulbricht, Grégoire Coiffard, Bruce Bumble, Gustavo Cancelo, Ted Zmuda, Ken Treptow, Neal Wilcer, Giulia Collura, Rupert Dodkins, Isabel Lipartito, Nicholas Zobrist, Michael Bottom, J. Chris Shelton, Dimitri Mawet, Julian C. van Eyken, Gautam Vasisht, and Eugene Serabyn. Darkness: A microwave kinetic inductance detector integral field spectrograph for high-contrast astronomy. Publications of the Astronomical Society of the Pacific, 130(988):065001, apr 2018.

[124] Avirukt Mittal, Francesco de Bernardis, and Michael D. Niemack. Optimizing measurements of cluster velocities and temperatures for ccat-prime and future surveys. Journal of Cosmology and Astroparticle Physics, 2018(02):032, feb 2018.

[125] L. Moncelsi, P. A. R. Ade, Z. Ahmed, M. Amiri, D. Barkats, R. Basu Thakur, C. A. Bischoff, J. J. Bock, V. Buza, J. R. Cheshire, J. Connors, J. Cornelison, M. Crumrine, A. J. Cukierman, E. V. Denison, M. Dierickx, L. Duband, M. Eiben, S. Fatigoni, J. P. Filippini, N. Goeckner-Wald, D. Goldfinger, J. A. Grayson, P. Grimes, G. Hall, M. Halpern, S. A. Harrison, S. Henderson, S. R. Hildebrandt, G. C. Hilton, J. Hubmayr, H. Hui, K. D. Irwin, J. H. Kang, K. S. Karkare, S. Kefeli, J. M. Kovac, C. L. Kuo, K. Lau, E. M. Leitch, K. G. Megerian, L. Minutolo, Y. Nakato, T. Namikawa, H. T. Nguyen, R. O'brient, S. Palladino, N. Precup, T. Prouve, C. Pryke, B. Racine, C. D. Reintsema, A. Schillaci, B. L. Schmitt, A. Soliman, T. St. Germaine, B. Steinbach, R. V. Sudiwala, K. L. Thompson, C. Tucker, A. D. Turner, C. Umiltà, A. G. Vieregg, A. Wandui, A. C. Weber, D. V. Wiebe, J. Willmert, W. L. K. Wu, E. Yang, K. W. Yoon, E. Young, C. Yu, L. Zeng, C. Zhang, and S. Zhang. Receiver development for BICEP Array, a next-generation CMB polarimeter at the South Pole. In Jonas Zmuidzinas and Jian-Rong Gao, editors, Millimeter, Submillimeter, and Far-Infrared Detectors and Instrumentation for Astronomy X, volume 11453 of Society of Photo-Optical Instrumentation Engineers (SPIE) Conference Series, page 1145314, December 2020.

[126] Monfardini, A., Swenson, L. J., Bideaud, A., Désert, F. X., Yates, S. J. C., Benoit, A., Baryshev, A. M., Baselmans, J. J. A., Doyle, S., Klein, B., Roesch, M., Tucker, C., Ade, P., Calvo, M., Camus, P., Giordano, C., Guesten, R., Hoffmann, C., Leclercq, S., Mauskopf, P., and Schuster, K. F. Nika: A millimeter-wave kinetic inductance camera. A&A, 521:A29, 2010.

[127] Ben Moore, Sebastiano Ghigna, Fabio Governato, George Lake, Thomas Quinn, Joachim Stadel, and Paolo Tozzi. Dark Matter Substructure within Galactic Halos. , 524(1):L19–L22, October 1999.

[128] M. J. Myers, William Holzapfel, Adrian T. Lee, Roger O'Brient, P. L. Richards, Huan T. Tran, Peter Ade, Greg Engargiola, Andy Smith, and Helmuth Spieler. An antenna-coupled bolometer with an integrated microstrip bandpass filter. Applied Physics Letters, 86(11):114103, Mar 2005.

[129] Daisuke Nagai, Monique Arnaud, Sarthak Dasadia, Michael McDonald, Ikuyuki Mitsuishi, and Andrea Morandi. Cluster Physics & Evolution. IAU Focus Meeting, 29B:70–78, January 2016.

[130] Peter C. Nagler, John E. Sadleir, and Edward J. Wollack. Transition-edge sensor detectors for the Origins Space Telescope. Journal of Astronomical Telescopes, Instruments, and Systems, 7:011005, January 2021.

[131] M. D. Niemack, P. A. R. Ade, J. Aguirre, F. Barrientos, J. A. Beall, J. R. Bond, J. Britton, H. M. Cho, S. Das, M. J. Devlin, S. Dicker, J. Dunkley, R. Dünner, J. W. Fowler, A. Hajian, M. Halpern, M. Hasselfield, G. C. Hilton, M. Hilton, J. Hubmayr, J. P. Hughes, L. Infante, K. D. Irwin, N. Jarosik, J. Klein, A. Kosowsky, T. A. Marriage, J. McMahon, F. Menanteau, K. Moodley, J. P. Nibarger, M. R. Nolta, L. A. Page, B. Partridge, E. D. Reese, J. Sievers, D. N. Spergel, S. T. Staggs, R. Thornton, C. Tucker, E. Wollack, and K. W. Yoon. ACTPol: a polarization-sensitive receiver for the Atacama Cosmology Telescope. In Wayne S. Holland and Jonas Zmuidzinas, editors, Millimeter, Submillimeter, and Far-Infrared Detectors and Instrumentation for Astronomy V, volume 7741 of Society of Photo-Optical Instrumentation Engineers (SPIE) Conference Series, page 77411S, July 2010.

[132] Omid Noroozian, Peter K. Day, Byeong Ho Eom, Henry G. Leduc, and Jonas Zmuidzinas. Crosstalk Reduction for Superconducting Microwave Resonator Arrays. IEEE Transactions on Microwave Theory Techniques, 60(5):1235–1243, May 2012.

[133] Roger C. O'Brient, Bryan Steinbach, James J. Bock, Albert Wandui, Hien Nguyen, and Anthony Turner. Thermal kinetic inductance detectors for CMB and sub millimeter observations (Conference Presentation). In Jonas Zmuidzinas and Jian-Rong Gao, editors, Millimeter, Submillimeter, and Far-Infrared Detectors and Instrumentation for Astronomy IX, volume 10708, page 1070809. International Society for Optics and Photonics, SPIE, 2018.

[134] C. S. Owen and D. J. Scalapino. Superconducting state under the influence of external dynamic pair breaking. Phys. Rev. Lett., 28:1559–1561, Jun 1972.

[135] L. Page, M. R. Nolta, C. Barnes, C. L. Bennett, M. Halpern, G. Hinshaw, N. Jarosik, A. Kogut, M. Limon, S. S. Meyer, H. V. Peiris, D. N. Spergel, G. S. Tucker, E. Wollack, and E. L. Wright. First-Year Wilkinson Microwave Anisotropy Probe (WMAP) Observations: Interpretation of the TT and TE Angular Power Spectrum Peaks. , 148(1):233–241, September 2003.

[136] L. Perivolaropoulos and F. Skara. Challenges for ΛCDM: An update. , 95:101659, December 2022.

[137] S. Perlmutter, G. Aldering, G. Goldhaber, R. A. Knop, P. Nugent, P. G. Castro, S. Deustua, S. Fabbro, A. Goobar, D. E. Groom, I. M. Hook, A. G. Kim, M. Y. Kim, J. C. Lee, N. J. Nunes, R. Pain, C. R. Pennypacker, R. Quimby, C. Lidman, R. S. Ellis, M. Irwin, R. G. McMahon, P. Ruiz-Lapuente, N. Walton, B. Schaefer, B. J. Boyle, A. V. Filippenko, T. Matheson, A. S. Fruchter, N. Panagia, H. J. M. Newberg, W. J. Couch, and The Supernova Cosmology Project. Measurements of Ω and Λ from 42 High-Redshift Supernovae. , 517(2):565–586, June 1999.

[138] Planck Collaboration, R. Adam, P. A. R. Ade, N. Aghanim, M. I. R. Alves, M. Arnaud, M. Ashdown, J. Aumont, C. Baccigalupi, A. J. Banday, R. B. Barreiro, J. G. Bartlett, N. Bartolo, E. Battaner, K. Benabed, A. Benoît, A. Benoit-Lévy, J. P. Bernard, M. Bersanelli, P. Bielewicz, J. J. Bock, A. Bonaldi, L. Bonavera, J. R. Bond, J. Borrill, F. R. Bouchet, F. Boulanger, M. Bucher, C. Burigana, R. C. Butler, E. Calabrese, J. F. Cardoso, A. Catalano, A. Challinor, A. Chamballu, R. R. Chary, H. C. Chiang, P. R. Christensen, D. L. Clements, S. Colombi, L. P. L. Colombo, C. Combet, F. Couchot, A. Coulais, B. P. Crill, A. Curto, F. Cuttaia, L. Danese, R. D. Davies, R. J. Davis, P. de Bernardis, A. de Rosa, G. de Zotti, J. Delabrouille, F. X. Désert, C. Dickinson, J. M. Diego, H. Dole, S. Donzelli, O. Doré, M. Douspis, A. Ducout, X. Dupac, G. Efstathiou, F. Elsner, T. A. Enßlin, H. K. Eriksen, E. Falgarone, J. Fergusson, F. Finelli, O. Forni, M. Frailis, A. A. Fraisse, E. Franceschi, A. Frejsel, S. Galeotta, S. Galli, K. Ganga, T. Ghosh, M. Giard, Y. Giraud-Héraud, E. Gjerløw, J. González-Nuevo, K. M. Górski, S. Gratton, A. Gregorio, A. Gruppuso, J. E. Gudmundsson, F. K. Hansen, D. Hanson, D. L. Harrison, G. Helou, S. Henrot-Versillé, C. Hernández-Monteagudo, D. Herranz, S. R. Hildebrandt, E. Hivon, M. Hobson, W. A. Holmes, A. Hornstrup, W. Hovest, K. M. Huffenberger, G. Hurier, A. H. Jaffe, T. R. Jaffe, W. C. Jones, M. Juvela, E. Keihänen, R. Keskitalo, T. S. Kisner, R. Kneissl, J. Knoche, M. Kunz, H. Kurki-Suonio, G. Lagache, A. Lähteenmäki, J. M. Lamarre, A. Lasenby, M. Lattanzi, C. R. Lawrence, M. Le Jeune, J. P. Leahy, R. Leonardi, J. Lesgourgues, F. Levrier, M. Liguori, P. B. Lilje, M. Linden-Vørnle, M. López-Caniego, P. M. Lubin, J. F. Macías-Pérez, G. Maggio, D. Maino, N. Mandolesi, A. Mangilli, M. Maris, D. J. Marshall, P. G. Martin, E. Martínez-González, S. Masi, S. Matarrese, P. McGehee, P. R. Meinhold, A. Melchiorri, L. Mendes, A. Mennella, M. Migliaccio, S. Mitra, M. A. Miville-Deschênes, A. Moneti, L. Montier, G. Morgante, D. Mortlock, A. Moss, D. Munshi, J. A. Murphy, P. Naselsky, F. Nati, P. Natoli, C. B. Netterfield, H. U. Nørgaard-Nielsen, F. Noviello, D. Novikov, I. Novikov, E. Orlando, C. A. Oxborrow, F. Paci, L. Pagano, F. Pajot, R. Paladini, D. Paoletti, B. Partridge, F. Pasian, G. Patanchon, T. J. Pearson, O. Perdereau, L. Perotto, F. Perrotta, V. Pettorino, F. Piacentini, M. Piat, E. Pierpaoli, D. Pietrobon, S. Plaszczynski, E. Pointecouteau, G. Polenta, G. W. Pratt, G. Prézeau, S. Prunet, J. L. Puget, J. P. Rachen, W. T. Reach, R. Rebolo, M. Reinecke, M. Remazeilles, C. Renault, A. Renzi, I. Ristorcelli, G. Rocha, C. Rosset, M. Rossetti, G. Roudier, J. A. Rubiño-Martín, B. Rusholme, M. Sandri, D. Santos, M. Savelainen, G. Savini, D. Scott, M. D. Seiffert, E. P. S. Shellard, L. D. Spencer, V. Stolyarov, R. Stompor, A. W. Strong, R. Sudiwala, R. Sunyaev, D. Sutton, A. S. Suur-Uski, J. F. Sygnet, J. A. Tauber, L. Terenzi, L. Toffolatti, M. Tomasi, M. Tristram, M. Tucci, J. Tuovinen, G. Umana, L. Valenziano, J. Valiviita, F. Van Tent, P. Vielva, F. Villa, L. A. Wade, B. D. Wandelt, I. K. Wehus, A. Wilkinson, D. Yvon, A. Zacchei, and A. Zonca. Planck 2015 results. X. Diffuse component separation: Foreground maps. , 594:A10, September 2016.

[139] Planck Collaboration, Adam, R., Ade, P. A. R., Aghanim, N., Akrami, Y., Alves, M. I. R., Argüeso, F., Arnaud, M., Arroja, F., Ashdown, M., Aumont, J., Baccigalupi, C., Ballardini, M., Banday, A. J., Barreiro, R. B., Bartlett, J. G., Bartolo, N., Basak, S., Battaglia, P., Battaner, E., Battye, R., Benabed, K., Benoît, A., Benoit-Lévy, A., Bernard, J.-P., Bersanelli, M., Bertincourt, B., Bielewicz, P., Bikmaev, I., Bock, J. J., Böhringer, H., Bonaldi, A., Bonavera, L., Bond, J. R., Borrill, J., Bouchet, F. R., Boulanger, F., Bucher, M., Burenin, R., Burigana, C., Butler, R. C., Calabrese, E., Cardoso, J.-F., Carvalho, P., Casaponsa, B., Castex, G., Catalano, A., Challinor, A., Chamballu, A., Chary, R.-R., Chiang, H. C., Chluba, J., Chon, G., Christensen, P. R., Church, S., Clemens, M., Clements, D. L., Colombi, S., Colombo, L. P. L., Combet, C., Comis, B., Contreras, D., Couchot, F., Coulais, A., Crill, B. P., Cruz, M., Curto, A., Cuttaia, F., Danese, L., Davies, R. D., Davis, R. J., de Bernardis, P., de Rosa, A., de Zotti, G., Delabrouille, J., Delouis, J.-M., Désert, F.-X., Di Valentino, E., Dickinson, C., Diego, J. M., Dolag, K., Dole, H., Donzelli, S., Doré, O., Douspis, M., Ducout, A., Dunkley, J.,

Dupac, X., Efstathiou, G., Eisenhardt, P. R. M., Elsner, F., Enßlin, T. A., Eriksen, H. K., Falgarone, E., Fantaye, Y., Farhang, M., Feeney, S., Fergusson, J., Fernandez-Cobos, R., Feroz, F., Finelli, F., Florido, E., Forni, O., Frailis, M., Fraisse, A. A., Franceschet, C., Franceschi, E., Frejsel, A., Frolov, A., Galeotta, S., Galli, S., Ganga, K., Gauthier, C., Génova-Santos, R. T., Gerbino, M., Ghosh, T., Giard, M., Giraud-Héraud, Y., Giusarma, E., Gjerløw, E., González-Nuevo, J., Górski, K. M., Grainge, K. J. B., Gratton, S., Gregorio, A., Gruppuso, A., Gudmundsson, J. E., Hamann, J., Handley, W., Hansen, F. K., Hanson, D., Harrison, D. L., Heavens, A., Helou, G., Henrot-Versillé, S., Hernández-Monteagudo, C., Herranz, D., Hildebrandt, S. R., Hivon, E., Hobson, M., Holmes, W. A., Hornstrup, A., Hovest, W., Huang, Z., Huffenberger, K. M., Hurier, G., Ili´c, S., Jaffe, A. H., Jaffe, T. R., Jin, T., Jones, W. C., Juvela, M., Karakci, A., Keihänen, E., Keskitalo, R., Khamitov, I., Kiiveri, K., Kim, J., Kisner, T. S., Kneissl, R., Knoche, J., Knox, L., Krachmalnicoff, N., Kunz, M., Kurki-Suonio, H., Lacasa, F., Lagache, G., Lähteenmäki, A., Lamarre, J.-M., Langer, M., Lasenby, A., Lattanzi, M., Lawrence, C. R., Le Jeune, M., Leahy, J. P., Lellouch, E., Leonardi, R., León-Tavares, J., Lesgourgues, J., Levrier, F., Lewis, A., Liguori, M., Lilje, P. B., Lilley, M., Linden-Vørnle, M., Lindholm, V., Liu, H., López-Caniego, M., Lubin, P. M., Ma, Y.-Z., Macías-Pérez, J. F., Maggio, G., Maino, D., Mak, D. S. Y., Mandolesi, N., Mangilli, A., Marchini, A., Marcos-Caballero, A., Marinucci, D., Maris, M., Marshall, D. J., Martin, P. G., Martinelli, M., Martínez-González, E., Masi, S., Matarrese, S., Mazzotta, P., McEwen, J. D., McGehee, P., Mei, S., Meinhold, P. R., Melchiorri, A., Melin, J.-B., Mendes, L., Mennella, A., Migliaccio, M., Mikkelsen, K., Millea, M., Mitra, S., Miville-Deschênes, M.-A., Molinari, D., Moneti, A., Montier, L., Moreno, R., Morgante, G., Mortlock, D., Moss, A., Mottet, S., Münchmeyer, M., Munshi, D., Murphy, J. A., Narimani, A., Naselsky, P., Nastasi, A., Nati, F., Natoli, P., Negrello, M., Netterfield, C. B., Nørgaard-Nielsen, H. U., Noviello, F., Novikov, D., Novikov, I., Olamaie, M., Oppermann, N., Orlando, E., Oxborrow, C. A., Paci, F., Pagano, L., Pajot, F., Paladini, R., Pandolfi, S., Paoletti, D., Partridge, B., Pasian, F., Patanchon, G., Pearson, T. J., Peel, M., Peiris, H. V., Pelkonen, V.-M., Perdereau, O., Perotto, L., Perrott, Y. C., Perrotta, F., Pettorino, V., Piacentini, F., Piat, M., Pierpaoli, E., Pietrobon, D., Plaszczynski, S., Pogosyan, D., Pointecouteau, E., Polenta, G., Popa, L., Pratt, G. W., Prézeau, G., Prunet, S., Puget, J.-L., Rachen, J. P., Racine, B., Reach, W. T., Rebolo, R., Reinecke, M., Remazeilles, M., Renault, C., Renzi, A., Ristorcelli, I., Rocha, G., Roman, M., Romelli, E., Rosset, C., Rossetti, M., Rotti, A., Roudier, G., Rouillé d´Orfeuil, B., Rowan-Robinson, M., Rubiño-Martín, J. A., Ruiz-Granados, B., Rumsey, C., Rusholme, B., Said, N., Salvatelli, V., Salvati, L., Sandri, M., Sanghera, H. S., Santos, D., Saunders, R. D. E., Sauvé, A., Savelainen, M., Savini, G., Schaefer, B. M., Schammel, M. P., Scott, D., Seiffert, M. D., Serra, P., Shellard, E. P. S., Shimwell, T. W., Shiraishi, M., Smith, K., Souradeep, T., Spencer, L. D., Spinelli, M., Stanford, S. A., Stern, D., Stolyarov, V., Stompor, R., Strong, A. W., Sudiwala, R., Sunyaev, R., Sutter, P., Sutton, D., Suur-Uski, A.-S., Sygnet, J.-F., Tauber, J. A., Tavagnacco, D., Terenzi, L., Texier, D., Toffolatti, L., Tomasi, M., Tornikoski, M., Tramonte, D., Tristram, M., Troja, A., Trombetti, T., Tucci, M., Tuovinen, J., Türler, M., Umana, G., Valenziano, L., Valiviita, J., Van Tent, F., Vassallo, T., Vibert, L., Vidal, M., Viel, M., Vielva, P., Villa, F., Wade, L. A., Walter, B., Wandelt, B. D., Watson, R., Wehus, I. K., Welikala, N., Weller, J., White, M., White, S. D. M., Wilkinson, A., Yvon, D., Zacchei, A., Zibin, J. P., and Zonca, A. Planck 2015 results - i. overview of products and scientific results. A&A, 594:A1, 2016.

[140] Planck Collaboration, P. A. R. Ade, N. Aghanim, M. Arnaud, M. Ashdown, J. Aumont, C. Baccigalupi, A. J. Banday, R. B. Barreiro, J. G. Bartlett, N. Bartolo, E. Battaner, R. Battye, K. Benabed, A. Benoît, A. Benoit-Lévy, J. P. Bernard, M. Bersanelli, P. Bielewicz, J. J. Bock, A. Bonaldi, L. Bonavera, J. R. Bond, J. Borrill, F. R. Bouchet, F. Boulanger, M. Bucher, C. Burigana, R. C. Butler, E. Calabrese, J. F. Cardoso, A. Catalano, A. Challinor, A. Chamballu, R. R. Chary, H. C. Chiang,

J. Chluba, P. R. Christensen, S. Church, D. L. Clements, S. Colombi, L. P. L. Colombo, C. Combet, A. Coulais, B. P. Crill, A. Curto, F. Cuttaia, L. Danese, R. D. Davies, R. J. Davis, P. de Bernardis, A. de Rosa, G. de Zotti, J. Delabrouille, F. X. Désert, E. Di Valentino, C. Dickinson, J. M. Diego, K. Dolag, H. Dole, S. Donzelli, O. Doré, M. Douspis, A. Ducout, J. Dunkley, X. Dupac, G. Efstathiou, F. Elsner, T. A. Enßlin, H. K. Eriksen, M. Farhang, J. Fergusson, F. Finelli, O. Forni, M. Frailis, A. A. Fraisse, E. Franceschi, A. Frejsel, S. Galeotta, S. Galli, K. Ganga, C. Gauthier, M. Gerbino, T. Ghosh, M. Giard, Y. Giraud-Héraud, E. Giusarma, E. Gjerløw, J. González-Nuevo, K. M. Górski, S. Gratton, A. Gregorio, A. Gruppuso, J. E. Gudmundsson, J. Hamann, F. K. Hansen, D. Hanson, D. L. Harrison, G. Helou, S. Henrot-Versillé, C. Hernández-Monteagudo, D. Herranz, S. R. Hildebrandt, E. Hivon, M. Hobson, W. A. Holmes, A. Hornstrup, W. Hovest, Z. Huang, K. M. Huffenberger, G. Hurier, A. H. Jaffe, T. R. Jaffe, W. C. Jones, M. Juvela, E. Keihänen, R. Keskitalo, T. S. Kisner, R. Kneissl, J. Knoche, L. Knox, M. Kunz, H. Kurki-Suonio, G. Lagache, A. Lähteenmäki, J. M. Lamarre, A. Lasenby, M. Lattanzi, C. R. Lawrence, J. P. Leahy, R. Leonardi, J. Lesgourgues, F. Levrier, A. Lewis, M. Liguori, P. B. Lilje, M. Linden-Vørnle, M. López-Caniego, P. M. Lubin, J. F. Macías-Pérez, G. Maggio, D. Maino, N. Mandolesi, A. Mangilli, A. Marchini, M. Maris, P. G. Martin, M. Martinelli, E. Martínez-González, S. Masi, S. Matarrese, P. McGehee, P. R. Meinhold, A. Melchiorri, J. B. Melin, L. Mendes, A. Mennella, M. Migliaccio, M. Millea, S. Mitra, M. A. Miville-Deschênes, A. Moneti, L. Montier, G. Morgante, D. Mortlock, A. Moss, D. Munshi, J. A. Murphy, P. Naselsky, F. Nati, P. Natoli, C. B. Netterfield, H. U. Nørgaard-Nielsen, F. Noviello, D. Novikov, I. Novikov, C. A. Oxborrow, F. Paci, L. Pagano, F. Pajot, R. Paladini, D. Paoletti, B. Partridge, F. Pasian, G. Patanchon, T. J. Pearson, O. Perdereau, L. Perotto, F. Perrotta, V. Pettorino, F. Piacentini, M. Piat, E. Pierpaoli, D. Pietrobon, S. Plaszczynski, E. Pointecouteau, G. Polenta, L. Popa, G. W. Pratt, G. Prézeau, S. Prunet, J. L. Puget, J. P. Rachen, W. T. Reach, R. Rebolo, M. Reinecke, M. Remazeilles, C. Renault, A. Renzi, I. Ristorcelli, G. Rocha, C. Rosset, M. Rossetti, G. Roudier, B. Rouillé d'Orfeuil, M. Rowan-Robinson, J. A. Rubiño-Martín, B. Rusholme, N. Said, V. Salvatelli, L. Salvati, M. Sandri, D. Santos, M. Savelainen, G. Savini, D. Scott, M. D. Seiffert, P. Serra, E. P. S. Shellard, L. D. Spencer, M. Spinelli, V. Stolyarov, R. Stompor, R. Sudiwala, R. Sunyaev, D. Sutton, A. S. Suur-Uski, J. F. Sygnet, J. A. Tauber, L. Terenzi, L. Toffolatti, M. Tomasi, M. Tristram, T. Trombetti, M. Tucci, J. Tuovinen, M. Türler, G. Umana, L. Valenziano, J. Valiviita, F. Van Tent, P. Vielva, F. Villa, L. A. Wade, B. D. Wandelt, I. K. Wehus, M. White, S. D. M. White, A. Wilkinson, D. Yvon, A. Zacchei, and A. Zonca. Planck 2015 results. XIII. Cosmological parameters. , 594:A13, September 2016.

[141] Planck Collaboration, N. Aghanim, Y. Akrami, M. Ashdown, J. Aumont, C. Baccigalupi, M. Ballardini, A. J. Banday, R. B. Barreiro, N. Bartolo, S. Basak, R. Battye, K. Benabed, J. P. Bernard, M. Bersanelli, P. Bielewicz, J. J. Bock, J. R. Bond, J. Borrill, F. R. Bouchet, F. Boulanger, M. Bucher, C. Burigana, R. C. Butler, E. Calabrese, J. F. Cardoso, J. Carron, A. Challinor, H. C. Chiang, J. Chluba, L. P. L. Colombo, C. Combet, D. Contreras, B. P. Crill, F. Cuttaia, P. de Bernardis, G. de Zotti, J. Delabrouille, J. M. Delouis, E. Di Valentino, J. M. Diego, O. Doré, M. Douspis, A. Ducout, X. Dupac, S. Dusini, G. Efstathiou, F. Elsner, T. A. Enßlin, H. K. Eriksen, Y. Fantaye, M. Farhang, J. Fergusson, R. Fernandez-Cobos, F. Finelli, F. Forastieri, M. Frailis, A. A. Fraisse, E. Franceschi, A. Frolov, S. Galeotta, S. Galli, K. Ganga, R. T. Génova-Santos, M. Gerbino, T. Ghosh, J. González-Nuevo, K. M. Górski, S. Gratton, A. Gruppuso, J. E. Gudmundsson, J. Hamann, W. Handley, F. K. Hansen, D. Herranz, S. R. Hildebrandt, E. Hivon, Z. Huang, A. H. Jaffe, W. C. Jones, A. Karakci, E. Keihänen, R. Keskitalo, K. Kiiveri, J. Kim, T. S. Kisner, L. Knox, N. Krachmalnicoff, M. Kunz, H. Kurki-Suonio, G. Lagache, J. M. Lamarre, A. Lasenby, M. Lattanzi, C. R. Lawrence, M. Le Jeune, P. Lemos, J. Lesgourgues, F. Levrier, A. Lewis, M. Liguori, P. B. Lilje, M. Lilley, V. Lindholm,

M. López-Caniego, P. M. Lubin, Y. Z. Ma, J. F. Macías-Pérez, G. Maggio, D. Maino, N. Mandolesi, A. Mangilli, A. Marcos-Caballero, M. Maris, P. G. Martin, M. Martinelli, E. Martínez-González, S. Matarrese, N. Mauri, J. D. McEwen, P. R. Meinhold, A. Melchiorri, A. Mennella, M. Migliaccio, M. Millea, S. Mitra, M. A. Miville-Deschênes, D. Molinari, L. Montier, G. Morgante, A. Moss, P. Natoli, H. U. Nørgaard-Nielsen, L. Pagano, D. Paoletti, B. Partridge, G. Patanchon, H. V. Peiris, F. Perrotta, V. Pettorino, F. Piacentini, L. Polastri, G. Polenta, J. L. Puget, J. P. Rachen, M. Reinecke, M. Remazeilles, A. Renzi, G. Rocha, C. Rosset, G. Roudier, J. A. Rubiño-Martín, B. Ruiz-Granados, L. Salvati, M. Sandri, M. Savelainen, D. Scott, E. P. S. Shellard, C. Sirignano, G. Sirri, L. D. Spencer, R. Sunyaev, A. S. Suur-Uski, J. A. Tauber, D. Tavagnacco, M. Tenti, L. Toffolatti, M. Tomasi, T. Trombetti, L. Valenziano, J. Valiviita, B. Van Tent, L. Vibert, P. Vielva, F. Villa, N. Vittorio, B. D. Wandelt, I. K. Wehus, M. White, S. D. M. White, A. Zacchei, and A. Zonca. Planck 2018 results. VI. Cosmological parameters. , 641:A6, September 2020.

[142] Planck Collaboration, Aghanim, N., Akrami, Y., Ashdown, M., Aumont, J., Baccigalupi, C., Ballardini, M., Banday, A. J., Barreiro, R. B., Bartolo, N., Basak, S., Benabed, K., Bernard, J.-P., Bersanelli, M., Bielewicz, P., Bock, J. J., Bond, J. R., Borrill, J., Bouchet, F. R., Boulanger, F., Bucher, M., Burigana, C., Butler, R. C., Calabrese, E., Cardoso, J.-F., Carron, J., Casaponsa, B., Challinor, A., Chiang, H. C., Colombo, L. P. L., Combet, C., Crill, B. P., Cuttaia, F., de Bernardis, P., de Rosa, A., de Zotti, G., Delabrouille, J., Delouis, J.-M., Di Valentino, E., Diego, J. M., Doré, O., Douspis, M., Ducout, A., Dupac, X., Dusini, S., Efstathiou, G., Elsner, F., Enßlin, T. A., Eriksen, H. K., Fantaye, Y., Fernandez-Cobos, R., Finelli, F., Frailis, M., Fraisse, A. A., Franceschi, E., Frolov, A., Galeotta, S., Galli, S., Ganga, K., Génova-Santos, R. T., Gerbino, M., Ghosh, T., Giraud-Héraud, Y., González-Nuevo, J., Górski, K. M., Gratton, S., Gruppuso, A., Gudmundsson, J. E., Hamann, J., Handley, W., Hansen, F. K., Herranz, D., Hivon, E., Huang, Z., Jaffe, A. H., Jones, W. C., Keihänen, E., Keskitalo, R., Kiiveri, K., Kim, J., Kisner, T. S., Krachmalnicoff, N., Kunz, M., Kurki-Suonio, H., Lagache, G., Lamarre, J.-M., Lasenby, A., Lattanzi, M., Lawrence, C. R., Le Jeune, M., Levrier, F., Lewis, A., Liguori, M., Lilje, P. B., Lilley, M., Lindholm, V., López-Caniego, M., Lubin, P. M., Ma, Y.-Z., Macías-Pérez, J. F., Maggio, G., Maino, D., Mandolesi, N., Mangilli, A., Marcos-Caballero, A., Maris, M., Martin, P. G., Martínez-González, E., Matarrese, S., Mauri, N., McEwen, J. D., Meinhold, P. R., Melchiorri, A., Mennella, A., Migliaccio, M., Millea, M., Miville-Deschênes, M.-A., Molinari, D., Moneti, A., Montier, L., Morgante, G., Moss, A., Natoli, P., Nørgaard-Nielsen, H. U., Pagano, L., Paoletti, D., Partridge, B., Patanchon, G., Peiris, H. V., Perrotta, F., Pettorino, V., Piacentini, F., Polenta, G., Puget, J.-L., Rachen, J. P., Reinecke, M., Remazeilles, M., Renzi, A., Rocha, G., Rosset, C., Roudier, G., Rubiño-Martín, J. A., Ruiz-Granados, B., Salvati, L., Sandri, M., Savelainen, M., Scott, D., Shellard, E. P. S., Sirignano, C., Sirri, G., Spencer, L. D., Sunyaev, R., Suur-Uski, A.-S., Tauber, J. A., Tavagnacco, D., Tenti, M., Toffolatti, L., Tomasi, M., Trombetti, T., Valiviita, J., Van Tent, B., Vielva, P., Villa, F., Vittorio, N., Wandelt, B. D., Wehus, I. K., Zacchei, A., and Zonca, A. Planck 2018 results - v. cmb power spectra and likelihoods. A&A, 641:A5, 2020.

[143] Carl D. Reintsema, Jörn Beyer, Sae Woo Nam, Steve Deiker, Gene C. Hilton, Kent Irwin, John Martinis, Joel Ullom, Leila R. Vale, and Mike MacIntosh. Prototype system for superconducting quantum interference device multiplexing of large-format transition-edge sensor arrays. Review of Scientific Instruments, 74(10):4500–4508, 2003.

[144] P. L. Richards. Bolometers for infrared and millimeter waves. Journal of Applied Physics, 76(1):1–24, July 1994.

[145] M. L. Ridder, P. Khosropanah, R. A. Hijmering, T. Suzuki, M. P. Bruijn, H. F. C. Hoevers, J. R. Gao, and M. R. Zuiddam. Fabrication of Low-Noise TES Arrays for the SAFARI Instrument on SPICA. Journal of Low Temperature Physics, 184(1-2):60–65, July 2016.

[146] Adam G. Riess, Stefano Casertano, Wenlong Yuan, Lucas M. Macri, and Dan Scolnic. Large Magellanic Cloud Cepheid Standards Provide a 1% Foundation for the Determination of the Hubble Constant and Stronger Evidence for Physics beyond ΛCDM. , 876(1):85, May 2019.

[147] Adam G. Riess, Alexei V. Filippenko, Peter Challis, Alejandro Clocchiatti, Alan Diercks, Peter M. Garnavich, Ron L. Gilliland, Craig J. Hogan, Saurabh Jha, Robert P. Kirshner, B. Leibundgut, M. M. Phillips, David Reiss, Brian P. Schmidt, Robert A. Schommer, R. Chris Smith, J. Spyromilio, Christopher Stubbs, Nicholas B. Suntzeff, and John Tonry. Observational Evidence from Supernovae for an Accelerating Universe and a Cosmological Constant. , 116(3):1009–1038, September 1998.

[148] K. Rostem, D. T. Chuss, K. L. Denis, and E. J. Wollack. Wide-stopband aperiodic phononic filters. Journal of Physics D Applied Physics, 49(25):255301, June 2016.

[149] J. Säily and A. V. Räisänen. Characterization of Submillimeter Wave Absorbers from 200 600 GHz. International Journal of Infrared and Millimeter Waves, 25(1):71–88, Jan 2004.

[150] M. Salatino, J. Austermann, K. L. Thompson, P. A. R. Ade, X. Bai, J. A. Beall, D. T. Becker, Y. Cai, Z. Chang, D. Chen, J. Connors, P. Chen, B. Dober, J. Delabrouille, S. M. Duff, G. Gao, R. C. Givhan, S. Ghosh, G. Hilton, B. Hu, J. Hubmayr, E. Karpel, C.-L. Kuo, H. Li, M. Li, S.-Y. Li, X. Li, M. Link, Y. Li, H. Liu, L. Liu, Y. Liu, F. Lu, T. Lukas, X. Lu, J. A. B. Mates, J. Mathewson, P. Mauskopf, J. Meinke, J. Montana-Lopez, J. Moore, J. Shi, A. K. Sinclair, R. Stephenson, W. Sun, Y.-H. Tseng, C. Tucker, J. Ullom, L. Vale, J. van Lanen, M. Vissers, S. Walker, B. Wang, G. Wang, J. Wang, E. Weeks, Di Wu, Y.-H. Wu, J. Xia, H. Xu, J. Yao, Y. Yao, K. W. Yoon, B. Yue, H. Zhai, A. Zhang, Laiyu Zhang, Le Zhang, P. Zhang, T. Zhang, Xinmin Zhang, Yifei Zhang, Yongjie Zhang, G.-B. Zhao, and W. Zhao. The design of the Ali CMB Polarization Telescope receiver. In Jonas Zmuidzinas and Jian-Rong Gao, editors, Millimeter, Submillimeter, and Far-Infrared Detectors and Instrumentation for Astronomy X, volume 11453, pages 341 – 360. International Society for Optics and Photonics, SPIE, 2020.

[151] Maria Salatino, Jason Austermann, Jeremy Meinke, Adrian K. Sinclair, Samantha Walker, Xiran Bai, James Beall, Jake Connors, Bradley Dober, Shannon M. Duff, Richard C. Givhan, Gene Hilton, Johannes Hubmayr, Ethan D. Karpel, Chao-Lin Kuo, Hamdi Mani, John A.B. Mates, Justin Mathewson, Philip Mauskopf, Jordi A. Montana-Lopez, Ryan Stephenson, Keith L. Thompson, Joel Ullom, Jeff van Lanen, Ki Won Yoon, Eric L. Weeks, Yi-Han Wu, and Xinmin Zhang. Current status of the ali cmb polarization telescope focal plane camera. IEEE Transactions on Applied Superconductivity, submitted.

[152] J. T. Sayre, C. L. Reichardt, J. W. Henning, P. A. R. Ade, A. J. Anderson, J. E. Austermann, J. S. Avva, J. A. Beall, A. N. Bender, B. A. Benson, F. Bianchini, L. E. Bleem, J. E. Carlstrom, C. L. Chang, P. Chaubal, H. C. Chiang, R. Citron, C. Corbett Moran, T. M. Crawford, A. T. Crites, T. de Haan, M. A. Dobbs, W. Everett, J. Gallicchio, E. M. George, A. Gilbert, N. Gupta, N. W. Halverson, N. Harrington, G. C. Hilton, G. P. Holder, W. L. Holzapfel, J. D. Hrubes, N. Huang, J. Hubmayr, K. D. Irwin, L. Knox, A. T. Lee, D. Li, A. Lowitz, J. J. McMahon, S. S. Meyer, L. M. Mocanu, J. Montgomery, A. Nadolski, T. Natoli, J. P. Nibarger, G. Noble, V. Novosad, S. Padin, S. Patil, C. Pryke, J. E. Ruhl, B. R. Saliwanchik, K. K. Schaffer, C. Sievers, G. Smecher, A. A. Stark, C. Tucker, K. Vanderlinde,

T. Veach, J. D. Vieira, G. Wang, N. Whitehorn, W. L. K. Wu, and V. Yefremenko. Measurements of *b*-mode polarization of the cosmic microwave background from 500 square degrees of sptpol data. Phys. Rev. D, 101:122003, Jun 2020.

[153] James A. Schlaerth. Microwave Kinetic Inductance Detector Camera Development for Millimeter-Wave Astrophysics. PhD thesis, University of Colorado Boulder, 2010.

[154] Neelima Sehgal, Hy Trac, Viviana Acquaviva, Peter A. R. Ade, Paula Aguirre, Mandana Amiri, John W. Appel, L. Felipe Barrientos, Elia S. Battistelli, J. Richard Bond, Ben Brown, Bryce Burger, Jay Chervenak, Sudeep Das, Mark J. Devlin, Simon R. Dicker, W. Bertrand Doriese, Joanna Dunkley, Rolando Dünner, Thomas Essinger-Hileman, Ryan P. Fisher, Joseph W. Fowler, Amir Hajian, Mark Halpern, Matthew Hasselfield, Carlos Hernández-Monteagudo, Gene C. Hilton, Matt Hilton, Adam D. Hincks, Renée Hlozek, David Holtz, Kevin M. Huffenberger, David H. Hughes, John P. Hughes, Leopoldo Infante, Kent D. Irwin, Andrew Jones, Jean Baptiste Juin, Jeff Klein, Arthur Kosowsky, Judy M. Lau, Michele Limon, Yen-Ting Lin, Robert H. Lupton, Tobias A. Marriage, Danica Marsden, Krista Martocci, Phil Mauskopf, Felipe Menanteau, Kavilan Moodley, Harvey Moseley, Calvin B. Netterfield, Michael D. Niemack, Michael R. Nolta, Lyman A. Page, Lucas Parker, Bruce Partridge, Beth Reid, Blake D. Sherwin, Jon Sievers, David N. Spergel, Suzanne T. Staggs, Daniel S. Swetz, Eric R. Switzer, Robert Thornton, Carole Tucker, Ryan Warne, Ed Wollack, and Yue Zhao. The Atacama Cosmology Telescope: Cosmology from Galaxy Clusters Detected via the Sunyaev-Zel'dovich Effect. , 732(1):44, May 2011.

[155] E. Shirokoff, P. S. Barry, C. M. Bradford, G. Chattopadhyay, P. Day, S. Doyle, S. Hailey-Dunsheath, M. I. Hollister, A. Kovács, C. McKenney, H. G. Leduc, N. Llombart, D. P. Marrone, P. Mauskopf, R. O'Brient, S. Padin, T. Reck, L. J. Swenson, and J. Zmuidzinas. MKID development for SuperSpec: an on-chip, mm-wave, filter-bank spectrometer. In Wayne S. Holland and Jonas Zmuidzinas, editors, Millimeter, Submillimeter, and Far-Infrared Detectors and Instrumentation for Astronomy VI, volume 8452 of Society of Photo-Optical Instrumentation Engineers (SPIE) Conference Series, page 84520R, September 2012.

[156] Sara M. Simon, Jason Austermann, James A. Beall, Steve K Choi, Kevin P. Coughlin, Shannon M. Duff, Patricio A. Gallardo, Shawn W. Henderson, Felicity B. Hills, Shuay-Pwu Patty Ho, Johannes Hubmayr, Alec Josaitis, Brian J. Koopman, Jeff J. McMahon, Federico Nati, Laura Newburgh, Michael D. Niemack, Maria Salatino, Alessandro Schillaci, Benjamin L. Schmitt, Suzanne T. Staggs, Eve M. Vavagiakis, Jonathan Ward, and Edward J. Wollack. The design and characterization of wideband spline-profiled feedhorns for Advanced ACTPol. In Wayne S. Holland and Jonas Zmuidzinas, editors, Millimeter, Submillimeter, and Far-Infrared Detectors and Instrumentation for Astronomy VIII, volume 9914, page 991416. International Society for Optics and Photonics, SPIE, 2016.

[157] G. F. Smoot, C. L. Bennett, A. Kogut, E. L. Wright, J. Aymon, N. W. Boggess, E. S. Cheng, G. de Amici, S. Gulkis, M. G. Hauser, G. Hinshaw, P. D. Jackson, M. Janssen, E. Kaita, T. Kelsall, P. Keegstra, C. Lineweaver, K. Loewenstein, P. Lubin, J. Mather, S. S. Meyer, S. H. Moseley, T. Murdock, L. Rokke, R. F. Silverberg, L. Tenorio, R. Weiss, and D. T. Wilkinson. Structure in the COBE Differential Microwave Radiometer First-Year Maps. , 396:L1, September 1992.

[158] Volker Springel, Carlos S. Frenk, and Simon D. M. White. The large-scale structure of the Universe. , 440(7088):1137–1144, April 2006.

[159] Johannes G. Staguhn. Scientific Capabilities Enabled by Future Millimeter through FIR instrumentation and observatories. In Physics and Chemistry of Star Formation: The Dynamical ISM Across Time and Spatial Scales, page 297, February 2023.

[160] B. A. Steinbach, J. J. Bock, H. T. Nguyen, R. C. O'Brient, and A. D. Turner. Thermal Kinetic Inductance Detectors for Ground-Based Millimeter-Wave Cosmology. Journal of Low Temperature Physics, 193(3-4):88–95, November 2018.

[161] Jason R. Stevens, Nicholas F. Cothard, Eve M. Vavagiakis, Aamir Ali, Kam Arnold, Jason E. Austermann, Steve K. Choi, Bradley J. Dober, Cody Duell, Shannon M. Duff, Gene C. Hilton, Shuay-Pwu Patty Ho, Thuong D. Hoang, Johannes Hubmayr, Adrian T. Lee, Aashrita Mangu, Federico Nati, Michael D. Niemack, Christopher Raum, Mario Renzullo, Maria Salatino, Trevor Sasse, Sara M. Simon, Suzanne Staggs, Aritoki Suzuki, Patrick Truitt, Joel Ullom, John Vivalda, Michael R. Vissers, Samantha Walker, Benjamin Westbrook, Edward J. Wollack, Zhilei Xu, and Daniel Yohannes. Characterization of Transition Edge Sensors for the Simons Observatory. Journal of Low Temperature Physics, 199(3-4):672–680, February 2020.

[162] R. A. Sunyaev and Ya. B. Zeldovich. The Spectrum of Primordial Radiation, its Distortions and their Significance. Comments on Astrophysics and Space Physics, 2:66, March 1970.

[163] R. A. Sunyaev and Ya. B. Zeldovich. The Observations of Relic Radiation as a Test of the Nature of X-Ray Radiation from the Clusters of Galaxies. Comments on Astrophysics and Space Physics, 4:173, November 1972.

[164] A. Suzuki, Kam Arnold, Jennifer Edwards, Greg Engargiola, Adnan Ghribi, William Holzapfel, Adrian T. Lee, Xiao Fan Meng, Michael J. Myers, Roger O'Brient, Erin Quealy, Gabriel Rebeiz, Paul Richards, Darin Rosen, and Praween Siritanasak. Multichroic dual-polarization bolometric detectors for studies of the cosmic microwave background. In , volume 8452 of Society of Photo-Optical Instrumentation Engineers (SPIE) Conference Series, page 84523H, Sep 2012.

[165] T. Suzuki, P. Khosropanah, M. L. Ridder, R. A. Hijmering, J. R. Gao, H. Akamatsu, L. Gottardi, J. van der Kuur, and B. D. Jackson. Development of Ultra-Low-Noise TES Bolometer Arrays. Journal of Low Temperature Physics, 184(1-2):52–59, July 2016.

[166] L. J. Swenson, P. K. Day, B. H. Eom, H. G. Leduc, N. Llombart, C. M. McKenney, O. Noroozian, and J. Zmuidzinas. Operation of a titanium nitride superconducting microresonator detector in the nonlinear regime. Journal of Applied Physics, 113(10), 03 2013. 104501.

[167] Q. Y. Tang, P. S. Barry, T. W. Cecil, and E. Shirokoff. Fabrication of omt-coupled kinetic inductance detector for cmb detection. Journal of Low Temperature Physics, (1).

[168] C. N. Thomas, S. Withington, Z. Sun, T. Skyrme, and D. J. Goldie. Nonlinear effects in superconducting thin film microwave resonators. New Journal of Physics, 22(7):073028, July 2020.

[169] Michael Tinkham. Introduction to Superconductivity. Dover Publications, 2 edition, June 2004.

[170] Joel N Ullom and Douglas A Bennett. Review of superconducting transition-edge sensors for x-ray and gamma-ray spectroscopy*. Superconductor Science and Technology, 28(8):084003, jul 2015.

[171] Floris van der Tak. Star & planet formation: Upcoming opportunities in the space-based infrared. In Physics and Chemistry of Star Formation: The Dynamical ISM Across Time and Spatial Scales, page 313, February 2023.

[172] Joaquin Vieira, James Aguirre, C. Matt Bradford, Jeffrey Filippini, Christopher Groppi, Dan Marrone, Matthieu Bethermin, Tzu-Ching Chang, Mark Devlin, Oliver Dore, Jianyang Frank Fu, Steven Hailey Dunsheath, Gilbert Holder, Garrett Keating, Ryan Keenan, Ely Kovetz, Guilaine Lagache, Philip Mauskopf, Desika Narayanan, Gergo Popping, Erik Shirokoff, Rachel Somerville, Isaac Trumper, Bade Uzgil, and Jonas Zmuidzinas. The Terahertz Intensity Mapper (TIM): a Next-Generation Experiment for Galaxy Evolution Studies. arXiv e-prints, page arXiv:2009.14340, September 2020.

[173] M. R. Vissers, J. E. Austermann, M. Malnou, C. M. McKenney, B. Dober, J. Hubmayr, G. C. Hilton, J. N. Ullom, and J. Gao. Ultrastable millimeter-wave kinetic inductance detectors. Applied Physics Letters, 116(3):032601, January 2020.

[174] Michael R. Vissers, Jiansong Gao, Martin Sandberg, Shannon M. Duff, David S. Wisbey, Kent D. Irwin, and David P. Pappas. Proximity-coupled Ti/TiN multilayers for use in kinetic inductance detectors. Applied Physics Letters, 102(23):232603, June 2013.

[175] George M. Voellmer, Christine A. Allen, Michael J. Amato, Sachidananda R. Babu, Arlin E. Bartels, Dominic J. Benford, Rebecca J. Derro, C. D. Dowell, D. A. Harper, Murzy D. Jhabvala, S. H. Moseley, Timothy Rennick, Peter J. Shirron, W. W. Smith, and Johannes G. Staguhn. Design and fabrication of two-dimensional semiconducting bolometer arrays for HAWC and SHARC-II. In Thomas G. Phillips and Jonas Zmuidzinas, editors, Millimeter and Submillimeter Detectors for Astronomy, volume 4855 of Society of Photo-Optical Instrumentation Engineers (SPIE) Conference Series, pages 63–72, February 2003.

[176] S. Walker, C. E. Sierra, J. E. Austermann, J. A. Beall, D. T. Becker, B. J. Dober, S. M. Duff, G. C. Hilton, J. Hubmayr, J. L. Van Lanen, J. J. McMahon, S. M. Simon, J. N. Ullom, and M. R. Vissers. Demonstration of 220/280 GHz Multichroic Feedhorn-Coupled TES Polarimeter. Journal of Low Temperature Physics, 199(3-4):891–897, January 2020.

[177] Samantha Walker, Jason E. Austermann, James A. Beall, Bradley J. Dober, Shannon M. Duff, Gene C. Hilton, Johannes Hubmayr, Joel N. Ullom, Jeffrey L. Van Lanen, and Michael R. Vissers. Measurements of AlMn TES bolometers well described by simple electrothermal model. In Jonas Zmuidzinas and Jian-Rong Gao, editors, Millimeter, Submillimeter, and Far-Infrared Detectors and Instrumentation for Astronomy X, volume 11453, page 1145326. International Society for Optics and Photonics, SPIE, 2021.

[178] Alexander B. Walter, Neelay Fruitwala, Sarah Steiger, John I. Bailey, Nicholas Zobrist, Noah Swimmer, Isabel Lipartito, Jennifer Pearl Smith, Seth R. Meeker, Clint Bockstiegel, Gregoire Coiffard, Rupert Dodkins, Paul Szypryt, Kristina K. Davis, Miguel Daal, Bruce Bumble, Giulia Collura, Olivier Guyon, Julien Lozi, Sebastien Vievard, Nemanja Jovanovic, Frantz Martinache, Thayne Currie, and Benjamin A. Mazin. The mkid exoplanet camera for subaru scexao. Publications of the Astronomical Society of the Pacific, 132(1018):125005, nov 2020.

[179] Albert Wandui, James J. Bock, Clifford Frez, M. Hollister, Lorenzo Minutolo, Hien Nguyen, Bryan Steinbach, Anthony Turner, Jonas Zmuidzinas, and Roger O'Brient. Thermal kinetic inductance detectors for millimeter-wave detection. Journal of Applied Physics, 128(4):044508, July 2020.

[180] Albert K. Wandui, James J. Bock, Clifford Frez, Jon Hunacek, Lorenzo Minutolo, Hien Nguyen, Bryan Steinbach, Anthony Turner, Jonas Zmuidzinas, and Roger O'Brient. Antenna-coupled thermal kinetic inductance detectors for ground-based millimeter-wave cosmology. In Jonas Zmuidzinas and Jian-Rong Gao, editors, Millimeter, Submillimeter, and Far-Infrared Detectors and Instrumentation

for Astronomy X, volume 11453 of Society of Photo-Optical Instrumentation Engineers (SPIE) Conference Series, page 114531E, December 2020.

[181] S. J. Weber, K. W. Murch, D. H. Slichter, R. Vijay, and I. Siddiqi. Single crystal silicon capacitors with low microwave loss in the single photon regime. Applied Physics Letters, 98(17):172510, April 2011.

[182] Abigail Wessels, Kelsey Morgan, Daniel T. Becker, Johnathon D. Gard, Gene C. Hilton, John A. B. Mates, Carl D. Reintsema, Daniel R. Schmidt, Daniel S. Swetz, Joel N. Ullom, Leila R. Vale, and Douglas A. Bennett. A Model for Excess Johnson Noise in Superconducting Transition-edge Sensors. arXiv e-prints, page arXiv:1907.11343, July 2019.

[183] Jordan Wheeler, Jason Austermann, Michael Vissers, James Beall, Jiansong Gao, Jozsef Imrek, Edwin Heilweil, Douglas Bennett, Johnathan Gard, Jeff van Lanen, Johannes Hubmayr, and Joel Ullom. Broadband kinetic inductance detectors for far-IR observations. In Jonas Zmuidzinas and Jian-Rong Gao, editors, Millimeter, Submillimeter, and Far-Infrared Detectors and Instrumentation for Astronomy XI, volume 12190 of Society of Photo-Optical Instrumentation Engineers (SPIE) Conference Series, page 1219006, August 2022.

[184] E. A. Williams, S. Withington, C. N. Thomas, D. J. Goldie, and D. Osman. Superconducting transition edge sensors with phononic thermal isolation. Journal of Applied Physics, 124(14):144501, October 2018.

[185] Grant W. Wilson, Sophia Abi-Saad, Peter Ade, Itziar Aretxaga, Jason Austermann, Yvonne Ban, Joseph Bardin, James Beall, Marc Berthoud, Sean Bryan, John Bussan, Edgar Castillo, Miguel Chavez, Reid Contente, N. S. Denigris, Bradley Dober, Miranda Eiben, Daniel Ferrusca, Laura Fissel, Jiansong Gao, Joseph E. Golec, Robert Golina, Arturo Gomez, Sam Gordon, Robert Gutermuth, Gene Hilton, Mohsen Hosseini, Johannes Hubmayr, David Hughes, Stephen Kuczarski, Dennis Lee, Emily Lunde, Zhiyuan Ma, Hamdi Mani, Philip Mauskopf, Michael McCrackan, Christopher McKenney, Jeffrey McMahon, Giles Novak, Giampaolo Pisano, Alexandra Pope, Amy Ralston, Ivan Rodriguez, David Sanchez-Argüelles, F. Peter Schloerb, Sara Simon, Adrian Sinclair, Kamal Souccar, Ana Torres Campos, Carole Tucker, Joel Ullom, Eric Van Camp, Jeff Van Lanen, Miguel Velazquez, Michael Vissers, Eric Weeks, and Min S. Yun. The toltec camera: An overview of the instrument and in-lab testing results. In Jonas Zmuidzinas and Jian-Rong Gao, editors, Millimeter, Submillimeter, and Far-Infrared Detectors and Instrumentation for Astronomy X, Proceedings of SPIE - The International Society for Optical Engineering. SPIE, 2020. Funding Information: This work is supported in-part by the National Science Foundation, grant 1636621. The Mexican collaborators on TolTEC acknowledge support by Conacyt project FDC2016-1848. We also thank the Northwestern University Research Shop for their assistance with the design and construction of the Half-wave Plate Rotator and Tom Scott in the UMass Astronomy machine shop for machining a significant number of parts for TolTEC. Publisher Copyright: © COPYRIGHT SPIE. Downloading of the abstract is permitted for personal use only.; Millimeter, Submillimeter, and Far-Infrared Detectors and Instrumentation for Astronomy X 2020 ; Conference date: 14-12-2020 Through 22-12-2020.

[186] Kenneth C. Wong, Sherry H. Suyu, Geoff C. F. Chen, Cristian E. Rusu, Martin Millon, Dominique Sluse, Vivien Bonvin, Christopher D. Fassnacht, Stefan Taubenberger, Matthew W. Auger, Simon Birrer, James H. H. Chan, Frederic Courbin, Stefan Hilbert, Olga Tihhonova, Tommaso Treu, Adriano Agnello, Xuheng Ding, Inh Jee, Eiichiro Komatsu, Anowar J. Shajib, Alessandro Sonnenfeld, Roger D. Blandford, Léon V. E. Koopmans, Philip J. Marshall, and Georges Meylan. H0LiCOW

- XIII. A 2.4 per cent measurement of H_0 from lensed quasars: 5.3σ tension between early- and late-Universe probes. , 498(1):1420–1439, October 2020.

[187] K. W. Yoon, J. W. Appel, J. E. Austermann, J. A. Beall, D. Becker, B. A. Benson, L. E. Bleem, J. Britton, C. L. Chang, J. E. Carlstrom, H. M. Cho, A. T. Crites, T. Essinger-Hileman, W. Everett, N. W. Halverson, J. W. Henning, G. C. Hilton, K. D. Irwin, J. McMahon, J. Mehl, S. S. Meyer, S. Moseley, M. D. Niemack, L. P. Parker, S. M. Simon, S. T. Staggs, K. U-yen, C. Visnjic, E. Wollack, and Y. Zhao. Feedhorn-Coupled TES Polarimeters for Next-Generation CMB Instruments. In Betty Young, Blas Cabrera, and Aaron Miller, editors, The Thirteenth International Workshop on Low Temperature Detectors - LTD13, volume 1185 of American Institute of Physics Conference Series, pages 515–518, December 2009.

[188] Jonas Zmuidzinas. Thermal noise and correlations in photon detection. Appl. Opt., 42(25):4989–5008, Sep 2003.

[189] Jonas Zmuidzinas. Superconducting microresonators: Physics and applications. Annual Review of Condensed Matter Physics, 3:169–214, 2012.

[190] F. Zwicky. On the Masses of Nebulae and of Clusters of Nebulae. , 86:217, October 1937.